University of Zagreb
FACULTY OF ELECTRICAL ENGINEERING AND COMPUTING

Mario Hrgetić

VEHICLE DYNAMICS STATE ESTIMATION BASED ON SENSOR FUSION BY ADAPTIVE KALMAN FILTER

DOCTORAL THESIS

Zagreb, 2015

University of Zagreb
FACULTY OF ELECTRICAL ENGINEERING AND COMPUTING

Mario Hrgetić

VEHICLE DYNAMICS STATE ESTIMATION BASED ON SENSOR FUSION BY ADAPTIVE KALMAN FILTER

DOCTORAL THESIS

Supervisor(s): Professor Mario Cifrek, PhD
Professor Joško Deur, PhD

Zagreb, 2015

Sveučilište u Zagrebu
FAKULTET ELEKTROTEHNIKE I RAČUNARSTVA

MARIO HRGETIĆ

PROCJENA STANJA DINAMIKE VOZILA ZASNOVANA NA FUZIJI SENZORA PRIMJENOM ADAPTIVNOGA KALMANOVA FILTRA

DOKTORSKI RAD

Mentor(i): Prof. dr. sc. Mario Cifrek
Prof. dr. sc. Joško Deur

Zagreb, 2015.

This PhD thesis has been made at University of Zagreb, at Faculty of Electrical Engineering and Computing, Department of Electronic Systems and Information Processing and at Faculty of Mechanical Engineering and Naval Architecture, Department of Robotics and Production System Automation, Chair of Engineering Automation.

Supervisor(s): Professor Mario Cifrek, PhD

Professor Joško Deur, PhD

This thesis has 180 pages.

Doctoral thesis no: _____

About supervisors

Mario Cifrek was born in Varaždin in 1964. He received B.Sc., M.Sc. and Ph.D. degrees in electrical engineering from the University of Zagreb, Faculty of Electrical Engineering and Computing (FER), Zagreb, Croatia, in 1987, 1992, and 1997, respectively.

Since December 1987 he has been working at the Department of Electronic Systems and Information Processing, FER. In December 2012 he was promoted to Tenured Full Professor. He participated in seven scientific projects financed by the Ministry of Science, Education and Sports of the Republic of Croatia, and was a leader of the bilateral Croatian-Chinese scientific and technological project. He led one Proof-of-Concept (PoC) project of the BICRO agency. Currently he is a leader of the research project "Wireless body area network based on intrabody communication" financed by the University of Zagreb, and a project coordinator of a PoC project "Intrabody communication system". He is a co-author of five chapters in scientific books, 20 journal papers, 12 of them CC (WOS more than 90 citations), and 140 conference papers in the field of sensors, electronic instrumentation and biomedical engineering.

Prof. Cifrek is a member of IEEE (senior member), IFMBE, ESEM, IFAC, CROMBES, KoREMA, and an associate member of the Croatian Academy of Engineering. He participated in eight scientific or program committees at international conferences and also serves as a technical reviewer for various international journals. He was awarded the silver "Josip Lončar" medals for outstanding Master of Science thesis in 1992 and the doctoral dissertation in 1997, Annual Award "Rikard Podhorsky" of the Croatian Academy of Engineering in 2014, and the Annual award of the City of Zagreb in 2014.

Mario Cifrek je rođen 1964. godine u Varaždinu. Diplomirao je, magistrirao i doktorirao u polju elektrotehnike na Sveučilištu u Zagrebu Fakultetu elektrotehnike i računarstva (FER), 1987., 1992., odnosno 1997. godine.

Od prosinca 1987. godine radi na Zavodu za elektroničke sustave i obradbu informacija FER-a. U prosincu 2012. godine izabran je u zvanje redovitog profesora u trajnom zvanju. Sudjelovao je ne sedam znanstvenih projekata Ministarstva znanosti, obrazovanja i sporta Republike Hrvatske, vodio je jedan bilateralni projekt znanstveno-tehnološke suradnje s NR Kinom i jedan projekt iz Programa provjere inovativnog koncepta za znanstvenike i istraživače (PoC PUBLIC) agencije BICRO. Trenutno je voditelj istraživačkog projekta

„Bežične tjelesne mreže temeljene na prijenosu signala ljudskim tijelom“ financiranog u sklopu kratkoročne financijske potpore istraživanju Sveučilišta u Zagrebu i projekta „Sustav za bežičnu komunikaciju putem ljudskog tijela“ financiranog iz programa PoC PUBLIC. Suautor je pet poglavlja u znanstvenim knjigama, objavio je 20 radova u časopisima od čega 12 CC (WOS više od 90 citata), te više od 140 radova na međunarodnim i domaćim znanstvenim skupovima u području senzora, elektroničke instrumentacije i biomedicinskog inženjerstva.

Prof. Cifrek član je stručnih udruga IEEE (seniorski status), IFMBE, ESEM, IFAC, HDMBT i KoREMA. Također je član suradnik Akademije tehničkih znanosti Hrvatske (HATZ). Sudjelovao je u organizaciji osam međunarodnih znanstvenih skupova kao član znanstvenog ili programskog odbora. Recenzent je u većem broju međunarodnih znanstvenih časopisa. Dodijeljene su mu srebrne plakete „Josip Lončar“ za značajan i uspješan magistarski rad te za posebno uspješnu doktorsku disertaciju 1992., odnosno 1997. godine, godišnja nagrada „Rikard Podhorsky“ Akademije tehničkih znanosti Hrvatske za 2014. te Nagrada grada Zagreba u 2014. godini.

Joško Deur was born in Zadar in 1966. He received B.Sc., M.Sc. and Ph.D. Degrees in Electrical Engineering from the University of Zagreb, Faculty of Electrical Engineering and Computing (FER), Zagreb, Croatia, in 1989, 1993 and 1999, respectively.

From May 1990 he is with the Department of Robotics and Production System Automation at the Faculty of Mechanical Engineering and Naval Architecture, University of Zagreb, Croatia. In November 2012 he was promoted to a Full Professor position. After the postdoc specialization at the Ford Research Laboratory, Dearborn, MI, USA (2000), he established a wide cooperation with Ford Motor Company and Jaguar Cars through more than dozen scientific-research projects in the filed of modeling and control of automotive systems. Currently he is a project leader of one research project supported by the Croatian Science Foundation, and two Work Packages within a collaborative FP7 project. He published one scientific book, three book chapters, 21 CC/SCI journal papers, 18 papers in other journals, 97 papers in conference proceedings, three patents, and several dozens surveys and reports.

Prof. Deur is a member of KoREMA, IEEE, SAE, and IFAC societies and a member of the IFAC’s “Technical Committee 7.1 Automotive Control” and “IEEE Technical Committee on Automotive Control”. He is a member of two journal editorial boards. He received National Science Award for 2006 in the category of Annual Award for exceptional achievements in the

field of technology sciences and Silver Medal "Josip Lončar" from FER for the outstanding Ph.D. theses. He is fluent in English and has basic knowledge of German language.

Joško Deur rođen je 1966. godine u Zadru. Diplomirao je 1989. godine na Elektrotehničkom fakultetu u Zagrebu, na smjeru Automatika. Na istom je Fakultetu magistrirao 1993. i doktorirao 1999. godine.

Od svibnja 1990. radi na Zavodu za robotiku i automatizaciju proizvodnih sustava, Fakulteta strojarstva i brodogradnje u Zagrebu. U zvanje redovitog profesora izabran je 2012 godine. Nakon znanstvenog usavršavanja u istraživačkom centru tvrtke Ford Motor Company u Dearbornu, SAD (2000), uspostavio je široku suradnju s tvrtkama Ford Motor i Jaguar Cars kroz više od deset znanstveno-istraživačkih projekata na području modeliranja i regulacije automobilskih sustava. Voditelj je jednog istraživačkog projekta prema Hrvatskoj zakladi za znanost, te dvaju dvaju radnih paketa unutar kolaboracijskog FP7 projekta. Autor je jedne znanstvene knjige, triju poglavlja u knjizi, 21 radova u CC/SCI časopisima, 18 radova u drugim časopisima, 97 radova u zbornicima skupova s međunarodnom recenzijom, tri patenta te više desetaka studija i izvještaja.

Prof. Deur je član društava KoREMA, IEEE, SAE i IFAC, te IFAC “Technical Committee 7.1 Automotive Control” i “IEEE Technical Committee on Automotive Control”. Član je uređivačkog odbora dvaju časopisa. Dobitnik je Državne nagrade za znanost za značajno znanstveno dostignuće u području tehničkih znanosti 2006. godine, te srebrne plakete "Josip Lončar" za izrazito uspješnu doktorsku disertaciju. Govori engleski i služi se njemačkim jezikom.

Acknowledgement

*I would like to thank my supervisors **Prof. Mario Cifrek** and **Prof. Joško Deur** for the opportunity to be able to work on this challenging research and for their kind support. Especially, I would like to thank them for theirs numerous suggestions, advices, discussions we had, and persistent encouragement.*

*I would like to acknowledge the support of the Ford Motor Company through a successful cooperation with their research centers in Dearborn, MI and Aachen, Germany. My special gratitude goes to **Dr. Eric Tseng** and **Dr. Vladimir Ivanović**, from the Ford Research and Innovation Center, Dearborn, for their kind support, numerous advices, and for supplying indispensable test-vehicle measurement data for estimator validation.*

I would like to thank Jaguar Cars, UK and their Research center in Coventry, for the financial support of a part of activity presented in this thesis and for supplying a detailed vehicle dynamics simulation model used for validation of the estimator algorithms.

*I would like to thank Assistant Professor **Danijel Pavković** for numerous discussions and ideas concerning the Kalman filter design and estimation theory in general.*

I would like to thank my parents for their support and encouragement throughout my education.

With particular regard, I would like to thank my wife Dubravka for her understanding, patience, and support.

Abstract

An increasing number of vehicle dynamics control systems are being embedded into modern vehicles in order to assure safety and comfort of driving. All of these systems require information on the vehicle dynamics state variables (e.g. yaw rate, sideslip angle, roll rate etc.). Some of them can be measured, while others need to be estimated based on available measurements and appropriate vehicle kinematics/dynamics models. This thesis presents a contribution to the research of yaw rate and sideslip angle estimation. More specifically, a kinematic sensor fusion-based yaw rate estimator has been proposed, which combines the wheel speeds measured by standard Anti-lock Braking System (ABS) sensors and the measurement of vehicle lateral acceleration obtained from two accelerometers placed diagonally upon the chassis. Similar fusion concept has been employed for development of a kinematic vehicle sideslip angle estimator utilizing information obtained by low-cost inertial sensors and single-antenna GPS receiver. Moreover, a sideslip angle estimator based on vehicle dynamics model with stochastic modeling of the tire forces has been proposed and used for concurrent estimation of other vehicle dynamics variables and parameters, such as the tire sideslip angles, lateral tire forces, tire cornering stiffness, and tire-road coefficient of friction. The research methodology includes: setup of appropriate kinematic and/or dynamic vehicle models; identification, open-loop compensation, and analysis of dominant sources of estimation errors; and design of estimators based on the sensor fusion principle by using the adaptive extended Kalman filter. Verification of the developed estimators has first been carried out by means of computer simulations based on an experimentally verified ten-degrees-of-freedom vehicle dynamics model comprising the magic-formula tire model. In the case of dynamic sideslip angle estimator with stochastic tire modeling, the estimation accuracy has also been verified experimentally, based on the data recorded on a test vehicle equipped with a high-precision inertial measurement unit and two-antenna GPS receiver, as well as by using a standard set of vehicle dynamics control system sensors. In order to obtain a favorable performance of the vehicle state variable estimation under the various operating conditions, a rule-based adaptation of the Kalman filter state covariance matrix has been utilized for kinematic estimators, while for the dynamic, model-based vehicle sideslip angle estimator an adaptive fading algorithm has been implemented for adaptation of the Kalman filter state and measurement covariance matrices.

Keywords: State estimation, vehicle dynamics, vehicle kinematics, Kalman filter, yaw rate, sideslip angle, adaptive filtering, sensor fusion.

Procjena stanja dinamike vozila zasnovana na fuziji senzora primjenom adaptivnoga Kalmanova filtra

U suvremena vozila ugrađuje se niz sustava aktivnog upravljanja dinamikom vozila s ciljem povećanja sigurnosti i udobnosti vožnje. Ovi sustavi zahtijevaju informacije o varijablama stanja i parametrima dinamike vozila poput brzine skretanja, kuta bočnog klizanja i kuta valjanja, inercije i mase vozila, statičkih karakteristika guma, te informacije o uvjetima na cesti (vrsti podloge tj. koeficijentu trenja kontakta guma-podloga, kutu nagiba ceste i sl.).

Neke od ovih varijabli mogu se izravno mjeriti, dok je druge potrebno procijeniti na temelju dostupnih mjerenja i odgovarajućih modela kinematike ili dinamike vozila. Intenzivan razvoj raznovrsnih sustava procjene (estimatora) varijabli dinamike vozila motiviran je s jedne strane zahtjevima za smanjenjem potrebnog broja senzora, te s time povezanim smanjenjem cijene sustava upravljanja dinamikom vozila. S druge strane, u posljednje vrijeme javlja se potreba za poboljšanjem performansi konvencionalnih sustava procjene korištenjem novih senzorskih tehnologija i kombiniranjem različitih modela estimatora, odnosno primjenom postupaka sažimanja mjerenja više različitih senzora. Na taj način, uz određivanje vrijednosti veličina koje nije moguće ili nije praktično izravno mjeriti, takvi estimatori također omogućuju visoku redundanciju rekonstrukcije varijabli stanja dinamike vozila, te s time povezanu detekciju kvarova senzora i poboljšanje ukupne pouzdanosti cjelokupnog sustava upravljanja dinamikom vozila. Nadalje, sve veći broj senzora koji se ugrađuju u suvremena vozila, kao što su na primjer GPS senzori za navigaciju, inercijski senzori ili inercijske mjerne jedinice (IMU), pružaju nove mogućnosti u pogledu točnijeg i pouzdanijeg određivanja dinamičkog ponašanja vozila. Temeljem dobivenih informacija moguće je predvidjeti i spriječiti kritične situacije kao što su proklizavanje kotača, odnosno pojava podupravljanja ili preupravljanja, odnosno gubitka kontrole nad vozilom.

Ovaj rad predstavlja prilog istraživanju i razvoju sustava procjene brzine skretanja i kuta bočnog klizanja vozila zasnovanih na primjeni adaptivnog Kalmanova filtra i načela fuzije (sažimanja) senzora. Pritom se razmatra i procjena popratnih parametara dinamike vozila poput gradijenta statičke karakteristike autogume za bočno gibanje i koeficijenta trenja između autogume i podloge. Metodologija istraživanja uključuje postavljanje odgovarajućih modela kinematike i dinamike vozila, analizu dominantnih izvora pogrešaka procjene dinamičkih varijabli i parametara, te sintezu i simulacijsku i eksperimentalnu provjeru razvijenih sustava procjene (estimatora).

Temeljna hipoteza ovog rada je da se korištenjem koncepata sažimanja mjerenja s više senzora primjenom objedinjenog pristupa zasnovanog na adaptivnom Kalmanovom filtru i prikladnim kinematskim i dinamičkim modelima vozila može postići kvalitetnija procjena ključnih varijabli stanja dinamike vozila.

Doktorska disertacija je organizirana kako slijedi. U **prvom poglavlju** dan je uvod u tematiku estimacije dinamičkih varijabli (varijabli stanja) modela vozila s posebnim naglaskom na kut skretanja i kut bočnog klizanja vozila, te pregled stanja tehnike u području estimacije varijabli stanja i estimacije parametara dinamičkog modela vozila (npr. nagiba statičkih karakteristika guma te koeficijenta trenja na kontaktu guma-podloga). Definirana je hipoteza disertacije i navedeni su očekivani znanstveni doprinosi istraživanja.

Drugo poglavlje daje pregled osnovnih dinamičkih i kinematskih modela vozila te uvodi osnovne pojmove vezane uz dinamiku vozila i modele gume.

Treće poglavlje opisuje osnovni (KF) i prošireni oblik (EKF) Kalmanova filtra te objašnjava postupak podešavanju parametara filtra koji ima za cilj postizanje optimalnog odnosa između brzine odziva filtra (tj. što točnijeg slijeđenja referentne vrijednosti u tranzijentima) i razine perturbacija (šuma) u stacionarnom stanju. Ovo poglavlje također opisuje različite izvedbe adaptivnog Kalmanova filtra koji se koriste za estimaciju varijabli stanja procesa s vremenski promjenjivim parametrima, s posebnim naglaskom na „Adaptive Fading“ izvedbu proširenog oblika filtra (AFEKF).

Četvrto poglavlje razrađuje problem estimacije kuta skretanja vozila zasnovane na primjeni različitih kinematskih modela za slučaj kada izravno mjerenje žiroskopom nije dostupno. Razrađen je i analiziran koncept kinematskog adaptivnog estimatora zasnovan na sažimanju (fuziji) mjerenja senzora brzine vrtnje nepogonjenih kotača i bočne akceleracije (koja se mjeri sa dva akcelerometra postavljena dijagonalno-simetrično u odnosu na težište vozila) uz primjenu Kalmanova filtra. Identificirani su dominantni izvori pogrešaka kinematskog estimatora brzine skretanja kod odvojene primjene dvaju razmatranih kinematskih modela (tj. modela zasnovanog na mjerenjima brzina vrtnje kotača i modela zasnovanog na mjerenju dvaju akcelerometara). Razmatra se i razmjerno jednostavan koncept adaptacije Kalmanova filtra s ciljem postizanja visoke točnosti procjene za širok raspon radnih režima, obzirom na činjenicu da se razine pouzdanosti dvaju međusobno komplementarnih kinematskih modela mijenjaju s radnom točkom. Točnost procjene brzine skretanja provjerena je simulacijskom usporedbom procijenjenog signala s referentnim signalom dobivenim iz modela dinamike vozila s 10 stupnjeva slobode gibanja.

U **petom poglavlju** opisan je kinematski estimator kuta bočnog klizanja vozila zasnovan na sažimanju mjerenja inercijskih senzora (akcelerometara i žiroskopa) i signala brzine vozila dobivenog iz GPS prijamnika, također unutar okvira dinamičkog estimatora zasnovanog na Kalmanovom filtru. Pritom se GPS mjerenja sa sporom vremenskom bazom tipično presporom za izravnu primjenu u procjeni varijabli dinamike vozila koriste za periodičku korekciju posmaka (drifta) u estimiranom signalu, a koji nastaje zbog inherentnog posmaka signala inercijskih senzora, čiji su signali dostupni s bržom vremenskom bazom. Provedena je detaljna analiza pogrešaka za razmatrane kinematske modele (tj. model vozila i model mjerenja GPS signala) i razvijen je mehanizam adaptacije Kalmanova filtra s ciljem poboljšanja točnosti slijeđenja estimatora u širokom rasponu radnih režima. Performanse adaptivnog estimatora provjerene su simulacijskom usporedbom estimiranog i referentnog signala dobivenog iz modela vozila s deset stupnjeva slobode.

Šesto poglavlje opisuje sintezu estimatora kuta bočnog klizanja vozila zasnovanog na nelinearnom modelu dinamike vozila sa stohastičkim modelom sila na kotačima, te primjeni proširenog oblika adaptivnog Kalmanova filtra. Navedeni koncept procjene kuta bočnog klizanja vozila je bitno manje osjetljiv na varijacije parametara determinističkog modela gume u odnosu na klasične estimatore, te je također manje osjetljiv na promjene tipa podloge (tj. koeficijenta trenja kontakta guma-podloga), čime se postiže poboljšanje u točnosti procjene kuta klizanja. Razvijeni estimator verificiran je na eksperimentalnim podacima snimljenim na testnom vozilu opremljenom, pored standardnih senzora dinamike vozila, i preciznom inercijskom mjernom jedinicom i sofisticiranim GPS prijemnikom s dvije antene. Pritom su analizirane performanse estimatora za slučaj korištenja kvalitetnih senzora za potrebe provjere ograničenja samog koncepta estimacije i određivanja optimalnih podešenja filtra, te degradacija točnosti estimatora za slučaj upotrebe standardnih senzora dinamike vozila. Također, razmotrene su mogućnosti djelomične kompenzacije pogrešaka i mogućnosti poboljšanja točnosti procjene uvođenjem adaptacijskog mehanizma s obzirom na pogreške u dinamičkom modelu vozila odnosno u mjernim signalima.

U **sedmom poglavlju** razmatraju se mogućnosti primjene koncepata prethodno opisanog dinamičkog estimatora razvijenog za procjenu kuta bočnog klizanja vozila u estimaciji drugih dinamičkih varijabli i parametara modela, kao što su kutovi klizanja kotača, određivanja nagiba statičkih karakteristika gume, te klasifikaciji tipa podloge, odnosno grube procjene koeficijenta trenja kontakta između gume i podloge.

Ključne riječi: Procjena varijabli stanja, dinamika vozila, kinematika vozila, Kalmanov filtar, brzina skretanja vozila, kut bočnog klizanja vozila, adaptivno filtriranje, fuzija senzora.

Table of Contents

1 Introduction

1.1 Motivation

Over the last two decades vehicle dynamics control systems, such as the Anti-lock Braking System (ABS), the Electronic Stability Program (ESP) and the Active Roll Control (ARC) have experienced an accelerated development. These systems are aimed at stabilizing the vehicle behaviors during critical cornering, braking, and accelerating maneuvers, thus facilitating enhanced vehicle handling, safety, and comfort performance [1,85-87]. These systems require the knowledge of relevant vehicle state variables and dynamics parameters, as well as the information on road condition (e.g. tire-road friction and road bank angle). However, some of these vehicle dynamics variables, such as the vehicle sideslip angle, are difficult to measure or may require expensive sensors whose application is limited to test vehicles. Therefore, they need to be estimated based on available measurements and a known kinematic or dynamic vehicle model. Having this in mind, the emphasis of this work will be given to design of advanced, sensor fusion-based yaw rate and sideslip angle estimators by using the adaptive Kalman filter methodology [2-4].

The reference mathematical models used for vehicle dynamics state estimator design are divided into kinematic and dynamic models, and, consequently, estimators can be categorized as kinematic, dynamic and combined. The essential difference between these estimators is that the kinematic estimators do not require knowledge of many, often time-varying vehicle dynamics and tire model parameters (e.g. vehicle mass and tire cornering stiffness), while the dynamic estimators are more robust to sensor offsets and road bank disturbances. The most commonly used vehicle dynamics model is the simple, linear, single-track (bicycle) model [5], which, unlike the more complex nonlinear two-track model, neglects the effects of roll and yaw dynamics to tire forces. The linear model accurately describes vehicle motion while operating within the linear region of tire lateral static curve, which in the critical case of understeering and oversteering conditions (when the lateral tire static curve saturates) shows significant deviations from the actual vehicle behavior thus introducing potentially large estimation errors.

1.2 State of the art

Overview of the state of the art in estimation of essential vehicle dynamics state variables and parameters that are in the focus of the research documented in this thesis (i.e. the vehicle yaw rate and sideslip angle, tire cornering stiffness, and tire-road contact coefficient of friction) is given in the following Subsections.

1.2.1 Yaw rate estimation

Vehicle yaw rate is typically measured by a gyroscope sensor. However, in order to reduce the cost of low-end production vehicles, yaw rate can be estimated by utilizing the measurements from other readily available and/or less expensive sensors and appropriate kinematic and dynamic vehicle models. Kinematic yaw rate estimation approaches are typically based upon: (i) non-driven wheel speed measurements [4,6,7], (ii) lateral acceleration measurement from single accelerometer placed in the vehicle center of gravity (CoG) [6], and (iii) measurements of two accelerometers placed outside of CoG [8,9]. However, the approach (i) is sensitive to variations of the effective tire radius and cannot be used during braking, the method (ii) yields accurate estimates only for quasi-static conditions of constant or slowly changing yaw rate, while the approach (iii) is generally sensitive to accuracy of sensor placement and orientation. Moreover, the method (iii) with laterally placed sensors [8] cannot provide the yaw rate sign and has a relatively unfavorable signal-to-noise ratio, while for the longitudinally placed accelerometers [9] the estimator is highly sensitive to sensor offsets resulting in emphasized drift-like estimation errors.

Dynamic yaw rate estimators are based on appropriate linear or nonlinear vehicle dynamic models. In [8] the Kalman filter is used in order to combine the kinematic approach (iii) and dynamic estimation based on the linear “bicycle” model of vehicle dynamics, while in [6] the initial estimate obtained from the two kinematic estimation approaches (i) and (ii) is used as an input to a nonlinear dynamic estimator producing the final estimate. The review of available literature has shown that neither a detailed comparison of lateral, longitudinal, and possibly diagonal configurations of dual accelerometer-based kinematic yaw rate estimators nor a systematic analysis of estimation errors and their compensation has been performed yet. In addition, a detailed analysis of combining different kinematic estimation approaches in order to design a robust, vehicle dynamics model-free, yaw rate estimator has not been proposed.

1.2.2 Sideslip angle estimation

Even though the vehicle sideslip angle can be directly measured by optical speed-over-ground sensors, this is impractical due to high sensor cost, so that the sideslip angle is typically estimated in production vehicles. Numerous estimation approaches from the literature typically use the available measurements of vehicle dynamics state variables, obtained by inertial sensors (INS), GPS receivers, or inertial measurement units (IMUs), and appropriate kinematic and dynamic vehicle models.

The commonly found techniques used for the **kinematic sideslip angle estimation** include the use of direct integration of standard ESP sensor readings for design of open-loop [1,10,11] or closed-loop [12,13,79] observers, or application of Inertial Measurement Unit (IMU) and appropriate, more complex 6DOF kinematic models is considered [14]. The same kinematic models are used in estimators based on GPS and inertial sensors fusion [15-17,88], wherein the low-rate GPS signals are typically used for the correction of emphasized drift-like estimation errors due to offsets in high-rate INS measurements. There are two basic concepts of kinematic GPS/INS fusion-based sideslip angle estimation. The first one uses the low-cost single-antenna GPS receiver to estimate the yaw rate gyro bias and improve the estimation accuracy. The second approach is based on a more expensive two-antenna GPS receiver, which provides direct low-rate sideslip and roll angle measurements, thus enabling an effective compensation of road bank and sensor bias-related estimation errors. An alternative approach to sensor bias estimation through a Recursive Least Square (RLS)-based estimator is given in [13].

The **dynamic model-based estimation** concepts include: (i) approaches based on utilization of nonlinear vehicle dynamics models and nonlinear observers and known tire road friction model [10,11], (ii) application of vehicle dynamic model with linear [7-9] or piecewise linear [2,3] tire characteristics and various types of observers, and (iii) application of nonlinear vehicle dynamics model with stochastic description of tire forces (e.g. random-walk state variables [18,20, and 28] or Gauss-Markov tire models [27]) as in [20] where the sliding mode-based tire forces estimator has been cascaded to an extended Kalman filter-based estimator of sideslip angle and cornering stiffness.

Combined estimators are aimed to benefit from the complementary advantages of kinematic and dynamic vehicle models and they are described in [1,10,11,21,22]. More specifically, the piecewise-linear tire model and a single-track vehicle model are combined with kinematic model-based direct integration approach in [10]. In [22] the kinematic, sensor fusion-based

estimator is proposed based on a linear vehicle/tire dynamic model fed by a low-cost single-antenna GPS receiver and standard INS signals.

In general, it can be concluded that the kinematic model-based sideslip angle estimators are highly sensitive to sensor offsets and road bank disturbances, resulting in potentially large drift-like estimation error. On the other hand, estimators using dynamic models with analytical or semi-empirical tire models are sensitive to model parameter uncertainties and unmodelled dynamics. The results in [22] indicate that for the presented combined estimator using a linear vehicle dynamics model predominant estimation errors can be expected for vehicle operation outside of the tire static curve linear region, with particular emphasis given on the requirement for tire cornering stiffness estimation. Having this in mind, and based on the given literature overview, it can be concluded that there are still significant possibilities for further research on: combining the kinematic estimators based on a fusion of low-cost GPS and standard INS. More specifically in the reviewed literature, the GPS/INS based sideslip angle estimators are mostly focused on the approach using the difference between the vehicle heading and course angle, and less on the methods relying upon the vehicle lateral and longitudinal velocities and underlying kinematic model. The former method typically requires the application of costly two antenna GPS receivers. Moreover, the systematic and thorough analysis of low cost GPS/INS-based kinematic sideslip estimator has not been carried out in the available literature yet.

The dynamic model-based sideslip angle estimators using the nonlinear vehicle dynamics model with stochastic modeling of tire are, unlike the ones using the deterministic models, robust against the uncertainties of tire model parameters and do not require the information on the tire-road interface coefficient of friction [29]. This concept, has been initially introduced in [18,20,28] for tire-road forces and coefficient of friction estimation. In this thesis an extended Kalman filter-based sideslip angle estimator has been proposed, which is based on a nonlinear single-track vehicle dynamics model with stochastic description of lateral and longitudinal tire forces. The proposed reduced-order estimator concept, unlike the one described in [18], deals primarily with the vehicle sideslip angle estimation, and uses the vehicle longitudinal velocity as an additional measurement in order to increase the estimator accuracy in the presence of braking torque measurements inaccuracies and uncertainties of vehicle dynamics model parameters.

1.2.3 Estimation of other vehicle dynamics variables

Although the main focus of this thesis is on estimation of yaw rate and vehicle sideslip angle, the same methodology can be directly or indirectly applied for estimation of other vehicle dynamics variables. Consequently, a short overview of tire cornering stiffness and tire-road friction coefficient estimation methods will be given hereinafter.

The front and rear tires cornering stiffness constitute the essential parameters of the linearized, analytical tire model commonly utilized for formulation of the simplified, single-track vehicle dynamics model (i.e. the "bicycle" model). The common tire cornering stiffness estimation methods [26,82,89] include: (i) direct method utilizing the state-space equation of the bicycle model, and its modifications (i.e. the lateral acceleration method, rdot method, and beta-less method) and (ii) transfer function method (i.e. utilizing the transfer function between steering input and yaw rate). Although direct method is straightforward and simple, the main problems regarding its implementation are related to the existence of singularities (e.g. when the vehicle is driving in straight line) and requirements for measurements or estimates of vehicle lateral velocity (i.e. vehicle sideslip angle) and derivative of the vehicle yaw rate. The most frequently used modification in the literature is beta-less method [19,20].

The tire-road friction coefficient is important to be estimated as an essential environmental parameter which determines the lateral tire force limits and consequently the margins of the safe, adhesion region [10]. Some methods used for estimation of the friction coefficient are based on monitoring the road surface by a sensor (e.g. camera, ultrasound, or temperature sensors) and running the classification algorithm to appoint/select the adequate surface type and corresponding friction coefficient. The alternative approaches are based on utilization of the vehicle and tire dynamics and related effects such as: tire tread deformation, wheel speed frequency content, longitudinal forces vs. tire slip ratio, front tire self-alignment torque etc. (see [25] and references therein). A robust estimator of road friction coefficient by utilizing both lateral and longitudinal vehicle dynamics is proposed in [25].

1.3 Hypothesis

Primary research objectives of this thesis are as follows: a) design of adaptive kinematic yaw rate estimator based on fusion of the dual diagonally-positioned accelerometer and standard non-driven wheel speed sensors measurements, b) design of kinematic sideslip angle estimator based on fusion of the standard inertial sensors and low-cost GPS receiver, and

c) design of adaptive sideslip angle estimator which combines the kinematic estimation concept with estimation based on dynamic vehicle model and stochastic tire force model.

The main hypothesis is that by using sensor fusion methodology and implementation of the adaptive Kalman filter utilizing the appropriate kinematic and dynamic vehicle models, the more accurate estimation of the key vehicle dynamics state variables can be achieved.

1.4 Thesis overview

This thesis deals with the design, implementation, and testing of vehicle dynamics state variable estimators with emphasis on yaw rate and sideslip angle estimation through a sensor fusion approach based on utilization of kinematic or dynamic models and an adaptive Kalman filter. **Chapter 2** introduces the main concepts of the vehicle dynamics theory, including definitions of different coordinate frames used for describing vehicle motion and formulations of vehicle kinematic and dynamics models, suitable for designing the estimators of relevant vehicle dynamics state variables. The Kalman filtering methodology, repeatedly used within this thesis for design of the estimators of various vehicle dynamics state variables, has been overviewed in **Chapter 3**.

Development of the sensor fusion-based adaptive yaw rate estimator utilizing an Extended Kalman Filter (EKF) has been described in **Chapter 4**. First, a detailed comparative analysis of the dominant sources of estimation errors has been conducted for each of the individual kinematic estimator concepts: the estimator based on the tire speed measurements and the estimator utilizing the two accelerometers placed in different configurations (lateral, longitudinal, and diagonal ones). Implementation and verification of the proposed kinematic estimators has been carried out by means of computer simulations in Matlab/Simulink environment, based on a detailed, experimentally-validated vehicle dynamics model with ten degrees of freedom (10 DoF) [23].

In order to be able to perform a detailed analysis of the accuracy of the proposed dual accelerometer-based yaw rate estimator and identify the major sources of estimation errors, a 3D acceleration measurement model is developed [30]. This model yields the acceleration measurements of an accelerometer arbitrarily placed on the vehicle chassis. In analyzing the estimator performance the impact of accelerometers configurations, unmodeled roll and pitch dynamics, precision of sensor placement/alignment, and the sensor offsets are taken into consideration. The analysis of performance of kinematic estimator based on non-driven wheel speed measurements is also carried out and dominant sources of the estimation errors are

identified, such as those related to the longitudinal wheel slip due to braking, variations of tire effective radius, tire dynamics, and disturbances due to road bumps.

An adaptive extended Kalman filter-based yaw rate estimator using fusion of the above two kinematic approaches is designed, and Kalman filter adaptation mechanism with respect to operating conditions is developed. The performance of such combined kinematic estimator is tested by means of computer simulations and compared with the performances of the individual estimators. Parameter tuning of adaptation mechanism and Kalman filter covariances is carried out in order to obtain more accurate estimation over a wide range of operating conditions.

Chapter 5 deals with the development of a kinematic sideslip angle estimator based on the sensor fusion methodology by means of an adaptive extended Kalman filter (AEKF). The fusion is based on combining measurements from standard automotive ESP sensors (i.e. the measurements of lateral acceleration, yaw rate, and wheel speeds) with vehicle velocity measurements acquired from low-cost single-antenna GPS receiver with a low sampling rate.

The vehicle longitudinal velocity pre-estimator based on non-driven (rear) wheel speed measurements is designed, and the impact of velocity pre-estimation accuracy on the quality of final sideslip angle estimation is investigated. The virtual sensors models within the Matlab simulation environment based on 10 DoF vehicle dynamics model [23] is implemented, with the emphasis on modeling of inertial sensors measurements and GPS-based vehicle speed measurements. The relevant error sources, with emphasis on inaccuracies and variable delays of GPS-based vehicle speed measurement, inertial sensors offsets, and road bank disturbances, are analyzed.

Furthermore, a comprehensive analysis is undertaken in order to gain the required insight in the benefits of utilizing the multi-rate Kalman filter for fusion of high-rate inertial sensors (INS) with the low-rate GPS receiver. The inertial sensors offsets are modeled as random-walk type state-space variables. The Kalman filter adaptation mechanism based on covariance matrix adaptation is implemented, in order to achieve a favorable trade-off between the estimator response time and noise suppression capability. The performance of the proposed adaptive kinematic estimator is analyzed by means of computer simulations for representative driving maneuvers (e.g. steady cornering, braking in cornering, and double lane change). Adequate sets of Kalman filter parameters are determined for different operating conditions, and the developed adaptation algorithm, aimed at increasing the overall estimation accuracy over a wide range of operating conditions, is tuned.

In **Chapter 6** another approach in sideslip angle estimation is considered, which is based on a nonlinear vehicle dynamics model and stochastic modeling of tire forces. Such approach does not require the knowledge of deterministic tire model (i.e. tire characteristics), and it is thus, not sensitive to tire model parameters uncertainties. The estimator is verified in off-line mode based on a wide set of experimental data acquired from the instrumented test vehicle. The estimator accuracy has been analyzed by identifying the estimator sensitivity to measurement errors and vehicle model uncertainties. Moreover, the estimator performance degradation has been analyzed in case of using the standard set of the vehicle dynamics sensors instead of high performance inertial measurement unit that is typically being used in the test vehicles. In order to improve the estimation accuracy, adaptation of the Kalman filter has been implemented by utilizing the switching off the estimator in conditions of decreased observability (i.e. straight driving) and adaptive fading methodology to mitigate estimation errors caused by unmodeled disturbances (i.e. decrease of the model reliability).

Chapter 7 considers the use of sideslip angle and tire lateral force estimates obtained by the estimator designed in Chapter 6 for application to concurrent estimation of tire cornering stiffness and tire/road friction coefficient, as two essential parameters used in describing vehicle dynamics. The aim of this chapter is to provide the initial formulation of the estimation concepts and to stipulate the feasibility of such approach.

In **Chapter 8** the main conclusions are given, as a summary of concluding remarks included in individual Chapters.

2 Vehicle dynamics

2.1 Coordinate frames

The rigid body movement can be described by a set of the kinematics equations containing translational and rotational velocities and accelerations [31]. In order to be able to write these equations, an appropriate coordinate frames need to be defined. The steady, inertial coordinate frame ($X\ Y\ Z$) is used as a reference frame (Fig. 2.1). The vehicle body fixed coordinate frame ($X_b\ Y_b\ Z_b$) is placed upon the moving object, with its origin in the body center of gravity (CoG) and its axes (x, y, and z) pointing in forward, lateral (on the left side), and upward direction.. Triplet of unit vectors uniquely defines the Cartesian coordinate frame (**i**, **j**, and **k** for inertial coordinate frame, and $\mathbf{i}_b$, $\mathbf{j}_b$, and $\mathbf{k}_b$ for body-fixed frame). Euler angles ($\phi, \theta,$ and ψ) are defined in the inertial reference coordinate frame and angular velocities (ω_x, ω_y, and ω_z) are defined in the body-fixed frame as shown in Fig 2.1.

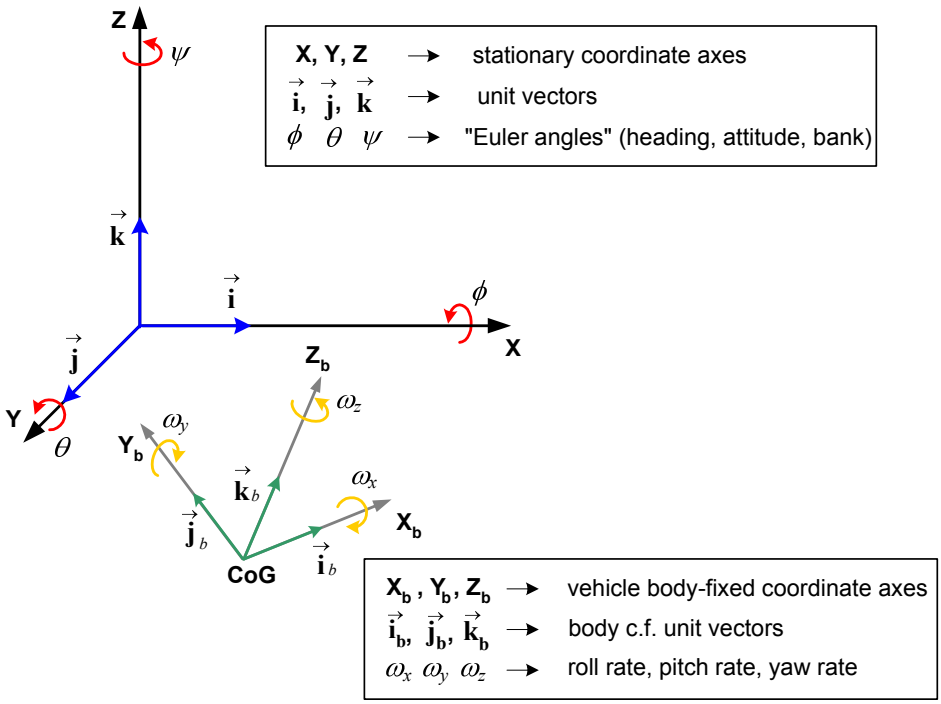

Fig. 2.1 *Coordinate frames.*

When analyzing the simple case of a pure rotational movement of the object and presuming that the origins of reference and body-fixed frame coincide, the relation between the fixed-point coordinates in these frames can be expressed by application of the Euler angles. The Euler angles represent the successive rotation angles of the corresponding axes of the inertial

coordinate frame required to match the inertial frame with instantaneous body-fixed frame (detailed derivation of Euler angles [31] from the angular velocities of the body-fixed frame is given in Appendix A). Namely, the term "Euler angles" is typically used for the particular sequence of successive axes rotations (3-1-3), but for the automotive application the rotational sequence (3-2-1 NASA Standard Airplane) is used as more appropriate. Here, the numbers represent the corresponding axes rotations (e.g. 1 about x axis, 2 about y axis, and 3 about the z axis). Also, the angles ϕ, θ, and ψ are in automotive applications known as: heading, attitude, and bank respectively [31], but most authors in the field of vehicle dynamics control (e.g. [1,17,23,32]) use different nomenclature: roll, pitch and yaw angle, respectively.

2.2 Vehicle dynamics models

Mathematical models of the vehicle dynamics are required for development and evaluation of vehicle dynamics controllers and estimators.

2.2.1 Dual-track model

The dual-track vehicle dynamics model with six degrees-of-freedom (6 DoF) [5,23], defined by Eqs. (2-1) to (2-6) and illustrated in Fig. 2.2, gives a precise description of the vehicle dynamics (it is often referred to as a 10DoF model, where the four wheel rotational speeds are typically considered as four additional states). This model defines the vehicle linear (longitudinal, lateral, and vertical) and rotational motion (roll, pitch, and yaw).

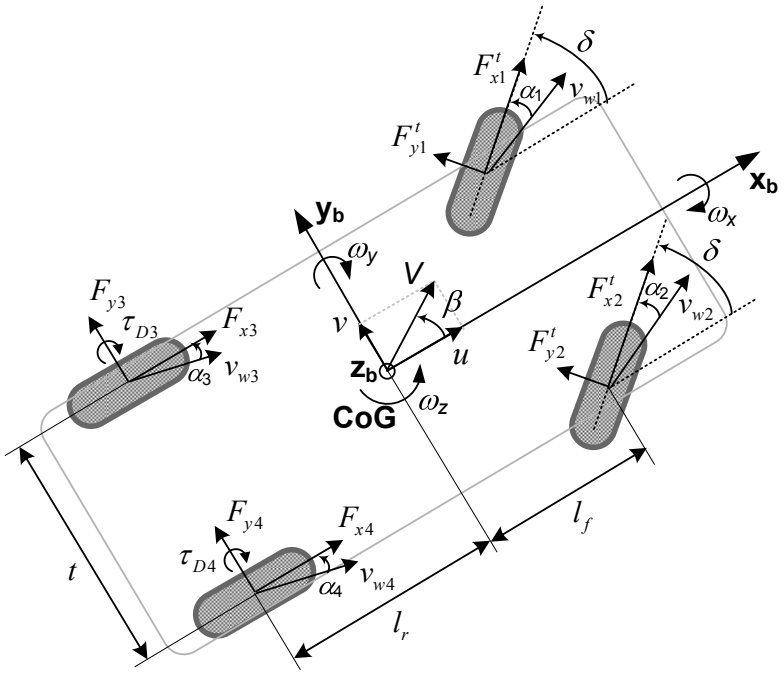

Fig. 2.2 *Two-track vehicle dynamics model.*

$$m(\dot{u} - v\omega_z) = \sum_{i=1}^{4} F_{xi} \tag{2-1}$$

$$m(\dot{v} + u\omega_z) = \sum_{i=1}^{4} F_{yi} \tag{2-2}$$

$$m\dot{w} = \sum_{i=1}^{4} F_{z,i} \tag{2-3}$$

$$I_x\dot{\omega}_x = \frac{t}{2}(F_{z1} + F_{z3}) - \frac{t}{2}(F_{z2} + F_{z4}) \tag{2-4}$$

$$I_y\dot{\omega}_y = -l_f(F_{z1} + F_{z2}) + l_r(F_{z3} + F_{z4}) \tag{2-5}$$

$$I_z\dot{\omega}_z = l_f(F_{y1} + F_{y2}) - l_r(F_{y3} + F_{y4}) - \frac{t}{2}(F_{x1} + F_{x3}) + \frac{t}{2}(F_{x2} + F_{x4}) \tag{2-6}$$

where I_x, I_y, and I_z are roll, pitch, and yaw moment of inertia, respectively. When compared with the 10DoF model, derived in [23] and used for simulation analysis in this thesis, the above vehicle dynamics model does not take into account the inclination of roll axis and position of the roll center above the vehicle CoG. The four additional state equations describe the dynamics of the four individual wheels [23]:

$$I_w\dot{\omega}_{w,i} = \tau_{D,i} - F_{x,i}^t r_w, \qquad i = 1,\ldots,4 \tag{2-7}$$

where I_w is the wheel moment of inertia, r_w is the wheel effective radius, and $\tau_{D,i}$ is the wheel driving torque.

The tire forces F_{xi}^t and F_{yi}^t are obtained from the appropriate tire models (e.g. Magic formula model [33]) as a function of the longitudinal slip η_i, the lateral slip α_i, and the normal load F_{zi} defined by equations (2-12a) to (2-12d). Here the subscript index i designates the individual tire/wheel (1 = front-left, 2 = front-right, 3 = rear-left, and 4 = rear-right, Fig. 2.2) while the superscript t denotes the tire coordinate frame.

$$\eta_i = \frac{r_w\omega_{w,i} - u_i}{u_i} \qquad \text{where } u_i = u + (-1)^i\frac{t}{2}\omega_z \tag{2-8}$$

$$\alpha_i = \delta_i - \operatorname{atan}\frac{v_i}{u_i} \qquad \text{where } v_{1,2} = v + l_f\omega_z,\ v_{3,4} = v - l_r\omega_z, \text{ and } \delta_{3,4} = 0 \tag{2-9}$$

The tire forces are transformed to the vehicle body coordinate frame by the following equations:

$$F_{xi} = F_{xi}^t\cos\delta_i - F_{yi}^t\sin\delta_i \tag{2-10}$$

$$F_{yi} = F_{xi}^t\sin\delta_i + F_{yi}^t\cos\delta_i \tag{2-11}$$

The tire vertical forces F_{zi} can be determined, in the case of neglecting roll, pitch and heave dynamics, from the following expressions [34,35]:

$$F_{z1} = \frac{l_r mg}{2(l_f + l_r)} - \frac{h_g}{2t}\sum_{i=1}^{4} F_{yi} - \frac{h_g}{2(l_f + l_r)}\sum_{i=1}^{4} F_{xi} \quad \text{(2-12a)}$$

$$F_{z2} = \frac{l_r mg}{2(l_f + l_r)} + \frac{h_g}{2t}\sum_{i=1}^{4} F_{yi} - \frac{h_g}{2(l_f + l_r)}\sum_{i=1}^{4} F_{xi} \quad \text{(2-12b)}$$

$$F_{z3} = \frac{l_f mg}{2(l_f + l_r)} - \frac{h_g}{2t}\sum_{i=1}^{4} F_{yi} + \frac{h_g}{2(l_f + l_r)}\sum_{i=1}^{4} F_{xi} \quad \text{(2-12c)}$$

$$F_{z4} = \frac{l_f mg}{2(l_f + l_r)} + \frac{h_g}{2t}\sum_{i=1}^{4} F_{yi} + \frac{h_g}{2(l_f + l_r)}\sum_{i=1}^{4} F_{xi} \quad \text{(2-12d)}$$

where h_g is the center of gravity height. The first right hand side terms in Eqs. (2-12) represent the static weight-relatednominal values of individual tire normal forces F_{zi0}. More reliable normal tire force dynamics model, typically used for the tire forces simulations, includes dynamic effects related to the roll, pitch, and heave motion and also incorporates the vehicle chassis suspension dynamics models (linear or nonlinear). Such model is documented in literature [23,35] and used by the researchers in the field [18,36].

2.2.2 Single track "bicycle model"

The most commonly used vehicle dynamics model in the field of vehicle dynamics control and estimation is single-track vehicle dynamics model (so-called “bicycle model”) [5], which is illustrated in Fig. 2.3. Within this simplified two-degree of freedom model (2 DoF), the two wheels on each axis (i.e. left and right wheels) are lumped together.

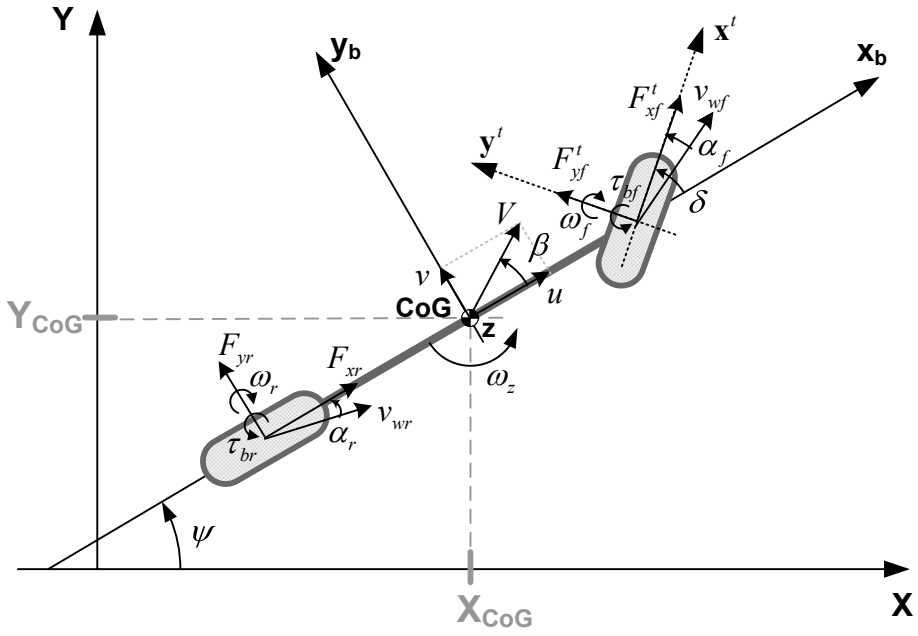

Fig. 2.3 *Single-track ("bicycle") vehicle dynamics model.*

The bicycle model is based on the following differential equations describing the vehicle lateral and yaw motion (cf. Eqs. (2-2) and (2-6)):

$$m\left(\dot{v}+u\omega_z\right)=ma_y=F_{yf}+F_{yr} \tag{2-13}$$

$$I_z\dot{\omega}_z=l_fF_{yf}-l_rF_{yr} \tag{2-14}$$

where $F_{yf}=F_{y1}+F_{y2}$ and $F_{yr}=F_{y3}+F_{y4}$ are lumped lateral forces at the front and rear axis of the vehicle. This model neglects vehicle roll and pitch dynamics, and utilizes the linear model of the tire forces. In the linearized model, the lateral forces acting on the front and rear axes are modeled as linear functions of the wheel slip angle, defined by Eqs. (2-8) and (2-9), wherein small angle-approximations of trigonometric functions have been applied:

$$F_{yf}=C_f\alpha_f=C_f\left(\delta-\beta-\frac{l_f\omega_z}{V}\right) \tag{2-15}$$

$$F_{yr}=C_r\alpha_r=C_r\left(-\beta+\frac{l_r\omega_z}{V}\right) \tag{2-16}$$

where β is the vehicle sideslip angle (Fig. 2.3), C_f and C_r are equivalent front and rear axis cornering stiffness, while α_f and α_r are front and rear wheel slip angles of a single-track vehicle model derived by presuming that the vehicle chassis and wheels have identical velocities at wheel ground contact point [5]. Thus, the velocity of the front wheel/road contact point is obtained as:

$$\begin{aligned} v_{wf}\sin\left(\delta-\alpha_f\right) &= V\sin\beta + l_f\omega_z \\ v_{wf}\cos\left(\delta-\alpha_f\right) &= V\cos\beta \end{aligned} \tag{2-17}$$

where V denotes the vehicle CoG velocity ($V \equiv V_{CoG}$, Fig. 2.3). By dividing the expressions in Eq. (2-17) the following equation is derived:

$$\tan\left(\delta-\alpha_f\right) = \frac{V\sin\beta + l_f\omega_z}{u} = \tan\beta + \frac{l_f\omega_z}{u} \tag{2-18}$$

As the small angles assumption holds for a stable vehicle (i.e. $\left(\delta-\alpha_f\right) <<$, $\alpha_f <<$, and $\beta <<$), the expression for front axis wheel slip angle reads (see Eq. (2-15)):

$$\alpha_f = \delta - \beta - \frac{l_f\omega_z}{V} \tag{2-19}$$

Similarly, the equations for the rear wheel are obtained:

$$\begin{aligned} v_{wr}\sin\alpha_r &= -V\sin\beta + l_r\omega_z \\ v_{wr}\cos\alpha_f &= V\cos\beta \end{aligned} \tag{2-20}$$

$$\tan\alpha_r = \frac{l_r\omega_z - V\sin\beta}{V\cos\beta} = \frac{l_r\omega_z}{V\cos\beta} - \tan\beta \tag{2-21}$$

$$\alpha_r = -\beta + \frac{l_r\omega_z}{V} \tag{2-22}$$

By substituting the expressions for the front and rear tire lateral forces (Eqs. (2-15) and (2-16)) into Eqs. (2-13) and (2-14), the following equations are obtained:

$$m(\dot{v}+u\omega_z) = C_f\left(\delta-\beta-\frac{l_f\omega_z}{V}\right) + C_r\left(-\beta+\frac{l_r\omega_z}{V}\right) \tag{2-23}$$

$$I_z\dot{\omega}_z = l_fC_f\left(\delta-\beta-\frac{l_f\omega_z}{V}\right) - l_rC_r\left(-\beta+\frac{l_r\omega_z}{V}\right) \tag{2-24}$$

Furthermore, by presuming that the small sideslip angle $\beta = \text{atan}\frac{v}{u}$ the approximations $\beta \approx \frac{v}{u}$ and $u \approx V$ can be applied, Eqs. (2-23) and (2-24) can be rewritten as:

$$m(\dot{v}+u\omega_z) = -\frac{v}{u}(C_f+C_r) - \frac{\omega_z}{u}(l_fC_f - l_rC_r) + \delta C_f \tag{2-25}$$

$$I_z\dot{\omega}_z = -\frac{v}{u}(l_fC_f - l_rC_r) - \frac{\omega_z}{u}(l_f^2C_f + l_r^2C_r) + \delta l_fC_f \tag{2-26}$$

After rearranging the above equations, the well-known state-space formulation of the bicycle model is obtained:

$$\dot{v} = -\frac{C_f + C_r}{mu} v - u\omega_z - \frac{l_f C_f - l_r C_r}{mu} \omega_z + \frac{C_f}{m} \delta \tag{2-27}$$

$$\dot{\omega}_z = -\frac{l_f C_f - l_r C_r}{uI_z} v - \frac{l_f^2 C_f + l_r^2 C_r}{uI_z} \omega_z + \frac{l_f C_f}{I_z} \delta \tag{2-28}$$

Alternatively, if the sideslip angle is to be used as a state variable, instead of lateral velocity and the approximate expression $\beta \approx \frac{v}{u}$ holds, the following equation for the sideslip angle first time derivative can be obtained:

$$\dot{\beta} = \frac{\dot{v}}{u} - \frac{v\dot{u}}{u^2} \approx \frac{\dot{v}}{u} \tag{2-29}$$

By combining Eq. (2-29) with Eqs. (2-27) and (2-28), the following model equations are obtained (cf. [19]):

$$\dot{\beta} = -\frac{C_f + C_r}{mu} \beta - \omega_z - \frac{l_f C_f - l_r C_r}{mu^2} \omega_z + \frac{C_f}{mu} \delta \tag{2-30}$$

$$\dot{\omega}_z = -\frac{l_f C_f - l_r C_r}{I_z} \beta - \frac{l_f^2 C_f + l_r^2 C_r}{uI_z} \omega_z + \frac{l_f C_f}{I_z} \delta \tag{2-31}$$

An alternative approach of sideslip angle modeling for application in the estimator design is based on utilization of the piecewise-linear tire model [10], instead of traditional, linear tire model approximation defined by Eqs. (2-15) and (2-16).

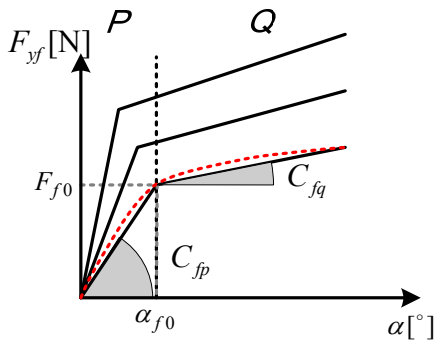

Fig. 2.4 *Bilinear tire static curve model [10].*

The nonlinear tire static curves have been approximated by piecewise-linear curves [10] in a way that the two intervals (*P* and *Q*) are defined; first corresponding to the adhesion conditions coinciding with small tire slip angles α, and the second interval representing the sliding conditions present at higher values of tire slip angles. *P* interval is equivalent to the

traditional linearized model. Based on this bilinear tire model, the lateral forces in *P* (adhesion) and *Q* (sliding) intervals are defined as:

$$F_{yfP} = \alpha_f C_{fp} = \left(\delta - \beta - \frac{l_f \omega_z}{u} \right) C_{fp} \tag{2-32}$$

$$F_{yrP} = \alpha_r C_{fp} = \left(-\beta + \frac{l_r \omega_z}{u} \right) C_{rp} \tag{2-33}$$

$$F_{yfQ} = \left(\alpha_f - \alpha_{f0} \right) C_{fq} + F_{f0} = \left(\delta - \beta - \frac{l_f \omega_z}{u} - \alpha_{f0} \right) C_{fq} + F_{f0} \tag{2-34}$$

$$F_{yrQ} = \left(\alpha_r - \alpha_{r0} \right) C_{rq} + F_{r0} = \left(-\beta + \frac{l_r \omega_z}{u} - \alpha_{r0} \right) C_{rq} + F_{r0} \tag{2-35}$$

By combining the above equations, the expressions for the lateral tire forces, which are valid in both operating intervals, can be derived as:

$$F_{yf} = \left(\alpha_f - \alpha_{f0} \right) C_f + F_{f0} = \left(\delta - \beta - \frac{l_f \omega_z}{u} - \alpha_{f0} \right) C_f + F_{f0} \tag{2-36}$$

$$F_{yr} = \left(\alpha_r - \alpha_{r0} \right) C_r + F_{r0} = \left(-\beta + \frac{l_r \omega_z}{u} - \alpha_{r0} \right) C_r + F_{r0} \tag{2-37}$$

where α_{f0}, F_{f0}, α_{r0}, and F_{r0} are known constants and

$$C_{f,r} = \begin{cases} C_{fp,rp} & \text{for } \alpha_{f,r} \le \alpha_{f0,r0} \\ C_{fq,rq} & \text{for } \alpha_{f,r} > \alpha_{f0,r0} \end{cases} \tag{2-38}$$

Inserting expressions for the lateral forces (2-36) and (2-37) into Eq. (2-13) yields:

$$ma_y = \left(\delta - \beta - \frac{l_f \omega_z}{u} - \alpha_{f0} \right) C_f + F_{f0} + \left(-\beta + \frac{l_r \omega_z}{u} - \alpha_{r0} \right) C_r + F_{r0} \tag{2-39}$$

After rearranging the above equation reads:

$$ma_y = -\beta \left(C_f + C_r \right) - \left(\frac{l_f C_f - l_r C_r}{u} \right) \omega_z + C_f \delta - \alpha_{f0} C_f - \alpha_{r0} C_r + F_{f0} + F_{r0} \tag{2-40}$$

Finally the expression for the sideslip angle can be expressed as:

$$\beta = \frac{1}{C_f + C_r} \left(-ma_y - \frac{l_f C_f - l_r C_r}{u} \omega_z + C_f \delta - \alpha_{f0} C_f - \alpha_{r0} C_r + F_{f0} + F_{r0} \right) \tag{2-41}$$

where a_y, ω_z, u, and δ represent the measured vehicle dynamics (state) variables.

2.3 Tire characteristics

Tire characteristics are integral part of every vehicle dynamics model. In general, there are three types of tire characteristics used for formulation and design of the vehicle dynamics state and parameter estimators [33]: analytical, empirical, and stochastic (e.g. tire forces modeled as random walk type or stochastic variable or Markov process [18,27]). The analytical models can be further classified as linear, piecewise-linear or nonlinear, while the empirical and stochastic models are typically nonlinear.

Fig. 2.5 shows the lateral and longitudinal static tire characteristics of a nonlinear, tire model as a function of the tire slip angle α, longitudinal slip η, and normal load F_z.

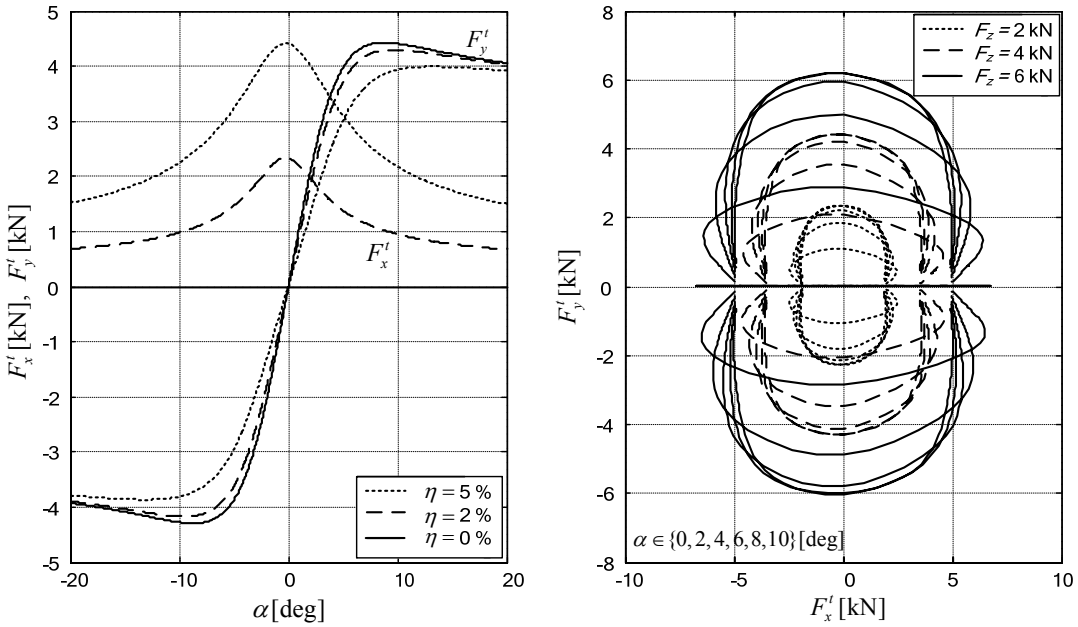

Fig. 2.5 *Tire static characteristics* [23,34].

The lateral static curves from Fig. 2.5 are obtained from the Magic formula model [33]. The tire cornering stiffness coefficient C_i (see Eqs. (2-15) and (2-16), and Fig. 2.4) is defined by the tire lateral force static curve gradient at zero tire slip angle (i.e. $F_y(\alpha)$ curve slope at its origin). As shown in previous Subsection, the cornering stiffness is one of the essential parameters of the linearized tire model. The uncertainty of tire cornering stiffness (front and rear), along with the uncertainties of other vehicle dynamics model parameters (e.g. vehicle mass and yaw moments of inertia), constitutes the main source of the errors in estimation of the vehicle states relying on such model. Moreover, the bicycle model cannot account for the effects of the roll and pitch dynamics, which in this case represent the disturbance. Therefore, it cannot be effectively used in case of the vehicle driving on the banked road. Also, it should

be noted that the linearized vehicle dynamics model is valid for the initial interval of the tire lateral static characteristics (i.e. linear, adhesion region, characterized with the small sideslip angles, in which the vehicle stability is well preserved). On the other hand, when vehicle approaches to the limit of the adhesion region and when it can become unstable the linearized model becomes unreliable.

3 Kalman filter

Kalman filter is a recursive estimator of state variables of the linear stochastic processes based on the noisy and frequently incomplete set of measurements implemented in the so-called predictor-corrector form [2, 3, 24, 37]. It has been developed in 1960's by a Hungarian mathematician R. E. Kalman [24] and successfully implemented in diverse applications ranging from inertial navigation and tracking, sensor calibration, manufacturing and economics, to signal processing, state variable and parameter estimation of dynamics models, nonlinear model predictive control etc. [2, 37].

3.1 Basic Kalman filter

Basic form of the Kalman filter is designed for application in estimation of states of the linear, time-variant, stochastic systems [24]. More specifically, the MIMO ("Multiple Input Multiple Output") type of such linear, stochastic, discrete-time systems can be represented by the process model illustrated in Fig. 3.1, and described by the following matrix equations [2]:

$$\mathbf{x}(k) = \mathbf{F}(k-1)\mathbf{x}(k-1) + \mathbf{G}(k-1)\mathbf{u}(k-1) + \mathbf{w}(k-1) \tag{3-1}$$

$$\mathbf{y}(k) = \mathbf{H}(k)\mathbf{x}(k) + \mathbf{v}(k) \tag{3-2}$$

where $\mathbf{x} \in \Re^n$ is the process state variables vector, $\mathbf{u} \in \Re^p$ is the control inputs vector, $\mathbf{y} \in \Re^m$ is the measurements vector, $\mathbf{w} \in \Re^n$ and $\mathbf{v} \in \Re^m$ are process and measurement noise vectors respectively, $\mathbf{F}_{n\times n}$ is the state transition matrix, $\mathbf{G}_{n\times p}$ is the input matrix, $\mathbf{H}_{m\times n}$ is the output or measurement matrix, and index k represents the sampling step.

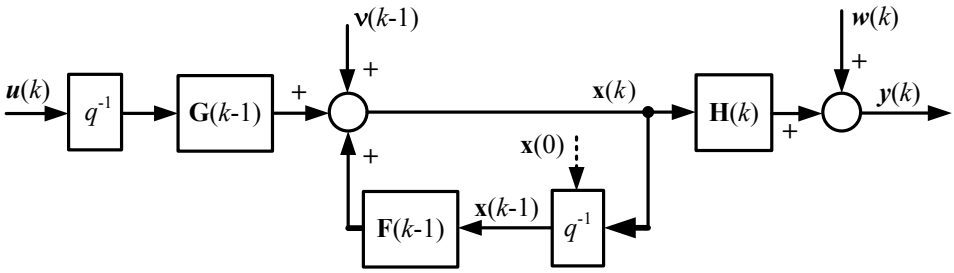

Fig. 3.1 *Time-variant stochastic MIMO process model.*

The discrete-time Kalman filter is utilized for estimation of the state variables of the process defined by Eqs. (3-1) and (3-2), under presumption that the process and measurement noises w_i (i = 1,…,n) and ν_j (j = 1,…,m) are Gaussian probability density distribution type random signals[1] (i.e. $p(w_i) = \aleph(0, q_i)$ and $p(\nu_j) = \aleph(0, r_j)$), characterized by zero mean values and unambiguously defined covariances q_i and r_j. Moreover, it is assumed that the measurement and the process noise vectors are independent (i.e. uncorrelated) and also that the individual elements of the process noise vector and measurement noise vector are uncorrelated, which can be formally expressed by the following expressions:

$$E\langle \mathbf{w}(k) \rangle = \underline{0}\,,\; E\langle \mathbf{v}(k) \rangle = \underline{0}$$

The $E\langle x \rangle \triangleq \bar{x}$ represents the expectation (mean value) value of the random variable x (i.e. the first order moment of random variable x).

$$E\langle w_i(k)\nu_j(k) \rangle = 0, \qquad \forall\; i, j$$

$$E\langle w_i(k)w_j(k) \rangle = \begin{cases} q_i\,, & \text{for } i = j \\ 1\,, & \text{for } i \neq j \end{cases}$$

$$E\langle \nu_i(k)\nu_j(k) \rangle = \begin{cases} r_i\,, & \text{for } i = j \\ 1\,, & \text{for } i \neq j \end{cases}$$

Consequently, the state and measurement noise covariance matrices **Q** and **R**, for such a case are defined as:

$$\begin{aligned} \mathbf{Q}_{nxn}(k) &= E\langle \mathbf{w}(k)\mathbf{w}^T(k) \rangle = \mathrm{cov}(\mathbf{w}(k)) \\ &= diag\left(\begin{bmatrix} \mathrm{var}(w_1) & \mathrm{var}(w_2) & \cdots & \mathrm{var}(w_n) \end{bmatrix} \right) = diag\left(\begin{bmatrix} q_1 & q_2 & \cdots & q_n \end{bmatrix} \right) \end{aligned} \tag{3-3}$$

$$\begin{aligned} \mathbf{R}_{mxm}(k) &= E\langle \mathbf{v}(k)\mathbf{v}^T(k) \rangle = \mathrm{cov}(\mathbf{v}(k)) \\ &= diag\left(\begin{bmatrix} \mathrm{var}(\nu_1) & \mathrm{var}(\nu_2) & \cdots & \mathrm{var}(\nu_m) \end{bmatrix} \right) = diag\left(\begin{bmatrix} r_1 & r_2 & \cdots & r_m \end{bmatrix} \right) \end{aligned} \tag{3-4}$$

Diagonal elements of the $\mathbf{Q}(k)$ and $\mathbf{R}(k)$ matrices correspond to the variances of the individual elements of the state and the measurement noise vectors **w** and **ν**, respectively. The elements of these two matrices represent the main tuning parameters of the Kalman filter, as shown bellow.

As mentioned in the chapter introduction, Kalman filter is a kind of the predictor/corrector recursive algorithm, and it is composed of the two distinctive estimation stages: the model based prediction (i.e. time-update) stage and measurement correction (i.e. measurement-

[1] Gaussian type random variable probability density distribution is defined as:
$p(x) = \left(\sigma\sqrt{2\pi}\right)^{-1} \exp\left(-(x-\bar{x})^2 / 2\sigma^2\right)$

update) stage, which also requires on-line calculation of optimal Kalman filter gain based on the presumed covariance properties. The Kalman filter algorithm for the linear, stochastic MIMO state-space process model defined by Eqs. (3-1) and (3-2) and illustrated in Fig. 3.1 is described by a block diagram given in the Fig. 3.2.

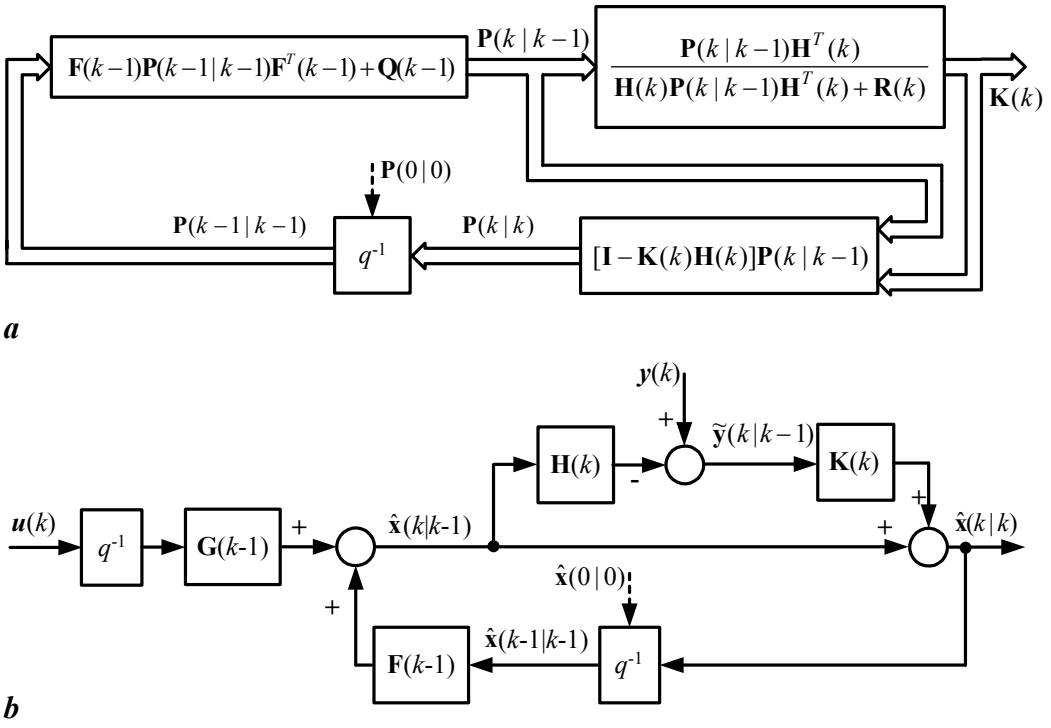

Fig. 3.2 *Block diagram of the calculation of the optimal Kalman gains (a) and basic discrete-time Kalman filter state estimator (b) for linear, time-variant MIMO process model.*

The estimator equations are defined as:

$$\hat{\mathbf{x}}(k \mid k-1) = \mathbf{F}(k-1)\hat{\mathbf{x}}(k-1 \mid k-1) + \mathbf{G}(k-1)\mathbf{u}(k-1) \tag{3-5}$$

$$\mathbf{P}(k \mid k-1) = \mathbf{F}(k-1)\mathbf{P}(k-1 \mid k-1)\mathbf{F}^T(k-1) + \mathbf{Q}(k-1) \tag{3-6}$$

$$\tilde{\mathbf{y}}(k \mid k-1) = \mathbf{y}(k) - \mathbf{H}(k)\hat{\mathbf{x}}(k \mid k-1) \tag{3-7}$$

$$\mathbf{K}(k) = \mathbf{P}(k \mid k-1)\mathbf{H}^T(k)\left[\mathbf{H}(k)\mathbf{P}(k \mid k-1)\mathbf{H}^T(k) + \mathbf{R}(k)\right]^{-1} \tag{3-8}$$

$$\hat{\mathbf{x}}(k \mid k) = \hat{\mathbf{x}}(k \mid k-1) + \mathbf{K}(k)\tilde{\mathbf{y}}(k \mid k-1) \tag{3-9}$$

$$\mathbf{P}(k \mid k) = \left[\mathbf{I} - \mathbf{K}(k)\mathbf{H}(k)\right]\mathbf{P}(k \mid k-1) \tag{3-10}$$

where $\hat{\mathbf{x}}(k \mid k-1)$, $\mathbf{P}_{nxn}(k \mid k-1)$ and $\hat{\mathbf{x}}(k \mid k)$, $\mathbf{P}_{nxn}(k \mid k)$ are the a-priori and a-posteriori state estimate vectors and state estimation error covariance matrices, respectively, $\mathbf{K}(k)$ is the matrix of optimal Kalman gains, and $\tilde{\mathbf{y}}(k \mid k-1)$ is the measurement residual (i.e. inovation).

In the prediction stage (Eqs. (3-5) and (3-6)), the a-priori state vector estimate (prediction) and a-priori state estimation error covariance matrix are being calculated. The predicted states are obtained by relying on the known deterministic part of the process model and known or estimated variances of the measurements and process model states (matrices **Q** and **R**). By utilizing the observation model (i.e. process model output equation) and current measurements $\mathbf{y}(k)$ the measurement residuals (3-7) are calculated. In the measurement update stage, represented by Eqs. (3-8) to (3-10), the optimal Kalman filter gain matrix $\mathbf{K}(k)$, a-posteriori state vector estimate $\hat{\mathbf{x}}(k\,|\,k)$, and state estimation error covariance matrix $\mathbf{P}(k\,|\,k)$ updates are obtained. The Kalman filter feedback gains (matrix **K**) are calculated based on the known or estimated state and measurement covariance matrices (**Q** and **R**), and they are optimal with respect to minimizing the covariance of the a-posteriori state estimation error $\tilde{\mathbf{x}}(k\,|\,k)$, according to the orthogonality principle [37]. The state estimate and estimation error covariance matrix are then updated in accordance with calculated optimal Kalman gains.

The a-priori and a-posteriori state estimation error covariance matrices from Eqs. (3-6) and (3-10) are defined as:

$$\mathbf{P}(k\,|\,k-1) \triangleq E\left\langle \tilde{\mathbf{x}}(k\,|\,k-1)\tilde{\mathbf{x}}^T(k\,|\,k-1)\right\rangle \tag{3-11}$$

$$\mathbf{P}(k\,|\,k) \triangleq E\left\langle \tilde{\mathbf{x}}(k\,|\,k)\tilde{\mathbf{x}}^T(k\,|\,k)\right\rangle \tag{3-12}$$

where $\tilde{\mathbf{x}}(k\,|\,k-1) \triangleq \mathbf{x}(k) - \hat{\mathbf{x}}(k\,|\,k-1)$ and $\tilde{\mathbf{x}}(k\,|\,k) \triangleq \mathbf{x}(k) - \hat{\mathbf{x}}(k\,|\,k)$ are a-priori and a-posteriori state estimation error vectors. The discrete-time form of Riccati equation (3-6) can be derived by equating the (3-11) by using Eqs. (3-1) and (3-5) (also see [37, 38]):

$$\tilde{\mathbf{x}}(k\,|\,k-1) = \mathbf{F}(k-1)\tilde{\mathbf{x}}(k-1) + \mathbf{w}(k-1) \tag{3-13}$$

$$\begin{aligned}\mathbf{P}(k\,|\,k-1) &\triangleq E\left\langle \left[\mathbf{F}(k-1)\tilde{\mathbf{x}}(k-1) + \mathbf{w}(k-1)\right]\cdot\left[\mathbf{F}(k-1)\tilde{\mathbf{x}}(k-1) + \mathbf{w}(k-1)\right]^T\right\rangle \\ &= E\left\langle \left[\mathbf{F}(k-1)\tilde{\mathbf{x}}(k-1) + \mathbf{w}(k-1)\right]\cdot\left[\tilde{\mathbf{x}}^T(k-1)\mathbf{F}^T(k-1) + \mathbf{w}^T(k-1)\right]\right\rangle\end{aligned} \tag{3-14}$$

after some rearranging and by acknowledging that the $\mathbf{w}(k-1)$ and $\tilde{\mathbf{x}}(k-1)$ are independent the former equation reads:

$$\begin{aligned}\mathbf{P}(k\,|\,k-1) &= \mathbf{F}(k-1)E\left\langle \tilde{\mathbf{x}}(k-1)\tilde{\mathbf{x}}^T(k-1)\right\rangle\mathbf{F}^T(k-1) + E\left\langle \mathbf{w}(k-1)\mathbf{w}^T(k-1)\right\rangle \\ &= \mathbf{F}(k-1)\mathbf{P}(k-1\,|\,k-1)\mathbf{F}^T(k-1) + \mathbf{Q}(k-1)\end{aligned} \tag{3-15}$$

Similarly, the equation (3-10) for calculation of the a-posteriori state estimation error covariance matrix $\mathbf{P}(k|k)$ can be derived from its definition (3-12) and the following expression for a-posteriori state estimation error:

$$\tilde{\mathbf{x}}(k|k) = \left[\mathbf{I} - \mathbf{K}(k)\mathbf{H}(k)\right]\tilde{\mathbf{x}}(k|k-1) - \mathbf{K}(k)\mathbf{v}(k) \tag{3-16}$$

$$\begin{aligned}
&\mathbf{P}(k|k-1) \hat{=} E\left\langle \tilde{\mathbf{x}}(k|k)\tilde{\mathbf{x}}^T(k|k)\right\rangle \\
&= E\left\langle \left\{\left[\mathbf{I} - \mathbf{K}(k)\mathbf{H}(k)\right]\tilde{\mathbf{x}}(k|k-1) - \mathbf{K}(k)\mathbf{v}(k)\right\}\cdot\left\{\left[\mathbf{I} - \mathbf{K}(k)\mathbf{H}(k)\right]\tilde{\mathbf{x}}(k|k-1) - \mathbf{K}(k)\mathbf{v}(k)\right\}^T\right\rangle \\
&= E\left\langle \left\{\left[\mathbf{I} - \mathbf{K}(k)\mathbf{H}(k)\right]\tilde{\mathbf{x}}(k|k-1) - \mathbf{K}(k)\mathbf{v}(k)\right\}\cdot\left\{\tilde{\mathbf{x}}^T(k|k-1)\left[\mathbf{I} - \mathbf{H}(k)\mathbf{K}(k)\right]^T - \mathbf{v}^T(k)\mathbf{K}^T(k)\right\}\right\rangle
\end{aligned} \tag{3-17}$$

However, $\tilde{\mathbf{x}}(k|k-1)$ and $\mathbf{v}^T(k)$ are independent [2], so the above equation reduces to:

$$\begin{aligned}
\mathbf{P}(k|k-1) &= E\left\langle \left[\mathbf{I} - \mathbf{K}(k)\mathbf{H}(k)\right]\tilde{\mathbf{x}}(k|k-1)\tilde{\mathbf{x}}^T(k|k-1)\left[\mathbf{I} - \mathbf{H}(k)\mathbf{K}(k)\right]^T\right\rangle \\
&\quad + E\left\langle \mathbf{K}(k)\mathbf{v}(k)\mathbf{v}^T(k)\mathbf{K}^T(k)\right\rangle \\
&= \left[\mathbf{I} - \mathbf{K}(k)\mathbf{H}(k)\right]\mathbf{P}(k|k-1)\left[\mathbf{I} - \mathbf{H}(k)\mathbf{K}(k)\right]^T + \mathbf{K}(k)\mathbf{R}(k)\mathbf{K}^T(k)
\end{aligned} \tag{3-18}$$

After inserting the equation (3-8) into (3-18) and rearranging the final expression for the a-posteriori state estimation error covariance matrix given in Eq. (3-10) is obtained.

In order to analyze the effect of the measurement covariance (**R**) and a-priori state prediction errors ($\mathbf{P}(k|k-1)$) upon the Kalman gains calculation and correction stage execution the following two marginal (extreme) cases have been considered. More precisely, if the ideal, noise-free measurements are assumed (measurement covariance **R** is a zero matrix), the Kalman gains matrix from Eq. (3-8) reads:

$$\mathbf{K}(k) = \lim_{\mathbf{R}(k)\to 0} \mathbf{P}(k|k-1)\mathbf{H}^T(k)\left[\mathbf{H}(k)\mathbf{P}(k|k-1)\mathbf{H}^T(k) + \mathbf{R}(k)\right]^{-1} = \mathbf{H}^{-1}(k) \tag{3-19}$$

and consequently, the a-posteriori state estimate vector from Eq. (3-9) can be rewritten in a form:

$$\hat{\mathbf{x}}(k|k) = \hat{\mathbf{x}}(k|k-1) + \mathbf{H}^{-1}(k)\left[\mathbf{y}(k) - \mathbf{H}(k)\hat{\mathbf{x}}(k|k-1)\right] = \mathbf{H}^{-1}(k)\mathbf{y}(k) \tag{3-20}$$

According to the above equations the a-posteriori state estimate is a function of the measurements and inverted measurement matrix (assuming matrix H is regular) and does not rely on the process model. The a-posteriori state estimation error covariance matrix equals zero ($\mathbf{P}(k|k) = \underline{0}$, cf. equation (3-10)), while the a-priori estimation error covariance matrix becomes equal to state covariance matrix ($\mathbf{P}(k|k-1) = \mathbf{Q}(k-1)$). Generally speaking, if the measurement covariances r_i are small in comparison to the state covariances q_i, the Kalman filter state estimates will predominantly rely upon the measurements model.

On the other hand, if the state covariance matrix $\mathbf{Q}(k)$ tends to zero matrix (perturbations in all states tend to zero) in conjunction with accurate deterministic model and nonzero measurement covariance matrix $\mathbf{R}(k)$, the a-priori state estimation error covariance matrix $\mathbf{P}(k \mid k-1)$ tends to zero matrix (cf. equation (3-6)) and, consequently, the Kalman gain matrix becomes zero as well.

$$\mathbf{K}(k) = \lim_{P(k|k-1)\to 0} \mathbf{P}(k \mid k-1)\mathbf{H}^T(k)\left[\mathbf{H}(k)\mathbf{P}(k \mid k-1)\mathbf{H}^T(k) + \mathbf{R}(k)\right]^{-1} = \underline{0} \qquad (3\text{-}21)$$

In such a theoretical case, the state estimates would rely solely upon the process model, and the correction (measurement update) phase would be unnecessary. In the real-world applications the state estimates relay on both the process and measurement models. The optimal Kalman gains and accurate state estimates rely on identification of realistic state and measurement covariance matrices which are the measure of the reliability of the process model and available measurements. More precisely, the ratio between the state and measurement covariance $\mathbf{Q}*\mathbf{R}^{-1}$ will determine whether the weight would be given to the model or to the measurements.

In most applications the measurement covariance matrix **R** is readily available, because it can be derived directly from the measured signals. On the other hand, the elements of the state perturbation covariance matrix **Q** are much more difficult to come by, since the states often cannot be measured and therefore the state covariance needs to be guessed based on the available measurements and physical properties. In consequence, the Kalman filter gains will be suboptimal. The tuning of Kalman filter is performed by setting the appropriate values of the state and measurement covariance matrices (commonly the **R** is kept constant and only **Q** is varied). As mentioned above, it relies on the ability to formulate an accurate description of the deterministic part of the process model, as well as the capability to account for all of the stochastic disturbances (noise) within the observed process. In particular, by tuning the Kalman filter with smaller covariance matrix **Q** values, the Kalman gains are decreased, and more weight is given to the state-estimate based on the deterministic part of the model, and reduces the impact of the measurement corrections upon the a-posteriori state estimate. At the same time, the filter ability to track fast changes in the states becomes less effective. On the other hand, by increasing the values of variances within **Q** matrix, the emphasis is shifted towards the measurements through increase of Kalman gain values that results with higher noise in the state estimates. The **Q** and **R** matrices are often time-variant because the levels of the reliability of the process model and measurements vary with the operating regimes ore

some external disturbances, and consequently they must be appropriately updated (see Subsection 3.3).

Apart from the state and measurement covariance matrices **Q** and **R**, the initial values of the states and a-priori state estimation error covariance matrix $\hat{\mathbf{x}}(0\,|\,0)$ and $\mathbf{P}(0\,|\,0)$, respectively, have large impact on the Kalman filter performance during initial transient (after the estimator is re-started). The initial transient tracking errors can be reduced if $\hat{\mathbf{x}}(0\,|\,0)$ and $\mathbf{P}(0\,|\,0)$ are set as close as possible to their true values. Generally, if the higher initial values of the state estimation error covariance matrix are used in the presence of the initial state estimation errors, the resulting higher Kalman gains ensure faster convergence of the state estimates to their true values, at the expense of the increased noise.

3.2 Extended Kalman filter

Extended Kalman filter (EKF) is a generalization of the basic Kalman filter algorithm for the application to state variable and parameter estimation of nonlinear, time variant, discrete-time processes described by the following nonlinear dynamic process model:

$$\mathbf{x}(k) = \mathbf{f}\left(\mathbf{x}(k-1), \mathbf{u}(k-1), \mathbf{w}(k-1)\right) \tag{3-22}$$

$$\mathbf{y}(k) = \mathbf{h}\left(\mathbf{x}(k), \mathbf{v}(k)\right) \tag{3-23}$$

where **f** and **h** are continuously differentiable matrix functions.

The nonlinear model approximation used for EKF design is based on the linearization of the model described by Eqs. (3-22) and (3-23) [2,38] around the operating point defined by the a-posteriori state estimates from the previous time step:

$$\mathbf{x}(k) = \mathbf{x}_0(k) + \mathbf{F}(k-1)\tilde{\mathbf{x}}(k-1\,|\,k-1) + \boldsymbol{\Omega}(k-1)\mathbf{w}(k-1) \tag{3-24}$$

$$\mathbf{y}(k) = \mathbf{h}\left(\mathbf{x}_0(k)\right) + \mathbf{H}(k)\left(\mathbf{x}(k) - \mathbf{x}_0(k)\right) + \boldsymbol{\Psi}(k)\mathbf{v}(k) \tag{3-25}$$

where $\mathbf{x}_0(k) = \mathbf{f}\left(\hat{\mathbf{x}}(k-1\,|\,k-1), \mathbf{u}(k-1)\right)$ represents the operating point.

The equations of extended Kalman filter read:

$$\hat{\mathbf{x}}(k\,|\,k-1) = \mathbf{f}\left(\hat{\mathbf{x}}(k-1\,|\,k-1), \mathbf{u}(k-1)\right) \tag{3-26}$$

$$\tilde{\mathbf{y}}(k\,|\,k-1) = \mathbf{y}(k) - \mathbf{h}\left(\hat{\mathbf{x}}(k\,|\,k-1)\right) \tag{3-27}$$

$$\mathbf{P}(k\,|\,k-1) = \mathbf{F}(k-1)\mathbf{P}(k-1\,|\,k-1)\mathbf{F}^T(k-1) + \boldsymbol{\Omega}(k-1)\mathbf{Q}(k-1)\boldsymbol{\Omega}^T(k-1) \tag{3-28}$$

$$\mathbf{K}(k) = \mathbf{P}(k\,|\,k-1)\mathbf{H}^T(k)\left[\mathbf{H}^T(k)\mathbf{P}(k\,|\,k-1)\mathbf{H}^T(k) + \boldsymbol{\Psi}(k)\mathbf{R}(k)\boldsymbol{\Psi}^T(k)\right]^{-1} \tag{3-29}$$

$$\hat{\mathbf{x}}(k\,|\,k) = \hat{\mathbf{x}}(k\,|\,k-1) + \mathbf{K}(k)\tilde{\mathbf{y}}(k\,|\,k-1) \tag{3-30}$$

$$\mathbf{P}(k \mid k) = \mathbf{P}(k \mid k-1) - \mathbf{K}(k)\mathbf{H}(k)\mathbf{P}(k \mid k-1) \tag{3-31}$$

where matrices $\mathbf{F}(k)$, $\mathbf{H}(k)$, $\mathbf{\Omega}(k)$, $\mathbf{\Psi}(k)$ are Jacobian matrices obtained as follows:

$$\mathbf{F}(k-1) = \left.\frac{\partial \mathbf{f}}{\partial \mathbf{x}}\right|_{\substack{\mathbf{x}=\mathbf{x}(k-1|k-1) \\ \mathbf{u}(k-1) \\ \mathbf{w}=\underline{0}}} \tag{3-32}$$

$$\mathbf{\Omega}(k-1) = \left.\frac{\partial \mathbf{f}}{\partial \mathbf{w}}\right|_{\substack{\mathbf{x}=\hat{\mathbf{x}}(k-1|k-1) \\ \mathbf{u}(k-1) \\ \mathbf{w}=\underline{0}}} \tag{3-33}$$

$$\mathbf{H}(k) = \left.\frac{\partial \mathbf{h}}{\partial \mathbf{x}}\right|_{\substack{\mathbf{x}=\mathbf{x}_0(k) \\ \mathbf{v}=\underline{0}}} \tag{3-34}$$

$$\mathbf{\Psi}(k) = \left.\frac{\partial \mathbf{h}}{\partial \mathbf{v}}\right|_{\substack{\mathbf{x}=\mathbf{x}_0(k) \\ \mathbf{v}=\underline{0}}} \tag{3-28}$$

Note that the EKF equations (3-26)-(3-31) are similar to the equations of a basic Kalman filter with the exception that the a-priori state estimate and measurement residual are being calculated from nonlinear state model and measurement equations. Kalman gain matrix $\mathbf{K}(k)$, state estimation error covariance matrices $\mathbf{P}(k|k\text{-}1)$ and $\mathbf{P}(k|k)$, and a-posteriori state estimate $\hat{\mathbf{x}}(k \mid k)$ are basically derived from the equations for the common KF, besides that the $\mathbf{F}(k)$, $\mathbf{H}(k)$, $\mathbf{\Omega}(k)$, $\mathbf{\Psi}(k)$ are Jacobian matrices obtained by linearization of the nonlinear process state and measurement equations (3-22) and (3-23).

EKF filter, unlike the basic KF, is suboptimal because the nonlinear transformation of the state and measurement variables, needed for the purpose of linearization of the process model, results in non-Gaussian probability distribution of the state and measurement noise [2, 3, 37, 38]. Moreover, the EKF algorithm tries to accomplish the aforementioned optimality at the expense of stability (estimator convergence). Namely, in the presence of the modeling errors and low excitation the estimated state variables can quickly diverge from their true values [41].

3.3 Adaptive Kalman filter

In the case of time-variant covariance models of the state and measurement noise vectors and/or change in the reliability levels of the state-space and measurement models related to external disturbances, unmodeled dynamics, parameter variations or structure change within the model, sensor bias, fault etc., the Kalman filter with fixed state and measurement matrices cannot provide accurate estimates. In such conditions the Adaptive Kalman Filter (AKF)

should be used, because it enables timely adaptation of the covariance matrices resulting in the appropriate tuning of the KF in order to compensate for the above disturbance effects or changes in the underlying models.

Consequently, various concepts of adaptive estimators utilizing Kalman filter methodology, such as Multiple Model-based estimator (MMAE), Innovation-based estimator (IAE), Residual-based estimator (RAE) etc., are proposed and evaluated in literature [37, 39, 40]. The MMAE runs multiple Kalman filters in parallel, each of them designed for specific, known disturbance or model error, so it requires the a-priori knowledge on disturbances, faults or possible model variations. The IAE and RAE estimate and adapt the state and measurement covariance matrices over the moving window based on the innovation or residual time sequence. Such approaches to adaptive Kalman filtering can be demanding with respect to computational burden (CPU power) and required memory resources, while, on the other hand, they are effective only if the measurement distribution and covariance model are consistent throughout the moving window. The adaptive fading Kalman filter (AFKF) represents a computationally more efficient algorithm derived from the IAE approach. AFKF adaptation mechanism is based on the scaling of the nominal covariance matrices **R** and **Q** by appropriate single or multiple scaling factors (i.e. Single Fading Factor method - SFF or Multiple Fading Factor method - MFF) [42, 43, 45].

Hereinafter, the SFF and MFF adaptive fading Kalman filter will be described in more detail with scaling of both the measurement and the state covariance matrices in order to be able to account for the errors/changes in measurements as well as in the process model.

3.3.1 Single fading factor AFKF

First step in SFF AFKF design is to calculate the measurement covariance scaling factor from the measurement innovation sequence, in order to account for the changes in the measurement model. The covariance of the measurement residuals (also known as innovation covariance) can be defined as:

$$\mathbf{C}_{\mathbf{r}}(k) \hat{=} E\left(\tilde{\mathbf{y}}(k \mid k-1) \cdot \tilde{\mathbf{y}}^{T}(k \mid k-1)\right) = \mathbf{H}(k)\,\mathbf{P}(k \mid k-1)\,\mathbf{H}^{T}(k) + \mathbf{R}(k) \tag{3-29}$$

This expression represents the theoretical value of the measurement residual covariance which is valid if the state and measurement covariance models are accurate. On the other hand, the true residual covariance matrix can be estimated as:

$$\hat{\mathbf{C}}_{\mathbf{r}}(k) = \frac{1}{M-1} \sum_{i=k-M+1}^{k} \tilde{\mathbf{y}}(k \mid k-1) \cdot \tilde{\mathbf{y}}^{T}(k \mid k-1) \tag{3-30}$$

where the M is the length of the time frame on which the innovation covariance estimate is calculated. The scaling factor is typically derived from the discrepancies between the theoretical and estimated values of the measurement innovation covariance (i.e. the difference between $\mathbf{C}_\mathbf{r}(k)$ and $\hat{\mathbf{C}}_\mathbf{r}(k)$).

The main distinction between various AFKF implementations is related to the particular approach of calculating the scaling coefficients. In this particular case, the first adaptation coefficient $\alpha_{ad} = f\left(\hat{\mathbf{C}}_\mathbf{r}(k)\mathbf{C}_r^{-1}(k)\right)$ is derived from the ratio of the estimated and theoretical innovation covariance matrices according to the following expression:

$$\alpha_{ad}(k) = \max\left\{1,\ \frac{1}{m} tr\left(\hat{C}_r(k) C_r^{-1}(k)\right)\right\} \tag{3-31}$$

where m is the size of the measurement vector $\mathbf{y}$. The second adaptation coefficient λ_{ad} is defined by considering the case of the incomplete information on the dynamic model equations. Generally, the estimation errors in such a case can be reduced by increasing the a-priori state estimation error covariance matrix. Thus the scalar adaptation factor $\lambda_{ad} \geq 1$ is introduced to account for the increased $\mathbf{P}(k \mid k-1)$ matrix, while α_{ad} is still determined by the related increase of the innovation covariance matrix. The λ_{ad} can be obtained by equating the following equation:

$$\alpha_{ad}(k)\mathbf{C}_r(k) = \lambda_{ad}(k)\mathbf{H}(k)\mathbf{P}(k \mid k-1)\mathbf{H}^T(k) + \mathbf{R}(k) \tag{3-32}$$

After inserting Eq. (3-29) into Eq. (3-32) and rearranging the final expression for calculation of the adaptation coefficient read:

$$\lambda_{ad}(k) \approx \frac{tr\left(\alpha_{ad}(k)\mathbf{H}(k)\mathbf{P}(k \mid k-1)\mathbf{H}^T(k) + \left(\alpha_{ad}(k)-1\right)\mathbf{R}(k)\right)}{tr\left(\mathbf{H}(k)\mathbf{P}(k \mid k-1)\mathbf{H}^T(k)\right)} \tag{3-33}$$

Finally, the Kalman filter equations (3-6) and (3-8) are modified (i.e. made adaptive) by utilizing these two adaptive coefficients:

$$\mathbf{P}_{ad}(k \mid k-1) = \lambda_{ad}(k)\left(\mathbf{F}(k-1)\mathbf{P}(k-1 \mid k-1)\mathbf{F}^T(k-1) + \mathbf{Q}(k-1)\right) \tag{3-34}$$

$$\mathbf{K}_{ad}(k) = \frac{\lambda_{ad}(k)}{\alpha_{ad}(k)} \cdot \frac{\mathbf{P}(k \mid k-1)\mathbf{H}^T(k)}{\mathbf{H}(k)\mathbf{P}(k \mid k-1)\mathbf{H}^T(k) + \mathbf{R}(k)} \tag{3-35}$$

Note that in case of measurement model-related errors the innovation covariance matrix is also increased ($\alpha_{ad} > 1$), in particular due to the increase of the measurement covariance matrix $\mathbf{R}$, while the a-priori state estimation matrix $\mathbf{P}(k \mid k-1)$ remains unchanged (which can

be facilitated by setting $\lambda_{ad} = 1$). The related estimation errors are thus reduced, according to Eq. (3-35) through the decrease of Kalman gains by means of a scaling factor $1/\alpha_{ad}$.

3.3.2 Multiple fading factor AFKF

The adaptive fading Kalman filter with multiple fading factors is derived by applying the same logic as in the case of AFKF with single fading factor described above. For the case of errors in the observation (measurement model), the scale matrix $\mathbf{\Gamma}_{\text{mxm}}$ is calculated from the prediction error (deviation) between the theoretical and estimated innovation covariance matrices. Since the error in the innovation covariance is assumed to originate from the mismatch in measurement covariance matrix, the appropriate scaling matrix $\mathbf{\Gamma}$ needed to compensate for those deviations is obtained as:

$$\hat{\mathbf{C}}_{\mathbf{r}}(k) = \mathbf{H}(k)\mathbf{P}(k \mid k-1)\mathbf{H}^{T}(k) + \mathbf{\Gamma}(k)\mathbf{R}(k) \tag{3-36}$$

$$\mathbf{\Gamma}(k) = \left[\hat{\mathbf{C}}_{\mathbf{r}}(k) - \mathbf{H}(k)\mathbf{P}(k \mid k-1)\mathbf{H}^{T}(k)\right] \mathbf{R}^{-1}(k) \tag{3-37}$$

However due to the numerical errors (computer floating point arithmetic round-off errors, approximation errors in the process and observation models due to EKF linearization, Taylor-series expansion-based approximation of the discrete-time model), the scaling matrix may neither be diagonal nor positive definite. Therefore the scaling matrix is derived by introducing the appropriate constraints to ensure the positive definiteness:

$$\mathbf{\Gamma}^{*}(k) = diag(\varphi_1^{*}, \varphi_2^{*} \cdots \varphi_m^{*}) \tag{3-38}$$

where $\varphi_i^{*}(k) = \max\{1,\ \varphi_{ii}(k)\} \qquad i = 1, \cdots, m$.

On the other hand, in the case of errors in the state-space model, the related adaptation i.e. fading matrix $\mathbf{\Lambda}(k)$ is defined as:

$$\hat{\mathbf{C}}_{\mathbf{r}}(k) = \mathbf{H}(k)\left[\mathbf{F}(k-1)\mathbf{P}(k-1 \mid k-1)\mathbf{F}^{T}(k-1) + \mathbf{\Lambda}(k)\mathbf{Q}(k)\right]\mathbf{H}^{T}(k) + \mathbf{R}(k) \tag{3-39}$$

$$\mathbf{\Lambda}(k) = \frac{\mathbf{H}^{-1}(k)\left[\hat{\mathbf{C}}_{\mathbf{r}}(k) - \mathbf{H}(k)\,\mathbf{F}(k-1)\,\mathbf{P}(k-1 \mid k-1)\,\mathbf{F}^{T}(k-1)\,\mathbf{H}^{T}(k) - \mathbf{R}(k)\right]}{\mathbf{Q}(k)\mathbf{H}^{T}(k)} \tag{3-40}$$

Similarly, as in the case of scaling matrix $\mathbf{\Gamma}(k)$, the final fading matrix is derived as:

$$\mathbf{\Lambda}^{*}(k) = diag(\kappa_1^{*}, \kappa_2^{*} \cdots \kappa_n^{*}) \tag{3-41}$$

where $\kappa_i^{*}(k) = \max\{1,\ \kappa_{ii}(k)\} \qquad i = 1, \cdots, n$.

The scaling matrix $\mathbf{\Gamma}^*$ and fading matrix $\mathbf{\Lambda}^*$ are applied in Kalman filter a-priori state error covariance and Kalman filter gain equations (3-6) and (3-8) in order to attenuate the effect of fixed-valued state-perturbation and measurement noise covariance matrices:

$$\mathbf{P}_{ad}(k \mid k-1) = \mathbf{F}(k-1)\mathbf{P}(k-1 \mid k-1)\mathbf{F}^T(k-1) + \mathbf{\Lambda}^*(k)\mathbf{Q}(k-1) \tag{3-42}$$

$$\mathbf{K}_{ad}(k) = \frac{\mathbf{P}(k \mid k-1)\mathbf{H}^T(k)}{\mathbf{H}(k)\mathbf{P}(k \mid k-1)\mathbf{H}^T(k) + \mathbf{\Gamma}^*(k)\mathbf{R}(k)} \tag{3-43}$$

In this way the adaptive fading Kalman filter with multiple fading factors is implemented, that is robust against the disturbances or changes in the state and measurement equations.

4 Yaw rate estimation

4.1 Background

The vehicle body yaw rate is essential information needed for vehicle dynamics control (VDC) systems implementation. The yaw rate signal is traditionally obtained by using a gyroscope placed in the vehicle CoG (i.e. by using a yaw rate gyro). Alternatively, the yaw rate can be estimated by using other existing vehicle dynamics sensors. For instance, in [4] the non-driven wheels rotational speed measurements from ABS sensors are utilized for yaw rate estimation. Furthermore, a single lateral accelerometer placed in CoG [6] or a pair of accelerometers placed outside of CoG [8,9] may also be used. The yaw rate estimation method proposed in [6] may not be accurate for all dynamic conditions due to possible disturbances in road surface and road bank. The approach based on two longitudinal accelerometers [9] does not provide direct steady-state information of yaw rate, and may be sensitive to vehicle dynamics modeling errors and accelerometer offset. The estimator based on a pair of lateral accelerometers [8] provides direct steady-state measurement of the yaw rate, but it may also be sensitive to modeling errors. In addition to longitudinal and lateral accelerometer configurations [8,9], one may also consider combined/diagonal configuration [30]. In general, the main disadvantage of the accelerometer approach is the sensor offset-related drift-like estimation error and a high sensitivity to sensor misalignment errors (see Section 4.3 and [30]).

The yaw rate estimates obtained by utilizing any of the aforementioned estimator configurations, can be used as redundant information for the gyroscope sensor fault detection [6,46] or it can be applied for implementation of accurate estimators (as a low-cost replacement for gyroscope) based on the sensor fusion methodology [6,30,46]. In general, the sensor fusion concept can be used to estimate different vehicle dynamics variables such as gyroscope offset [4,46], sideslip angle [6], and heading angle [47].

The sensor fusion concept for yaw rate estimation, combining two diagonally placed accelerometers and the non-driven wheel speed sensors has been proposed by the author in [47]. This chapter describes the development and verification results of such a combined adaptive estimator. In order to gain more profound insight on the overall accuracy of this adaptive, Extended Kalman Filter (EKF)-based, kinematic yaw rate estimator a detailed analysis of estimation errors for each of the two utilized concepts has been carried out [30,49].

The non-driven wheel speed sensor-based yaw rate estimation is essentially very simple. However, there are numerous effects, such as braking forces, effective tire radius variations, measurement delay due to tire dynamics, and road bump disturbances, which affect the estimation accuracy (see Section 4.2). A detailed algebraic and simulation analysis of estimation errors has been carried out and appropriate open-loop compensation routines have been proposed [48]. The remaining, uncompensated errors are significantly reduced by proper tuning of sensor fusion estimation algorithm [30] that combines the two aforementioned kinematic estimation approaches.

4.2 Estimation based on wheel speed measurements

For the front wheel drive vehicles the yaw rate can be estimated from the measured non-driven rear wheel rotational speeds ω_{rl} and ω_{rr} [6,30,46,47]. From the kinematic relationships shown in Fig. 4.1, the rear wheels velocities u_{rl} and u_{rr} are related to the vehicle longitudinal speed u, the yaw rate ω_z, and the vehicle track t according to the expression (4-1).

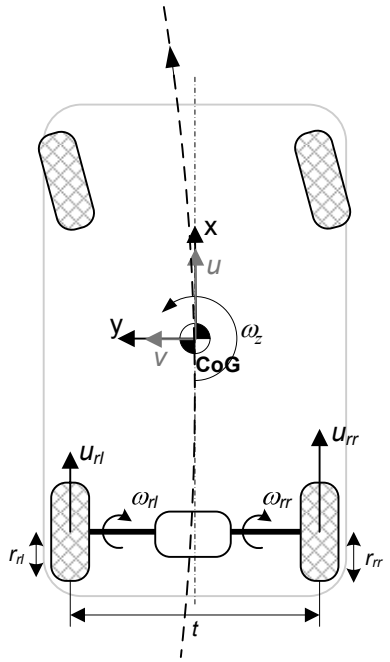

Fig. 4.1 *Concept of yaw rate estimation based on non-driven wheel speed measurements.*

$$u_{rl} = u + \omega_z \frac{t}{2}, \quad u_{rr} = u - \omega_z \frac{t}{2} \tag{4-1}$$

The longitudinal vehicle speed and the yaw rate can, thus, be calculated as:

$$u = \frac{u_{rl} + u_{rr}}{2} = \frac{\omega_{rl} r_{rl} + \omega_{rr} r_{rr}}{2} \tag{4-2}$$

$$\omega_z = \frac{u_{rr} - u_{rl}}{t} = \frac{\omega_{rr} r_{rr} - \omega_{rl} r_{rl}}{t} \tag{4-3}$$

where r_{rl} and r_{rr} are the unknown effective tire radii (see Fig. 4.2). The effective tire radius r_e shown in Fig. 4.2a is defined as a distance of the imaginary slip point S (normally located slightly below the road surface) from the wheel centre [49]. The rolling velocity of the wheel is then defined as a product of the angular velocity of the wheel and its effective radius $V_r = r_e \omega_w$. The longitudinal slip velocity V_{sx} at the slip point is defined as difference between the wheel centre forward velocity V_x and the rolling velocity V_r:

$$V_{sx} = V_x - V_r = V_x - r_e \omega_w \tag{4-4}$$

In the case of free rolling tire (i.e. zero longitudinal slip velocity) the effective rolling radius is defined as $r_e = V_x / \omega_w$. Furthermore, the effective tire radius r_e decreases with increase of the tire normal load F_z, as illustrated in Fig. 4.2b. The effective radii vs. tire normal load characteristic can be modeled by the following third order polynomial in the square root of F_z [7]:

$$r_e = q_3 \sqrt{F_z^3} + q_2 \sqrt{F_z^2} + q_1 \sqrt{F_z} + q_0 + q_{v1} \omega_w^2 \tag{4-5}$$

where the coefficients $q_0,\ldots,q_3$ and q_{v1} are the tire parameters. The coefficient q_0 corresponds to the unloaded tire rolling radius r_0 that changes with the tire pressure p and the tire tread wear, while the last right-hand side term in Eq. (4-5) relates to the centrifugal effect of the wheel rotational speed on the effective radius.

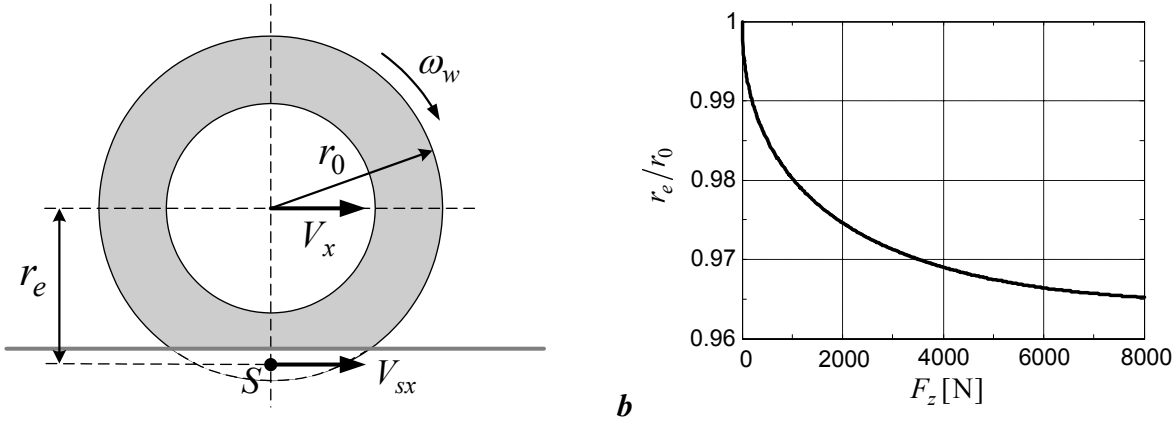

Fig. 4.2 *Effective tire rolling radius r_e: definition (a) and characteristic of tire effective radius versus normal load F_z (b).*

The effective tire radii are difficult to measure (and they change during driving maneuvers). Therefore, the constant nominal effective tire radius r_n can be used for both wheels instead, as an approximation for estimation of the longitudinal velocity and the yaw rate:

$$\hat{u} = \frac{r_n}{2}(\omega_{rr} + \omega_{rl}) \tag{4-6}$$

$$\hat{\omega}_z = \frac{r_n}{t}(\omega_{rr} - \omega_{rl}) \tag{4-7}$$

The yaw rate estimation error derived from Eqs. (4-3) and (4-7) reads:

$$\tilde{\omega}_z \triangleq \hat{\omega}_z - \omega_z = \frac{1}{t}\left[\omega_{rr}(r_n - r_{rr}) - \omega_{rl}(r_n - r_{rl})\right] \tag{4-8}$$

This error is introduced by the difference between the actual effective tire radii r_{rr} and r_{rl} and the nominal tire radius r_n used in the estimation equation. The effective tire radii change with the tire pressure and wear, roll and pitch dynamics, loaded vehicle mass, road bank and road bumps. Also, during braking maneuvers the measured wheel rotational speeds ω_{rr} and ω_{rl} will differ from the nominal rolling values due to the longitudinal slip.

In the yaw rate estimation problem the tire should be considered as a nonlinear velocity sensor (e.g. the velocity u_{rr} in Eq. (4-3) is reconstructed by measuring the tire speed ω_{rr}). The tire longitudinal dynamics introduces a variable delay of such velocity measurement, which can result in a transient yaw rate estimation error. The tire response is analyzed below based on a linearized wheel dynamics model.

Under the presumption that the tire operates within the adhesion region of the tire static curve characteristic (see Section 2.3), the longitudinal linearized tire model is given by [50]:

$$\tilde{\tau}_t = r_e \tilde{F}_x = R_t \tilde{\omega}_w \tag{4-9}$$

where R_t is the tire damping coefficient, F_x is the tire longitudinal force, and ω_w is the wheel rotational speed. Symbol '~' denotes small signal variations around an operating point of the linearized tire model characteristic (ω_{w0}, τ_{t0}). The tire damping coefficient used in Eq. (4-9) is given by:

$$R_t = \frac{d\tau_t}{d\omega_w} = r_e \frac{dF_x}{d\eta}\frac{d\eta}{d\omega_w} = k_x \frac{r_e^2}{u_w} \tag{4-10}$$

where $\eta = (r_e\omega_w - u_w)/u_w$ is the longitudinal slip (see Eq. (2-8)), u_w is the wheel center velocity, and the tire static curve stiffness k_x is defined as (see Fig. 4.3):

$$k_x = \frac{dF_x}{d\eta} = \frac{u_w}{r_e}\frac{dF_x}{d\omega_w} \tag{4-11}$$

The change of vehicle/wheel velocity u_w induces a longitudinal microslip η of the rolling tire. The tire responses by generating a small longitudinal force F_x, which forces the tire rotational

speed ω_w to follow the velocity u_w/r_e. The dynamics of this process is described by following equations [30]:

$$I_w \dot{\tilde{\omega}}_w + \tilde{\tau}_t = I_w \dot{\tilde{\omega}}_w + R_t \tilde{\omega}_w = \tilde{\tau}_{driven} = 0 \quad \Rightarrow \quad T_w \dot{\tilde{\omega}}_w + \tilde{\omega}_w = 0 \tag{4-11}$$

$$T_w = \frac{I_w}{R_t} = \frac{I_w u_w}{k_x r_e^2} \tag{4-12}$$

where I_w is the wheel inertia.

The time constant T_w characterizes a delay in the wheel speed "sensing", which causes a transient error in the yaw rate estimate. The time constant T_w varies with the changes of the wheel/vehicle speed ($u_w \approx u$) and the tire static curve stiffness k_x. On the other hand, the wheel inertia I_w is constant and variations of the tire effective radius r_e are small. Note that the time constant T_w can be different for the left and right wheel due to different tire static curve stiffness ($k_{x,rl} \neq k_{x,rr}$) and different wheel speeds ($u_{w,rl} \neq u_{w,rr}$, Eq. (4-1)) during cornering. This difference in tire dynamics time constants and related wheel speed measurement delays introduces further errors in yaw rate estimation during transient conditions.

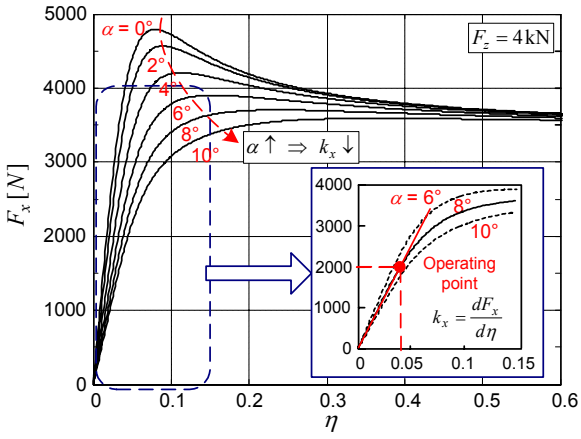

Fig. 4.3 *Longitudinal tire static characteristic for various tire slip angles α.*

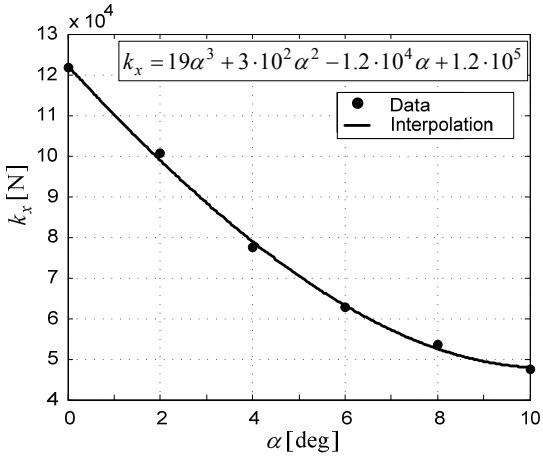

Fig. 4.4 *Longitudinal stiffness k_x vs. tire slip angle α.*

The longitudinal tire static curve given in Fig. 4.3 indicates that the longitudinal stiffness k_x decreases with the increase of the tire slip angle α. As illustrated in Fig. 4.4, the stiffness k_x vs. the slip angle α curve can be approximated by a 3th-order polynomial. Furthermore, for a constant slip angle α the stiffness k_x increases approximately linearly with the tire normal load F_z (see Fig. 4.5 for illustration) $k_x(F_z)\,\big|_{\alpha=2°} = 22F_z + 9.5\cdot10^3$.

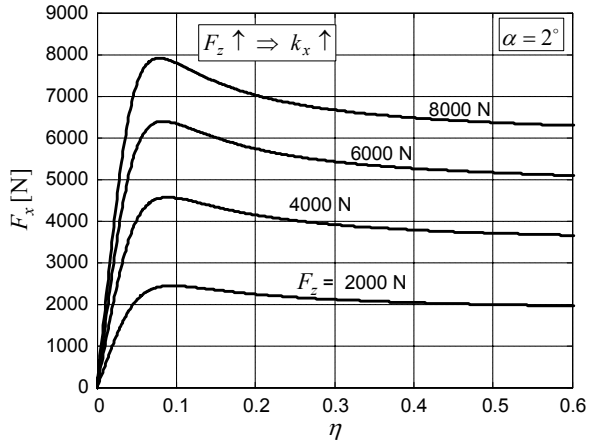

Fig. 4.5 *Tire longitudinal force static characteristic vs. tire normal load F_z.*

Table 4.1 *Summary of the variables affecting speed "sensing" delay T_w and related yaw rate estimation transient error*

$u \uparrow \Rightarrow u_w \uparrow \Rightarrow T_w \uparrow \Rightarrow \tilde{\omega}_z \uparrow$
$F_z \uparrow \Rightarrow k_x \uparrow \Rightarrow T_w \downarrow \Rightarrow \tilde{\omega}_z \downarrow$
$\alpha \uparrow \Rightarrow k_x \downarrow \Rightarrow T_w \uparrow \Rightarrow \tilde{\omega}_z \uparrow$
$\mu \uparrow \Rightarrow k_x \uparrow \Rightarrow T_w \downarrow \Rightarrow \tilde{\omega}_z \downarrow$

Table 4.1 summarizes the influences of tire parameters (including the tire-road friction coefficient μ) on the speed "sensing" delay and the transient error of yaw rate estimation. For the nominal tire parameters (I_w = 1 kgm^2, F_z = 4 kN, and r_n = 0.337 m), k_x values in the range of 50-120 kN (see Fig. 4.4), and vehicle velocity of 20 m/s, the time constant T_w has values in the range of 1.5 - 3.5 ms. The delay and the estimation error become larger for higher vehicle velocities, smaller tire loads, larger tire slip angles, and lower tire-road friction coefficients (see Subsection 4.2.1 d) and simulation results given in Fig. 4.13).

4.2.1 Estimation error analysis

An analysis of the various sources of the yaw rate estimation errors is conducted. The obtained results are illustrated by computer simulations utilizing a 10 degrees-of-freedom vehicle dynamics model [23].

a) Braking related errors

The kinematic yaw rate estimate (4-7) is valid for the case of free rolling non-driving (rear) wheels. However, the rear wheels are normally braked (in addition to the front wheels), which can introduce significant estimation errors due to the presence of a large longitudinal slip η:

$$\eta = \frac{r_e \omega_w - u_w}{u_w} \tag{4-13}$$

This is because the longitudinal slip-related wheel speed offset (i.e. $r_e\omega_w \neq u_w$) may be comparable to the small wheel speed difference $(\omega_{rr} - \omega_{rl})$ appearing in the estimation equation (4-7). By inserting the wheel speeds $u_{w,rl}$ and $u_{w,rr}$ from Eq. (4-1) in Eq. (4-13) the longitudinal slips for the rear left and rear right wheels read:

$$\eta_{rl} = \frac{r_n \omega_{rl} - u + \omega_z \, t/2}{u - \omega_z \, t/2}, \qquad \eta_{rr} = \frac{r_n \omega_{rr} - u - \omega_z \, t/2}{u + \omega_z \, t/2} \tag{4-14}$$

In order to focus the analysis on an impact of the longitudinal slip η on the estimation error, the rear tires effective radii are assumed to be constant and equal to the nominal tire radius r_n. The estimation error is then given by:

$$\tilde{\omega}_z \triangleq \hat{\omega}_z - \omega_z = r_n \frac{\omega_{rr} - \omega_{rl}}{t} - \omega_z \tag{4-15}$$

Combining Eqs. (4-14) and (4-15), and rearanging yields

$$\tilde{\omega}_z = \frac{u}{t}(\eta_{rr} - \eta_{rl}) + \frac{\omega_z}{2}(\eta_{rr} + \eta_{rl}) \tag{4-16}$$

For the normal driving conditions, where $\eta \cong F_x / k_x = \tau_b / r_n / k_x$ (Fig. 4.6; τ_b = braking torque per wheel), Eq. (4-16) is transformed to

$$\tilde{\omega}_z = \frac{\tau_b}{r_n}\left[\frac{u}{t}\left(\frac{1}{k_{x,rr}} - \frac{1}{k_{x,rl}}\right) + \frac{\omega_z}{2}\left(\frac{1}{k_{x,rr}} + \frac{1}{k_{x,rl}}\right)\right] \tag{4-17}$$

where $k_{x,rl}$ and $k_{x,rr}$ are the left and right longitudinal tire stiffnesses.

According to Eq. (4-17) and the simulation results for the braking in a turn maneuver, given in Figs. 4.6 and 4.7, the braking related yaw rate estimation errors increase with the braking torque τ_b. For the fixed, relatively small yaw rate amplitude of 0.11 rad/s the peak estimation error rises almost linearly up to 150% for the braking torques reaching 500Nm per wheel ().

Furthermore, the estimation error depends on the tire stiffness coefficients $k_{x,rl}$ and $k_{x,rr}$, which change approximately linearly with the tire normal load F_z (see Fig. 4.5):

$$k_{x,rl} = a\left(F_{zn} \mp \delta F_z\right) + b, \quad k_{x,rr} = a\left(F_{zn} \pm \delta F_z\right) + b \tag{4-18}$$

where δF_z denotes the cornering-related lateral tire load transfer. According to Eq. (4-17), the estimation error increases with the tire load decrease (e.g. due to the braking-related longitudinal load transfer which results in reduced rear wheels stiffnesses $k_{x,ij}$, see Fig. 4.5) and is amplified by both vehicle velocity u and the yaw rate ω_z. Simulation results in Fig. 4.8a confirm that the higher the yaw rate, the higher the estimation error. However, the relative estimation error $\varepsilon_{\omega z}$ shows small variations with the yaw rate amplitude ω_z, especially at higher yaw rate values (see Fig. 4.8b).

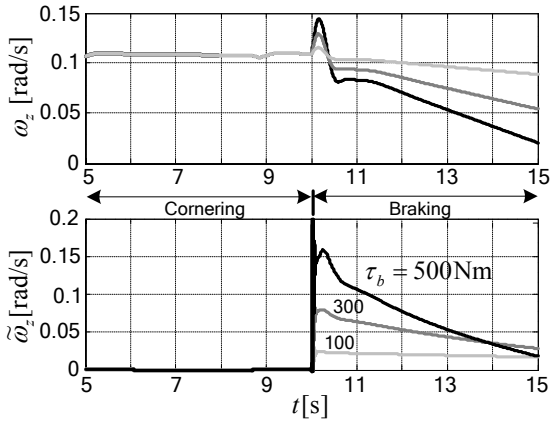

Fig. 4.6 *Yaw rate and yaw rate estimation error response for braking in a turn maneuvers and various braking torques per wheel τ_b*

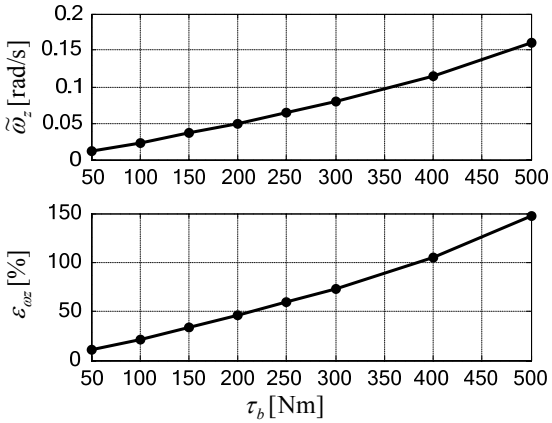

Fig. 4.7 *Yaw rate peak estimation errors (absolute and relative) vs. braking torque τ_b (ω_z = 0.11 rad/s, u = 20 m/s)*

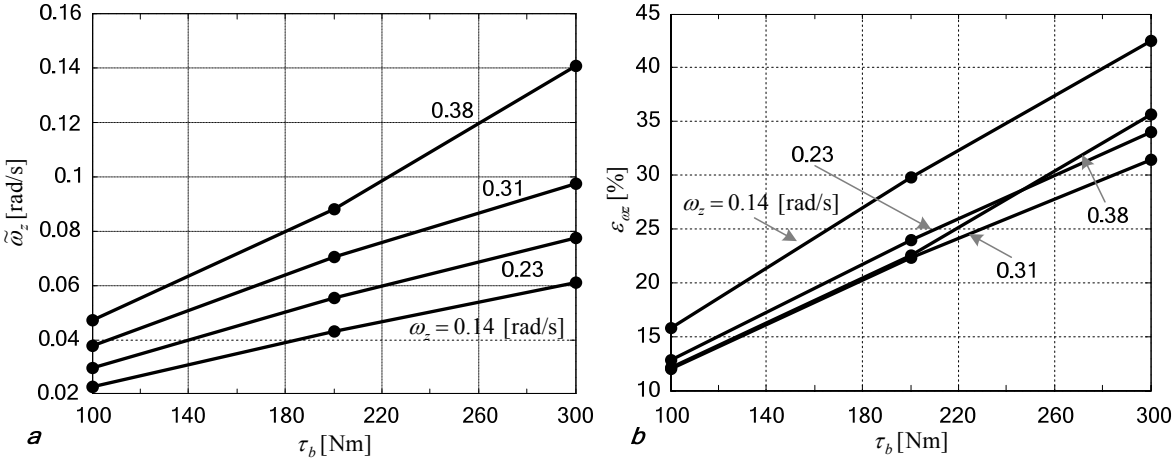

Fig. 4.8 *Quasi-steady-state yaw rate estimation errors vs. applied braking torque for step-steer maneuver: absolute error (a), relative error (b)*

b) Errors caused by effective radius variations

Another major source of the yaw rate estimation error is related to difference between the tire effective radii $r_{rl,rr}$ and the nominal radius r_n (see Eq. (4-8)). It is, therefore, of interest to analyze in detail how the tire effective radii change in various maneuvers and what kind of impact this change has on the estimation accuracy. In this regard, the effective tire radii can be defined by the following expressions:

$$\begin{aligned} r_{rl} &= r_n - \Delta_r + \delta_r \\ r_{rr} &= r_n - \Delta_r - \delta_r \end{aligned} \tag{4-19}$$

where Δ_r is a common component and δ_r is a differential component of the effective tire radii variation. These components are illustrated in Fig. 4.9 for a step-steer maneuver and they are given by:

$$\Delta_r \triangleq r_n - \frac{r_{rl} + r_{rr}}{2} = r_n - \bar{r}_e \tag{4-20}$$

where $\bar{r}_e$ is the effective tire radii mean. The common variation component Δ_r corresponds to variation of tire radii mean (same for both wheels), while the differential component δ_r is equal but of opposite sign for the inner and outer wheels. Simulation results in Fig. 4.9 indeed illustrate that a pure cornering maneuver dominantly induces the differential component δ_r due to the lateral tire load transfer, while a slight change of the common component Δ_r is caused by a certain vehicle deceleration during cornering. It should be noted that the nominal tire radius r_n in Fig. 4.9 is chosen to be lower than the actual tire effective radius mean value, in order to introduce a persistent (positive) common radii variation component Δ_r for the sake of illustration.

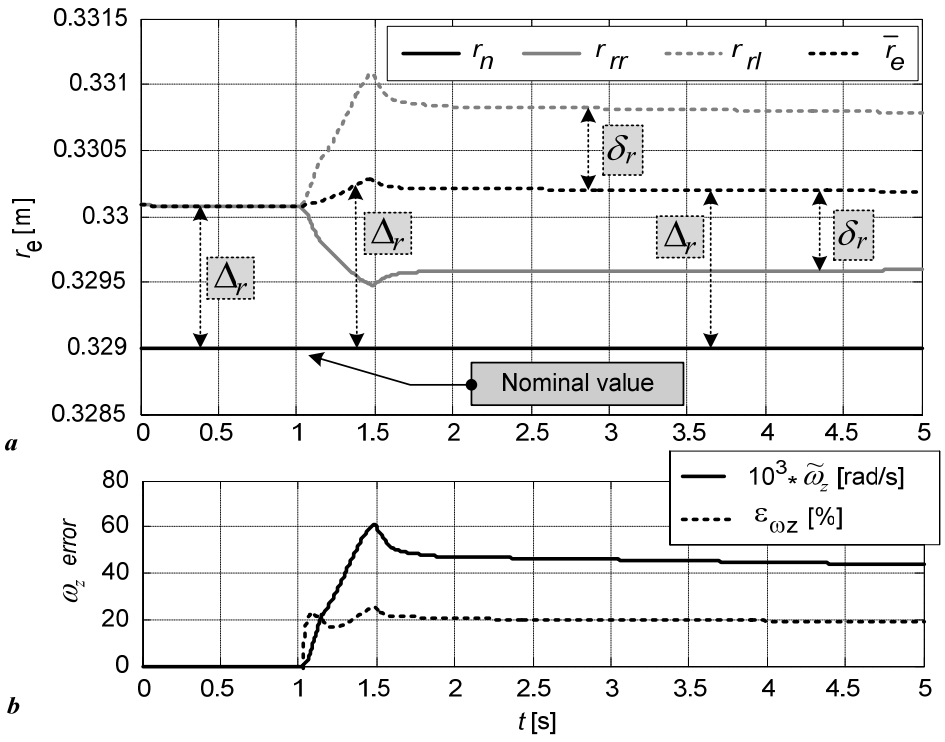

Fig. 4.9 *Step-steer maneuver (ω_z=0.23 rad/s, u=20 m/s): effective rolling radii of the rear wheels (a), absolute and relative estimation errors (b).*

Substituting Eq.(4-19) in Eq. (4-8) yields the following absolute estimation error equation in terms of the common and differential components of effective tire radii variations:

$$\tilde{\omega}_z \triangleq \hat{\omega}_z - \omega_z = \Delta_r \frac{\omega_{rr} - \omega_{rl}}{L} + \delta_r \frac{\omega_{rr} + \omega_{rl}}{L} \tag{4-21}$$

Since $(\omega_{rr} + \omega_{rl}) >> (\omega_{rr} - \omega_{rl})$, it is clear from Eq. (4-21) that the differential radii variation δ_r has much larger impact on the estimation error then the common variation Δ_r. This is

confirmed by the algebraic sensitivity analysis of the relative estimation error Eq. (4-22) (δ_r sensitivity is much larger than Δ_r sensitivity, see Eqs. (4-23) and (4-24)), as well as by the simulation results in Fig. 4.9 (the error is large when δ_r is large, $t > 1$s).

$$\varepsilon_{\omega z} \hat{=} \frac{\tilde{\omega}_z}{\omega_z} = \frac{\Delta_r(\omega_{rr} - \omega_{rl}) - \delta_r(\omega_{rr} + \omega_{rl})}{(r_n - \Delta_r)(\omega_{rr} - \omega_{rl}) + \delta_r(\omega_{rr} + \omega_{rl})} = \frac{f_n(\Delta_r, \delta_r)}{f_d(\Delta_r, \delta_r)} \tag{4-22}$$

The sensitivities of the above relative estimation error function with respect to Δ_r and δ_r read:

$$\frac{\partial \varepsilon_{\omega z}}{\partial \Delta_r} = \frac{r_n(\omega_{rr} - \omega_{rl})^2}{f_d^2} \tag{4-23}$$

$$\frac{\partial \varepsilon_{\omega z}}{\partial \delta_r} = \frac{r_n(\omega_{rl} - \omega_{rr})(\omega_{rl} + \omega_{rr})}{f_d^2} \tag{4-24}$$

For the purpose of a more detailed analysis, the relative error equation (4-22) is split into Δ_r and δ_r-related terms:

$$\varepsilon_{\omega z}(\Delta_r) = \frac{\Delta_r}{r_n - \Delta_r} \approx \frac{\Delta_r}{r_n} \tag{4-25}$$

$$\varepsilon_{\omega z}(\delta_r) = \frac{-\delta_r(\omega_{rr} + \omega_{rl})}{r_n(\omega_{rr} - \omega_{rl}) + \delta_r(\omega_{rr} + \omega_{rl})} \tag{4-26}$$

By introducing the characteristic wheel speed coefficient:

$$k_\omega \hat{=} \frac{\omega_{rr} - \omega_{rl}}{\omega_{rr} + \omega_{rl}} \tag{4-27}$$

Eq. (4-26) is rewritten as:

$$\varepsilon_{\omega z}(\delta_r) = \frac{-\delta_r}{r_n k_\omega + \delta_r} \tag{4-28}$$

The coefficient k_ω increases with increase of the yaw rate $\omega_z \approx r_n(\omega_{rr} - \omega_{rl})/t$ and decrease of the vehicle speed $u \approx r_n(\omega_{rr} + \omega_{rl})/2$. The common radii variation-induced estimation error $\varepsilon_{\omega z}(\Delta_r)$ is small and it is approximately equivalent to the relative radii change (i.e. 5% radii change results in approximately 5% estimation error, see Fig. 4.10a). On the other hand, the differential radii variation of 3% can result in an estimation error $\varepsilon_{\omega z}(\delta_r)$ from approximately 20% to 90% depending on the vehicle velocity-related coefficient k_ω (the lower the coefficient k_ω, i.e. the larger the vehicle velocity and the lower the yaw rate, the larger the error, Fig. 4.10b).

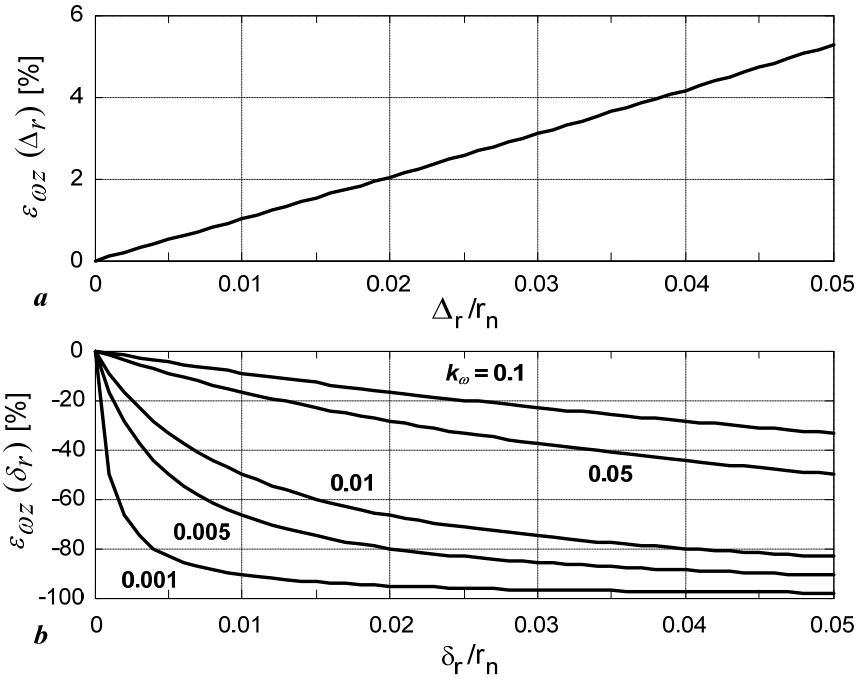

Fig. 4.10 *Yaw rate relative estimation errors as function of normalized effective radii variations: common (a) and differential (b).*

In order to further clarify the impact of the yaw rate ω_z and the vehicle speed u on the yaw rate estimation error, the following analysis is carried out. Based on Eq. (4-1) the wheels rotational speeds can be expressed as

$$\omega_{rl} = \frac{2u - t\omega_z}{2r_{rl}}, \qquad \omega_{rr} = \frac{2u + t\omega_z}{2r_{rr}} \tag{4-29}$$

By inserting the tire effective radii equations (4-19) and the wheel speed equations (4-29) into Eq. (4-8) yields the following estimation error equation:

$$\tilde{\omega}_z = \frac{\Delta_r(r_n - \Delta_r) + \delta_r^2}{(r_n - \Delta_r)^2 - \delta_r^2} \cdot \omega_z - \frac{2\, r_n \delta_r}{(r_n - \Delta_r)^2 - \delta_r^2} \cdot \frac{u}{t} \tag{4-30}$$

The second right-hand side term in Eq. (4-30) is a dominant source of the estimation error, because the vehicle velocity u/t has much larger magnitudes than the yaw rate (i.e. $\omega_z \approx 0$ - 0.4 rad/s, while $u \approx 0$ - 40 m/s).

The simulation results in Fig. 4.11a confirm that the relative estimation error significantly increases with the vehicle velocity (up to 45% for u = 30m/s), while the relative error is almost constant ($\varepsilon_{\omega z} \approx 20\%$) for a wide range of yaw rates (Fig. 4.11b).

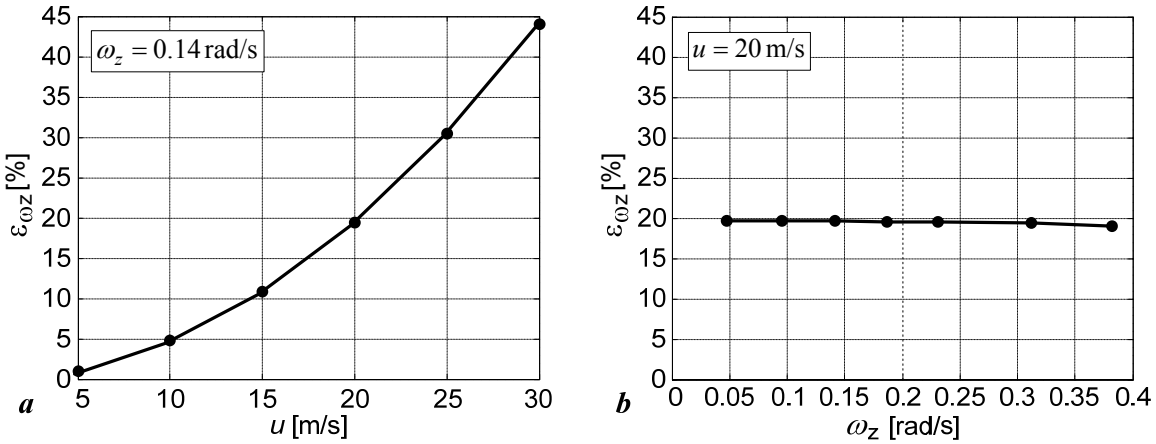

Fig. 4.11 *Yaw rate estimation relative error for step-steer maneuver with respect to vehicle speed (a) and yaw rate amplitude (b).*

c) The road bank-related estimation errors

The road bank also affects the tire effective radii and consequently the yaw rate estimation accuracy trough a change of the tire nominal load $F_{z0} = m_r \cdot g/2$ (m_r is the vehicle mass over the rear axle). On a road with the bank angle ϕ_B the tire normal loads F_{zl} and F_{zr} are given by (see Fig. 4.12a):

$$F_{zl}(\phi_B) = \frac{m_r g}{2}\cos\phi_B - \frac{m_r g h}{t}\sin\phi_B \tag{4-31}$$

$$F_{zr}(\phi_B) = \frac{m_r g}{2}\cos\phi_B + \frac{m_r g h}{t}\sin\phi_B \tag{4-32}$$

Refereing to Eq. (4-19), the cosine terms in Eqs. (4-31) and (4-32) would cause the common effective tire radii variation Δ_r, while the sine terms would induce the differential radii variation δ_r. Therefore, according to discussion from previous subsection, the sine terms $\sin\phi_B \approx \phi_B$ are dominant sources of the road bank-related estimation error.

According to the simulation results in Fig. 4.12b the road bank induces an additional estimation error of up to 12% for $\phi_B = 10°$ and $u = 10$ m/s. The initial relative estimation error of 5% obtained for the zero road bank angle ϕ_B is predominantly caused by the vehicle velocity (in this case $u = 10$ m/s, cf. Fig. 4.11a). Thus, variation of the vehicle velocity u will shift up the relative yaw rate error vs. road bank angle characteristic in Fig. 4.12b.

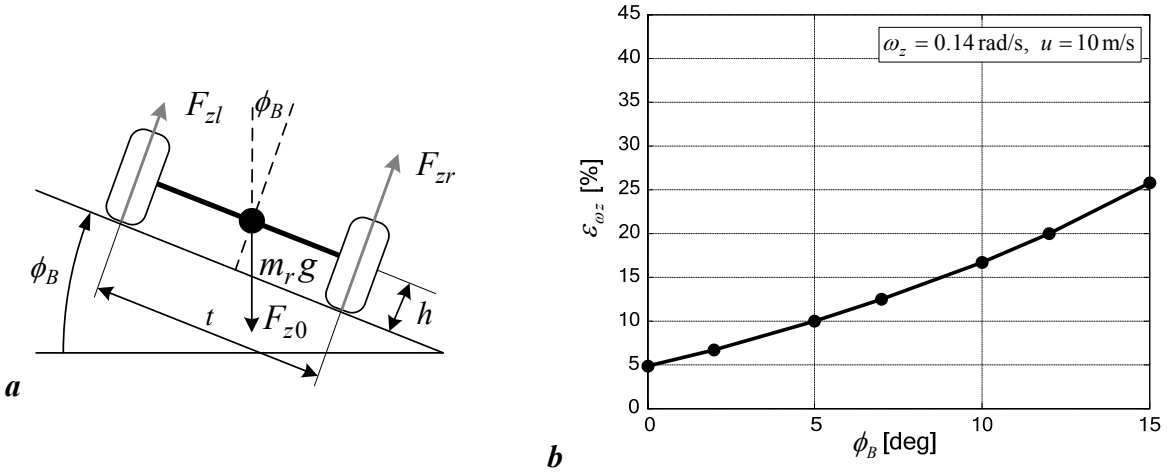

Fig. 4.12 *Road bank-related yaw rate estimation errors: illustration of road bank impact on tire normal loads (a), and relative estimation error for step-steer maneuver (b).*

The sources of effective tire radii variations are summarized in Table 4.2. The effective tire radii variations and the corresponding yaw rate estimation errors can be classified as static and dynamic. The static errors are mostly caused by tire deflation (e.g. single tire deflation results in differential tire radii variation δ_r) or tire tread wear (both tires are evenly worn causing the common radii variation Δ_r). On the other hand, dynamic errors are related to the vehicle roll motion and road bank or to the vehicle pitch motion and road grade. The roll/bank dynamics are more critical since they cause differential tire radii variation δ_r, as oppose to pitch/grade dynamics that cause common tire radii variation Δ_r.

Table 4.2 *Summary of effective radii variation sources*
(yellow shaded rows designate dominant sources of estimation errors)

Error source	Δ_r	δ_r	Error type
Tire pressure (p)	+	+	Static
Tire tread wear (uniform for left/right)	+	–	Static
Braking/accelerating (pitch angle - θ)	+	–	Dynamic
Cornering (roll angle -ϕ)	–	+	Dynamic
Road bank (bank angle -ϕ_B)	+	+	Dynamic
Road grade (grade angle)	+	–	Dynamic

d) Transient estimation errors

Transient yaw rate estimation errors are predominantly caused by two effects: (i) the effect of tire longitudinal dynamics on variable delay of tire velocity measurement and (ii) road bump disturbances [48].

The former type of transient estimation errors, caused by tire dynamics (see Subsection 4.2, Eq. (4-11), and Table 4.1), are characterized by the wheel/tire time constant T_w given by Eq. (4-12). According to Table 4.1, the time constant T_w and the corresponding transient estimation errors increase with the vehicle speed u and the tire slip angle α.

Fig. 4.13 shows the relevant vehicle dynamics state variables and estimation errors for the double lane change maneuver on a low-μ surface, with an emphasized oversteer behavior. In such a maneuver, large yaw accelerations $\dot{\omega}_z$ and tire slip angles α are present, as a worst-case scenario with respect to estimation errors due to the tire dynamics. For the sake of clear illustration of tire dynamics influence, the tire radii are set to their nominal value in the simulations.

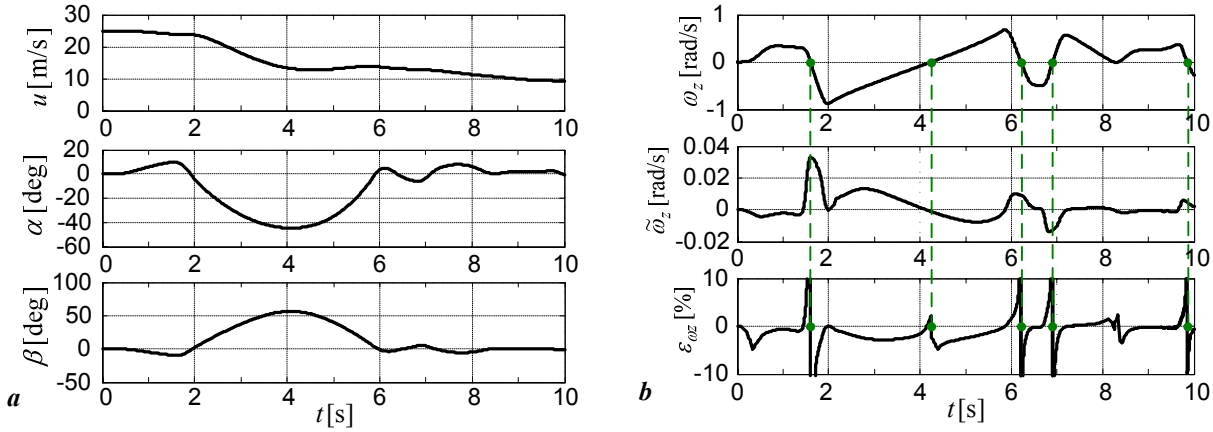

Fig. 4.13 *Vehicle dynamics state variables (a) and yaw rate estimation errors (b) for double lane change maneuver ($\mu = 0.4$).*

Intervals with relatively large transient estimation errors coincide with the presence of high yaw accelerations, large tire slip angles, and higher vehicle velocity (Fig. 4.13b). This is in accordance with the analysis summarized in Table 4.1 and the fact that the tire delay effect on the estimation error is more emphasized at larger yaw accelerations (faster dynamics). The peak estimation error of 0.03 rad/s is observed during the initial period of oversteer (Fig. 4.14, $t \approx 1.85$ s) on the yaw rate scale of approximately 0.3 rad/s, i.e. the peak error is

approximately 10%. Mostly, the relative estimation error resides well within 10% except for the high gradients and yaw rates around zero (a singularity in $\varepsilon_{\omega z}$ equation).

The second source of the transient estimation errors is road-induced disturbance when the wheel suddenly comes across the bump on the road and the pulse-like disturbance in the measured wheel speed occurs. Since the yaw rate estimate is based on the small difference between the wheel speeds (cf. Eq. (4-7)), this disturbance can cause a significant pulse-like estimation error. The effect of road bump-related error is illustrated in Fig. 4.14 for the case of a step-steer maneuver with the steady-state yaw rate of 0.23 rad/s and the road bump disturbance pulse initiated at t = 3s. More precisely, the road bump disturbance has been simulated by adding the sine-wave-shaped pulse with amplitude of ω_{wbmp} = 1 rad/s and frequency of 2.5 Hz to the left rear wheel speed signal. In the considered maneuver, the magnitude of thereby induced pulse-like yaw rate estimation error amounts up to 80% of the actual yaw rate. Therefore, the road-bump disturbance conditions must be monitored (the road bump disturbance detection method implemented in the combined adaptive EKF estimator is described in Section 4.4) and in its presence the yaw rate should be estimated by using some alternative estimation method (e.g. dual-accelerometer based estimator, see Section 4.3), because this potentially large estimation error cannot be otherwise suppressed or compensated for.

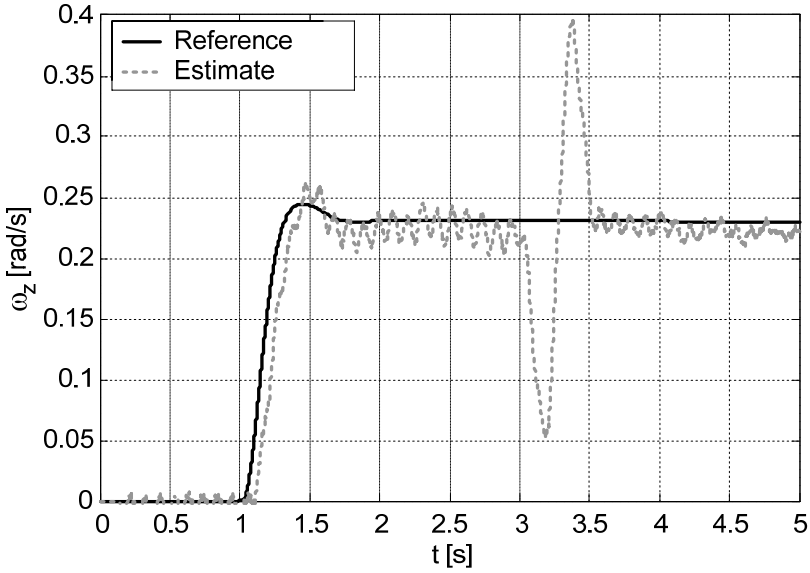

Fig. 4.14 *Illustration of road bump-related wheel speed sensor-based yaw rate estimation error.*

4.2.2 Improvement of estimation accuracy by open-loop compensations

The dominant tire radii variation-related static and dynamic yaw rate estimation errors (see Table 4.2) can be significantly reduced by applying relatively simple open-loop compensation algorithms. On the other hand, robust compensations of estimation errors caused by braking, tire dynamics, and road bump disturbance do not appear to be feasible. Thus, the sensor fusion approach, described in Section 4.4, should be utilized in order to avoid or mitigate impacts of these effects.

a) Compensation of estimation errors related to static tire radii variations

Compensation of the static estimation errors (primarily caused by a single tire deflation) is based on the difference between the measured rear wheel speeds during straight driving. For the case of straight driving and different tire radii $r_{rl,s}$ and $r_{rr,s}$, the tire rotational speeds $\omega_{rl,s}$ and $\omega_{rr,s}$ differ from each other and satisfy the expression:

$$u = r_{rr,s}\omega_{rr,s} = r_{rl,s}\omega_{rl,s}\,, \qquad \text{where} \quad \omega_{rr,s} \neq \omega_{rl,s} \tag{4-33}$$

From the averaged wheel speeds (or eventually wheel positions) during straight driving the effective tire radii ratio can be identified:

$$k_{c,s} = \frac{r_{rl.s}}{r_{rr.s}} = \frac{\overline{\omega}_{rr.s}}{\overline{\omega}_{rl.s}} \tag{4-34}$$

This ratio is then used for compensation of the static yaw rate estimation error according to either of the following expressions:

$$\hat{\omega}_{zc,1} = \frac{r_n}{t}\left(\omega_{rr} - k_{c,s}\omega_{rl}\right) \qquad \text{or} \qquad \hat{\omega}_{zc,2} = \frac{r_n}{t}\left(\frac{1}{k_{c,s}}\omega_{rr} - \omega_{rl}\right) \tag{4-35}$$

The coefficient $k_{c,s}$ modifies the initial estimation equation (4-7), so that the estimated yaw rate for the straight driving equals zero. This provides compensation of the static differential radius error δ_r. The error due to the common radii variation (Δ_r) remains uncompensated, but this error is negligible, anyway (see Section 4.2).

Figure 4.15a illustrates the effectiveness of the static error compensation. The small remaining error (for small ω_z) is due to the uncompensated roll-related tire radii differential variation. Fig. 4.15b shows that the compensation is highly sensitive to inaccuracies of the compensation ratio $k_{c,s}$. However, this should not be critical, because $k_{c,s}$ could be estimated very accurately by averaging speed signals in Eq. (4-34) over a relatively long periods of straight driving.

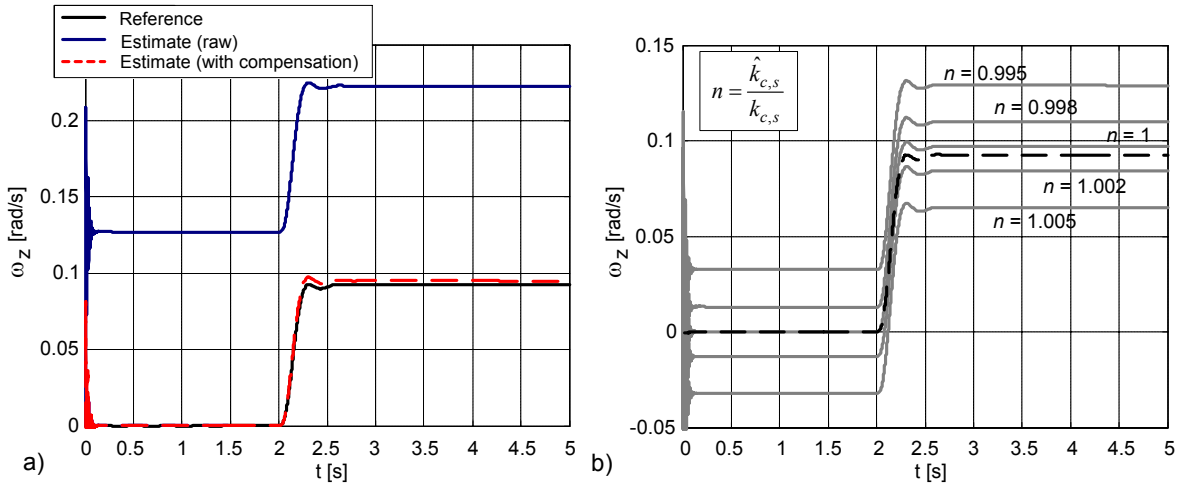

Fig. 4.15 *Compensation of static tire radius variations errors for step-steer maneuver (u = 20 m/s): yaw rate estimates w/ and w/o compensation (a) and compensation sensitivity with respect to accuracy of coefficient $k_{c,s}$ (b).*

b) Compensation of estimation errors related to dynamic tire radii variations

Dynamic effective tire radii variations and related yaw rate estimation error are mostly caused by the vehicle roll motion and road bank, and corresponding lateral load transfer (see Table 4.2). In order to be able to compensate for this dynamic error, the following tire load transfer function $\delta F_z(s)/a_y(s)$ has been derived from a simplified vehicle roll motion model extracted from the full vehicle model [23]:

$$\frac{\delta F_z(s)}{a_y(s)} = \frac{m_r h_1 t}{2} \cdot \frac{b_r s + k_r}{I_{rc} s^2 + b_1 s + k_1} \tag{4-36}$$

where I_{rc} is the roll moment of inertia with respect to roll center, δF_z is the tire normal load transfer, m_r is the vehicle mass over the rear axle, h_1 is the height of the vehicle CoG over its roll axis, b_r is the suspension damping rate for the rear wheels, and k_r is the suspension spring rate of the rear wheels, while $b_1 = b_r t^2/2$ and $k_1 = k_r t^2/2$. The well-damped transfer function (4-36) may be simplified by a first-order lag model:

$$\frac{\delta F_z(s)}{a_y(s)} = \frac{K_{eq}}{1 + T_{eq} s} \tag{4-37}$$

where $K_{eq} = \frac{m_r h_1 t}{2} \frac{k_r}{k_1}$ and $T_{eq} = \frac{b_1}{k_1} - \frac{b_r}{k_r}$.

Fig. 4.16 shows comparative simulation responses of the tire load transfer. The second-order model (4-36) shows a good accuracy, except for missing a sharp load transfer peak caused by

nonlinear dampers in the full 10 DoF model. The first-order model predicts correct settling time and steady-state value, but the response overshoot cannot be captured.

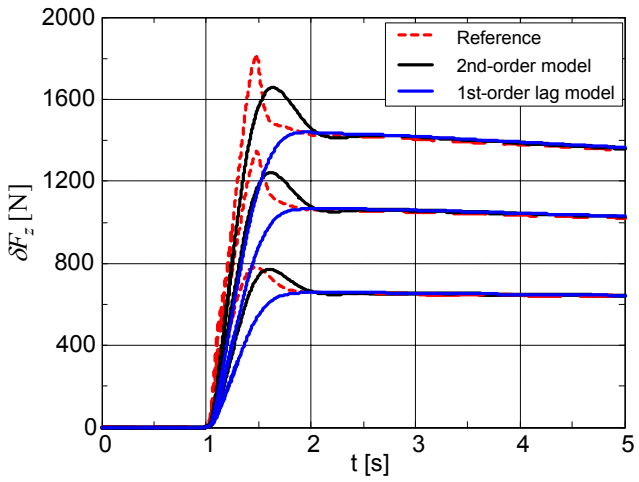

Fig. 4.16 *Lateral tire load transfer for step-steer maneuver (u = 20 m/s, ω_z = 0.14, 0.23, 0.31 rad/s).*

By utilizing the described (open-loop) model (4-36) or (4-37) and the lateral accelerometer measurement a_y, the lateral load transfer-related differential tire radii variation component δ_r can be obtained from Eq. (4-5) (with the non-dominant speed term neglected):

$$\delta_r = (\delta r_{in} + \delta r_{out})/2 \tag{4-38}$$

$$\delta r_{out,in} = \underbrace{q_3\sqrt{(F_{zn} \pm \delta F_z)^3} + q_2\sqrt{(F_{zn} \pm \delta F_z)^2} + q_1\sqrt{F_{zn} \pm \delta F_z} + q_0}_{r_e} - r_n \tag{4-39}$$

where F_{zn} and r_n are the nominal tire load and effective radius.

The effective tire radius vs. load nonlinear characteristic obtained from Eq. (4-39) is given in Fig. 4.17 (black trace) and the nominal operating point (F_{zn}, r_n) is marked. The normal load change $\pm\delta F_z$ due to the lateral transfer causes the rear wheels radii to change by the amounts; $+\delta r_{in}$ (inner wheel) and $-\delta r_{out}$ (outer wheel).

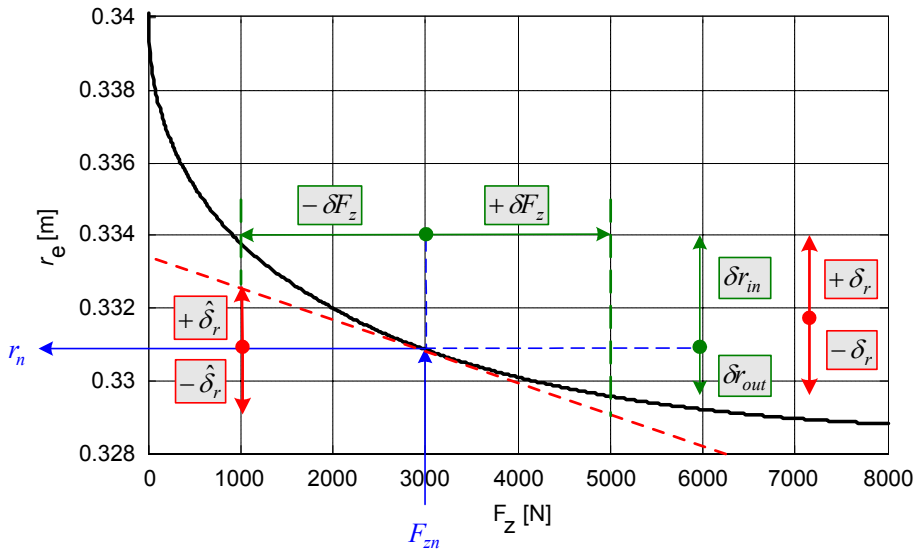

Fig. 4.17 *Illustration of tire effective radii differential variation due to tire normal load transfer.*

For the purpose of dynamic estimation error compensation, the linearized model of the tire radii vs. load characteristic (red dashed trace in Fig. 4.17) may be used instead of the full nonlinear model given by Eq. (4-39). The relevant differential radii variation approximation $\hat{\delta}_r = k_{c,d} \cdot \delta F_z$, obtained from the linearized model, does not differ much from the true value δ_r, although it may differ significantly with respect to δr_{in} or δr_{out}. Hence, the simple linearized model can give a good approximation of the tire radius in a relatively wide range of tire load changes (±2kN, Fig. 4.17). The benefit of this approach is that a single parameter $k_{c,d}$ is required instead of four parameters $q_{1\text{-}3}$ for the nonlinear approach.

Compensation of the dynamic radii variation is based on including the differential radii variation term $\hat{\delta}_r$ into the nominal estimation equation (4-7):

$$\hat{\omega}_{z,d} = \frac{(r_n - \hat{\delta}_r)\,\omega_{rr} - (r_n + \hat{\delta}_r)\,\omega_{rl}}{t} \tag{4-40}$$

If the linearized tire effective radius characteristic is utilized ($\hat{\delta}_r = k_{c,d} \cdot \delta F_z$), and the static compensation (4-35) is accounted for, the final compensation expression reads:

$$\hat{\omega}_{z,d} = \frac{r_n}{t}\left(\omega_{rr} - k_{c,s}\,\omega_{rl}\right) - \frac{k_{c,d}\,\delta F_z}{t}\left(\omega_{rr} + \omega_{rl}\right) \tag{4-41}$$

The simulation results in Fig. 4.18 demonstrate the effectiveness of dynamic compensation during cornering maneuver, for the case of using second-order roll model. Furthermore, the

road bank effect is inherently compensated for (Fig. 4.19), because the bank information is contained in the lateral accelerometer signal a_y in Eq. (4-36) or (4-37).

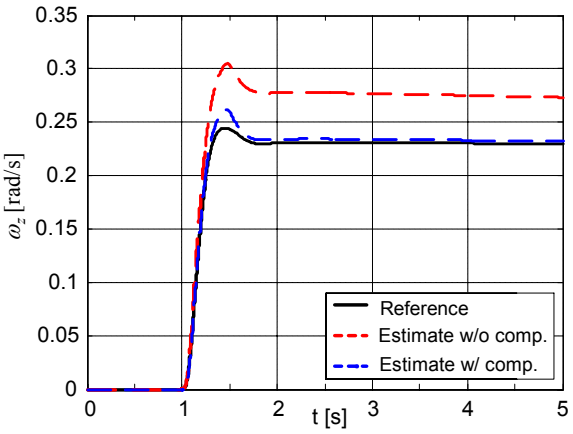

Fig. 4.18 *Comparative simulation results of dynamic compensation of effective radii variation for step-steer maneuver.*

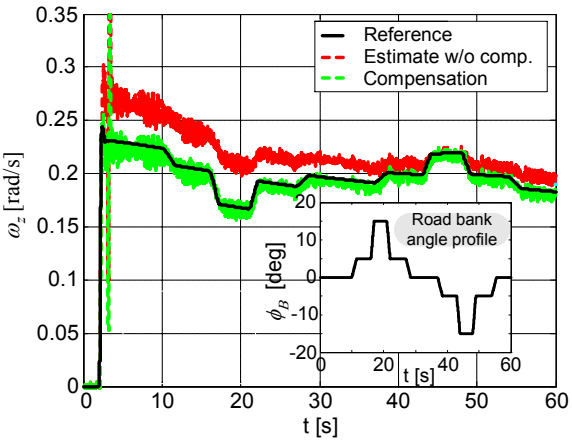

Fig. 4.19 *The effect of dynamic compensation on yaw rate estimation errors for banked road.*

4.2.3 Concluding remarks

The major limitations of the non-driven wheel speed sensor-based yaw rate estimator include a significant offset-type estimation error during braking maneuvers and a dynamics error during transitions over road bumps. Furthermore, effective tire radii variations due to: deflation of tire, roll and pitch dynamics, and road bank, introduce additional error components. Finally, the non-driven tire dynamics introduce a variable delay and related transient error of yaw rate estimation. This error increases with vehicle velocity, tire/vehicle slip angle, and yaw acceleration, and it is relatively small (up to 10%).

In regard to tire effective radii variation effect, the differential tire radii change δ_r (caused by roll dynamics, road bank, and single tire deflation) has much larger effect on the yaw rate estimation inaccuracy (typical errors up to 40-60%) than the common radius change Δ_r (caused by both tire deflation/wear, road grade, and pitch dynamics with typical errors up to 5%). Moreover, the tire radii variation relative estimation errors increase rapidly with the vehicle speed u and they are not influenced by the yaw rate level. The road bank introduces additional estimation errors due to the differential radii change (up to approximately 12% for the bank angle of 10°). However, the tire radii variation error components can be effectively reduced by using open-loop compensators based on an estimated tire radii ratio for straight driving (static compensation), and a vehicle roll and tire vertical deflection models fed by lateral acceleration (dynamics compensation) in cornering.

4.3 Estimation based on acceleration measurements

Apart from the non-driven wheel speed sensor-based yaw rate estimator approach described in Section 4.2, kinematic estimator of the yaw rate can be designed by utilizing the measurements of two accelerometers placed outside of the vehicle centre of gravity (see Section 4.1 and references therein. In order to develop such a kinematic estimator, first the kinematic model of the accelerometer measurements needs to be derived.

4.3.1 Accelerometer measurement kinematic model

The accelerometer measurement kinematic model is considered for the case of accelerometer fixed at an arbitrary point *M* of the vehicle chassis horizontal plane containing the CoG point (see Fig. 4.20). Thus, the sensor placement at point *M* is defined by two parameters: the senor placement angle α_0 and its distance $\mathbf{r}_M$ from the CoG.

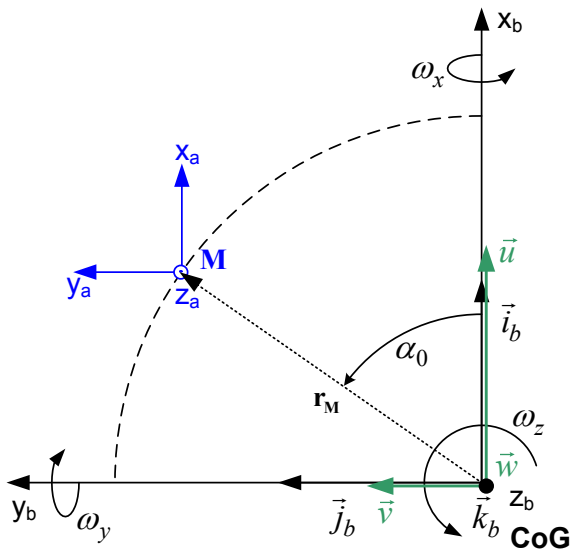

Fig. 4.20 *Vehicle chassis frame with aligned accelerometer placed in point M.*

The velocity of point M in the moving vehicle frame (x_b, y_b, z_b) is given by the following matrix equation [39]:

$$\mathbf{v}_M = \mathbf{v}_o + \mathbf{v}_{Mrel} + \boldsymbol{\omega} \times \mathbf{r}_M \tag{4-42}$$

where $\mathbf{v}_o = \begin{bmatrix} u & v & w \end{bmatrix}^T$ is the velocity vector at the vehicle center of gravity, $\mathbf{v}_{Mrel}$ is relative velocity of the point M (e.g. $\mathbf{v}_{Mrel} = 0$ for this particular system), $\boldsymbol{\omega} = \begin{bmatrix} \omega_x & \omega_y & \omega_z \end{bmatrix}^T$ is the vector of angular velocities of the moving frame, and $\mathbf{r}_M$ is distance of the point M from the moving frame origin (i.e. CoG).

The third term on the right-hand side of (4-42) relates to the transport velocity due to the rotation of the moving frame. Accordingly, the velocity of point M can be derived as:

$$\begin{aligned}\mathbf{v_M} &= \left(u - \omega_z l_{df} \sin\alpha_0\right)\mathbf{i_b} + \left(v + \omega_z l_{df} \cos\alpha_0\right)\mathbf{j_b} \\ &+ \left[w + \omega_x l_{df} \sin\alpha_0 - \omega_y l_{df} \cos\alpha_0\right]\mathbf{k_b}\end{aligned} \tag{4-43}$$

Acceleration of the point M is expressed as a time derivative of (4-43), and according to the transport theorem equation [39] it reads:

$$a_{\mathbf{M}} = \frac{d\,\mathbf{v_M}}{dt} = \left(\frac{d\mathbf{v_M}}{dt}\right)_{rel} + \boldsymbol{\omega} \times \mathbf{v_M} \tag{4-44}$$

From equation (4-44) the acceleration components at the point M can be obtained. However, the accelerometer placed at the point M senses an additional acceleration component due to the earth gravity. This component depends on the orientation of the moving frame with respect to ground, which is described by the Euler angles (ϕ, θ, and ψ, see Chapter 2), and it is proportional to the gravity acceleration g. The gravity acceleration vector resolved on its components in the vehicle body frame can be defined as:

$$\mathbf{g_b} = \begin{bmatrix} g\sin\theta & -g\sin\phi\cos\theta & -g\cos\phi\cos\theta \end{bmatrix}^T \tag{4-45}$$

Based on Eq. (4-44) and taking into account the gravity related components (4-45), the general equations for the measured accelerations a_x, a_y, and a_z are expressed as:

$$\begin{aligned}a_x &= \underbrace{\dot{u} - \omega_z v + \omega_y w}_{a_{xCoG}} - l_{df}\cos\alpha_0\left(\omega_y^2 + \omega_z^2\right) \\ &+ l_{df}\sin\alpha_0\left(\omega_x\omega_y - \dot{\omega}_z\right) - g\sin\theta\end{aligned} \tag{4-46}$$

$$\begin{aligned}a_y &= \underbrace{\dot{v} + \omega_z u - \omega_x w}_{a_{yCoG}} - l_{df}\left(\omega_x^2 + \omega_z^2\right)\sin\alpha_0 \\ &+ l_{df}\left(\omega_x\omega_y + \dot{\omega}_z\right)\cos\alpha_0 + g\sin\phi\cos\theta\end{aligned} \tag{4-47}$$

$$\begin{aligned}a_z &= \underbrace{\dot{w} - \omega_y u + \omega_x v}_{a_{zCoG}} + l_{df}\left(\dot{\omega}_x + \omega_y\omega_z\right)\sin\alpha_0 \\ &+ l_{df}\left(\omega_x\omega_z - \dot{\omega}_y\right)\cos\alpha_0 + g\cos\phi\cos\theta\end{aligned} \tag{4-48}$$

where a_{xCoG}, a_{yCoG}, and a_{zCoG} are the accelerations at the vehicle CoG without additive gravity components. Due to the opposite directions of the accelerometer seismic mass displacement and the related measured acceleration, the signs of the gravity acceleration components in Eqs. (4-46) to (4-48) are inverted when compared to the signs given in Eq. (4-45).

4.3.2 Two accelerometers measurement configurations

The accelerometer kinematic measurement model equations (4-46) to (4-48) are used to derive the kinematic estimator equations for the longitudinal, lateral, and diagonal accelerometer configurations illustrated in Fig. 4.21.

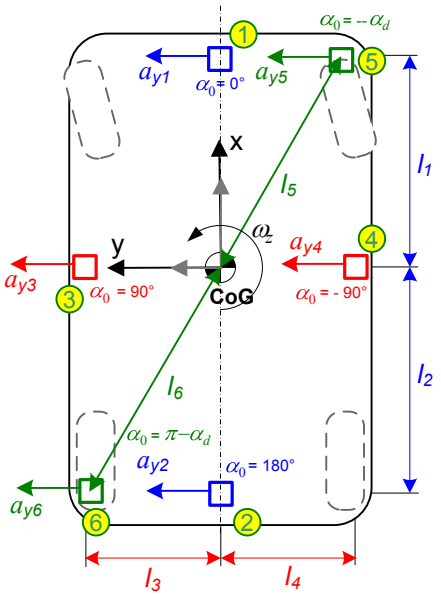

Fig. 4.21 *Accelerometer placement configurations: longitudinal - sensors 1&2, lateral - sensors 3&4, and diagonal - sensors 5&6.*

Longitudinal (tangential) configuration

The acceleration signals a_{y1} and a_{y2}, measured by the accelerometers 1 and 2 in Fig. 4.21, are derived from Eq. (4-47) for $\alpha_0 = 0°$ and $\alpha_0 = 180°$, respectively:

$$a_{y1} = a_{yCoG} + l_1\left(\omega_x\omega_y + \dot{\omega}_z\right) + g\sin\phi\cos\theta \tag{4-49}$$

$$a_{y2} = a_{yCoG} - l_2\left(\omega_x\omega_y + \dot{\omega}_z\right) + g\sin\phi\cos\theta \tag{4-50}$$

Adding up the measured signals given by (4-49) and (4-50) yields the lateral acceleration estimation equation:

$$\hat{a}_y = \frac{a_{y1} + a_{y2}}{2} = a_{yCoG} + \frac{l_1 - l_2}{2}\left(\omega_x\omega_y + \dot{\omega}_z\right) + g\sin\phi\cos\theta \tag{4-51}$$

On the other hand, subtracting the expressions (4-49) and (4-50) yields the yaw acceleration estimate:

$$\hat{\dot{\omega}}_z = \frac{a_{y1} - a_{y2}}{l_1 + l_2} = \dot{\omega}_z + \omega_x\omega_y \tag{4-52}$$

The yaw rate ω_z can be estimated by means of integration of the yaw acceleration estimate [4,9].

$$\hat{\omega}_z = \int \hat{\dot{\omega}}_z \, dt = \frac{1}{l_1 + l_2} \cdot \int \left(a_{y1} - a_{y2} \right) dt = \omega_z + \int \omega_x \omega_y dt \tag{4-53}$$

Lateral (radial) configuration

The signals measured by the accelerometers 3 and 4 in Fig. 4.21 read:

$$a_{y3} = a_{yCoG} - l_3 \left(\omega_x^2 + \omega_z^2 \right) + g \sin\phi \cos\theta \tag{4-54}$$

$$a_{y4} = a_{yCoG} + l_4 \left(\omega_x^2 + \omega_z^2 \right) + g \sin\phi \cos\theta \tag{4-55}$$

This yields the following kinematic estimators equations:

$$\hat{a}_y = \frac{a_{y3} + a_{y4}}{2} = a_{yCoG} - \frac{l_3 - l_4}{2} \left(\omega_x^2 + \omega_z^2 \right) + g \sin\phi \cos\theta \tag{4-56}$$

$$\hat{\omega}_z^2 = \frac{a_{y4} - a_{y3}}{l_3 + l_4} = \omega_z^2 + \omega_x^2 \tag{4-57}$$

In this case the square power of yaw rate is directly derived by subtracting the accelerometers measurements:

$$\hat{\omega}_z = \operatorname{sgn}(\omega_z) \cdot \sqrt{\frac{a_{y4} - a_{y3}}{l_3 + l_4}} \tag{4-58}$$

what imposes the requirement on yaw rate sign estimation [4,8].

Diagonal (combined) configuration

The readings of new measurement configuration of diagonally placed accelerometers 5 and 6 in Fig. 4.21, proposed and applied for design of the kinematic yaw rate estimator in this thesis, are given by:

$$a_{y5} = a_{yCoG} + l_5 (\omega_x^2 + \omega_z^2) \sin\alpha_0 + l_5 (\omega_x \omega_y + \dot{\omega}_z) \cos\alpha_0 + g \sin\phi \cos\theta \tag{4-59}$$

$$a_{y6} = a_{yCoG} - l_6 (\omega_x^2 + \omega_z^2) \sin\alpha_0 - l_6 (\omega_x \omega_y + \dot{\omega}_z) \cos\alpha_0 + g \sin\phi \cos\theta \tag{4-60}$$

Eqs. (4-59) and (4-60) yield the following estimation equations:

$$\hat{a}_y = \frac{a_{y5} + a_{y6}}{2} = a_{yCoG} + g\sin\phi\cos\theta + \frac{l_5 - l_6}{2}\left(\omega_x^2 + \omega_z^2\right)\sin\alpha_0 + \frac{l_5 - l_6}{2}\left(\omega_x\omega_y + \dot{\omega}_z\right)\cos\alpha_0 \tag{4-61}$$

$$\chi = \frac{a_{y5} - a_{y6}}{\left(l_5 + l_6\right)\cos\alpha_0} = \dot{\omega}_z + \omega_x\omega_y + \left(\omega_x^2 + \omega_z^2\right)\tan\alpha_0 \tag{4-62}$$

where χ denotes the accelerometer measurement term [4].

After neglecting the small roll and pitch rate terms on the right-hand side of Eq. (4-62), the following estimator nonlinear differential equation is derived:

$$\hat{\dot{\omega}}_z + \tan\alpha_0 \cdot \hat{\omega}_z^2 - \chi = 0 \tag{4-63}$$

This estimator combines the features of the algebraic estimator (4-58) and the "dynamic" estimator (4-53). The following subsection describes a detailed algebraic analysis of the estimation errors and evaluation of the dominant error sources for these three kinematic models/estimators configurations (i.e. longitudinal, lateral, and diagonal).

4.3.3 Algebraic analysis of estimation errors

The estimation equations (4-51), (4-56), and (4-61) indicate that the estimated lateral acceleration corresponds to the aimed one measured at the CoG ($\hat{a}_y = a_{yCoG} + g\sin\phi\cos\theta$), provided that the two accelerometers are placed at equidistant positions with respect to CoG (the nominal case: $l_1 = l_2$, $l_3 = l_4$, $l_5 = l_6$). The below algebraic analysis is, thus, focused on the yaw rate estimation error for the same nominal case.

The performance of derived kinematic estimators has been analyzed against the major sources of estimation errors by means of computer simulations and utilizing the appropriate validation model structure outlined in Fig. 4.22. More precisely, a passenger vehicle 10DOF chassis model [23] implemented in Matlab-Simulink is used in order to generate the vehicle dynamics quantities signals, required for calculating the vehicle acceleration components based on the realistic 6DOF kinematic measurement model described by Eqs. (4-46)-(4-48). Thus obtained accelerations are then used as inputs for the derived yaw rate estimators defined by Eqs. (4-53), (4-58), and (4-63). At the estimator outputs the vehicle lateral acceleration, yaw rate, and yaw acceleration estimates are obtained. They are compared to the reference values from the 10DOF model, in order to determine the estimation accuracy.

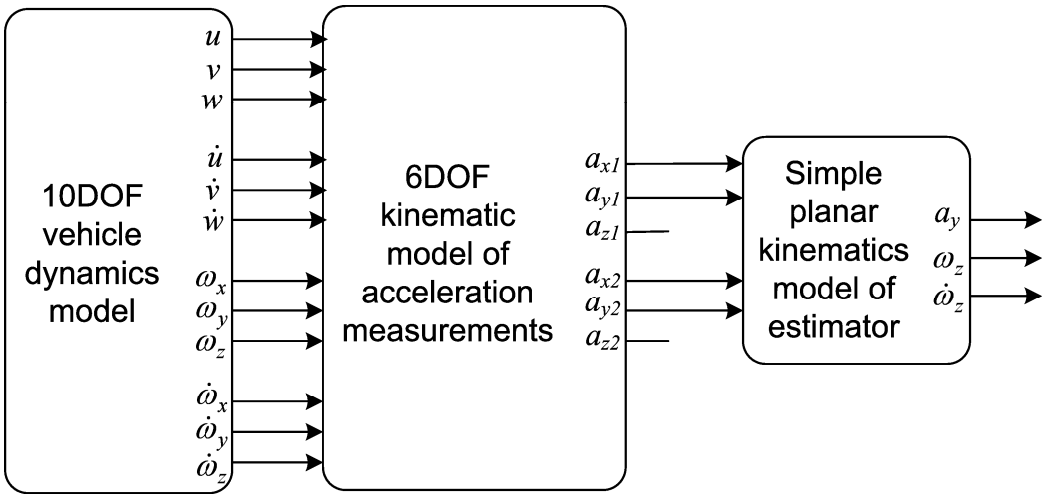

Fig. 4.22 *Block diagram of validation model for evaluation of two-accelerometers-based kinematic yaw rate estimators.*

For the subsequent error analysis the following definition of the relative estimation error $\varepsilon_{\omega z}$ has been utilized:

$$\varepsilon_{\omega z} \hat{=} \frac{\tilde{\omega}_z}{\omega_z} = \frac{\hat{\omega}_z - \omega_z}{\omega_z} \tag{4-64}$$

where $\tilde{\omega}_z$ represents the absolute estimation error.

a) Vehicle roll and pitch dynamics-related errors

For the **longitudinal accelerometer configuration** the following expressions for the estimation errors are derived from Eqs. (4-52) and (4-64):

$$\tilde{\dot{\omega}}_z = \omega_x \omega_y \quad \Rightarrow \quad \tilde{\omega}_z = \int \tilde{\dot{\omega}}_z dt = \int \omega_x \omega_y dt \tag{4-65}$$

$$\varepsilon_{\omega z} = \frac{1}{\omega_z} \int \omega_x \omega_y dt \tag{4-66}$$

The roll and pitch rate transients are not expected to induce any significant peaks of the yaw rate estimation error, because the product $\omega_x \omega_y$ is small and the integration process in (4-66) further rejects the transient error. However, integration of the even small steady-state error term $\omega_x \omega_y$ can result in a slow accumulation of yaw rate estimation error (a drift-like behavior).

For the **lateral configuration** estimator expression (4-58), the related absolute yaw rate estimation error reads:

$$\tilde{\omega}_z = \omega_z \left(\sqrt{1 + \frac{\omega_x^2}{\omega_z^2}} - 1 \right) \tag{4-67}$$

For the case of $x = \omega_x^2 / \omega_z^2 << 1$ the square root term in (4-67) may be approximated by the Taylor series expression:

$$f(x) = \sqrt{1+x} = \sum_{n=0}^{\infty} \frac{(x - x_0)^n}{n!} f^{(n)}(x_0) = \sum_{n=0}^{\infty} \frac{(-1)^n (2n)!}{(1-2n) n!^2 4^n} \cdot x^n \tag{4-68}$$

where $|x| < 1$ and $x_0 = 0$. After neglecting the higher series members ($n \geq 2$) in (4-68), the following approximate equation for the yaw rate estimation error is obtained:

$$\varepsilon_{\omega z} \approx \frac{1}{2} \frac{\omega_x^2}{\omega_z^2} \tag{4-69}$$

According to the above expression, the yaw rate estimation accuracy of the lateral configuration-based estimator is not affected by the vehicle pitch rate ω_y, but only the roll rate ω_x.

Finally, for the **diagonal configuration** estimator (4-63), the estimation error is given by:

$$\varepsilon_{\omega z} = \frac{\sqrt{\chi}}{\sqrt{\omega_z^2 \tan \alpha_0}} \left(1 - \sqrt{1 - \frac{\tilde{\chi}}{\chi}} \right), \quad \text{for } \dot{\omega}_z = 0 \tag{4-70}$$

$$\tilde{\chi} = \omega_x \omega_y + \omega_x^2 \tan \alpha_0 \tag{4-71}$$

In this case, both roll and pitch disturbance terms $\omega_x \omega_y$ and ω_x^2 from the longitudinal and lateral configuration error expressions (4-66) and (4-69) are present in the combined (diagonal) configuration error (4-70). Also, the integration process, needed to obtain $\hat{\omega}_z$ from (4-63), is expected to result in a drift-like error due to the disturbance term $\tilde{\chi}$.

Figure 4.23 shows the roll and pitch dynamics-related yaw rate estimation errors (i.e. its peak values) as functions of the steering wheel magnitude δ for the step steer maneuver, and the braking torque (per wheel) τ_b for braking in turn maneuver.

The lateral configuration estimator has the largest errors in both maneuvers (ω_z = 7-22% for cornering and ω_z < 2% for braking), because it is sensitive to roll dynamics. The longitudinal and diagonal estimators provide similar performance in braking maneuvers, but the longitudinal one is somewhat better for cornering. For all estimators the error increases with

increase of the steering wheel angle (for cornering) and increase of the braking torque (for braking), because in that cases the related roll (ω_x) and pitch (ω_y) rates increase, as well. Altogether, these errors are rather small (lower than 5%) for the longitudinal and diagonal configurations.

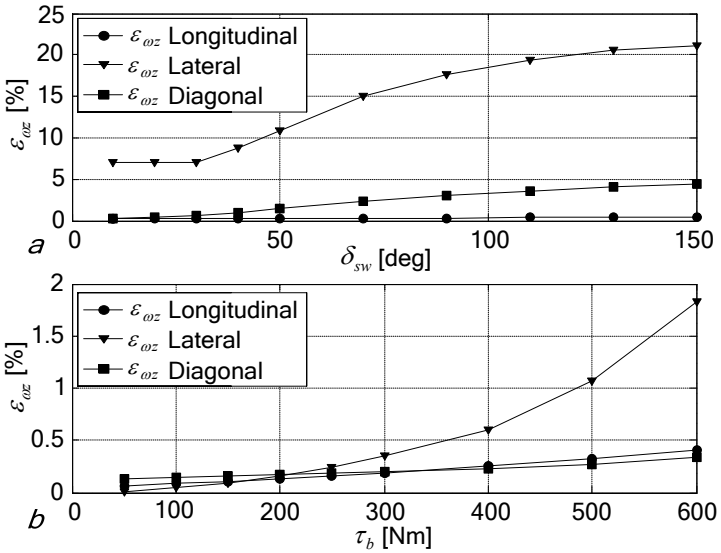

Fig. 4.23 *Roll and pitch dynamics-related yaw rate estimation transient errors for cornering maneuvers (a) and braking in turn maneuvers (b).*

b) Accelerometer misalignment angle-related errors

Another major source of errors of the accelerometer-based kinematic yaw rate estimators is related to sensor misalignment. More precisely, the constraints in the accuracy of vehicle assembly may cause a misalignment of the accelerometer axes (x_a, y_a, z_a) with respect to the vehicle body frame (x_b, y_b, z_b), as shown in Fig. 4.24. This misalignment is characterized by the misalignment angle γ, as illustrated in Fig. 4.24.

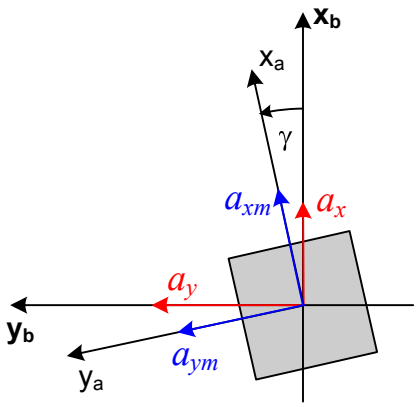

Fig. 4.24 *Accelerometer axis misalignment.*

The measurement of the misaligned accelerometer can be expressed as:

$$a_{ym,i} = a_{y,i}\cos\gamma_i - a_{x,i}\sin\gamma_i \tag{4-72}$$

where the subscript i=1,2,…,6 denotes the accelerometer number, as illustrated in Fig. 4.21.

The misalignment-related relative yaw rate estimation error is calculated by comparing the yaw rate estimates of misaligned and aligned accelerometers:

$$\varepsilon_{\omega zm} = \frac{\hat{\omega}_{zm} - \hat{\omega}_z}{\hat{\omega}_z} \tag{4-73}$$

The accelerometers are assumed to be placed equidistant from the vehicle CoG (i.e. $l_1 = l_2 = l_x$, $l_3 = l_4 = l_y$, and $l_5 = l_6 = l_d$).

Combining Eqs. (4-46), (4-47), and (4-72), and rearranging gives the following equations for measurements of the misaligned accelerometers placed in the **longitudinal configuration**:

$$\begin{aligned} a_{y1m} = {} & \left(a_{yCoG} + g\sin\phi\cos\theta\right)\cos\gamma_1 + l_x\left(\omega_y^2 + \omega_z^2\right)\sin\gamma_1 \\ & - \left(a_{xCoG} - g\sin\theta\right)\sin\gamma_1 + l_x\left(\omega_x\omega_y + \dot{\omega}_z\right)\cos\gamma_1 \end{aligned} \tag{4-74}$$

$$\begin{aligned} a_{y2m} = {} & \left(a_{yCoG} + g\sin\phi\cos\theta\right)\cos\gamma_2 - l_x\left(\omega_y^2 + \omega_z^2\right)\sin\gamma_2 \\ & - \left(a_{xCoG} - g\sin\theta\right)\sin\gamma_2 - l_x\left(\omega_x\omega_y + \dot{\omega}_z\right)\cos\gamma_2 \end{aligned} \tag{4-75}$$

From these measurements the yaw rate is estimated according to Eq. (4-53). The related misalignment error defined by Eq. (4-73) is:

$$\varepsilon_{\omega zm} = \frac{1}{\hat{\omega}_z}\left(\int\hat{\dot{\omega}}_{zm}dt - \int\hat{\dot{\omega}}_z dt\right) = \frac{1}{\hat{\omega}_z}\int(\hat{\dot{\omega}}_{zm} - \hat{\dot{\omega}}_z)dt \tag{4-76}$$

Applying Eq. (4-52) and using the approximate terms for trigonometric functions of small angles (i.e. $\sin\gamma \approx \gamma$ and $\cos\gamma \approx 1$ for $\gamma \approx 0$) gives:

$$\begin{aligned} \hat{\dot{\omega}}_{zm} - \hat{\dot{\omega}}_z = {} & \frac{a_{y1m} - a_{y2m}}{2l_x} - \frac{a_{y1} - a_{y2}}{2l_x} \approx \left(a_{yCoG} + g\sin\phi\cos\theta\right)\frac{\sqrt{1-\gamma_1^2} - \sqrt{1-\gamma_2^2}}{2l_x} \\ & + \left(\omega_y^2 + \omega_z^2\right)\frac{\gamma_1 + \gamma_2}{2} - \left(a_{xCoG} - g\sin\theta\right)\frac{\gamma_1 - \gamma_2}{2l_x} \end{aligned} \tag{4-77}$$

The third right-hand side term of Eq. (4-77) represents the dominant source of misalignment error, because $\gamma_{1,2}^2$ and $\omega_{y,z}^2$ are relatively small. Namely, in the presence of large vehicle longitudinal acceleration a_{xCoG} and road grade (large θ) the error may be quite high even for small misalignment angles γ_1 and γ_2.

Combining (4-46), (4-47), (4-57), and (4-72) gives the following expression for square power of the yaw rate estimate for the **lateral configuration** of misaligned accelerometers:

$$\begin{aligned}\hat{\omega}_{zm}^2 \approx &\left(a_{yCoG} + g\sin\phi\cos\theta\right)\frac{\sqrt{1-\gamma_4^2}-\sqrt{1-\gamma_3^2}}{2l_y} + \omega_x^2 \\ &+\left(a_{xCoG} - g\sin\theta\right)\frac{\gamma_3-\gamma_4}{2l_y} + \omega_z^2 - \dot{\omega}_z\frac{\gamma_3+\gamma_4}{2}\end{aligned} \tag{4-78}$$

The misalignment-related relative error reads:

$$\varepsilon_{\omega zm} = \frac{\hat{\omega}_{zm}-\hat{\omega}_z}{\hat{\omega}_z} = \frac{\sqrt{\hat{\omega}_z^2+\varepsilon_m}-\hat{\omega}_z}{\hat{\omega}_z} \tag{4-79}$$

with

$$\begin{aligned}\varepsilon_m \approx &\left(a_{yCoG} + g\sin\phi\cos\theta\right)\frac{\sqrt{1-\gamma_4^2}-\sqrt{1-\gamma_3^2}}{2l_y} \\ &+\left(a_{xCoG} - g\sin\theta\right)\frac{\gamma_3-\gamma_4}{2l_y} - \dot{\omega}_z\frac{\gamma_3+\gamma_4}{2}\end{aligned} \tag{4-80}$$

In addition to the aforementioned dominant influence of the longitudinal acceleration/road grade, estimation based on the lateral configuration of misaligned accelerometers is sensitive to abrupt changes of yaw rate (i.e. to yaw acceleration $\dot{\omega}_z$). Due to the absence of integration (filtering) process in (4-79) when compared to (4-76), it is expected that the misalignment errors will be larger than for the longitudinal configuration, but the drift-like effect will not be present.

The measurement term χ for the **diagonal configuration** defined by (4-63) is given in (4-62). When the accelerometers are misaligned by the angles γ_5 and γ_6, the measurement term χ_{MA} reads:

$$\begin{aligned}\chi_{MA} = \frac{a_{ym5}-a_{ym6}}{2l_d\cos\alpha_0} = &\chi - \left(a_{xCoG} - g\sin\theta\right)\frac{\gamma_5-\gamma_6}{2l_d\cos\alpha_0} \\ &+\left(a_{yCoG} + g\sin\phi\cos\theta\right)\frac{\sqrt{1-\gamma_5^2}-\sqrt{1-\gamma_6^2}}{2l_d\cos\alpha_0} \\ &+\left(\omega_z^2+\omega_y^2\right)\frac{\gamma_5+\gamma_6}{2} + \left(\omega_x\omega_y - \dot{\omega}_z\right)\tan\alpha_0\frac{\gamma_5+\gamma_6}{2}\end{aligned} \tag{4-81}$$

The dominant misalignment error terms proportional to (a_{xCoG}-$g$sinθ) and $\dot{\omega}_z$ are filtered by the estimator differential equation (4-63), so that the error should be significantly smaller than in the case of the lateral configuration.

Simulation results in Figs. 4.25 and 4.26 indicate that the accelerometer misalignment error of only a few degrees can easily cause excessive yaw rate estimation errors. Moreover, the lateral configuration estimator is found to be the most sensitive to the misalignment related errors (red trace in Figs. 4.25 and 4.26). This is because the abrupt yaw rate changes (large $\dot{\omega}_z$ during step steer maneuver) and large longitudinal accelerations (large $a_{x\mathrm{CoG}}$ during braking maneuver) affect the estimation error in a direct, algebraic manner (see Eq. (4-80)). On the other hand, for longitudinal and diagonal configurations the integration process (see e.g. Eq. (4-76)) filters the $\dot{\omega}_z$ and $a_{x\mathrm{CoG}}$ disturbance terms. Consequently, the error peaks are largely rejected, but a drift-like behavior (slow increase of error) is present. The braking maneuver is more critical then cornering, because of larger forward accelerations (e.g. $a_{x\mathrm{CoG}} \approx$ -2 m/s^2 for the braking in Fig. 4.26 and $a_{x\mathrm{CoG}} \approx$ -0.2 m/s2 for the cornering in Fig. 4.25).

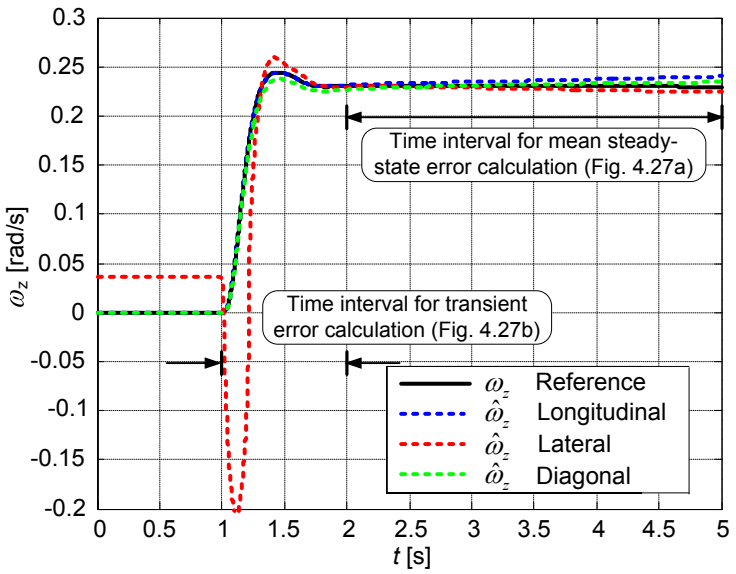

Fig. 4.25 *Misalignment-related yaw rate estimation errors for step steer cornering maneuver (δ_{sw} = 50°, T_b = 0, α_1 = 2°, α_2 = 3°).*

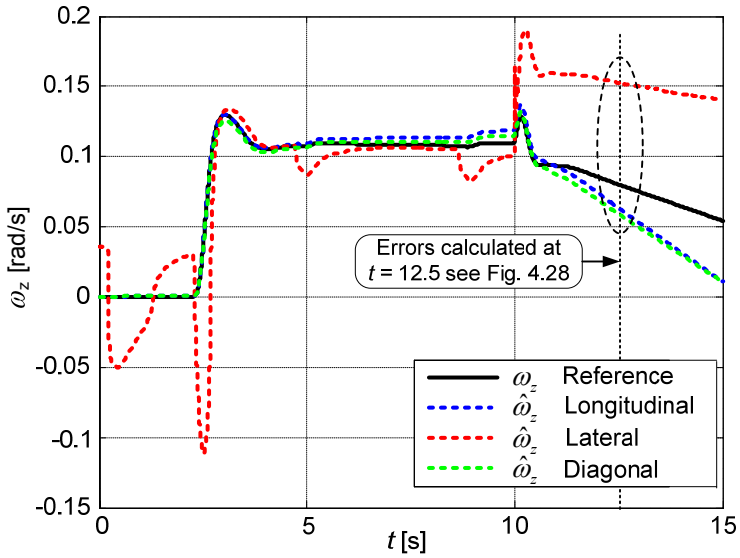

Fig. 4.26 *Misalignment-related yaw rate estimation errors for combined, step steer (controlled velocity) and braking maneuver (δ_{sw} = 23°, τ_b = 300 Nm, α_1 = 2°, α_2 = 3°).*

The misalignment-related estimation errors as functions of the accelerometer misalignment angles (up to 5°) for maneuvers from Figs. 4.25 and 4.26 and different accelerometer configurations are shown in Figs. 4.27 and 4.28, respectively.

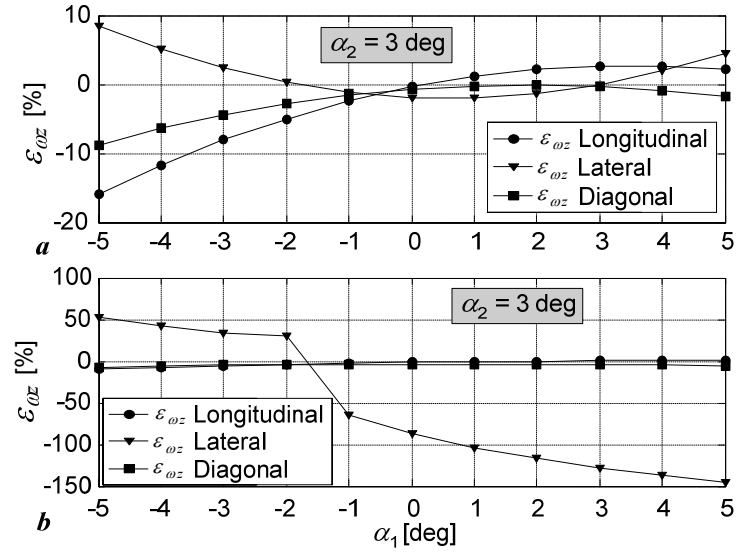

Fig. 4.27 *Influence of accelerometer misalignment angles on yaw rate estimation error for cornering maneuver (see Fig. 4.25): steady-state mean errors calculated in the time interval 2-5 s (a) and transient (peak) errors calculated in the time interval 1-2 s (b).*

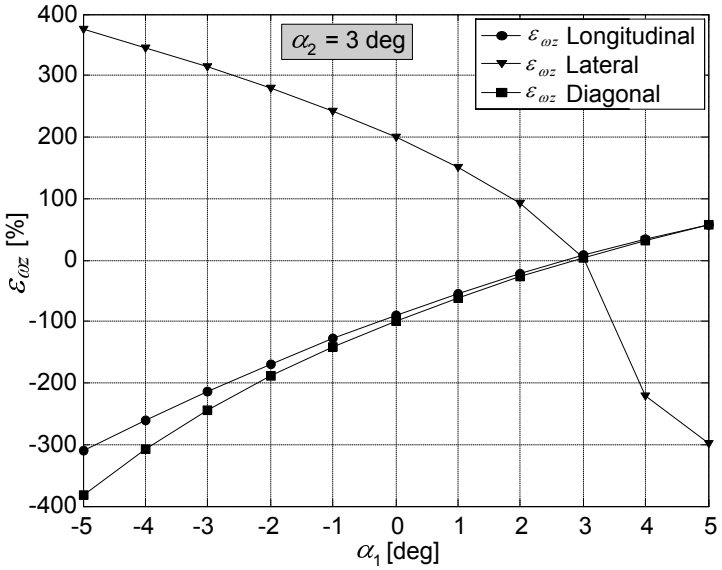

Fig. 4.28 *Yaw rate estimation errors vs. misalignment angles for combined, step steer and braking maneuver in Fig. 4.26 at t = 12.5 s.*

The relative steady-state estimation errors for the cornering maneuver and any of accelerometer configurations are within 15% for the considered misalignment angle span (Fig. 4.27a). However, the lateral estimator has a disadvantage of a substantial transient error (over 50%, Fig. 4.27b, see also Fig. 4.25). For the case of excessive braking the misalignment related errors are unacceptable for all three accelerometer configurations (Fig. 4.28) The errors diminishes for $\gamma_i = \gamma_j$, because the dominant forward acceleration (a_{xCoG}) disturbance term is canceled in that case (see Eqs. (4-77), (4-80), and (4-81)).

c) Accelerometer measurement noise-related errors

The impact of the measurement noise on the performance of all three estimator configurations has also been considered and evaluated. Thus, for the noisy accelerometer measurements and the lateral accelerometer configuration the noisy yaw rate estimate $\hat{\omega}_{zn}$ can be expressed as (cf. Eq. (4-57)):

$$\hat{\omega}_{zn}^2 = \frac{a_{y4} + n_4 - a_{y3} - n_3}{2l_y} = \hat{\omega}_z^2 + \frac{n_4 - n_3}{2l_y} \tag{4-82}$$

where n_3 and n_4 are the sensor additive noise signals with the Root Mean Square (RMS) value σ_0, and $\hat{\omega}_z$ is the corresponding noise-free yaw rate estimate. If the condition

$(n_4 - n_3)/2l_y < \hat{\omega}_z^2$ is satisfied, and after applying Taylor series expansion according to Eq. (4-68), the noisy yaw rate estimate can be expressed as:

$$\hat{\omega}_{zn} = \hat{\omega}_z \left[1 + \frac{1}{2}\frac{n_4 - n_3}{\hat{\omega}_z^2 2l_y} - \frac{1}{8}\frac{(n_4 - n_3)^2}{\hat{\omega}_z^4 4l_y^2} + \cdots + \frac{(-1)^n (2n)!}{(1-2n)n!^2 4^n}\frac{(n_4 - n_3)^n}{\hat{\omega}_z^{2n} 2^n l_y^n} \right] \tag{4-83a}$$

Furthermore, for $(n_4 - n_3)/2l_y << \hat{\omega}_z^2$ the above estimate can be approximated as:

$$\hat{\omega}_{zn} \approx \hat{\omega}_z + \frac{1}{4}\frac{n_4 - n_3}{\hat{\omega}_z l_y} \tag{4-83b}$$

In the case of steady-state conditions ($\hat{\omega}_z(i) = \hat{\omega}_z = \overline{\hat{\omega}}_{zn}$) and after applying the rule for the variance of the sum of random variables $\sigma^2(x_1 + x_2) = \sigma^2(x_1) + \sigma^2(x_2)$, the noise RMS value of the estimated yaw rate $\sigma_{\hat{\omega}_{zn}}$ can be derived according to the following equation:

$$\begin{aligned} \sigma_{\hat{\omega}_{zn}} &= \sqrt{\frac{1}{k-1}\sum_{i=1}^{k}\left(\hat{\omega}_z(i) + \frac{n_4(i) - n_3(i)}{4l_y\hat{\omega}_z(i)} - \overline{\hat{\omega}}_{zn} \right)^2} \\ &= \frac{1}{2l_y\hat{\omega}_z}\sqrt{\frac{1}{k-1}\sum_{i=1}^{k}\left(n_4(i) - n_3(i)\right)^2} = \frac{\sqrt{2}\cdot\sigma_0}{2l_y\hat{\omega}_z} \end{aligned} \tag{4-83c}$$

The higher the yaw rate ω_z and the larger the accelerometer distance $2l_y$, the lower the noise RMS value $\sigma_{\hat{\omega}_{zn}}$.

The **longitudinal and diagonal configuration** estimators (4-53) and (4-63) integrate the accelerometers measurement signals, and they are, therefore, much less sensitive to the measurement noise.

The yaw rate estimate noise RMS levels given in Table 4.3 are obtained from simulations for the step steer cornering maneuver with the constant yaw rate of 0.14 rad/s and the following distances of the accelerometers from the CoG: l_x = 1.5 m, l_y = 1 m, and l_d = 1.8 m. Table 4.3 confirms that the longitudinal and diagonal estimators have significantly lower noise RMS values (approximately by two orders of magnitude) due to the integration process.

Table 4.3 *Yaw rate estimation noise RMS values*

Estimator configuration	**Noise RMS**	
	Absolute [rad/s]	**Relative [%]**
Lateral	3.173e-3	2.25
Longitudinal	1.146e-5	8.10e-3
Diagonal	1.067e-5	7.52e-3

d) Accelerometer offset-related error

The inherent offset of the accelerometer measurement affects the accuracy of yaw rate estimation. According to Eq. (4-57), the constant small accelerometer offset introduces a constant small yaw rate estimation error for the lateral accelerometer configuration. On the other hand, the longitudinal and diagonal configurations estimators (see Eqs. (4-53) and (4-63)) integrate the acceleration signal, and therefore they accumulate a drift-like estimation error whenever the offset is present. The drift effect is generally less emphasized for the diagonal configuration, because the first-order lag reconstruction is used instead of pure integration.

A more detailed analysis of the accelerometer offset related drift-like estimation error, for diagonal sensor configuration, has been carried out in order to gain better insight into limitations of the pure-kinematic accelerometers-based yaw rate estimators. Namely, the application of closed-loop estimator utilizing the EKF methodology (see Section 3.2) has been considered in order to find out if such approach could ensure inherently smaller estimation errors when compared to the estimates obtained from the basic open-loop kinematic estimator (Eq. (4-63)). Thus, after linearization of the kinematic estimator equation (4-63) the following continuous-time domain first-order lag-type transfer function model can be derived:

$$G(s)=\frac{\omega_z(s)}{\chi_m(s)}=\frac{1}{s+2\omega_{z0}\tan\alpha_0}=\frac{\frac{1}{2\omega_{z0}\tan\alpha_0}}{1+\frac{s}{2\omega_{z0}\tan\alpha_0}}=\frac{K_e}{1+T_e s} \tag{4-84}$$

where the process model gain K_e and the time constant T_e depend on the sensor placement angle α_0 and the current yaw rate magnitude ω_{z0} (i.e. the operating point). More precisely, at smaller yaw rates (i.e. the worse signal-to-noise ratio), the process time constant T_e and gain K_e are larger. Hence, the inherent process model noise filtering feature is improved (i.e. the process is characterized by improved noise suppression capabilities at smaller yaw rates), while at the same time due to the larger K_e the estimator sensitivity is increased. Note that as the yaw rate decreases the accelerometers measurement signal χ_m becomes smaller as well.

In the process of formulation of the closed-loop Kalman filter-based estimator, the following discrete-time representation of the state-space process model is used as a basis for further analysis:

$$\mathbf{x}(k) = \mathbf{F}\,\mathbf{x}(k-1) + \mathbf{\Omega}\,\boldsymbol{\upsilon}(k-1), \tag{4-85}$$

The state vector **x,** state transition matrix **F**, state perturbation matrix **Ω,** and state noise vector **υ** are given by:

$$\mathbf{x} = \begin{bmatrix} \omega_z \\ \dot{\omega}_z \end{bmatrix},\ \mathbf{F} = \begin{bmatrix} 1 & T \\ 0 & 1 \end{bmatrix},\ \mathbf{\Omega} = \begin{bmatrix} T & 0 \\ 0 & T \end{bmatrix},\ \boldsymbol{\upsilon} = \begin{bmatrix} \upsilon_\omega \\ \upsilon_{\dot{\omega}} \end{bmatrix}$$

where T is the sampling time. The nonlinear output equation in the presence of the accelerometer offsets read (cf. Eq. (4-63)):

$$\chi_m(k) = \mathbf{h}(\mathbf{x}(k)) + \delta_\chi(k) + e_\chi(k) = \dot{\omega}_z(k) + \tan\alpha_0\,\omega_z^2(k) + \delta_\chi(k) + e_\chi(k) \tag{4-86}$$

where χ_m (unlike the measurement term χ in Eq. (4-63)) is the accelerometers measurement with included additive accelerometer offsets term δ_χ , while e_χ is the zero mean Gaussian measurement noise. The above measurement offset term can be obtained from the following expression:

$$\delta_\chi = \frac{a_{y5o} - a_{y6o}}{2l_d\cos\alpha_0}$$

where the a_{y5o} and a_{y6o} are the individual accelerometers offsets for diagonal measurement configuration (cf. Fig. 4.21).

The particular EKF algorithm is described by the following equations (see Section 3.2):

$$\hat{\mathbf{x}}(k \mid k-1) = \mathbf{F}\,\hat{\mathbf{x}}(k-1 \mid k-1) \tag{4-87}$$

$$\begin{aligned} \tilde{\mathbf{y}}(k \mid k-1) &= \mathbf{y}(k) - \mathbf{h}\left(\hat{\mathbf{x}}(k \mid k-1)\right) \\ &= \chi_m(k) - \left[tg\alpha_0\hat{\omega}_z^2(k \mid k-1) + \hat{\dot{\omega}}_z(k \mid k-1)\right] \end{aligned} \tag{4-88}$$

$$\mathbf{P}(k \mid k-1) = \mathbf{F}\,\mathbf{P}(k-1 \mid k-1)\mathbf{F}^T + \mathbf{\Omega}\mathbf{Q}\mathbf{\Omega}^T \tag{4-89}$$

$$\mathbf{K}(k) = \begin{bmatrix} K_\omega \\ K_{\dot{\omega}} \end{bmatrix} = \frac{\mathbf{P}(k \mid k-1)\mathbf{H}^T(k)}{\mathbf{H}^T(k)\mathbf{P}(k \mid k-1)\mathbf{H}^T(k) + \mathbf{R}} \tag{4-90}$$

$$\hat{\mathbf{x}}(k \mid k) = \hat{\mathbf{x}}(k \mid k-1) + \mathbf{K}(k)\tilde{\mathbf{y}}(k \mid k-1) \tag{4-91}$$

$$\mathbf{P}(k \mid k) = \mathbf{P}(k \mid k-1) - \mathbf{K}(k)\mathbf{H}(k)\mathbf{P}(k \mid k-1) \tag{4-92}$$

where the output matrix **H**(k) is obtained by linearization of the nonlinear output matrix equation **h**(**x**) (i.e. by calculating the below Jacobian matrix):

$$\mathbf{H}(k) = \left.\frac{\partial\mathbf{h}}{\partial\mathbf{x}}\right|_{\mathbf{x}=\mathbf{x}_0(k)} = \begin{bmatrix} 2\tan\alpha_0 \cdot \hat{\omega}_z(k \mid k-1) & 1 \end{bmatrix} \tag{4-93}$$

Note that, instead of the unknown true instantaneous yaw rate ω_{z0}, the a-priori state estimate $\hat{\omega}_z(k \mid k-1)$ is used in calculating the update of the output matrix $\mathbf{H}(k)$. The state covariance matrix $\mathbf{Q}$ and measurement covariance $\mathbf{R}$ read:

$$\mathbf{Q} = diag([q_\omega \quad q_{\dot{\omega}}]), \quad \mathbf{R} = r_\chi .$$

For the considered EKF algorithm, the transfer functions $G_{\omega\chi}$ and $G_{\dot{\omega}\chi}$ between the corresponding state variables and the nominal, offset-free measurement χ can be obtained from the following matrix equation [51]:

$$\mathbf{G}_{xy}(z) = \begin{bmatrix} G_{\omega\chi}(z) \\ G_{\dot{\omega}\chi}(z) \end{bmatrix} = z\mathbf{I}\left[z\mathbf{I} - (\mathbf{I} - \overline{\mathbf{K}}\mathbf{H})\mathbf{F}\right]^{-1}\overline{\mathbf{K}} \tag{4-94}$$

where $\overline{\mathbf{K}}$ is the steady-state stationary Kalman gains matrix and $\mathbf{I}$ is the unit matrix. For the consequent analysis only the transfer function $G_{\omega\chi}(z) = \omega_z(z)/\chi(z)$ is relevant:

$$G_{\omega\chi}(z) = \frac{\omega_z(z)}{\chi(z)} = \frac{z\left(K_\omega z - K_\omega + K_{\dot{\omega}} T\right)}{z^2 + \left[b_0 \omega_{z0}\left(K_\omega + K_{\dot{\omega}} T\right) + K_{\dot{\omega}} - 2\right]z - b_0 \omega_{z0} K_\omega - K_{\dot{\omega}} + 1} \tag{4-95}$$

where K_ω and $K_{\dot{\omega}}$ are Kalman gains and $b_0 = 2\tan\alpha_0$.

In the presence of the accelerometers offsets the measurement model from Eq. (4-86) applies. Consequently, by applying the Z-transform based on the zero-order-hold element, the process model output equation is transformed into the following discrete-time model

$$\chi_m(z) = \frac{1}{\rho} \cdot \frac{z-\rho}{z}\omega_z(z) + \frac{z}{z-1}\delta_\chi , \tag{4-96}$$

where:

$$\rho = \frac{T}{1 + 2T \cdot \tan\alpha_0} \tag{4-97}$$

and the second right-hand side term relate to the accelerometers offset. In order to analyze the effects of accelerometer offset to the EKF-based yaw rate estimation error $\tilde{\omega}_z$, the transfer function model given in Eq. (4-95) is employed:

$$\tilde{\omega}_z(z) = \hat{\omega}_z(z) - \omega_z(z) = G_{\omega\chi}(z)\chi_m(z) - \omega_z(z) \tag{4-98}$$

After inserting $\chi_m(z)$ from Eq. (4-96) into the Eq. (4-98), the yaw rate estimation error reads:

$$\tilde{\omega}_z(z) = \hat{\omega}_z(z) - \omega_z(z) = \left(G_{\omega\omega}(z) - 1\right)\omega_z(z) + G_{\omega\chi 0}(z)\delta_\chi \tag{4-99}$$

where:

$$G_{\omega\omega}(z)=\frac{\hat{\omega}_z(z)}{\omega_z(z)}=G_{\omega\chi}(z)\cdot\frac{1}{\rho}\cdot\frac{z-\rho}{z} \tag{4-100}$$

$$G_{\omega\chi 0}(z)=\frac{\hat{\omega}_z(z)}{\delta_\chi(z)}=G_{\omega\chi}(z)\cdot\frac{z}{z-1} \tag{4-101}$$

By inserting the Kalman filter transfer function (4-95) into Eq. (4-101) yields the following expression for yaw rate estimate vs. measurement offset transfer function:

$$\begin{aligned}G_{\omega\chi 0}(z)&=\frac{\hat{\omega}_z(z)}{\delta_\chi(z)}\\&=\frac{z}{z-1}\cdot\frac{z\left(K_\omega z-K_\omega+K_{\dot\omega}T\right)}{z^2+\left[b_0\omega_{z0}\left(K_\omega+K_{\dot\omega}T\right)+K_{\dot\omega}-2\right]z-b_0\omega_{z0}K_\omega-K_{\dot\omega}+1}\end{aligned} \tag{4-102}$$

The steady-state yaw rate estimation error can be obtained from Eq. (4-99) by applying the final value theorem [52,53]:

$$\begin{aligned}\tilde{\omega}_z(k\to\infty)&=\lim_{z\to 1}(z-1)\tilde{\omega}_z(z)\\&=\lim_{z\to 1}(z-1)\left(G_{\omega\omega}(z)-1\right)\omega_z(z)+\lim_{z\to 1}(z-1)G_{\omega\chi 0}(z)\delta_\chi(z)\end{aligned} \tag{4-103}$$

The measurement offset δ_χ and yaw rate ω_z are assumed to be constant. The second right-hand side term in Eq. (4-103) defines the steady-state estimation error induced exclusively by the measurement offset. Inserting the transfer function $G_{\omega\chi 0}(z)$ from Eq. (4-102) into Eq. (4-103) yields the following expression for steady-state offset-related estimation error $\tilde{\omega}_{z0}$:

$$\begin{aligned}\tilde{\omega}_{z0}(k\to\infty)&=\lim_{z\to 1}(z-1)G_{\omega\chi 0}\cdot\delta_\chi\\&=\lim_{z\to 1}(z-1)\frac{z}{z-1}\cdot\frac{z\left(K_\omega z-K_\omega+K_{\dot\omega}T\right)}{z^2+\left[b_0\omega_{z0}\left(K_\omega+K_{\dot\omega}T\right)+K_{\dot\omega}-2\right]z-b_0\omega_{z0}K_\omega-K_{\dot\omega}+1}\delta_\chi\end{aligned} \tag{4-104}$$

After some rearranging the final equation for the estimation error is obtained:

$$\tilde{\omega}_{z0}(k\to\infty)=\frac{1}{2\tan\alpha_0\cdot\omega_{z0}}\cdot\delta_\chi \tag{4-105}$$

Equation (4-104) indicates that the offset-related steady-state estimation error does not depend on the choice of the estimator parameters (i.e. estimation gains K_ω and $K_{\dot\omega}$) but only on the operating point ω_{z0}. Therefore, the estimator which utilizes accelerometer measurements only cannot compensate for the additive measurement offset error. The above equation also suggests that the relative steady-state estimation error can be very large for small yaw rates, because the relative error $r=\tilde{\omega}_{z0}/\omega_{z0}$ is inversely proportional to the yaw rate squared. Consequently, the drift effect for the diagonal configuration is most emphasized at small yaw rates (large error transfer function gains).

The results illustrated in Fig. 4.29 are obtained from simulations for the diagonal measurement configuration and the following accelerometer offsets a_{off5} = 0.05 m/s^2 and a_{off6} = -0.03 m/s^2 (i.e. χ_{off} = 0.0314 s^{-2}). The drift-like estimation error accumulates quite rapidly (according to the 2nd-order dynamics described by Eq. (4-102)) for t < 1s when ω_{z0} = 0, while later it increases at much slower rate. This is because the rate of the error increase is inversely proportional to the yaw rate magnitude as shown in the above analysis, while the longitudinal configuration is characterized by constant/high error accumulation rate for a given sensor offset and sampling time.

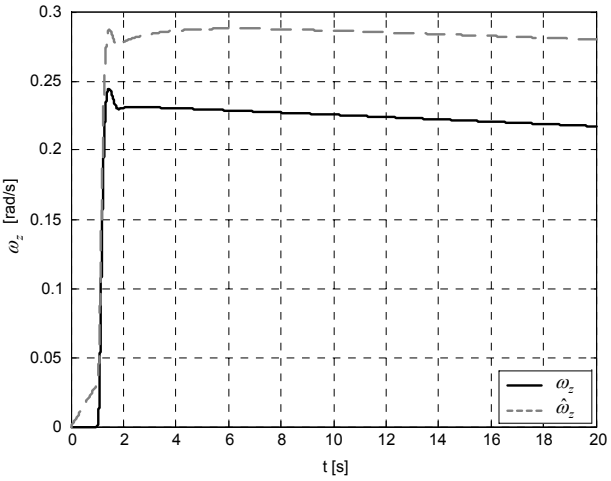

Fig. 4.29 *Illustration of acceleration offset-related errors for diagonal estimator and step steer maneuver.*

4.4 Fusion of the wheel-speeds and acceleration based estimation approaches

The combined kinematic estimator concept described herein is based on the fusion of measurements of two accelerometers placed in diagonal configuration upon the vehicle chassis (this configuration is favored over the lateral and longitudinal ones illustrated in Fig. 4.21, because it has the best overall performance in terms of the estimation accuracy) and the speed sensors of the rear non-driven wheels (i.e. the front wheel drive vehicle is implied). The sensor setup is illustrated in Fig. 4.30. This fusion estimator utilizing the adaptive extended Kalman filter (EKF) methodology (see Chapter 3) is used in order to overcome the restrictions upon the estimation accuracy of the previously described, individual kinematic estimators (cf. Sections 4.2 and 4.3) and to benefit from their complementary advantages. More precisely, the main disadvantage of the accelerometer approach is the sensor offset-related drift-like estimation error and a high sensitivity to sensor misalignment errors, while

the ABS yaw rate estimation approach is compromised in the cases of braking, tire deflation, or road disturbance. Within the proposed sensor fusion-based kinematic estimator the ABS measurements are used to compensate for the accelerometer offset-related estimation errors, while the accelerometers compensate for the inaccuracy of the ABS sensors-based yaw rate estimate during braking. The developed estimator also takes into account the effects of the effective tire radii variation due to tire deflation, vehicle lateral load transfer, and road disturbances.

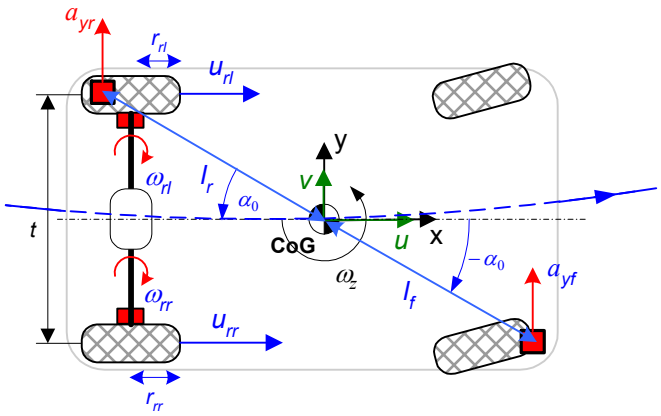

Fig. 4.30 *Illustration of the sensor configuration for the combined, fusion-based kinematic yaw rate estimator.*

For the purpose of fusion-based estimator design, the process model is established based on Eq. (4-41) (i.e. the wheel speed sensor-based yaw rate estimation equation including the compensation coefficients $k_{c,s}$ and $k_{c,d}$ for eliminating the static and dynamic effective tire radii variations-related errors) and Eq. (4-63) (i.e. diagonal accelerometers measurement-based yaw rate estimation equation) extended by the accelerometer offset:

$$\omega_{zx} = \frac{r_n}{t}\left(\omega_{rr} - k_{c,s}\omega_{rl}\right) - \frac{k_{c,d}\,\delta F_z}{t}\left(\omega_{rr} + \omega_{rl}\right) \tag{4-106a}$$

$$\chi_m = \frac{a_{yf} - a_{yr}}{2l_d\cos\alpha_0} + \frac{a_{yfo} - a_{yro}}{2l_d\cos\alpha_0} = \dot{\omega}_z + \omega_z^2\, tg\alpha_0 + \delta_\chi \tag{4-106b}$$

where a_{yfo} and a_{yro} are the accelerometers offsets, and δ_χ is the offset-related measurement error term. For the analysis, these quantities may be considered to have constant values, while usually they slowly change with temperature, aging etc.

The process model is represented by the following set of state-space equations:

$$\frac{d\omega_z}{dt} = \dot{\omega}_z + \upsilon_\omega, \qquad \frac{d\dot{\omega}_z}{dt} = \upsilon_\omega, \qquad \frac{d\delta_\chi}{dt} = \upsilon_\delta \tag{4-107}$$

where the yaw rate ω_z, the yaw acceleration $\dot{\omega}_z$, and the accelerometer measurement offset δ_χ are modeled as random walk-type stochastic states. By applying the Z-transform based on the zero-order-hold element, Eq. (4-107) can be transformed into the following discrete-time model:

$$\mathbf{x}(k) = \mathbf{F}\,\mathbf{x}(k-1) + \mathbf{\Omega}\,\boldsymbol{\upsilon}(k-1) \tag{4-108}$$

with $\mathbf{x}$, $\boldsymbol{\upsilon}$, $\mathbf{F}$, and $\mathbf{\Omega}$ defined as (T = sampling time):

$$\mathbf{x} = \begin{bmatrix} \omega_z \\ \dot{\omega}_z \\ \delta_\chi \end{bmatrix},\ \boldsymbol{\upsilon} = \begin{bmatrix} \upsilon_\omega \\ \upsilon_{\dot{\omega}} \\ \upsilon_{\delta\chi} \end{bmatrix},\ \mathbf{F} = \begin{bmatrix} 1 & T & 0 \\ 0 & 1 & 0 \\ 0 & 0 & 1 \end{bmatrix},\ \text{and}\ \mathbf{\Omega} = \begin{bmatrix} T & 0 & 0 \\ 0 & T & 0 \\ 0 & 0 & T \end{bmatrix}$$

The following process model output (measurement) equation comprises the combined measurements of accelerometers χ_m and wheel speed sensors ω_{zw}:

$$\begin{gathered} \mathbf{y}(k) = \mathbf{h}(\mathbf{x}(k)) + \mathbf{e}(k) \\ \begin{bmatrix} \chi_m(k) \\ \omega_{zw}(k) \end{bmatrix} = \begin{bmatrix} \tan\alpha_0\,\omega_z^2(k) + \dot{\omega}_z(k) + \delta_\chi(k) \\ \omega_z(k) \end{bmatrix} + \begin{bmatrix} e_\chi(k) \\ e_w(k) \end{bmatrix} \end{gathered} \tag{4-109}$$

where e_χ and e_w are zero-mean Gaussian measurement noise components with the variances r_χ and r_w, respectively. Note that the state-space process model from Eq. (4-108) is linear while the nonlinearity is only present in the output equation (4-109).

The Extended Kalman Filter (EKF) equations (see Subchapter 3.2) for the stochastic system defined by Eqs. (4-108) and (4-109) read [2]:

$$\hat{\mathbf{x}}(k \mid k-1) = \mathbf{F}\,\hat{\mathbf{x}}(k-1 \mid k-1) \tag{4-110}$$

$$\begin{aligned} \tilde{\mathbf{y}}(k \mid k-1) &= \mathbf{y}(k) - \mathbf{h}(\hat{\mathbf{x}}(k \mid k-1)) \\ &= \begin{bmatrix} \chi_m(k) \\ \omega_{zw}(k) \end{bmatrix} - \begin{bmatrix} tg\alpha_0\hat{\omega}_z^2(k \mid k-1) + \hat{\dot{\omega}}_z(k \mid k-1) + \delta_\chi(k \mid k-1) \\ \hat{\omega}_z(k \mid k-1) \end{bmatrix} \end{aligned} \tag{4-111}$$

$$\mathbf{P}(k \mid k-1) = \mathbf{F}\,\mathbf{P}(k-1 \mid k-1)\mathbf{F}^T + \mathbf{\Omega}\,\mathbf{Q}(k-1)\mathbf{\Omega}^T \tag{4-112}$$

$$\mathbf{K}(k) = \frac{\mathbf{P}(k \mid k-1)\mathbf{H}^T(k)}{\mathbf{H}^T(k)\mathbf{P}(k \mid k-1)\mathbf{H}^T(k) + \mathbf{R}(k)} \tag{4-113}$$

$$\hat{\mathbf{x}}(k \mid k) = \hat{\mathbf{x}}(k \mid k-1) + \mathbf{K}(k)\tilde{\mathbf{y}}(k \mid k-1) \tag{4-114}$$

$$\mathbf{P}(k \mid k) = \mathbf{P}(k \mid k-1) - \mathbf{K}(k)\mathbf{H}(k)\mathbf{P}(k \mid k-1) \tag{4-115}$$

where $\mathbf{\Omega}$ is the state noise conditioning matrix defined as $\mathbf{\Omega} = T \cdot \mathbf{I}_n$.

The observation matrix **H** is obtained by linearizing the nonlinear process model output equation (4-106), which yields:

$$\chi_m = \dot{\omega}_z + 2\tan\alpha_0\,\omega_{z0} + \delta_\chi \tag{4-116}$$

where ω_{z0} is the yaw rate operating point. For the purpose of the convenience, the yaw rate a-priori estimate $\hat{\omega}_z(k\,|\,k-1)$ is used within the EKF algorithm for calculating the output matrix update:

$$\mathbf{H}(k) = \begin{bmatrix} 2\tan\alpha_0\hat{\omega}_z(k\,|\,k-1) & 1 & 1 \\ 1 & 0 & 0 \end{bmatrix}.$$

Assuming that the stochastic state perturbations (υ_ω, $\upsilon_{\dot{\omega}}$, and $\upsilon_{\delta\chi}$) and the measurements noises (e_χ and e_w) are mutually independent, the state covariance matrix **Q** and the measurement noise covariance matrix **R** are defined as:

$$\mathbf{Q}(k) = diag\left(\begin{bmatrix} q_\omega & q_{\dot{\omega}} & q_\delta(k) \end{bmatrix}\right), \quad \mathbf{R}(k) = diag\left(\begin{bmatrix} r_\chi & r_\omega(k) \end{bmatrix}\right) \tag{4-117}$$

where q_δ and r_ω are set to be time-variant in order to implement an adaptive feature of the extended Kalman filter. The elements of these matrices represent the EKF tuning parameters.

The adaptive yaw rate estimator based on the sensor fusion concept and the EKF methodology is shown in Fig. 4.31. The combined accelerometer measurement χ_m, which comprises the individual accelerometer measurements a_{yf} and a_{yr} according to Eq. (4-106) and the wheel speed sensor-based yaw rate estimate $\hat{\omega}_{zwf}$ are used as input signals to the Kalman filter. The initial, wheel speed measurement-based yaw rate estimate $\hat{\omega}_{zwc}$ is obtained by compensating the dominant, effective tire radii variation-related estimation errors from the raw estimate $\hat{\omega}_{zw}$ (see Subsection 4.2.2 and [48,49]). This signal is then applied as the input to the RBD block which detects the road bump disturbance as explained below. Within the RBD block, the $\hat{\omega}_{zwc}$ signal is filtered by a moving average filter in order to suppress oscillations in the estimation signal caused by the wheel speed sensor imbalance (lower frequencies and higher amplitudes) and tooth width errors (lower amplitudes and higher frequencies).

Within the Kalman filter, the yaw rate, yaw acceleration, and accelerometers measurement offset (ω_z, $\dot{\omega}_z$, and δ_χ) are defined as Kalman states. Depending on the confidence levels for each of the utilized sensors, the related elements of the state covariance matrix **Q** and

measurement noise covariance matrix **R** are adapted. Thus, when the accelerometers approach is to be utilized the $q_\delta(k) \in \mathbf{Q}$ and $r_\omega(k) \in \mathbf{R}$ should be set to high values (in case of low confidence of the wheel speed difference-measurement). On the other hand, if these Kalman filter tuning parameters are set to low values, the wheel speed sensors approach is used.

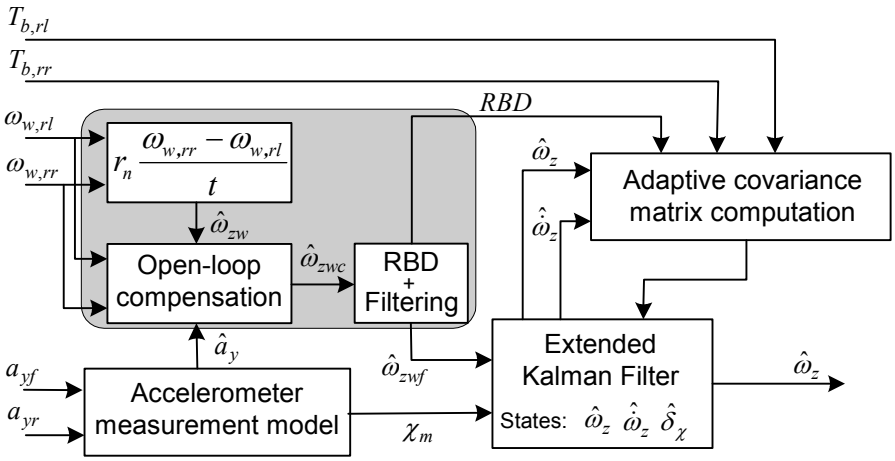

Fig. 4.31 *Block diagram of adaptive EKF-based yaw rate estimator.*

The EKF adaptation algorithm is shown in Fig. 4.32. It switches the state variance $q_\delta(k)$ and the measurement noise variance $r_\omega(k)$ from Eq. (4-117) to discrete predefined values according to Eq. (4-118). The variance values correspond to confidence levels of the individual sensor measurements. The Boolean condition function $C(k)$ (Fig. 4.32) is defined based on the braking status (i.e. "Braking Status" flag, BRS(k) = 1 for braking), magnitudes of the yaw rate and yaw acceleration, and the road bump disturbances detection (i.e. "Road Bump Disturbance" status flag, RBD(k) = 1 when the road bump disturbance is detected).

$$\left[q_\delta(k) \quad r_\omega(k)\right] = \begin{cases} q_{\delta H}, & r_{\omega H} \quad \text{if } C(k) = \text{TRUE} \\ q_{\delta L}, & r_{\omega L} \quad \text{if } C(k) = \text{FALSE} \end{cases} \tag{4-118}$$

In former equation, the subscripts L and H denote 'low' and 'high' value of the related parameter. The above, relatively crude logic is used here for the sake of illustration. In application, it may be refined by using weighting functions and similar.

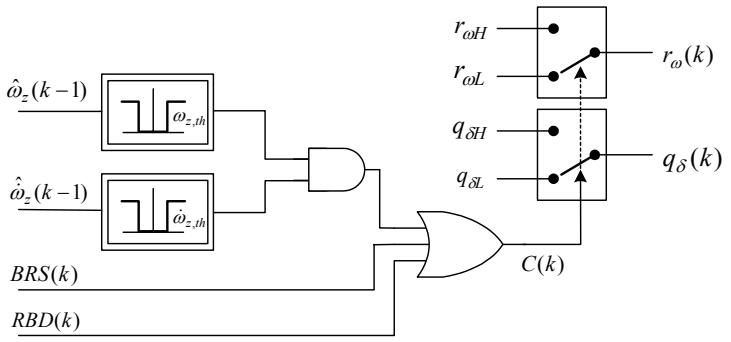

Fig. 4.32 *Block diagram of adaptation mechanism.*

Accelerometers are predominantly used ($C(k)$ = TRUE) during intervals of emphasized yaw rate change (e.g. step-steer maneuver) and when the wheel speed sensors accuracy is compromised (i.e. during braking or in presence of road bump disturbance). On the other hand, the wheel speed sensors are utilized ($C(k)$ = FALSE) during quasi-steady state intervals (e.g. steady cornering maneuvers or straight driving), especially for small yaw rates at which the accelerometer-based estimate drift errors are the most emphasized (see Subsection 4.3.3d).

According to the analysis given in Subsection 4.2.1d the road bump disturbance can introduce a significant pulse-like error into wheel speed sensor-based yaw rate estimation. Namely, due to the large magnitude of such abrupt estimation errors the road-bump disturbance conditions must be monitored, and in the case of detection, the estimator should be switched to the accelerometer mode. To this end a detection algorithm and corresponding *RBD* status flag assignment have been implemented by monitoring the variance of the wheel speed sensor-based yaw rate estimate. Note that, abrupt changes of the yaw rate during step-steer maneuvers also result in an increased yaw rate estimate variance. The detection algorithm cannot make a distinction between these two cases. However, this is not a critical constraint, because the accelerometer mode should be used for both cases.

In order to detect the road bump disturbance, the signal variance $\sigma^2(\hat{\omega}_{zwc})$ is calculated on-line over a fixed time window by utilizing the delay buffer of length N_d. If the calculated variance is larger than the preset threshold value V_{th} for at least $N_{off} < N_d$ consecutive samples the *RBD* status flag is set and the wheel speed sensor-based estimation is disabled. Similarly, the *RBD* flag is reset and the wheel speed-based estimation is enabled if the variance is lower than the threshold value for at least $N_{on} < N_d$ consecutive samples.

In order to benefit from this detection algorithm the time delayed copy of the initial wheel speed sensor-based yaw rate estimate $\hat{\omega}_{zwc}(t - N_d T)$ should be applied to the Kalman filter

input. However, this delay will not have significant effect on the estimation accuracy, because the wheel speed sensors estimation mode is used for the slowly changing yaw rates.

The adaptive EKF estimator performance has been analyzed by comparing the estimated yaw rate signal with the reference obtained from a detailed 10DOF vehicle dynamics model [23] for various driving maneuvers. In these simulations the realistic wheel speed sensor model with imbalance and tooth width errors has been used. Accelerometers offsets has been set to a_{yfo} = 0.005g and a_{yro} = - 0.003g (this corresponds to δ_χ = 0.0314 s^{-2}).

Comparison of the adaptive EKF-based estimator performance with respect to those of individual kinematic estimators for the step-steer maneuver is given in Fig. 4.33. In this maneuver the braking torque of τ_b = 300 Nm per wheel is applied in the time intervals 3-5 s and 11-14 s and the road bump disturbance is applied at t = 10 s. The wheel speed sensors-based approach has large estimation errors during braking periods and road bump disturbance, while accelerometer approach has significant drift-like error, particularly at low yaw rates (Fig. 4.33a).

The estimation results for the adaptive EKF based estimator (Fig. 4.33c) show that all dominant estimation errors are significantly reduced by applying the proposed sensor fusion concept. The remaining errors are mostly well within 10% of the reference value (Fig. 4.33d). The condition function $C(t)$ is shown in Fig. 4.33b in order to illustrate the adaptation feature of the estimator. It is evident that estimator operates in the accelerometer-mode ($C(t)$=1) during time intervals with significant wheel speed sensor errors (braking, road bump, and transients). On the other hand, the wheel speed sensor mode is active during quasi-steady-state yaw rate intervals only ($C(t)$ = 0), and it enables the accelerometer drift-like error compensation.

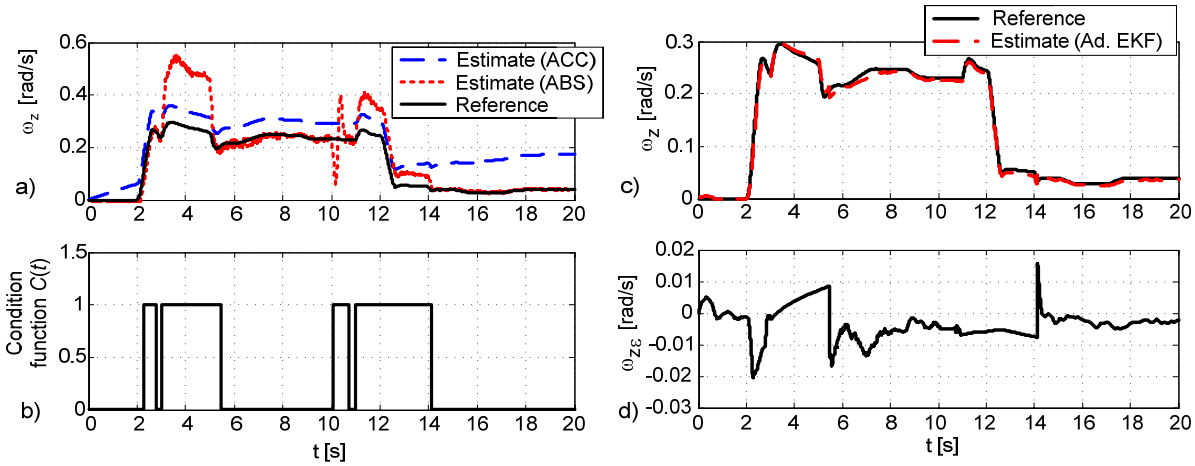

Fig. 4.33 *Illustration of adaptive EKF-based yaw rate estimator accuracy for step-steer maneuver.*

Fig. 4.34 shows the results for the case of a double lane change maneuver with emphasized oversteer intervals, which are characterized with large yaw rate amplitudes and lateral sliding of the rear (non-driven) wheels. In this maneuver, the brakes are kept inactive and no road bump disturbance is considered. Therefore, the wheel speed sensor-based estimator does not have significant estimation errors, while accelerometers still accumulate drift-like error (Fig. 4.34a). When using the adaptive EKF, the estimation errors are rather small, mostly within 0.05 rad/s, when compared to the yaw rate span of ± 1 rad/s (i.e. under 10%).

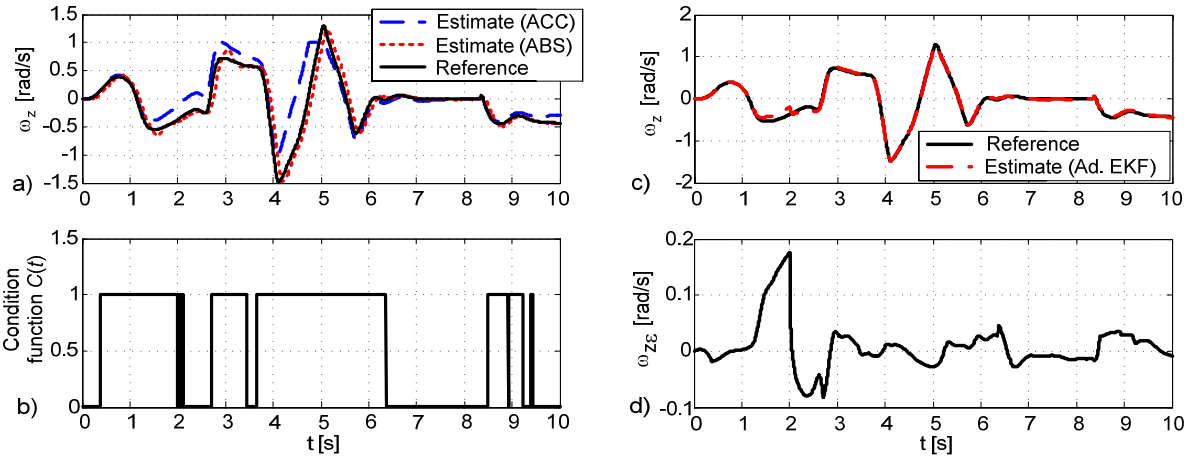

Fig. 4.34 *Illustration of adaptive EKF-based yaw rate estimator accuracy for double lane change maneuver including oversteer behavior.*

4.5 Summary

The adaptive Extended Kalman Filter (EKF)-based kinematic yaw rate estimator has been designed. It combines two basic kinematic estimation approaches: the two-accelerometers approach with diagonal sensor placement, and the non-driven wheels speed sensors approach.

Such a combined estimator, implementing the sensor fusion approach, is aimed at taking advantage form the complement advantages and disadvantages of the two individual estimation concepts.

In order to pave the ground for maximizing the efficiency of the fusion methodology and minimizing the estimation errors, a detailed analysis of the major error sources of individual approaches has been carried out. The major source of estimation errors for first approach is the accelerometer offset that causes the drift-like estimation error, while the second approach cannot be used during braking and it is sensitive to the tire effective radii variations and road bump disturbance.

The proposed adaptive Extended Kalman Filter (EKF)-based estimator significantly reduces the overall estimation errors by utilizing the fusion concept of the two kinematic estimation approaches. Accelerometers are predominantly used during yaw rate transients and when the accuracy of the wheel speed sensors is compromised, while the wheel speed sensors are utilized during the quasi-steady-state yaw rate intervals.

In order to further improve the reliability of the wheel speed sensors, the open-loop compensation of the dominant wheel speed sensors-based estimation errors has been implemented. These static and dynamic compensation algorithms have been derived and embedded into the estimator to reduce the tire deflation/wear and lateral load transfer-related estimation errors. Furthermore, the adaptation algorithm is equipped with the road bump disturbance detection feature, in order to remove the potentially large, environment-related wheel speed sensors-based estimation errors.

The adaptive EKF-based estimator performance has been verified by simulation, and it has been shown that in various driving maneuvers the proposed estimator provides superior overall estimation accuracy when compared to performances of the individual kinematic estimators. The estimation errors are mostly well below 10% for a wide range of driving conditions.

5 Kinematic GPS/INS fusion-based sideslip angle estimation

5.1 Background

Existence of accurate sideslip angle information allows for implementation of a sideslip feedback loop in addition to the traditional yaw rate control loop (a state-space controller). This can improve robustness of the overall vehicle dynamics control strategy. The main obstacle for a successful implementation of such a state-space controller relates to difficulties with sideslip measurement (high cost) or estimation (inaccuracy/sensitivity).

This Chapter deals with kinematic sideslip angle estimation based on the application of Kalman filter methodology and fusion of standard inertial sensors (lateral accelerometer and yaw gyroscope) and low-cost GPS receiver measurements.

Recent introduction of new vehicle dynamics sensors such as Global Positioning System (GPS) receivers [7,13,16,56-58] or 6DOF inertial measurement units [14] opens significant new possibilities towards viable sideslip angle estimation based on advanced sensor fusion concepts utilizing the Kalman filtering methodology [2,14,30]. More precisely, the inertial sensors can provide fast sideslip angle estimate response, but it suffers from potentially large drift due to the inertial sensor offsets, and it is sensitive to modeling errors (e.g. road bank influence). On the other hand, the GPS can provide accurate velocity estimates, but its sampling rate (typically 1 Hz) is too low for vehicle dynamics control applications and it has a limited availability (e.g. in urban canyon regions). The fusion of these two concepts has a good potential to benefit from the complementary advantages of the two individual approaches (i.e. sensors technologies).

The concept of GPS/INS sensor fusion proposed herein and in [54] relies on a kinematic vehicle model for fast sideslip angle estimation, while it utilizes slow GPS velocity measurements to compensate for the inertial sensor offset effect and modeling errors. The sensor fusion is conducted through Extended Kalman Filtering (EKF) approach [2,14,30]. The process model includes the kinematic vehicle model extended with random walk processes for accelerometer and gyro offsets. The GPS correction is conducted through model output

equation giving velocities in the inertial coordinate frame. The estimator has been verified by computer simulations using the 10DOF vehicle dynamics model [23].

5.2 Kinematic models and related kinematic estimators

The vehicle body motion and related inertial sensors and GPS measurements can be described by a set of kinematics equations. In order to formulate these equations, which are essential for designing the kinematic sideslip angle estimator based on the fusion of the INS and GPS measurements, an appropriate coordinate frames need to be defined (Fig. 5.1). The inertial coordinate frame ($X\ Y\ Z$) is used as a reference frame, while the moving frame ($X_b\ Y_b\ Z_b$) is fixed to the vehicle body (Fig. 5.1a). Within the inertial frame the vehicle heading/yaw angle ψ, the vehicle track angle/course φ, and the vehicle velocity V are defined. The vehicle body-fixed frame origin resides in the vehicle body center of gravity (CoG) and its axes point in the forward, lateral, and upward direction. Within this moving frame, the vehicle velocities (u - longitudinal, v - lateral, and w - vertical) and angular speeds (ω_x - roll rate, ω_y - pitch rate, and ω_z - yaw rate) are defined as illustrated in Fig. 5.1b (see also Chapter 2).

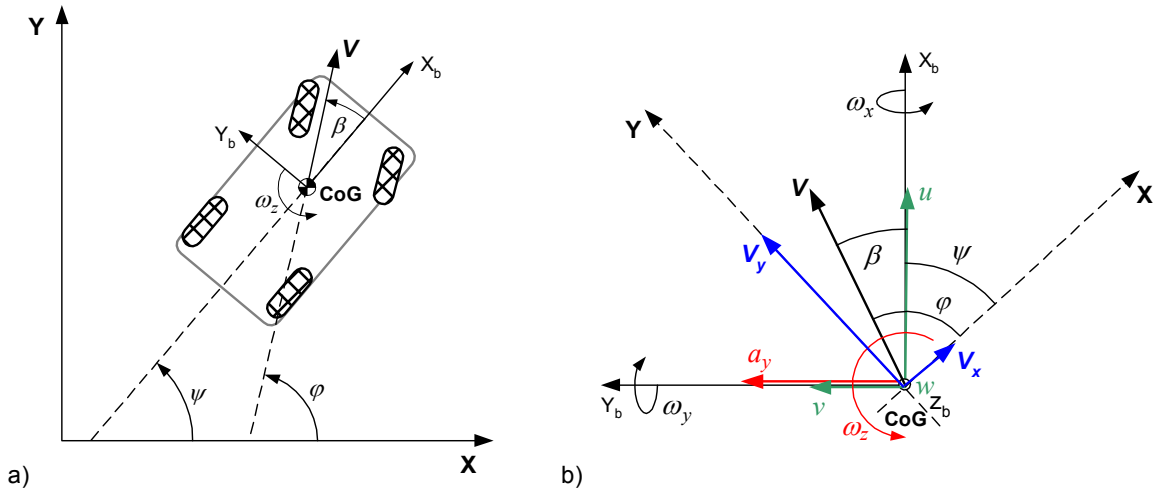

Fig. 5.1 *Definition of vehicle motion kinematic model coordinate frames (a) and kinematic state variables (b) with application to development of the GPS/INS fusion-based sideslip angle estimator.*

The vehicle sideslip angle β can be defined within the inertial coordinate frame (Fig. 5.1a), as a difference between the vehicle course and heading angles, Eq. (5-1), or alternatively it can be derived according to Eq. (5-2) from the vehicle velocity components defined within the vehicle body-fixed coordinate frame (Fig. 5.1b):

$$\beta = \varphi - \psi \tag{5-1}$$

$$\beta = \text{atan}(\frac{v}{u}) = \text{asin}(\frac{v}{V}) \tag{5-2}$$

The absolute vehicle velocity V can be expressed by means of corresponding kinematic variables (i.e. the velocity components), in both inertial and vehicle body-fixed frames:

$$V = \sqrt{u^2 + v^2} = \sqrt{V_x^2 + V_y^2} \tag{5-3}$$

$$V = u\cos\beta + v\sin\beta = V_x\cos\varphi + V_y\sin\varphi \tag{5-4}$$

The components of the vehicle velocity V in the inertial coordinate frame V_x and V_y can be derived from the vehicle velocities in the vehicle body-fixed frame (u and v) and vice versa:

$$V_x = u\cos\psi - v\sin\psi \tag{5-5}$$

$$V_y = u\sin\psi + v\cos\psi \tag{5-6}$$

The considered vehicle motion kinematic model and related state variable estimator rely on the measurements of lateral accelerometer $a_{y,m}$ and yaw rate gyro $\omega_{z,m}$, which are placed in the vehicle CoG and represent the inertial sensors typically used within VDC ("Vehicle Dynamics Control") systems. These measurements are described by the following expressions (see [30]):

$$a_{y,m} = \dot{v} + \omega_z u - \omega_x w + g\sin\phi\cos\theta + a_{y,off} + \upsilon_{ay} \tag{5-7}$$

$$a_{x,m} = \dot{u} - \omega_z u + \omega_x w - g\sin\theta + a_{x,off} + \upsilon_{ax} \tag{5-8}$$

$$\omega_{z,m} = \omega_z + \omega_{z,off} + \upsilon_{\omega} \tag{5-9}$$

where $a_{y,off}$ and $\omega_{z,off}$, and $\upsilon_{ax,y}$ and υ_{ω} are accelerometer and gyro offsets and measurement noise, respectively, while ϕ (suspension roll and road bank) and θ (suspension pitch and road grade) are total roll and pitch Euler angles, respectively. For most applications the third right-hand side term in Eq. (5-7) can be neglected, because the vertical velocity component w is small and it may be conveniently modeled as an additional noise component in υ_{ay}. Furthermore, the approximation of trigonometric functions ($\sin\phi \approx \phi$ and $\cos\theta \approx 1$) can be applied for the small-angle assumption. Thus, the following approximate expression of lateral acceleration measurement holds:

$$a_{y,m} \approx \dot{v} + \omega_z u + g\phi + a_{y,off} + \upsilon_a \tag{5-10}$$

The offsets of inertial sensors measurements $a_{y,off}$ and $\omega_{z,off}$ represent a dominant source of errors in estimating the lateral velocity v and the heading angle ψ. Namely, since these

estimates are obtained by direct integration of inertial measurements, they are prone to drift in the presence of sensor offsets.

Apart form the inertial sensors, the GPS receiver**,** typically used for navigational purposes (i.e. vehicle position monitoring), can be utilized to obtain vehicle velocity, heading, and course [16,58]. Namely, the GPS receiver can provide three-dimensional vehicle velocity measurements in the inertial coordinate frame, V_{GPS}^{N} , V_{GPS}^{E} , and V_{GPS}^{up} , whereof the north and east velocity components are of the main interest for the automotive applications. These velocities are given by (see Fig. 5.1b and Eqs. (5-5) and (5-6)):

$$V_{GPS}^{N} \hat{=} V_x + e_n = u\cos\psi - v\sin\psi + e_n \tag{5-11a}$$

$$V_{GPS}^{E} \hat{=} V_y + e_e = u\sin\psi + v\cos\psi + e_e \tag{5-11b}$$

where e_n and e_e are measurement errors of north and east velocity components, respectively. The GPS-based velocity measurement errors change with satellite geometry or PDOP (Position Dilution of Precision) and/or multi-path errors [68,69]. Typical velocity measurement accuracies (1σ confidence range) are 2-5 cm/s for the horizontal velocity components (i.e. north and east) and 4-10 cm/s for the vertical component [16].

Unlike the inertial sensors, the GPS receiver provides unbiased velocity measurements. However, the main drawbacks of the GPS-based measurements are related to occasional loss of signal and a low update rate (typically 1Hz for low cost receivers) that is insufficient for the vehicle dynamics control applications.

The sideslip angle estimators can be derived by utilizing the vehicle kinematic models derived solely from inertial sensors measurement equations, but in that case they should rely also on some kind of vehicle dynamics model (as proposed in [18]) in order to be able to compensate for drift-like estimation errors inherent to kinematic INS-based estimators. Derivation of such kinematic models aimed for the sideslip angle estimation, relying only on the measurements of the inertial sensors (i.e. accelerometers and gyros) is overviewed hereafter.

Based on the basic kinematic equations (5-3) and (5-4) and definitions of the vehicle velocity components (u and v) in the vehicle body coordinate frame (see Fig.5.1) the following expressions can be obtained:

$$\begin{aligned} u &= V\cos\beta \\ v &= V\sin\beta \end{aligned} \tag{5-12}$$

The following equations for the longitudinal and lateral vehicle accelerations are obtained by presuming zero roll and pitch angles and zero road grade and bank angle (i.e. driving on a flat road is assumed so that the unknown gravity acceleration components in the accelerometers measurement can be omitted, cf. Eqs. (5-7) and (5-8)).

$$\begin{aligned} a_x &= \dot{u} - \omega_z v = \dot{V}\cos\beta - V\dot{\beta}\sin\beta - \omega_z V\sin\beta \\ a_y &= \dot{v} + \omega_z u = \dot{V}\sin\beta + V\dot{\beta}\cos\beta + \omega_z V\cos\beta \end{aligned} \tag{5-13}$$

$$a_y = \left[\frac{a_x}{\cos\beta} + V\tan\beta\left(\dot{\beta} + \omega_z\right)\right]\sin\beta + V\dot{\beta}\cos\beta + \omega_z V\cos\beta \tag{5-14}$$

After rearranging, Eq. (5-14) reads:

$$\dot{\beta} + \omega_z = \frac{a_y - a_x\tan\beta}{V\left(\tan\beta\sin\beta + \cos\beta\right)} \tag{5-15}$$

If the small angle approximation applies (i.e. $\sin\beta \approx \beta$, $\tan\beta \approx \beta$, and $\cos\beta \approx 1$) the following expressions are obtained:

$$\dot{\beta} + \omega_z = \frac{a_y - a_x\beta}{V\left(\beta^2 + 1\right)} \tag{5-16}$$

$$\dot{\beta} = \frac{1}{\beta^2 + 1}\left\{\frac{a_y}{V} - \beta\frac{a_x}{V}\right\} - \omega_z \tag{5-17}$$

Finally, after some rearranging of the above equation, the following expression (given in [1]) is obtained:

$$\dot{\beta} = \frac{1}{1+\beta^2}\left\{\frac{a_y}{V} - \omega_z - \beta\frac{a_x}{V} - \beta^2\omega_z\right\} \tag{5-18}$$

Presuming that β << and that a_x is small or moderate, the above equation can be reduced to:

$$\dot{\beta} = \frac{a_y}{V} - \omega_z \tag{5-19}$$

Alternatively, the same approximate expression (i.e. Eq. (5-19)) can be derived starting from:

$$a_y = \dot{v} + \omega_z u \tag{5-20}$$

$$\beta = \operatorname{atan}\frac{v}{u} \approx \frac{v}{u} \tag{5-21}$$

Presuming small or moderate longitudinal acceleration a_x (i.e. small and moderate $\dot{u}$ typical for cornering maneuvers), Eq. (5-22a), obtained by differentiating Eq. (5-21), can be approximated according to expression (5-22b):

$$\dot{v} = \dot{\beta} u + \beta \dot{u} \tag{5-22a}$$

$$\dot{v} \approx \dot{\beta} u \tag{5-22b}$$

For most driving conditions the longitudinal velocity u is much larger than the lateral velocity v, so that the expression $u \approx V$ holds, and, therefore, the sideslip rate can be obtained as:

$$\dot{\beta} = \frac{a_y}{u} - \omega_z \tag{5-23}$$

Consequently the lateral acceleration reads:

$$a_y = (\dot{\beta} + \omega_z) u \tag{5-24}$$

In the case of the vehicle spinout the second right hand side term in Eq. (5-22a) can no longer be neglected and consequently Eq. (5-22b) does not hold. The expression for the lateral acceleration can be obtained by inserting Eq. (5-22a) into Eq. (5-24) and it reads:

$$a_y = (\dot{\beta} + \omega_z) u + \beta \dot{u} \tag{5-25}$$

After rearranging the equation for the sideslip rate can be obtained [10]:

$$\dot{\beta} = \frac{a_y}{u} - \frac{\beta \dot{u}}{u} - \omega_z \tag{5-26}$$

The basic sideslip angle kinematic estimator utilizing solely the inertial sensors and state space representation (5-28) of the vehicle kinematic model is originally proposed in [12].

$$\begin{aligned} \dot{u} &= v\omega_z + a_x \\ \dot{v} &= -u\omega_z + a_y \end{aligned} \tag{5-27}$$

$$\begin{aligned} \dot{\mathbf{x}} &= \mathbf{A}\mathbf{x} + \mathbf{B}\mathbf{u} \\ y &= \mathbf{C}\mathbf{x} \end{aligned} \tag{5-28}$$

The state-space model vectors/matrices are defined as $\mathbf{x} = \begin{bmatrix} u & v \end{bmatrix}^T$, $\mathbf{u} = \begin{bmatrix} a_x & a_y \end{bmatrix}^T$, $\mathbf{A} = \begin{bmatrix} 0 & \omega_z \\ -\omega_z & 0 \end{bmatrix}$, $\mathbf{B} = \begin{bmatrix} 1 & 0 \\ 0 & 1 \end{bmatrix}$, and $\mathbf{C} = \begin{bmatrix} 1 & 0 \end{bmatrix}$ whereat u, a_x, a_y, and ω_z represent the available measurements of the vehicle dynamics variables. This model becomes unobservable in the circumstances of the straight line driving (i.e. for $\omega_z \approx 0$). For that reason the original estimator equation. (5-29) is in [70,71] extended with the physical model of the vehicle lateral dynamics given in Eq. (5-30).

$$\begin{bmatrix} \dot{\hat{u}} \\ \dot{\hat{v}} \end{bmatrix} = \begin{bmatrix} 0 & \omega_z \\ -\omega_z & 0 \end{bmatrix} \begin{bmatrix} \hat{u} \\ \hat{v} \end{bmatrix} + \begin{bmatrix} a_x \\ a_y \end{bmatrix} + \begin{bmatrix} k_1 \\ k_2 \end{bmatrix} (\hat{u} - u) \tag{5-29}$$

$$\dot{\hat{v}} = -u\omega_z + \hat{a}_y, \quad \hat{u} \hat{=} u$$
$$\hat{a}_y = \frac{1}{m}\left[2C_f\left(\tan^{-1}\left(\frac{\hat{v}+l_f\omega_z}{u}\right)-\delta\right)+2C_r\tan^{-1}\left(\frac{\hat{v}-l_r\omega_z}{u}\right)\right] \tag{5-30}$$

Combining the two above defined kinematic estimators provides the more robust estimator. However, it still has the problem with accumulation of drift-like error due to integration of the inertial sensor measurement offset.

5.3 Basic estimation concept

The basic concept of the proposed EKF-based sideslip angle estimator [54] utilizes the sensor fusion concept by combining the high rate, biased inertial sensors measurements with the low rate, unbiased GPS velocity measurements. The considered vehicle motion kinematic model and the related estimator rely on the measurements of lateral accelerometer and yaw rate gyro ($a_{y,m}$ and $\omega_{z,m}$):

$$a_{y,m} = \dot{v} + \omega_z u + a_{y,off} + \upsilon_a \tag{5-31}$$

$$\dot{\psi} = \omega_{z,m} = \omega_z + \omega_{z,off} + \upsilon_\omega \tag{5-32}$$

where $a_{y,off}$ and $\omega_{z,off}$, and υ_a and υ_ω are accelerometer and gyro offsets and measurement noise, respectively. The approximate equation (5-31) is derived from the exact model given in Eq. (5-7), by neglecting the small vertical velocity-related term $\omega_x w$ and the gravity acceleration-related component $g\sin\phi\cos\theta$ whose impact on the estimator performance will be analyzed later in Subsection 5.3.2. The kinematic model of GPS-based north and east vehicle velocity measurements V_{GPS}^N and V_{GPS}^E is defined as:

$$\begin{aligned} V_{GPS}^N &= V_x + e_n = u\cos\psi - v\sin\psi + e_n \\ V_{GPS}^E &= V_y + e_e = u\sin\psi + v\cos\psi + e_e \end{aligned} \tag{5-33}$$

where e_n and e_e are the measurement errors of north and east velocity components, respectively.

The model equations (5-31)-(5-33) can be extended with random walk processes for the unknown inertial sensor offset variables $a_{y,off}$ and $\omega_{z,off}$, and rewritten into the following time-variant continuous-time state-space process model form:

$$\begin{bmatrix} \dot{v} \\ \dot{\psi} \\ \dot{a}_{y,off} \\ \dot{\omega}_{z,off} \end{bmatrix} = \begin{bmatrix} 0 & 0 & -1 & \hat{u} \\ 0 & 0 & 0 & -1 \\ 0 & 0 & 0 & 0 \\ 0 & 0 & 0 & 0 \end{bmatrix} \begin{bmatrix} v \\ \psi \\ a_{y,off} \\ \omega_{z,off} \end{bmatrix} + \begin{bmatrix} 1 & -\hat{u} \\ 0 & 1 \\ 0 & 0 \\ 0 & 0 \end{bmatrix} \begin{bmatrix} a_{y,m} \\ \omega_{z,m} \end{bmatrix} + \mathbf{I} \cdot \begin{bmatrix} \upsilon_v \\ \upsilon_\omega \\ \upsilon_{yoff} \\ \upsilon_{\omega off} \end{bmatrix} \tag{5-34a}$$

$$\dot{\mathbf{x}} = \mathbf{A} \cdot \mathbf{x} + \mathbf{B} \cdot \mathbf{u} + \mathbf{W} \cdot \boldsymbol{\upsilon}$$

$$\begin{bmatrix} V_{GPS}^E \\ V_{GPS}^N \end{bmatrix} = \begin{bmatrix} \hat{u}\sin\psi + v\cos\psi \\ \hat{u}\cos\psi - v\sin\psi \end{bmatrix} + \begin{bmatrix} e_e \\ e_n \end{bmatrix} \tag{5-34b}$$

$$\mathbf{y} = \mathbf{c(x)} + \mathbf{e}$$

where the lateral accelerometer and yaw gyro measurements $a_{y,m}$ and $\omega_{z,m}$ are inputs, while the vehicle lateral velocity v, the yaw angle ψ, and the accelerometer and gyro offsets $a_{y,off}$ and $\omega_{z,off}$ are process state variables. The vehicle longitudinal velocity pre-estimate $\hat{u}$ is derived from the non-driven (rear)[2] wheel speed measurements by utilizing the following equation (see Chapter 4):

$$\hat{u} = \frac{r_n}{2}(\omega_{rl} + \omega_{rr}), \tag{5-35}$$

and this pre-estimate is treated as a slowly varying parameter of the state-space process model given in Eq. (5-34). Therefore, the state-space model (5-34a) has a linear, time-variant form. On the other hand, the output equation (5-34b) is nonlinear.

The linearized discrete-time process model needed for the EKF design can be obtained from the continuous-time model (5-34) by applying the Z-transform based upon the Zero-Order-Hold (ZOH) method and linearizing the nonlinear output equation (5-30b) around the operating point (v_0, ψ_0) [54]:

$$\mathbf{x}(k) = \mathbf{F}(k-1)\mathbf{x}(k-1) + \mathbf{G}(k-1)\mathbf{u}(k-1) + \boldsymbol{\Omega}(k-1)\boldsymbol{\upsilon}(k-1) \tag{5-36a}$$

$$\mathbf{y}(k) = \mathbf{H}(k)\mathbf{x}(k) + \mathbf{e}(k) \tag{5-36b}$$

where $\mathbf{x}(k) = [v \;\; \psi \;\; a_{y,off} \;\; \omega_{z,off}]^T$, $\mathbf{u}(k) = [a_{y,m} \;\; \omega_{z,m}]^T$, and $\mathbf{y}(k) = [V_{GPS}^E \;\; V_{GPS}^N]^T$, and the matrices of the discrete-time process read:

[2] For the FWD vehicles the front wheel speeds measurements should be used and the effect of the steering wheel angle should be accounted for.

$$\mathbf{F}(k)=\begin{bmatrix}1 & 0 & -T_s & \hat{u}(k)T_s\\ 0 & 1 & 0 & -T_s\\ 0 & 0 & 1 & 0\\ 0 & 0 & 0 & 1\end{bmatrix},\qquad \mathbf{G}(k)=\begin{bmatrix}T_s & -\hat{u}(k)T_s\\ 0 & T_s\\ 0 & 0\\ 0 & 0\end{bmatrix},\qquad \mathbf{\Omega}(k)=\mathbf{I}_{4x4}\,T_s$$

$$\mathbf{H}(k)=\frac{\partial\mathbf{c}(\mathbf{x})}{\partial\mathbf{x}}=\begin{bmatrix}\cos\psi_0(k) & \hat{u}(k)\cos\psi_0(k)-v_0(k)\sin\psi_0(k) & 0 & 0\\ -\sin\psi_0(k) & -\hat{u}(k)\sin\psi_0(k)-v_0(k)\cos\psi_0(k) & 0 & 0\end{bmatrix} \tag{5-37}$$

The parameter T_s denotes the sampling time of the inertial sensors measurement signals. It should be noted that the GPS-based vehicle velocity measurements are sampled at much higher sampling basis $T_g = nT_s$ (e.g. T_s = 20 ms, and T_g = 1000 ms).

The Extended Kalman Filter (EKF) equations for a general case of the nonlinear process and measurement model, given in Chapter 3, applied to this particular process model read:

$$\hat{\mathbf{x}}(k\mid k-1)=\mathbf{F}(k-1)\hat{\mathbf{x}}(k-1\mid k-1)+\mathbf{G}(k-1)\mathbf{u}(k-1) \tag{5-38a}$$

$$\mathbf{P}(k\mid k-1)=\mathbf{F}(k-1)\mathbf{P}(k-1\mid k-1)\mathbf{F}^T(k-1)+\mathbf{\Omega}\,\mathbf{Q}(k-1)\mathbf{\Omega}^T \tag{5-38b}$$

$$\tilde{\mathbf{y}}(k\mid k-1)=\mathbf{y}(k)-\mathbf{h}(\hat{\mathbf{x}}(k\mid k-1)) \tag{5-38c}$$

$$\mathbf{K}(k)=\frac{\mathbf{P}(k\mid k-1)\mathbf{H}^T(k)}{\mathbf{H}^T(k)\mathbf{P}(k\mid k-1)\mathbf{H}^T(k)+\mathbf{R}(k)} \tag{5-38d}$$

$$\hat{\mathbf{x}}(k\mid k)=\hat{\mathbf{x}}(k\mid k-1)+\mathbf{K}(k)\tilde{\mathbf{y}}(k\mid k-1) \tag{5-38e}$$

$$\mathbf{P}(k\mid k)=\mathbf{P}(k\mid k-1)-\mathbf{K}(k)\mathbf{H}(k)\mathbf{P}(k\mid k-1) \tag{5-38f}$$

where the output matrix $\mathbf{H}(k)$ is derived from Eq. (5-37) by using the current operating point ($v_0(k)$, $\psi_0(k)$), as defined by a-posteriori state estimates calculated in the preceding correction phase of the Kalman filter algorithm:

$$\psi_0(k)=\hat{\psi}(k-1\mid k-1),\ v_0(k)=\hat{v}(k-1\mid k-1).$$

Assuming that the stochastic state perturbations ($\upsilon_v, \upsilon_\psi, \upsilon_{yoff}$, and $\upsilon_{\omega off}$) and the measurement errors (e_E and e_N) are mutually independent, the state covariance matrix **Q** and the measurement noise covariance matrix **R** are defined as:

$$\mathbf{Q}=diag\left(\begin{bmatrix}q_v & q_\psi & q_{aoff} & q_{\omega off}\end{bmatrix}\right),\quad \mathbf{R}=diag\left(\begin{bmatrix}r_{gps}^e & r_{gps}^n\end{bmatrix}\right) \tag{5-39}$$

where the components of matrix **Q** corresponds to the variance of the state perturbations and the components of matrix **R** correspond to the variance of the measurement noise.

In general, the Kalman filter algorithm constitutes of two distinct phases that are usually performed at each time step: prediction and correction (see Chapter 3). However, in this particular case, the inertial sensors measurements $a_{y,m}$ and $\omega_{z,m}$ are sampled with the sampling rate T_s = 20 ms, while the GPS-based vehicle velocity measurements are sampled at a lower rate $T_g = nT_s$ = 1 s (i.e. the GPS measurement update is performed every n = 50 samples of the faster inertial sensors measurements). Since the process model outlined in Eq. (5-34) can be classified as a multi-rate system, the Kalman filter-based state estimation methodology for multi-rate and multi-resolution systems (described in more detail in [61,62]) is utilized. More precisely, in the case when the GPS measurements are not available the estimator performs the time-update according to Eqs. (5-38d)-(5-38f) where the output matrix $\mathbf{H}(k)$ equals zero, and consequently the Kalman gain matrix $\mathbf{K}(k)$ equals zero, as well. The estimator is executed in the open-loop manner based only on inertial sensor measurements. Namely, the correction of the a-priori estimates is excluded due to the fact that the needed recent GPS measurements are unavailable. Nevertheless, **F** and **G** matrices are continuously updated in order to keep the track of the current operating point of the process model.

On the other hand, when the GPS measurements V_{GPS}^{N} and V_{GPS}^{E} are available (at the step nk, where for a given sample rates of the inertial and GPS sensors n = 50, k = 1, 2, ...), the output matrix $\mathbf{H}(k)$ is updated with respect to changes of the operating point $\left(\hat{u}, v_0, \psi_0\right)$. Based on the updated matrix $\mathbf{H}(k)$, the estimator gain matrix $\mathbf{K}(k)$ and the measurement update are calculated, and the estimated state variables are corrected in the closed-loop manner.

5.3.1 Observability analysis

In order to examine the feasibility of the proposed EKF-based estimator concept, the observability analysis has been first conducted for the utilized discrete-time process model given by Eq. (5-36).

In general, for a linear time-varying discrete-time system state-space model

$$\begin{aligned}\mathbf{x}(k) &= \mathbf{F}(k-1)\mathbf{x}(k-1) + \mathbf{G}(k-1)\mathbf{u}(k-1)\\ \mathbf{y}(k) &= \mathbf{H}(k)\mathbf{x}(k)\end{aligned} \tag{5-40}$$

the following observation matrix $\mathbf{O_b}$ is defined:

$$\mathbf{O_b} = \begin{bmatrix}\mathbf{H} & \mathbf{HF} & \cdots & \mathbf{HF}^{n-1}\end{bmatrix}^T \tag{5-41}$$

where n is the system order. The system (5-40) is observable if the observation matrix $\mathbf{O_b}$ has the number of independent rows equal to the number of the state variables (i.e. $\text{rank}(\mathbf{O_b}) = n$, [60]).

The particular process state-space model (5-36), used for sideslip angle and inertial sensors offsets estimator design, has four states (n = 4), two inputs (p = 2), and two outputs (l = 2). This is a time-variant linearized MIMO system whose system matrices **F**, **G,** and **H** defined by Eq. (5-36) are functions of inertial sensors sample rate T_s, pre-estimated longitudinal velocity input $\hat{u}$, and system operating point defined by vehicle lateral velocity v_0 and yaw angle ψ_0 (v and ψ are state variables). The observability matrix $\mathbf{O_b}$ is found to be given by:

$$\mathbf{O_b}(T_s,\hat{u},v_0,\psi_0)=\begin{bmatrix} \cos\psi_0 & \hat{u}\cos\psi_0 - v_0\sin\psi_0 & 0 & 0 \\ -\sin\psi_0 & -\hat{u}\sin\psi_0 - v_0\cos\psi_0 & 0 & 0 \\ \cos\psi_0 & \hat{u}\cos\psi_0 - v_0\sin\psi_0 & -T_s\cos\psi_0 & v_0 T_s\sin\psi_0 \\ -\sin\psi_0 & -\hat{u}\sin\psi_0 - v_0\cos\psi_0 & T_s\sin\psi_0 & v_0 T_s\cos\psi_0 \\ \cos\psi_0 & \hat{u}\cos\psi_0 - v_0\sin\psi_0 & -2T_s\cos\psi_0 & 2v_0 T_s\sin\psi_0 \\ -\sin\psi_0 & -\hat{u}\sin\psi_0 - v_0\cos\psi_0 & 2T_s\sin\psi_0 & 2v_0 T_s\cos\psi_0 \\ \cos\psi_0 & \hat{u}\cos\psi_0 - v_0\sin\psi_0 & -3T_s\cos\psi_0 & 3v_0 T_s\sin\psi_0 \\ -\sin\psi_0 & -\hat{u}\sin\psi_0 - v_0\cos\psi_0 & 3T_s\sin\psi_0 & 3v_0 T_s\cos\psi_0 \end{bmatrix}.$$

The rank of this matrix has been computed by applying the singular value decomposition (SVD) algorithm within the Matlab Symbolic toolbox™. For the nominal case, and when the trivial solutions (e.g. zero velocity $\hat{u}$ and zero operating point $\langle v_0, \psi_0 \rangle$) are excluded, the algorithm computed observation matrix rank (rank($\mathbf{O_b}$) = 4 = n), what indicates that the considered system is observable. A numerical analysis has also been carried out in order to identify the conditions, related to the trivial solution, in which the system observability is compromised. This analysis showed that the system becomes unobservable for zero lateral velocity (v_0 = 0, i.e. straight line driving, for which the sideslip angle is also zero). On the other hand, zero values of the trigonometric functions (obtained for $\psi_0 = k\cdot\pi/2$, where k = 0,1,2…) do not affect the observability. Thus, for the zero vehicle heading (ψ_0 = 0) the observation matrix rank is still 4 (i.e. the vehicle model remains observable).

5.3.2 Simulation environment

Performance of the proposed EKF-based estimator is analyzed by means of computer simulation. For that purpose, the simulation environment outlined in Fig. 5.2 is applied. The

vehicle dynamics variables needed for testing the estimator are generated "off-line" from the 10DOF vehicle dynamics model [23]. This model provides selection of a desired driving maneuver (e.g. step-steer, double lane change, j-turn, etc.) and setting of specific maneuver-related parameters (e.g. initial vehicle speed u_0, steering wheel angle φ, etc.). The signals of vehicle lateral acceleration a_y and the yaw rate ω_z, derived from the 10DOF model, along with a preset sensor parameters (i.e. offsets $a_{y,off}$ and $\omega_{z,off}$ and measurement noise variances υ_a and υ_ω), are used for generating the inertial sensors measurements signals $a_{y,m}$ and $\omega_{z,m}$ (EKF inputs). Within the Kalman filter, the vehicle lateral velocity v, the heading/yaw angle ψ, the accelerometer offset $a_{y,off}$, and the gyro offset $\omega_{z,off}$ are defined as state variables (see Eq. (5-36)). The GPS-based vehicle velocity measurements V_{GPS}^{E} and V_{GPS}^{N} are calculated from Eq. (5-33) by utilizing the vehicle longitudinal velocity u, lateral velocity v, and yaw angle ψ signals obtained from the reference 10DOF model. For this initial testing phase the error components e_i in Eq. (5-33) are neglected. The vehicle longitudinal velocity u, comprised in the proposed state-space discrete-time process model equation (5-36) and used for design of the EKF estimator, should be estimated from the ABS wheel speed measurements $\boldsymbol{\omega}_\mathbf{w} = [\omega_{fl}, \omega_{fr}, \omega_{rl}, \omega_{rr}]^T$ (see Eq. (5-35) and [49]). However, for the initial verification of the estimator performance, the reference longitudinal velocity signal u obtained directly from 10DOF model has been used.

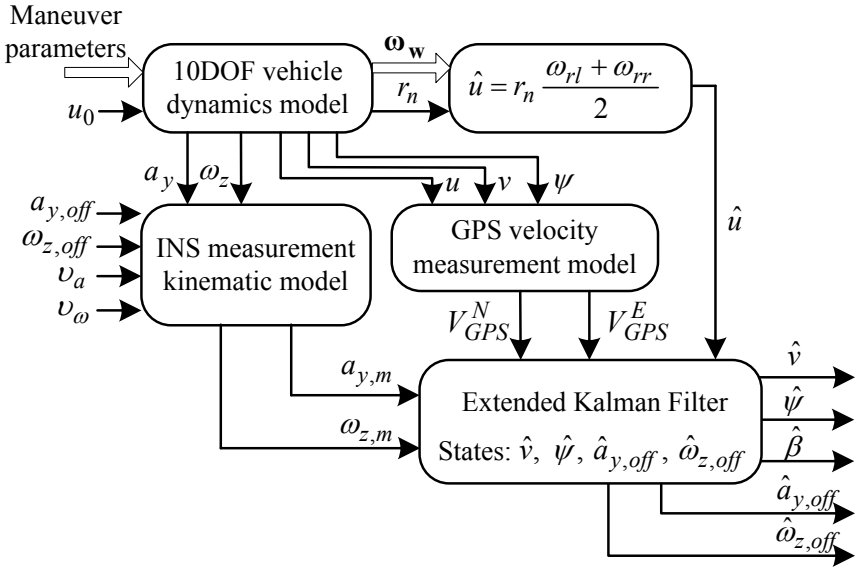

Fig. 5.2 *Illustration of the EKF-based sideslip angle estimator simulation environment.*

For testing the estimator, two distinct driving maneuvers are used: **step-steer** maneuver (as illustrated in Fig. 5.3) representing the conditions of "regular" dynamics after the step steer change, and **double lane change** maneuver including emphasized oversteer instability dynamics (see Fig. 5.4). The step-steer driving maneuver is characterized by the initial vehicle velocity u_0 = 20 m/s, and quasi steady-state lateral acceleration and yaw rate of $a_y \approx 5$ m/s^2 and $\omega_z \approx 0.38$ rad/s, respectively (see Fig. 5.3a). Even larger amplitudes of these variables (towards the stability margin) are obtained for double lane change maneuver with the same initial velocity u_0, as shown in Fig. 5.4a. Figures 5.3b and 5.4b show the absolute vehicle velocity signals measured by GPS receiver, sampled with sample rate of T_g = 1 s, and used as the estimator inputs.

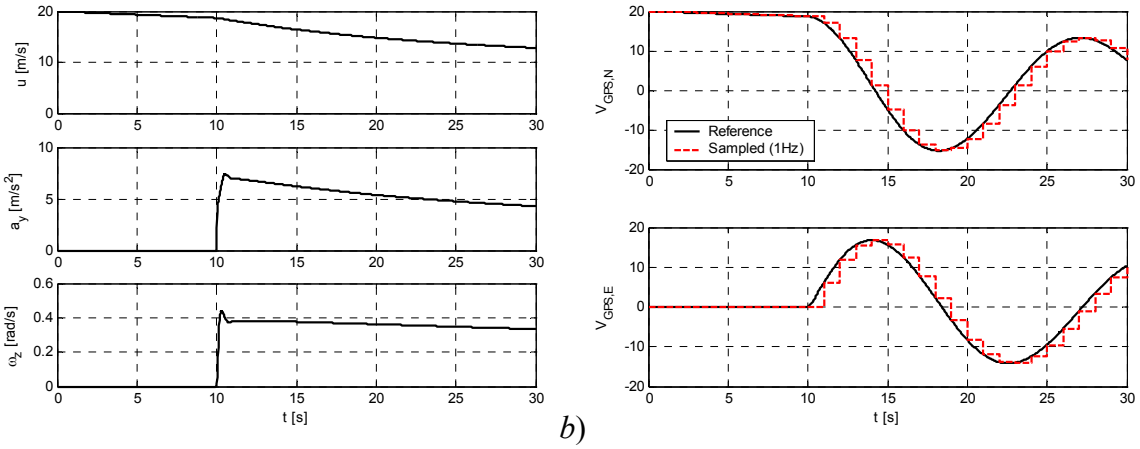

a) *b*)

Fig. 5.3 *Step-steer driving maneuver (u_{init} = 20 m/s, δ_s = 90°): vehicle dynamics variables derived from the 10DOF model (a) and calculated GPS velocity measurements signals (b).*

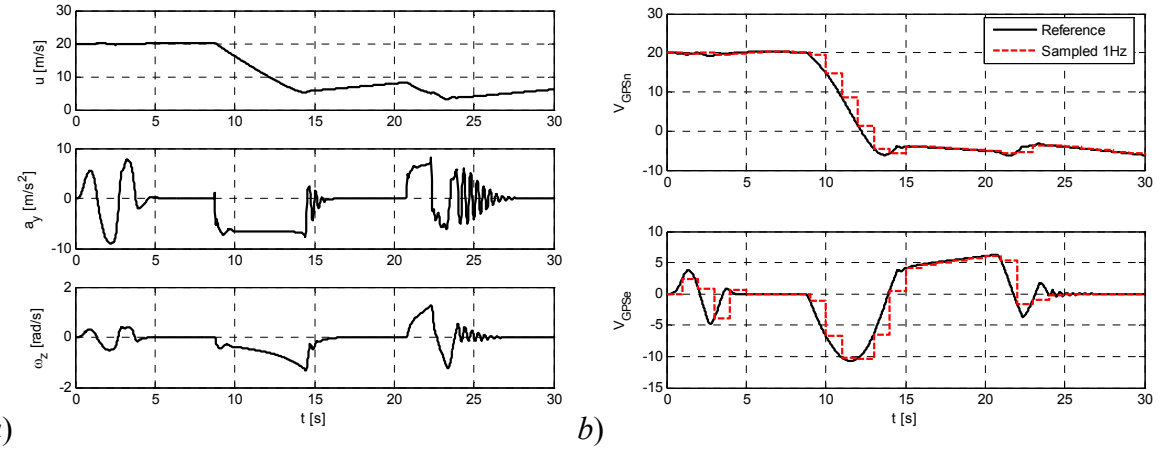

a) *b*)

Fig. 5.4 *Double lane change driving maneuver (u_{init} = 20 m/s): vehicle dynamics variables derived from the 10DOF model (a) and calculated GPS velocity measurements signals (b).*

The simulation results regarding the estimation error analysis presented in the Section 5.4 are obtained for the sample rate of inertial sensors measurements T_s = 20 ms and the sample rate of GPS-based velocity measurements T_g = 1s. The sensor offsets are set to the constant values $a_{y,off}$ = 0.05 m/s^2 and $\omega_{z,off}$ = 0.006 rad/s, if not stated otherwise.

Initially, the estimator has been tuned and its performance has been analyzed by using the "idealized" basic planar vehicle model, instead of the 10DOF model, for generating the EKF input variables:

$$\begin{aligned} \dot{v} &= a_y - \omega_z u \\ \dot{\psi} &= \omega_z \end{aligned} \tag{5-42}$$

thus neglecting the impact of roll and pitch dynamics. Since the basic process model (5-42) corresponds to the model used in the estimator design, the goal of the initial tests is to verify the design itself. The related simulation results for the step-steer and double lane change maneuvers defined above are presented in Fig. 5.5. The state and measurement noise covariance are set to the following values: q_v = 1, q_ψ = 0.3, q_{aoff} = 10^3, $q_{\omega off}$ = 500, $r^n_{gps} = 1$, and $r^e_{gps} = 9.6$ (see Subsection 5.3.1. and Eq. (5-39)).

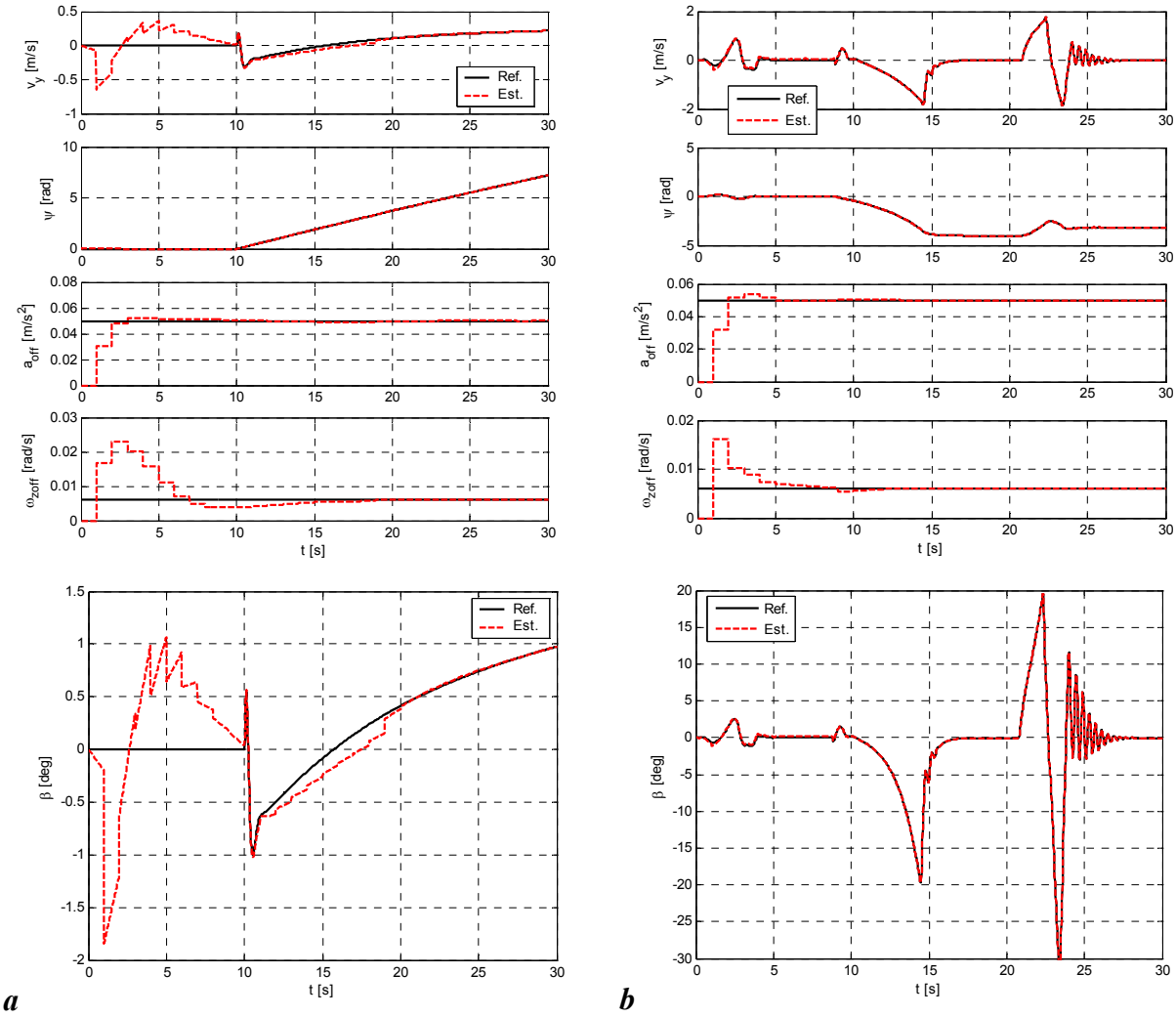

Fig. 5.5 *Estimated state variables and sideslip angle for the "idealized" case of basic process model and step steer maneuver (a) and double lane change maneuver (b)*

The results clearly indicate that the proposed estimator provides accurate offset estimates $a_{y,off}$ and $\omega_{z,off}$ with the response time of approximately 10 s. The initial overshoot is larger in gyro offset estimate than in estimate of the accelerometer offset for both maneuvers. The lateral velocity estimation accuracy is also very good. Exceptionally, relatively large lateral velocity estimation errors appear in the initial time interval of the step-steer maneuver. These errors are related to the low model observability during the zero lateral velocity conditions and still large errors in estimated sensor offsets. Namely, it appears that the lateral velocity estimation becomes less sensitive to the observability issues when the sensor offsets are accurately estimated.

5.4 Estimation errors analysis and compensation

Various sources of estimation errors has been separately identified and analyzed, by evaluating the performance of the proposed, basic (i.e. non-adaptive) fusion-based EKF estimator configuration for the driving maneuvers specified in the former Subsection and the full 10 DoF vehicle model.

5.4.1 Pre-estimated longitudinal velocity related errors

The vehicle longitudinal velocity u is not measured directly, but it is estimated from the non-driven, free-rolling wheels rotational speeds according to Eq. (5-35), presuming the constant tire effective radius r_n (cf. Section 4.2). However, the tire effective radius changes with the wheels normal load (Chapter 4). On the other hand, braking induces large longitudinal slip that largely affects the accuracy of longitudinal velocity estimation (detailed analysis of braking-related sideslip estimation errors is given at the end of this Section). In order to be able to analyze the effect of tire radii variations upon the EKF-based sideslip estimator accuracy, the tire dynamic effective radius model is integrated within the reference 10DOF model [49]. The true effective tire radius can be expressed as:

$$r_e = r_n + \delta_{r,st} + \delta_{r,dyn} \tag{5-43}$$

where r_n is the nominal tire radius, $\delta_{r,st}$ is the static radius error (e.g. due to tire deflation), and $\delta_{r,dyn}$ is the dynamic radius error (e.g. due to accelerating/braking, road grade). These tire radii errors cause an error of the pre-estimated vehicle longitudinal velocity, which is given by:

$$\varepsilon_u = \frac{\hat{u} - u}{u} = -(\delta_{r,st} + \delta_{r,dyn}) \frac{\omega_{rl} + \omega_{rr}}{2} \tag{5-44}$$

The relative and absolute longitudinal velocity pre-estimation errors for a double lane change maneuver are shown in Fig. 5.6. In the presence of both, static and dynamic tire radius errors the arithmetic mean of the vehicle velocity pre-estimation relative error for this maneuver equals 0.3% (blue trace in Fig. 5.6b). However, if the tire radius static error is compensated/set to zero ($\delta_{r,st} = 0$), the velocity estimation error can be significantly reduced (red trace in Fig. 5.6).

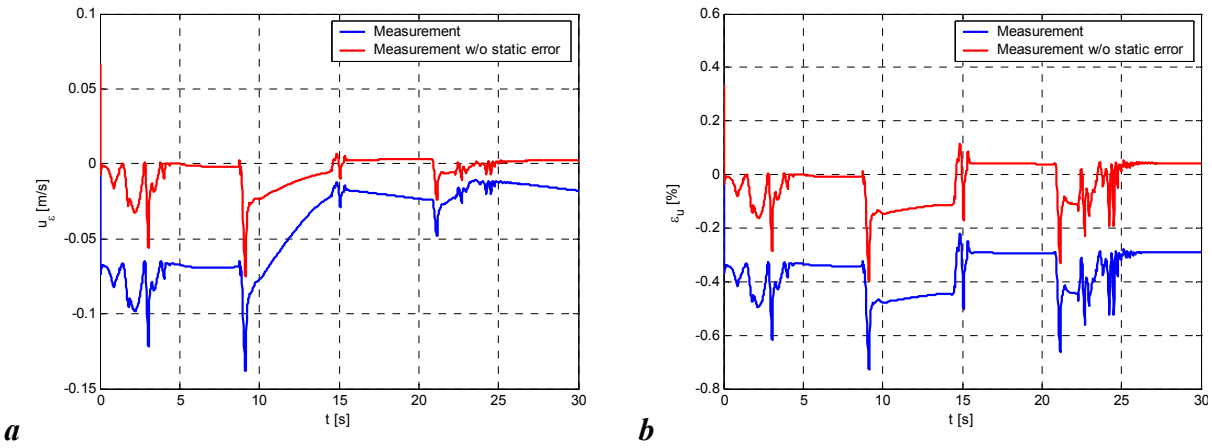

Fig. 5.6 *Longitudinal vehicle velocity estimation errors for double lane change maneuver with emphasized oversteer: absolute errors (a), relative (b).*

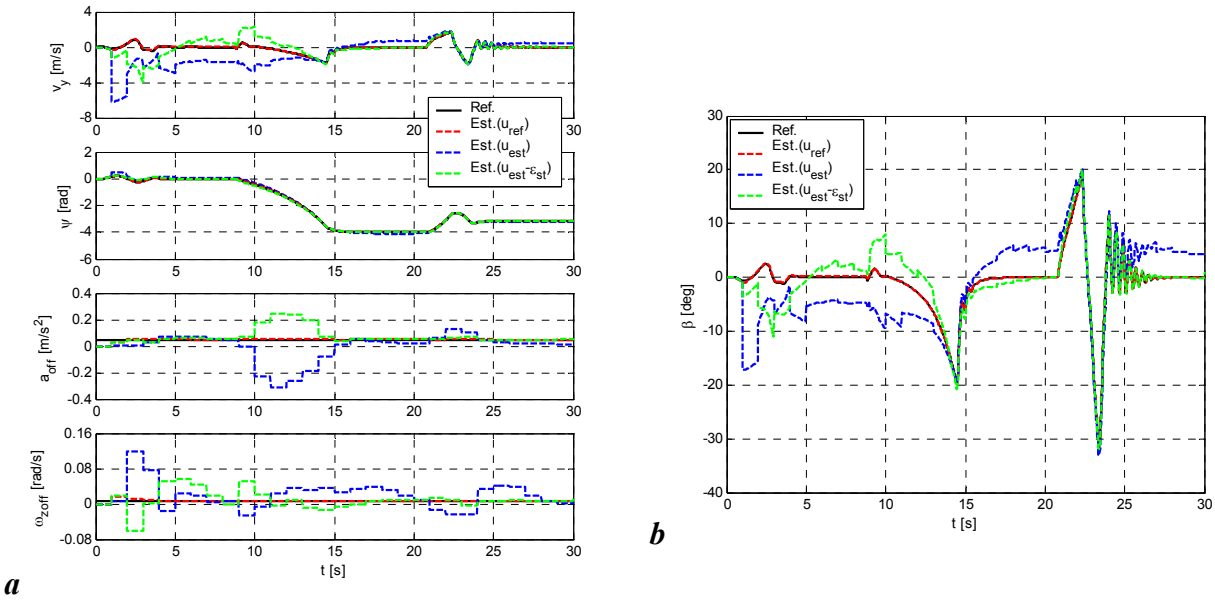

Fig. 5.7 *Impact of the inaccuracy of pre-estimated vehicle longitudinal velocity on the estimator performance with respect to the process state variables (a) and sideslip angle (b) estimation for double lane change maneuver.*

The relatively small vehicle velocity pre-estimation error of only 0.3% can still induce significant lateral velocity/sideslip angle and sensor offsets estimation errors [14]. Thus the vehicle longitudinal velocity should be estimated separately by a dedicated kinematic estimator, in order to enable sufficient accuracy of the velocity pre-estimate signal needed for superimposed sideslip angle estimator. An initial analysis indicated that the vehicle velocity pre-estimation errors were predominantly propagated to the final sideslip angle estimation errors through the process output equation (5-36b) during the measurement update phase.

Therefore, the process output equation, constituting the GPS velocities measurement model illustrated in Fig. 5.8, is subject to a more detailed simulation analysis presented below.

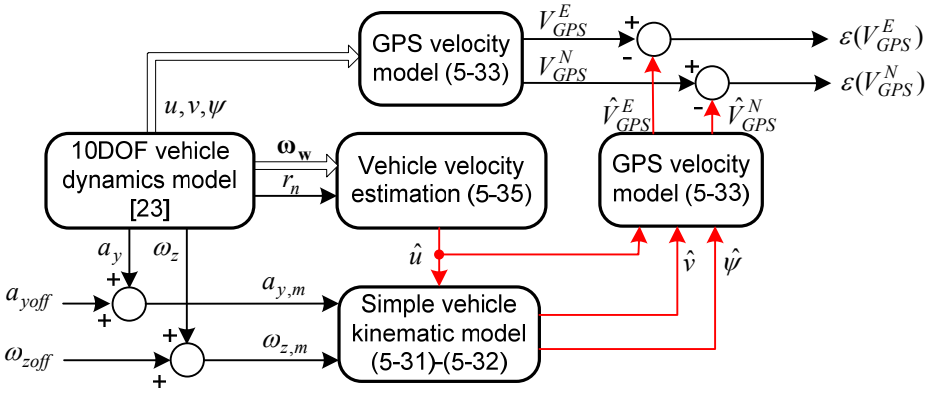

Fig. 5.8 *Block diagram of GPS velocity measurements reference and open-loop estimation error model.*

The reference GPS velocities V^E_{GPS} and V^N_{GPS} are obtained from the GPS velocity measurement model (i.e. Eq. (5-33) whereat the measurement errors e_e and e_n are set to zero), with the vehicle dynamics variables u, v, and ψ obtained directly from the reference 10DOF vehicle dynamics model. On the other hand, the GPS velocities estimates $\hat{V}^E_{GPS}$ and $\hat{V}^N_{GPS}$ are calculated by using the same GPS velocity measurement model, but this time the estimates of the vehicle dynamic variables $\hat{u}$, $\hat{v}$, and $\hat{\psi}$ are used instead. These open-loop estimates have been derived by using the simple vehicle kinematic model defined by Eqs. (5-31),(5-32), and (5-35) and utilized by the EKF estimator. The GPS velocity open-loop estimation errors $\varepsilon\left(V^E_{GPS}\right)$ and $\varepsilon\left(V^N_{GPS}\right)$ represent the outputs of the above model.

Firstly, in order to analyze to which extent the difference between the used vehicle models (i.e. the reference 10DOF model and the simple kinematic one) induces the open-loop GPS velocity estimation errors, the sensor offsets and velocity estimation error are set to zero (i.e. $a_{yoff} = 0$, $\omega_{zoff} = 0$, and $\hat{u} = u$). In this case the GPS velocity estimation errors arise only from the difference between the reference values of the vehicle lateral velocity and heading angle (v and ψ) and the related estimates $\hat{v}$, and $\hat{\psi}$ obtained from the model. These estimation errors are illustrated in Fig. 5.9b by green dashed line. The said errors are emphasized during dynamic conditions and are very small in steady-state intervals. In the considered double lane change maneuver, the GPS velocity estimation errors are in the range of 1-2% of the reference signals given in Fig. 5.9a.

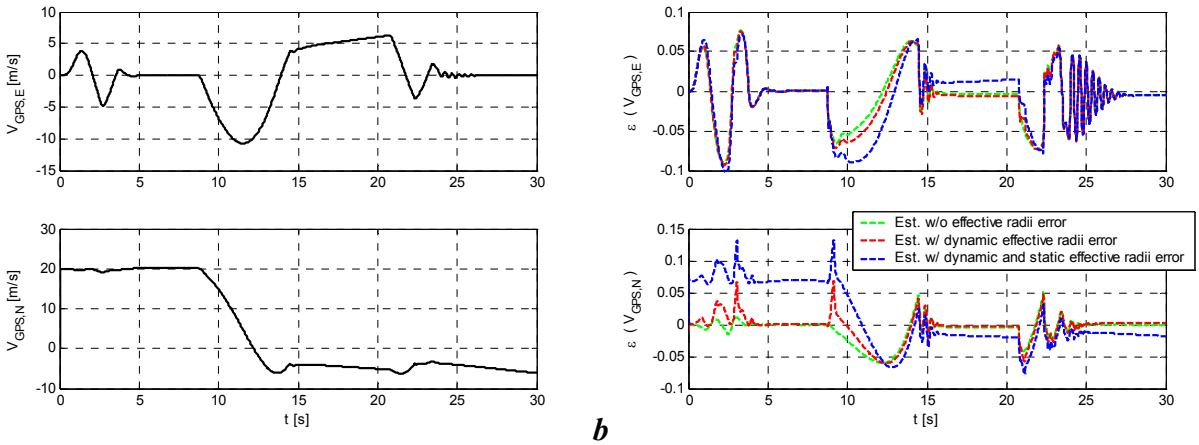

a ***b***

Fig. 5.9 *Impact of the vehicle longitudinal velocity pre-estimation error on open-loop estimation accuracy of the vehicle velocity components in inertial coordinate frame: reference velocities measured by single GPS receiver (a), and GPS velocities absolute estimation errors in relation to effective tire radii errors (b).*

Moreover, the effect of the vehicle velocity pre-estimate errors, related to both static and dynamic tire effective radius errors, on the accuracy of the GPS velocity estimates is also shown in Fig. 5.9b (red and blue dashed lines). It is evident that the vehicle velocity pre-estimate errors due to static tire radii errors have a dominant effect upon the accuracy of the GPS velocity estimation even during steady-state intervals.

In the next step the inertial sensor offsets, as a dominant source of errors, are included in the GPS velocity open-loop estimation error model given in Fig. 5.8. The related GPS velocity estimation errors for the a_{yoff} = - 0.05 m/s^2 and ω_{zoff} = 0.006 rad/s are shown in Fig. 5.10a for the same maneuver from Fig. 5.9a. When compared with the inertial sensor offsets effect, the impact of the vehicle longitudinal velocity pre-estimation errors on the GPS velocities open-loop estimates can be neglected. Furthermore, the open-loop sideslip angle estimates shown in Fig. 5.10b have emphasized drift and quickly accumulate large errors. The impact of the tire effective radii-related longitudinal velocity pre-estimation errors on the open-loop sideslip angle estimation accuracy is minor (i.e. sensor offset effect is much more emphasized).

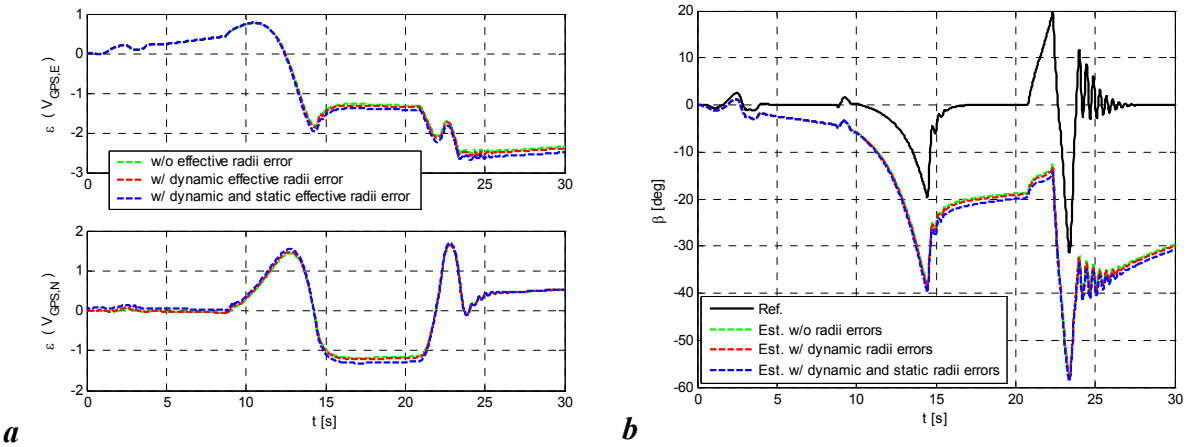

a ***b***

Fig. 5.10 *Open-loop GPS velocities estimation errors (a) and open-loop vehicle sideslip angle estimates (b) (inertial sensor measurement offsets included).*

Finally, the impact of both inertial sensors offsets and longitudinal velocity pre-estimation errors on the performance of the proposed EKF sideslip angle estimator is analyzed (closed-loop estimation). The estimates of the sideslip angle and process state variables for the double lane change maneuver without any a-priori information of the sensor offsets (i.e. initial states of all state variables are set to zero value), are shown in Fig. 5.11.

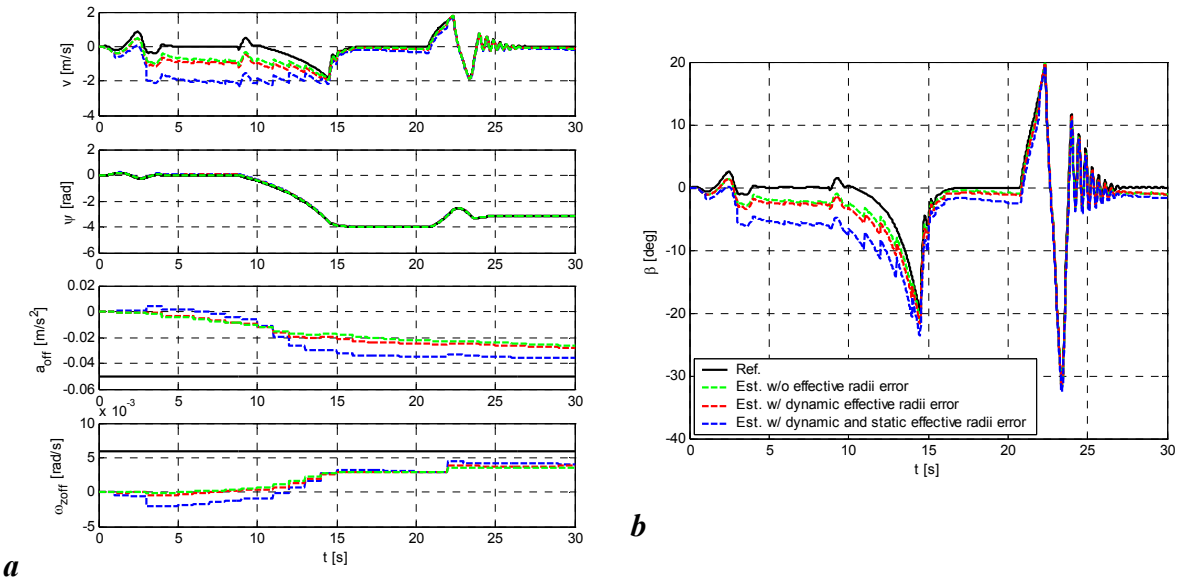

a ***b***

Fig. 5.11 *Illustration of estimation errors due to the tire radii-related longitudinal velocity inaccuracies and inertial sensor offsets: process model state estimates (a) and vehicle sideslip angle estimate (b) (no a-priori knowledge on state variables including offsets).*

5.4.2 GPS velocity measurements related errors

The GPS velocity measurement errors, alike the longitudinal velocity pre-estimation errors, propagate to the sideslip angle estimate through the process model output equation (5-34b)

and they result in an increased a-priori estimation errors $\hat{\tilde{y}}(k \mid k-1)$, defined by Eq. (5-38c). In order to simulate these effects, the GPS velocity errors are modeled as Gaussian random variables with the standard deviation of 5 cm/s (correspond to typical accuracy of low cost receivers [16]). The corresponding sideslip angle estimates for the double lane change and double step steer maneuvers are shown in Fig. 5.12. These results are obtained for the non-adaptive estimator with the slow EKF tuning, zero static tire radii variations-related longitudinal velocity pre-estimation errors, and accurate a-priori information of the inertial sensor offsets. They indicate that the GPS velocity measurement errors can induce sideslip angle estimation errors up to 3 degrees.

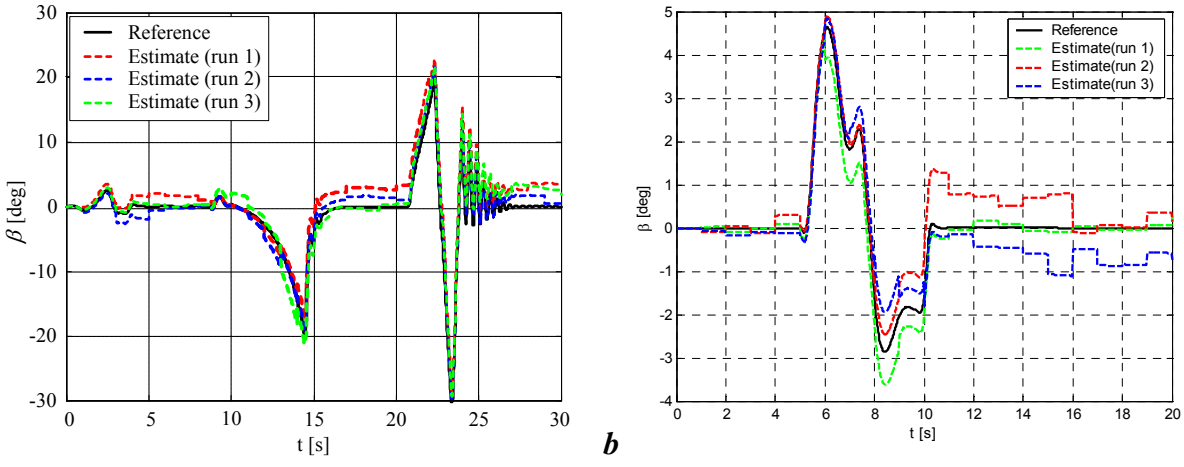

a ***b***

Fig. 5.12 *Impact of GPS velocities random errors on accuracy of sideslip angle estimation for double lane change maneuver (a) and double step steer maneuver (b).*

Another source of the sideslip angle estimation errors is related to GPS velocity measurement latency. Namely, the GPS receivers measure the velocity by internal averaging of the velocity data calculated at a higher rate within the receiver sample time period. This gives a theoretical velocity-measurement latency of a half of the sample time period [61]. Furthermore, the finite time required for processing and transmission of the receiver data may contribute to the total latency [61,62].

In order to emulate this GPS measurement latency, the reference GPS velocity signals obtained from Eq. (5-33) at a higher sample rate of $1/T_s$ = 50Hz are filtered by an moving average filter, thus calculating the arithmetic mean of the reference signal on the 1 Hz basic sample rate. It has been found out that the measurement latency is manifested in a measurement delay of $T_g/2$ = 0.5 s and certain response damping (e.g. the effect of the measurement latency upon the GPS velocity signals for a double lane change maneuver is

illustrated in Fig. 5.13). This latency in the GPS measurement can apparently represent a major source of the sideslip estimation errors, because it causes large velocity measurement dynamic errors.

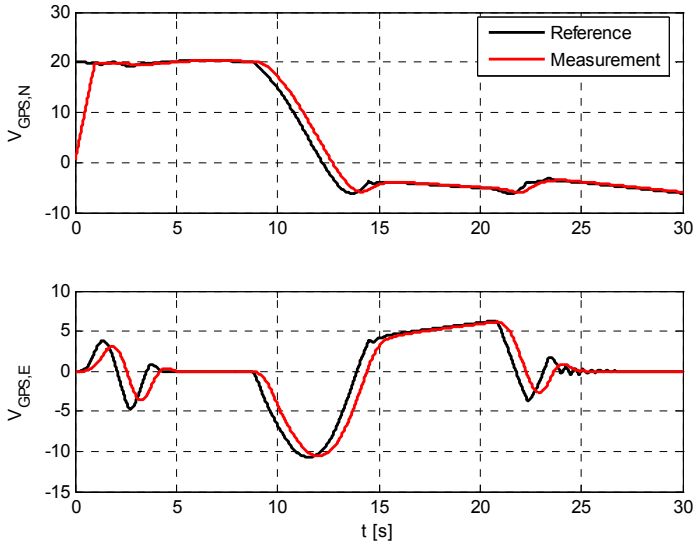

Fig. 5.13 *Effect of the GPS velocity measurement latency for the double lane change maneuver.*

The GPS latency-related estimation errors for the double lane change maneuver are given by the red trace line in Fig. 5.14. As anticipated, the estimation errors are unacceptably high during transient conditions, when the GPS latency errors are emphasized. These large estimation errors of sideslip angle are caused by inaccurate measurement update and related correction relying on faulty a-priori prediction error (5-38c). Namely, the current measurements $\mathbf{y}(k)$ represent, in fact, a filtered and delayed copy of the original measurements and do not match the current a-priori output estimate $\hat{\mathbf{y}}(k \mid k-1)$. Thus, in order to compensate for the GPS latency errors, the a-priori output estimates should be synchronized with the measurements. Presuming that the GPS measurement latency of one half of the sample time is time invariant, the same moving averaging filter as for the GPS velocity measurements, should be applied to the output estimates. Thus, the GPS measurements and output estimates are effectively synchronized and correct a-priori prediction error can be calculated as:

$$\hat{\tilde{y}}(k \mid k-1) = \mathbf{y}(k) - \bar{\hat{\mathbf{y}}}(k \mid k-1) \tag{5-45}$$

were $\bar{\hat{\mathbf{y}}}(k \mid k-1) = \frac{1}{n}\sum_{l=1}^{n} \hat{\mathbf{y}}(k-l \mid k-l-1)$ and $n = T_g / T_s = 50$. The efficiency of such compensation action is illustrated in Fig. 5.14 (green trace line).

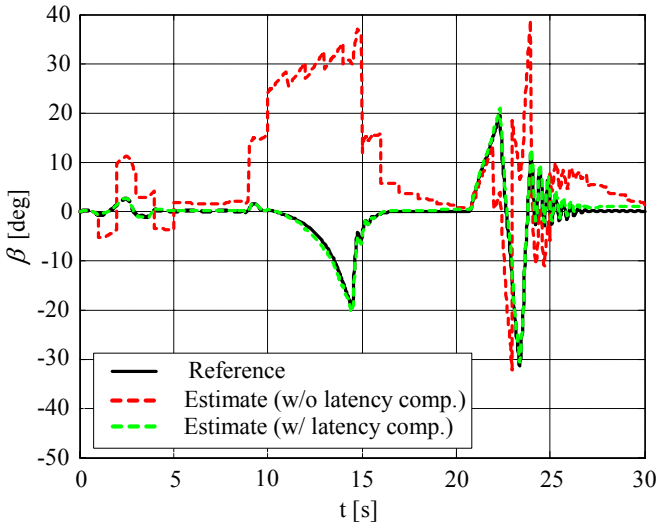

Fig. 5.14 *Impact of GPS velocity measurement latency on sideslip angle estimation without and with latency compensation action applied.*

5.4.3 Errors related to roll and pitch dynamics

In order to determine the impact of unmodeled roll and pitch dynamics on the estimator accuracy, the more realistic 10DOF reference vehicle model [23] is used instead of the simple planar model (5-42) (see Fig. 5.2). The related simulation results for step steer and double lane change driving maneuvers and two sets of state covariance components (i.e. the Kalman filter tuning settings) are shown in Fig. 5.15.

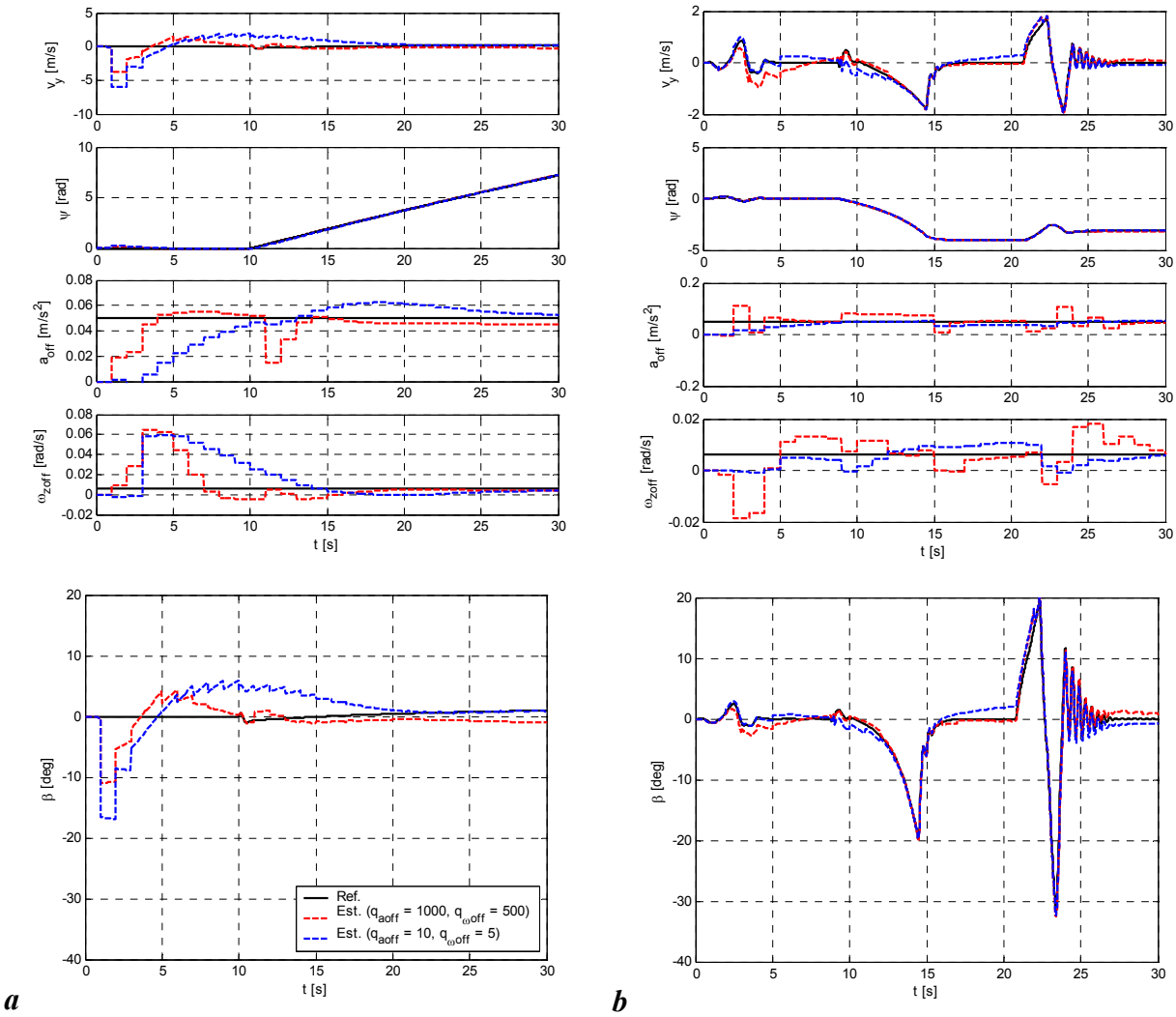

Fig. 5.15 *Impact of unmodeled vehicle roll and pitch dynamics on estimation accuracy of the process state variables and sideslip angle for step steer maneuver (a) and double lane change maneuver (b).*

The vehicle lateral velocity/sideslip angle estimation accuracy is, unlike the vehicle heading estimate, reduced compared with the "idealized" case in Fig. 5.5. This holds especially for the step-steer maneuver (Fig. 5.15a) characterized by very small lateral velocities. From the double lane change maneuver results (Fig. 5.15b) it is evident that the lateral velocity/sideslip angle estimates are more accurate during transient than steady-state conditions. Moreover, when comparing the two maneuvers, it can be noted that the higher estimation accuracy is achieved for larger values of the lateral velocity, because in such cases the ratio of the lateral and longitudinal velocities is conveniently larger. The estimation accuracy of the sensor offsets is also affected by the roll and pitch related disturbances, where the gyro offset estimation is more critical. However, the sensor offsets are typically slowly varying with temperature and aging. Thus, by increasing the offsets estimation equivalent time constants

the impact of roll and pitch disturbance on the offsets estimation accuracy should be substantially decreased. This is done by decreasing the corresponding (offset-related) state covariance matrix coefficients. As shown in Fig. 5.15, by decreasing of the offsets covariance coefficients q_{aoff} and $q_{\omega off}$ the oscillations in estimated offsets signals are reduced, especially for the double lane change maneuver. However, for the double lane change maneuver the gyro offset estimate signal is still oscillatory, thus requiring further decrease of the corresponding covariance parameter $q_{\omega off}$ and corresponding slow-down the offset estimate response.

5.4.4 Braking related errors

Braking is another source of estimation errors, which are caused by inaccuracy of longitudinal velocity pre-estimate $\hat{u}$ due to a large longitudinal slip. The impact of braking on the accuracy of sideslip angle estimation is illustrated in Fig. 5.16 on an example of a braking in turn maneuver with the initial velocity u_0 = 25 m/s, steering wheel angle δ_s = 30°, and braking torque τ_b = 300 Nm per wheel initiated at t = 15 s. The estimator performance is analyzed for the cases of dynamic (red trace) and static (blue trace) tire radii variations. The offsets are taken to be initially known. During a pure cornering over a period (t = 2÷15s in Fig 5.16), the longitudinal velocity pre-estimation error due to dynamic radii variations is less then 0.1%, while for the static radii error the estimation error is approximately 0.4%. However, the errors are significantly increased during braking, which results in significant sideslip angle estimation inaccuracy, as shown by solid lines in Fig. 5.16b.

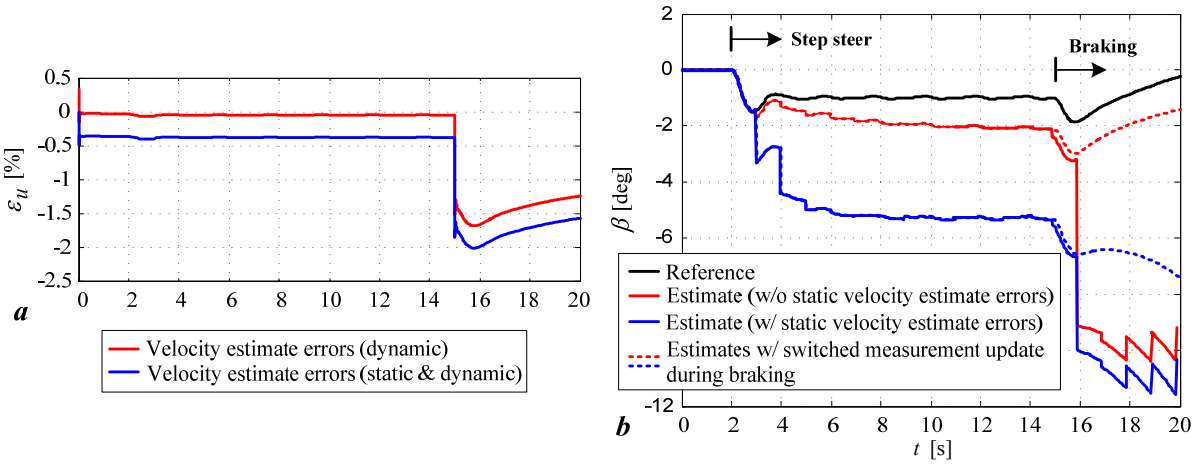

Fig. 5.16 *Braking-related errors of pre-estimated longitudinal velocity (a) and corresponding sideslip angle estimator responses (b).*

Here, the compensation of static tire radii variations-related errors by itself would not provide significant gain under the braking conditions. On the other hand, it is difficult to compensate

for the braking-related estimation errors, because the exact braking force and related tire slip could not be reliably determined due to uncertainties of the brake model and longitudinal tire static curve. Therefore, during the temporary braking intervals, the sideslip angle should be estimated in the open-loop mode using inertial sensors measurements only, without performing the GPS-based measurement correction. More precisely, the open-loop estimation mode can be activated by setting the observation matrix **H** to null matrix (the Kalman gain matrix **K** is also null matrix), upon detection of pressed braking pedal, thus making the measurement correction inactive. The sideslip angle estimates obtained by implementing such an intervention are illustrated by dashed traces in Fig. 5.16b. These results indicate that the open-loop estimation, applied during braking, eliminates the braking-related estimation errors.

5.4.5 Road bank related errors

The road bank angle ϕ also represents a major source of estimation errors, because the effect of the gravity acceleration component $g\sin\phi \approx g\phi$ (see Eq. (5-9)) measured by the lateral accelerometer has not been included in the process model given by Eq. (5-34). Thus, the road bank represents an unmodeled disturbance for the estimation of the sideslip angle β.

The road bank impact has been analyzed for the step-steer maneuver (steering wheel angle δ_s = 50° and initial velocity u_0 = 20m/s) on the banked road with stepwise bank angle changes up to ±15° (see black line trace in Fig. 5.18a). The corresponding sideslip estimate is shown in Figure 5.18b (red dashed line), and it is obtained for accurate vehicle longitudinal velocity pre-estimate and correct a-priori information on inertial sensor offsets. According to these results, the road bank causes unacceptably high sawtooth-like oscillations in the estimated signal. These oscillations are directly induced by a large gravity acceleration component acting as additional sensor offset $a^*_{y,off} = a_{y,off} + g\sin\phi$. Namely, the difference between the estimated accelerometer offset and the actual value $a_{y,off}^*$ causes a drift in the sideslip angle estimate during the open-loop estimation between the two consecutive GPS velocity measurements.

In order to reduce the road bank impact on the estimator accuracy, the gravity component, measured by the lateral accelerometer, should be estimated. Such estimation may rely on the following expression:

$$\hat{a}_{y,grav} = g\hat{\phi} = a_{y,m} - \hat{a}_{y,off} - \hat{\dot{v}} - \left(\omega_{z,m} - \hat{\omega}_{z,off}\right)\hat{u} \tag{5-46}$$

which is obtained from Eq. (5-31) after neglecting the measurement noise component υ_a. However, in order to avoid additional closed loops in sideslip estimator and potential stability issues, the above gravity estimate equation is simplified and only the inputs of the original EKF estimator are used. The sensor offsets are relatively small when compared to the gravity acceleration component even for small bank angles, and also $\dot{v}$ is considered to be small for steady-state driving conditions. In addition, the contribution of dynamic component $\dot{v}$ to the estimated, relatively slow gravity acceleration component can be effectively filtered by applying a low pass filter. These approximations result in the simple road bank-related acceleration term estimator given by the following expression and illustrated in Fig. 5.17, and used for compensation of the related sideslip angle estimation errors:

$$\hat{a}_{y,grav} = G_{LP}(s) \cdot \left(a_{y,m} - \omega_{z,m} \hat{u} \right) \tag{5-47}$$

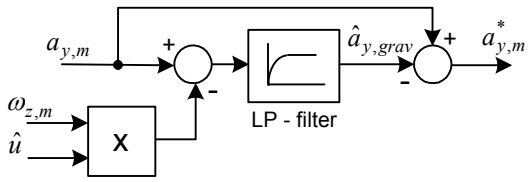

Fig. 5.17 *Elimination of road bank-related gravity acceleration component from accelerometer measurement.*

The results of the estimated road bank angle $\hat{\phi} = \hat{a}_{y,grav} / g$ for the considered step-steer maneuver on a banked road are given in Fig. 5.18a (red dashed line). The observed bank estimation error, of approximately 1 degree is primarily induced as a result of neglecting the $\omega_{z,off} u$ acceleration component.

The gravity acceleration component estimate (5-47) is subtracted from the original accelerometer measurement $a_{y,m}$, as illustrated in Fig. 5.17 and $a^*_{y,m}$ is then used by the sideslip angle estimator instead of the raw measurement. According to the simulation results shown in Fig. 5.18b, this compensation method effectively suppresses the drift-like oscillations in the sideslip estimation signals and confines the estimation error within 1.5 deg for the considered, quite excessive road bank disturbance of 5-15 degrees.

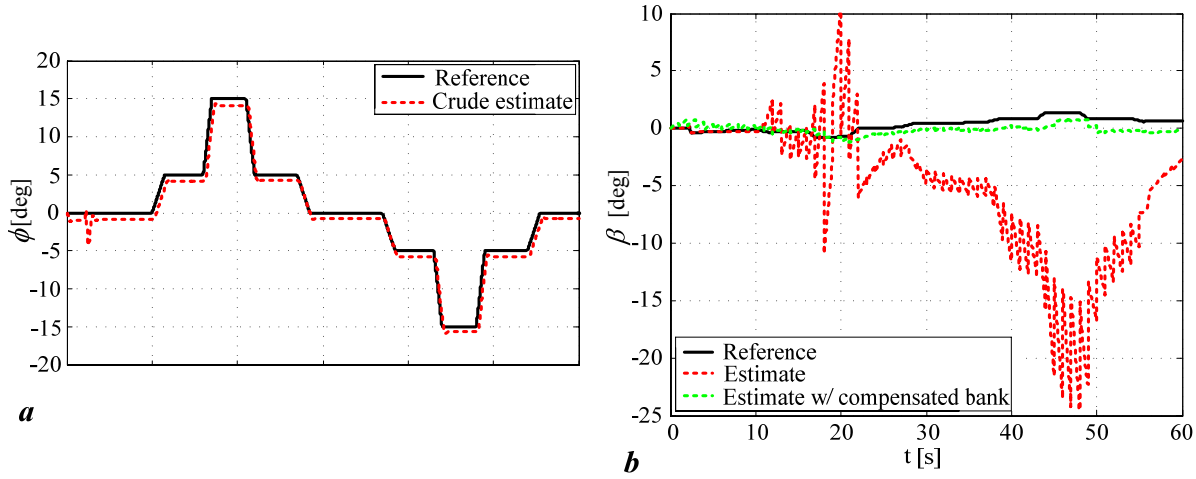

Fig. 5.18 *Illustration of road bank-related sideslip estimation errors and related compensation algorithm: road bank angle estimate (a) and sideslip angle estimate (b).*

Alternatively, the road bank angle may be estimated by using a dedicated estimator by utilizing the measurements of additional sensors (e.g. the roll rate gyro and/or vertical accelerometer) or the vehicle dynamics model and standard set of vehicle dynamics sensors, as documented in [30,48]. In that case the estimated road bank/roll angle could be integrated in the state-space process model in Eq. (5-34) and added as additional input of the EKF-based sideslip estimator in order to account for the superimposed gravity acceleration component.

5.5 Design of the adaptive estimator

The proposed basic EKF estimator design has been extended by implementing an adaptation algorithm in order to provide a good trade-off between fast convergence of inertial sensors offset estimates and a low level of their steady-state perturbations. The adaptation algorithm is implemented through a change of the elements of state covariance matrix Q. During the highly dynamic driving maneuvers the estimator should be made slower in order to decrease perturbations in sensor offsets estimates and suppress the related sideslip estimation errors. On the other hand, the faster tuning is more appropriate for quasi-steady state maneuvers, in order to speed up the convergence of the sensor offsets estimates under the conditions of decreased estimator excitation (see Fig. 5.19). Consequently, the two sets of state covariance parameters are predefined: Q_D for slow EKF tuning and Q_S for fast EKF tuning.

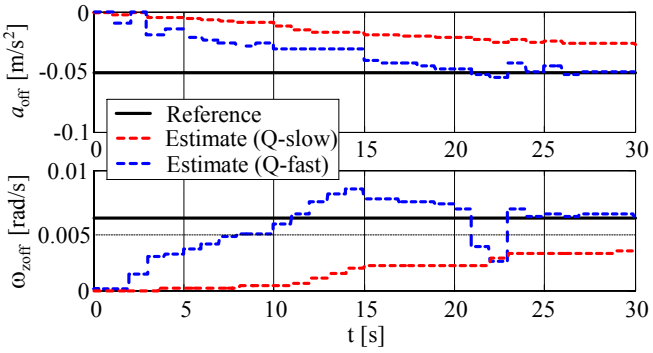

Fig. 5.19 *Illustration of impact of state covariance matrix tuning on sensor offset estimation.*

Fig. 5.20 shows a simple adaptation procedure for selecting the appropriate covariance matrix based on the vehicle dynamics conditions. The required information about the vehicle dynamics conditions are obtained by monitoring the lateral accelerometer measurement $a_{y,m}$ and the estimate of $\dot{v}$. This estimate is derived from the EKF a-priori and a-posteriori estimates of the vehicle lateral velocity, according to:

$$\hat{\dot{v}}(k) = \frac{\hat{v}(k \mid k-1) - \hat{v}(k-1 \mid k-1)}{T_s} \tag{5-48}$$

where T_s is the inertial sensors measurement sampling rate.

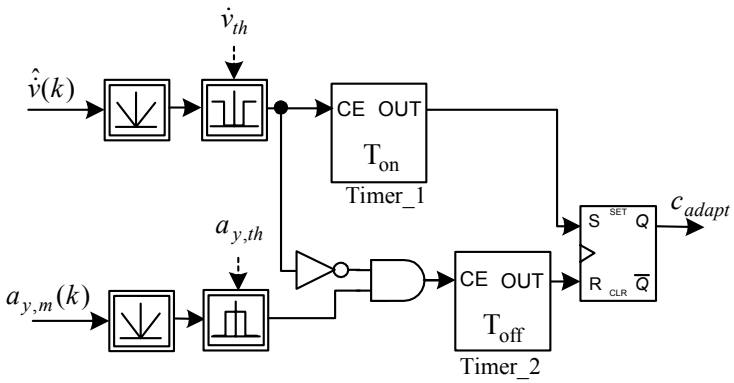

Fig. 5.20 *Estimator adaptation algorithm.*

The basic idea of the adaptation procedure is to set the flag c_{adapt} if the absolute value of estimated lateral velocity derivative $\hat{\dot{v}}(k)$ is higher than some threshold value $\dot{v}_{th}$ for a period longer than a preset time T_{on}. Namely, the lateral velocity time derivative $\dot{v}$ represents a good indicator of dynamic driving conditions (i.e. it can be quite large during transients, while it is approximately zero during quasi steady-state conditions). On the other hand, c_{adapt} is reset if both $\left|\hat{\dot{v}}(k)\right|$ and $\left|a_{y,m}(k)\right|$ are less than their threshold values $\dot{v}_{th}$ and $a_{y,th}$, respectively, for a

period longer than T_{off}. The additional condition related to the lateral acceleration $a_{y,m}$ is used in order to prevent resetting the flag c_{adapt} in the case of oversteer conditions that are characterized by relatively low $\dot{v}$ (compared to, e.g. step steer maneuvers) but high a_y. Hence, in transients when c_{adapt} = TRUE, the covariance matrix Q_D is selected to limit the perturbations in estimated signals, while under the quasi-steady-state conditions, when c_{adapt} = FALSE, the Q_S is utilized to obtain faster convergence of estimates towards true values. The adaptation procedure should abruptly detect an extensive dynamic behavior to timely slow down the estimator, while switching to the steady-state mode should be made more conservative in order to avoid chattering in adaptation. Thus, the timers parameters should be set such that $T_{on} << T_{off}$.

5.5.1 Evaluation of the adaptive estimator

In order to illustrate the effectiveness of the proposed adaptive estimation approach, the sideslip angle estimate of the adaptive EKF estimator has been compared to the ones obtained for the slow and fast-tuning non-adaptive case. The estimation results are shown in Fig. 5.21 for double lane change and double step-steer maneuvers, and the following tuning parameters: T_{on} = 60ms, T_{off} = 400ms, $\dot{v}_{th}$ = 0.2 m/s^2, and $a_{y,th}$ = 6 m/s^2. The response of the adaptation flag trace c_{adapt} is included in the plots. The results are obtained for the case of no a-priori information on sensor offsets and with only dynamic tire radii variations-related velocity pre-estimation errors taken into account.

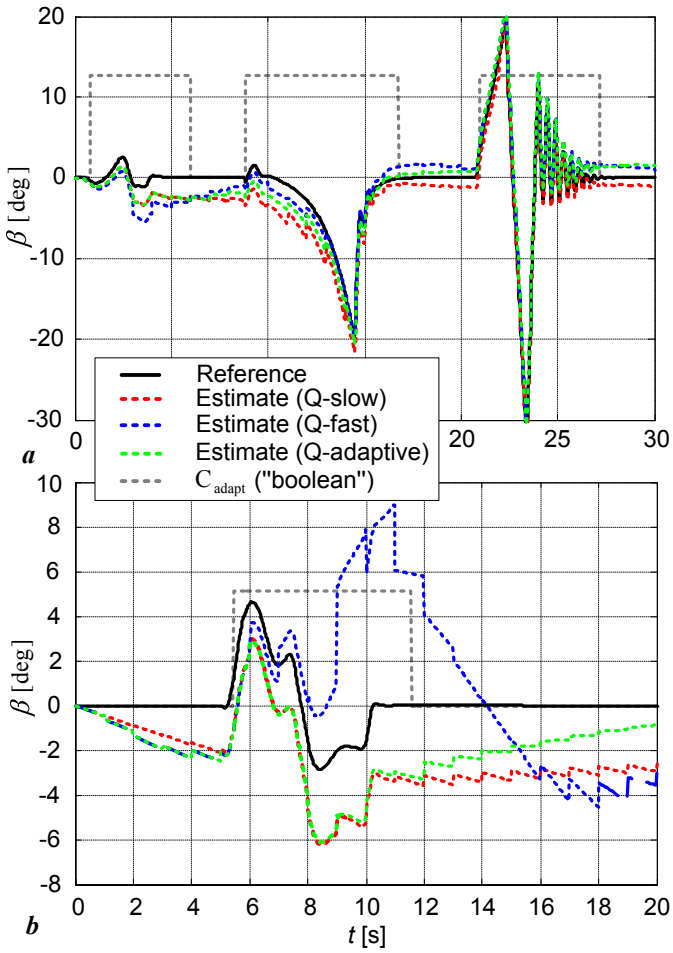

Fig. 5.21 *Comparison of sideslip estimation performance without and with estimator adaptation applied: for double lane change maneuver (a) and double step steer maneuver (b).*

The comparative responses indicate that the adaptive estimate represents a good trade-of between the two non-adaptive estimates. Namely, the adaptive estimate provides a faster convergence of the estimated sideslip values than the slow non-adaptive EKF. On the other hand the steady-state error after the emphasized transient (e.g. for 15s < t < 20s in Fig. 5.21a) is smaller than with the fast non-adaptive EKF estimator. The estimation errors in the initial period are due to initially inaccurate offset estimates.

The final results, given in Fig. 5.22, are obtained for the fully tuned and compensated adaptive sideslip estimator in the presence of longitudinal pre-estimation errors (due to the dynamic tire effective radii discrepancies) while presuming accurate a-priori information on inertial sensor offsets (i.e. the estimator has been active long enough to converge to the true offset values). The estimator performance is tested for the double lane change maneuver and double step-steer maneuver on a flat road.

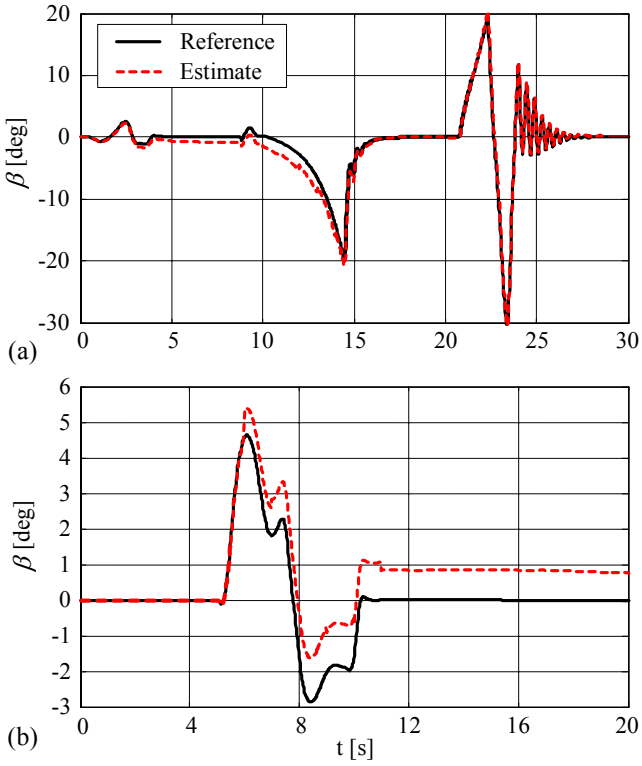

Fig. 5.22 *Final results of tuned adaptive EKF-based sideslip angle estimator performance for double lane change maneuver (a) and double step steer maneuver (b).*

The estimator provides reasonably accurate sideslip angle estimates (the error is less than 1,5° on a large sideslip angle span of ±20°). Generally, the estimator has been found to perform better in highly dynamic maneuvers with relatively short intervals of the steady-state driving conditions. Namely, the accumulated errors are more difficult to correct during the steady-state conditions (especially during straight line driving), because of the lack of process model excitation.

5.6 Summary for GPS/INS kinematic approach

An adaptive EKF-based sideslip angle estimator has been proposed. It combines the low sampling rate GPS-based vehicle velocity measurements with the high sampling rate inertial sensors measurements (lateral acceleration and yaw rate), in order to compensate for the drift-like sideslip angle estimation errors caused by the inertial sensor offsets.

The simulation analysis has indicated that the estimator can be rather sensitive to small errors of pre-estimated longitudinal vehicle velocity, caused by the static and dynamic tire radii variations. Dominant estimation errors related to static tire radii variation can be effectively compensated during straight driving by comparing the GPS velocity and wheel speeds measurements. The remaining errors related to dynamic tire radii variations are relatively

small. Further refinements of the longitudinal velocity pre-estimation may include the dynamic errors compensation proposed in Chapter 4, as well. On the other hand, braking can cause large sideslip angle estimation errors, because of relatively large longitudinal velocity pre-estimation errors caused by the tire longitudinal slip. In order to compensate for these errors, the sideslip is estimated in the open-loop mode during braking intervals, because of uncertainty of slip estimation.

GPS measurement latency represents another source of the sideslip estimation errors, because it causes large transient velocity measurement errors. However, presuming that this latency is constant it can be compensated by introducing the same latency (averaging) in the EKF prediction error calculation.

Road bank represents a potentially large unmodeled disturbance that may cause significant sideslip estimation errors. Namely, the road bank induces high drift-like behavior of the sideslip estimate, related to the additional accelerometer offset caused by gravity acceleration component. In order to reduce the estimation errors, two compensation methods have been suggested. First method modifies the EKF tuning (speeds up the accelerometer offset estimation) in order to account for the additional offset. However, this method becomes ineffective in the case of averaging of the EKF output estimates needed for compensation of the GPS measurement latency-related errors. The second compensation approach, which is based on estimation of the bank-related gravity acceleration component, has been proven to be rather effective.

The designed adaptation algorithm modifies the state covariance matrix in order to account for the changes in the vehicle dynamics conditions. More specifically, two sets of state variables covariance parameters are used; one for quasi-steady-state conditions and other for intense dynamic behavior. The sensor offset estimation is made faster during the steady-state conditions and slower during transients. Adaptation relies on the measured lateral acceleration and estimated time derivative of the lateral velocity signals. This procedure enables adjusting optimal estimator performance with respect to estimator response time and damping of oscillations in the estimated sensor offsets and consequently the magnitude of errors in sideslip angle estimate.

Finally, the performance of fully tuned, adaptive EKF-based estimator has been tested for the double lane change and double step-steer maneuvers. The simulation results have shown that the sideslip estimation error of less than approximately 2 deg is achievable for a wide range of non-braking operating conditions, provided that the static tire radii, bank, and GPS

measurement latency errors are accurately pre-compensated and the offset estimates transients are settled.

6 Sideslip estimator based on nonlinear vehicle dynamics and stochastic tire models

6.1 Background

The sideslip angle estimator based on a nonlinear vehicle dynamics model that utilizes stochastic, random walk-type models of the tire forces has been initially proposed in [55]. The estimator has then been extended, refined, and validated as described in detail hereinafter. Such approach eliminates sensitivity of the sideslip angle estimation to uncertainties of the deterministic tire model parameters, and makes the laborious and costly tire model identification unnecessary [18]. The proposed estimator has been verified through off-line processing of the experimental data recorded on a test vehicle, equipped with a high-performance inertial measurement unit (IMU), during various realistic driving maneuvers performed on low-μ and high-μ surfaces (e.g. snow, ice, concrete surfaces).

The estimator performance has been first analyzed for the case of utilizing a high-precision inertial measurement unit with two antenna GPS receiver, in order to verify the proof of concept. Later, the deterioration of the estimator performance has been analyzed for the case of utilizing only the standard set of vehicle dynamics sensors. The main sources of the estimation errors have been identified and adequate error compensation methods have been proposed, when applicable. In order to obtain more accurate estimates, the tuning of the state covariance matrix has been conducted and analyzed, and finally an adaptive extended Kalman filter-based estimator configuration has been designed.

6.2 Basic estimation concept

The single-track nonlinear vehicle dynamics model with five degrees of freedom (see Chapter 2, Fig. 2.3) has been utilized as a basis for the design of sideslip angle estimator. This vehicle dynamics model is defined by the following expressions:

$$\dot{u} = \frac{1}{m}\left[F_{xf}\cos\delta - F_{yf}\sin\delta + F_{xr}\right] + v\omega_z \tag{6-1}$$

$$\dot{v} = \frac{1}{m}\left[F_{yf}\cos\delta + F_{xf}\sin\delta + F_{yr}\right] - u\omega_z \tag{6-2}$$

$$\dot{\omega}_z = \frac{1}{I_z}\left[b\left(F_{yf}\cos\delta + F_{xf}\sin\delta\right) - cF_{yr}\right] \tag{6-3}$$

$$\dot{\omega}_{w,f} = \frac{1}{I_w}\left[F_{xf}r_w - \tau_{bf}\right] \tag{6-4}$$

$$\dot{\omega}_{w,r} = \frac{1}{I_w}\left[F_{xr}r_w - \tau_{br}\right] \tag{6-5}$$

where u and v are the longitudinal and lateral velocities, respectively, ω_z is the yaw rate, $\omega_{w,f}$ and $\omega_{w,r}$ are the front and rear rotational wheel speeds, δ is the front wheel steering angle, b and c denote distances of the front and rear axles from the vehicle CoG, respectively, r_w and I_w are the wheel radius and the wheel moment of inertia, τ_{bf} and τ_{br} are the front and rear braking torques (see Fig. 2.3). The tire forces F_{xf}, F_{xr}, F_{yf}, and F_{yr} are modeled as first-order random walk-type stochastic variables.

The state vector **x** of the continuous-time state-space model representation (Eq. (6-6)) of the utilized 5DoF vehicle dynamic model (6-1) to (6-5), is augmented with four additional state variables corresponding to the front and rear axles lumped tire forces.

$$\begin{aligned}\dot{\mathbf{x}} &= \mathbf{\Phi}(\mathbf{x}) + \mathbf{B}\mathbf{u} + \mathbf{W}\upsilon \\ \mathbf{y} &= \mathbf{C}\mathbf{x} + \mathbf{e}\end{aligned} \tag{6-6}$$

The input vector **u** comprises the front and rear wheels braking torques, and the output vector **y** comprises the measurements of yaw rate, front and rear wheel speeds, lateral and longitudinal accelerations and vehicle longitudinal velocity. The input vector **u**, the state vector **x**, and the measurement vector **y,** are defined as: $\mathbf{u} = \begin{bmatrix}\tau_{bf} & \tau_{br}\end{bmatrix}^T$, $\mathbf{x} = \begin{bmatrix}u & v & \omega_z & \omega_{w,f} & \omega_{w,r} & F_{xf} & F_{xr} & F_{yf} & F_{yr}\end{bmatrix}^T$, and $\mathbf{y} = \begin{bmatrix}\omega_z & \omega_{w,f} & \omega_{w,r} & a_x & a_y & u\end{bmatrix}^T$.

The input and output matrices read:

$$\mathbf{B} = \begin{bmatrix} 0 & 0 & 0 & -\frac{1}{I_w} & 0 & 0 & 0 & 0 & 0 \\ 0 & 0 & 0 & 0 & -\frac{1}{I_w} & 0 & 0 & 0 & 0 \end{bmatrix}^T, \quad \mathbf{C} = \begin{bmatrix} 0 & 0 & 1 & 0 & 0 & 0 & 0 & 0 & 0 \\ 0 & 0 & 0 & 1 & 0 & 0 & 0 & 0 & 0 \\ 0 & 0 & 0 & 0 & 1 & 0 & 0 & 0 & 0 \\ 0 & 0 & 0 & 0 & 0 & \frac{\cos\delta}{m} & \frac{1}{m} & \frac{-\sin\delta}{m} & 0 \\ 0 & 0 & 0 & 0 & 0 & \frac{\sin\delta}{m} & 0 & \frac{\cos\delta}{m} & \frac{1}{m} \\ 1 & 0 & 0 & 0 & 0 & 0 & 0 & 0 & 0 \end{bmatrix}$$

Furthermore, the state noise matrix is equal to unit matrix ($\mathbf{W} = \mathbf{I}_{9x9}$), and front wheel steering angle δ has been considered as a time variant model parameter in the state transition

function $\mathbf{\Phi}(\mathbf{x})$ and output matrix $\mathbf{C}$, updated to an instantaneous value of the steering angle measurement at each time step t_k.

Note that the model nonlinearities reside only in the state equation, more precisely in Eqs. (6-1) and (6-2) through the terms $v\omega_z$ and $u\omega_z$, while the output equation (i.e. output matrix $\mathbf{C}$) is linear function of the state variables. Therefore, in order to implement the Kalman filter, the state-space model nonlinear state transition function $\mathbf{\Phi}(\mathbf{x})$ needs to be linearized around the operating point (u_{0k}, v_{0k}, ω_{z0k}) at each time step t_k in order to derive the state transition matrix $\mathbf{A}$:

$$\mathbf{A}_k = \left.\frac{\partial \mathbf{\Phi}(\mathbf{x})}{\partial \mathbf{x}}\right|_{\substack{\mathbf{x}=\mathbf{x}_0 \\ t=t_k}} \tag{6-7}$$

The observability of the linearized state-space model (6-6) has been tested by means of algebraic analysis of the observability matrix $\mathbf{O_b} = \begin{bmatrix}\mathbf{C} & \mathbf{CA} & \mathbf{CA}^2 & \cdots & \mathbf{CA}^{n-1}\end{bmatrix}^T$ and by calculating its rank [51]. This analysis has shown that the considered model becomes unobservable in the case of near zero yaw rate and lateral acceleration (i.e. in straight driving conditions). However, in these conditions the sideslip angle also equals zero, so that the estimator should be switched off in order to prevent the estimation error build-up.

The discrete-time vehicle dynamics model, needed for implementation of EKF-based estimator, is obtained from continuous-time model given by Eq. (6-6) after applying Z-transform based upon the Zero-Order-Hold (ZOH) method:

$$\begin{aligned}\mathbf{x}(k) &= \mathbf{F}(k-1)\,\mathbf{x}(k-1) + \mathbf{G}(k-1)\,\mathbf{u}(k-1) + \mathbf{\Omega}(k-1)\,\boldsymbol{\upsilon}(k-1)\\ \mathbf{y}(k) &= \mathbf{H}(k)\,\mathbf{x}(k) + \mathbf{e}(k)\end{aligned} \tag{6-8}$$

where the discrete-time model matrices have been derived numerically from the following approximate expressions [38]:

$$\mathbf{F} = e^{\mathbf{A}T_s} \approx \mathbf{I} + \mathbf{A}T_s,\ \mathbf{G} \approx \mathbf{B}T_s,\ \mathbf{\Omega} \approx \mathbf{W}T_s \text{ and } \mathbf{H} = \mathbf{C}.$$

Consequently the discrete model matrices read:

$$\mathbf{F}(k)=\begin{bmatrix} 1 & T_s\omega_z(k) & T_s v(k) & 0 & 0 & \frac{T_s\cos\delta(k)}{m} & \frac{T_s}{m} & \frac{-T_s\sin\delta(k)}{m} & 0 \\ -T_s\omega_z(k) & 1 & -T_s u(k) & 0 & 0 & \frac{T_s\sin\delta(k)}{m} & 0 & \frac{T_s\cos\delta(k)}{m} & \frac{T_s}{m} \\ 0 & 0 & 1 & 0 & 0 & \frac{aT_s\sin\delta(k)}{I_z} & 0 & \frac{aT_s\cos\delta(k)}{I_z} & \frac{-T_s b}{I_z} \\ 0 & 0 & 0 & 1 & 0 & \frac{-T_s r_w}{I_w} & 0 & 0 & 0 \\ 0 & 0 & 0 & 0 & 1 & 0 & \frac{-T_s r_w}{I_w} & 0 & 0 \\ \multicolumn{5}{c}{\mathbf{0}_{4x5}} & \multicolumn{4}{c}{\mathbf{I}_{4x4}} \end{bmatrix}$$

$$\mathbf{G}=\begin{bmatrix} 0 & 0 & 0 & -\frac{T_s}{I_w} & 0 & 0 & 0 & 0 & 0 \\ 0 & 0 & 0 & 0 & -\frac{T_s}{I_w} & 0 & 0 & 0 & 0 \end{bmatrix}^T,\quad \mathbf{\Omega}=T_s\mathbf{I}_{9x9}$$

$$\mathbf{H}(k)=\begin{bmatrix} 0 & 0 & 1 & 0 & 0 & 0 & 0 & 0 & 0 \\ 0 & 0 & 0 & 1 & 0 & 0 & 0 & 0 & 0 \\ 0 & 0 & 0 & 0 & 1 & 0 & 0 & 0 & 0 \\ 0 & 0 & 0 & 0 & 0 & \frac{\cos\delta(k)}{m} & \frac{1}{m} & \frac{-\sin\delta(k)}{m} & 0 \\ 0 & 0 & 0 & 0 & 0 & \frac{\sin\delta(k)}{m} & 0 & \frac{\cos\delta(k)}{m} & \frac{1}{m} \\ 1 & 0 & 0 & 0 & 0 & 0 & 0 & 0 & 0 \end{bmatrix}$$

The Kalman filter equations in this particular case read (cf. Eqs. (3-26) to (3-31)):

$$\hat{\mathbf{x}}(k\mid k-1)=\mathbf{f}\left(\hat{\mathbf{x}}(k-1\mid k-1)\right)+\mathbf{G}(k-1)\mathbf{u}(k-1) \tag{6-9}$$

$$\mathbf{P}(k\mid k-1)=\mathbf{F}(k-1)\,\mathbf{P}(k-1\mid k-1)\mathbf{F}^T(k-1)+\mathbf{\Omega}\,\mathbf{Q}(k-1)\mathbf{\Omega}^T \tag{6-10}$$

$$\tilde{\mathbf{y}}(k\mid k-1)=\mathbf{y}(k)-\mathbf{h}\left(\hat{\mathbf{x}}(k\mid k-1)\right) \tag{6-11}$$

$$\mathbf{K}(k)=\left(\mathbf{P}(k\mid k-1)\mathbf{H}^T(k)\right)\left[\mathbf{H}^T(k)\mathbf{P}(k\mid k-1)\mathbf{H}^T(k)+\mathbf{R}(k)\right]^{-1} \tag{6-12}$$

$$\hat{\mathbf{x}}(k\mid k)=\hat{\mathbf{x}}(k\mid k-1)+\mathbf{K}(k)\,\tilde{\mathbf{y}}(k\mid k-1) \tag{6-13}$$

$$\mathbf{P}(k\mid k)=\mathbf{P}(k\mid k-1)-\mathbf{K}(k)\,\mathbf{H}(k)\,\mathbf{P}(k\mid k-1) \tag{6-14}$$

Assuming that the stochastic state perturbations and the measurement errors are mutually independent, the state covariance matrix **Q** and the measurement noise covariance matrix **R** are defined as:

$$\mathbf{Q}=diag\left(\begin{bmatrix} q_u & q_v & q_{\omega z} & q_{\omega wf} & q_{\omega wr} & q_{Fxf} & q_{Fxr} & q_{Fyf} & q_{Fyr} \end{bmatrix}\right)$$

$$\mathbf{R} = diag\left(\begin{bmatrix} r_{\omega z} & r_{\omega wf} & r_{\omega wr} & r_{ax} & r_{ay} & r_u \end{bmatrix}\right)$$

where the components of matrix **Q** correspond to the variance of the state perturbations and the components of matrix **R** correspond to the variance of the measurement noise.

The sideslip angle estimate has been derived by using the estimated vehicle lateral and longitudinal velocities (i.e. the elements of the a-posteriori updates of the state vector estimate), according to the following expression:

$$\hat{\beta}(k) = \text{atan}\left(\frac{\hat{v}(k \mid k)}{\hat{u}(k \mid k)}\right) \tag{6-15}$$

6.3 Simulation environment

Performance of the proposed EKF-based sideslip angle estimator is first analyzed by means of computer simulation. For that purpose, the simulation framework outlined in Fig. 6.1 is applied, based on the 10DoF vehicle dynamics model [4], implemented in Matlab Simulink™. This model enables selection of different driving maneuvers and setting of relevant maneuver parameters in order to generate the reference vehicle dynamics signals and inputs for the single-track 5DoF model used for estimation (i.e. front wheel steering angle δ and braking torques $\mathbf{T_b} = \begin{bmatrix} \tau_{bf} & \tau_{br} \end{bmatrix}^T$ for front and rear axles. Initially, the 5DoF model outputs have been used as measurements signals **y** for the EKF estimator, as illustrated in Fig. 6.1, in order to test its nominal performance and emphasize the difference between the underlying 5DoF and referent 10DoF vehicle dynamics model. The presented simulation results correspond to the high-mu conditions ($\mu = 1$).

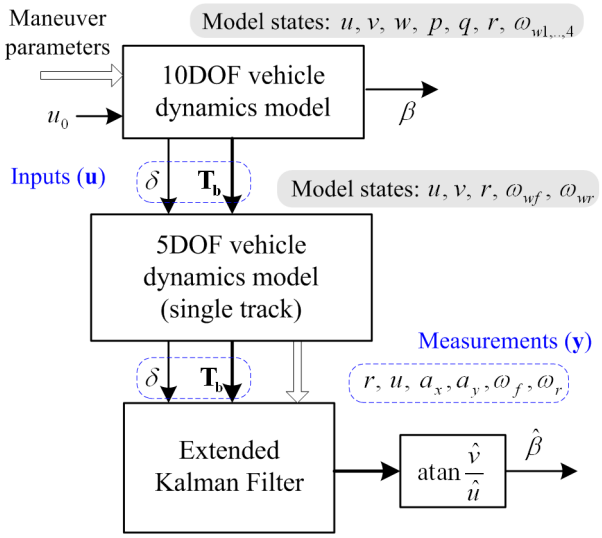

Fig. 6.1 *Illustration of the EKF estimator simulation environment.*

Typical simulation results for a double step-steer and braking in turn maneuvers are presented in Fig. 6.2a and Fig. 6.2b, respectively. The double step steer maneuver is characterized by a high peak lateral acceleration of 8.6 m/s^2, the initial velocity of 72 kph, and no braking action. Braking in a turn maneuver is carried out for the initial velocity of 90 kph, the braking torques of 300Nm per wheel, and the steering wheel amplitude of 28 deg, characterized by the peak lateral acceleration of 4.2 m/s^2 and small sideslip angle values. The sideslip angle estimate has been compared with the actual outputs of the underlying 5DoF model and the true reference yielded from the 10DoF vehicle dynamics model. Based on the simulation result in Fig. 6.2, it can be concluded that the estimate coincide well with the reduced dynamics model output while discrepancies between the estimate and 10DoF reference are clearly the result of an unmodeled roll and pitch dynamics.

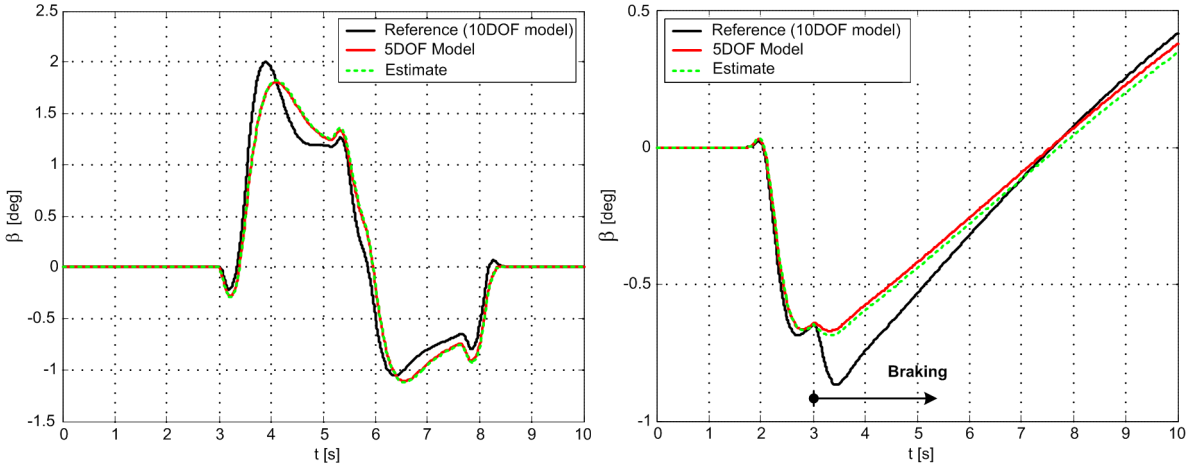

Fig. 6.2 *Simulation results of the sideslip angle estimation for double step steer maneuver (a) and braking in a turn maneuver (b).*

Impact of the state covariance matrix **Q** tuning on the convergence of the Kalman filter sideslip angle residuals (i.e. the estimation errors) are illustrated in Fig. 6.3 for the step-steer maneuver with the following parameters: μ = 0.6, u_0 = 90kph, and $\Delta\delta_{SW}$ = 80 deg (index SW indicates the steering wheel). The large initial sideslip angle estimation error has been generated by setting the faulty, nonzero initial value of the lateral velocity state variable, while the estimates of the other state variables have been initialized to their true values. The simulation results indicate that the convergence rate of the sideslip angle estimator is primarily influenced by the quality of excitation [60] (i.e. in conditions of high excitation of the lateral vehicle dynamics, t > 3s, a fast convergence of the estimation residuals is observed) and state covariance matrix tuning (i.e. higher convergence rates are obtained for larger values of individual elements of the **Q** matrix, but at the cost of increasing the noise in the estimation

signal, not included in this simulation). Based on this analysis, the nominal setting ($10q_{v0}$) of the state covariance matrix **Q** has been set for further analysis and experimental validation of estimator performance.

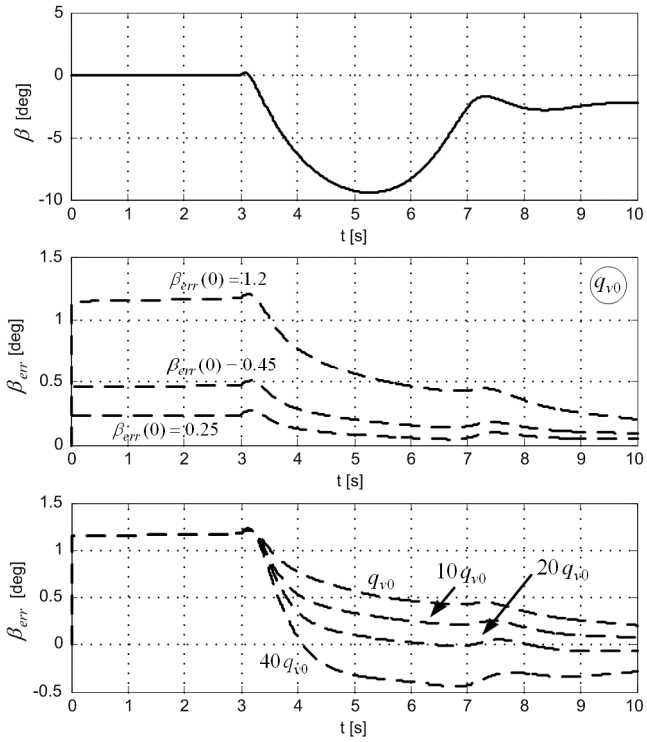

Fig. 6.3 *Illustration of the impact of the state covariance matrix tuning on the convergence of the estimation errors: reference sideslip angle (a), estimation errors vs. initial condition offset error magnitude for q_{v0} (b), and estimation errors for different covariance matrix settings (c).*

6.4 Experimental results for high-performance IMU measurements

The estimator performance has been verified by running the estimation algorithm off-line, on a set of experimental data obtained from a rear-wheel-drive Jaguar S-type test vehicle equipped with the Oxford Technical Solutions RT3003 measurement unit (the specifications are given in the Appendix B). The estimator performance has been tested for various driving maneuvers (e.g. double lane change, slalom, J-turn, steady cornering) carried out during the winter tests on low-μ surfaces (mostly concrete flat road covered with packed snow) and relevant maneuvers on dry asphalt. The sample time of the experimental data was 50ms or 10ms depending on the driving maneuvers.

The results analyzed herein and shown in Figs. 6.4 to 6.7, are obtained by using high accuracy vehicle dynamics measurements obtained from the RT3003 unit instead of using the equivalent signals from standard vehicle dynamics sensors. More specifically, the signals used for testing the proposed estimator include: the lateral and longitudinal acceleration,

lateral and longitudinal velocity, yaw rate, and sideslip angle measurements obtained from the RT3003 unit, and data acquired directly from the vehicle CAN bus system such as front wheel steering angle δ, front and rear wheel speeds, front and rear braking torques (τ_{bf} and τ_{br}, calculated based on the brake caliper pressure measurements). The simulation results have been obtained for fixed settings of the state and measurement covariance matrices, **Q** and **R**, respectively.

Since the tire forces are not measured on the test vehicle, and in order to analyze the accuracy of the simultaneous lateral tire force estimation, which is vital for the later cornering stiffness estimation (addressed in more detail in Chapter 7), the reference values of the front and rear tire lateral forces F_{yf} and F_{yr} have been reconstructed from the available measurements, according to the following expressions [61]:

$$F_{yf} = \frac{cma_y + I_z\dot{\omega}_z}{(b+c)\cos\delta} \tag{6-16a}$$

$$F_{yr} = \frac{bma_y - I_z\dot{\omega}_z}{b+c} \tag{6-16b}$$

where the above expression for F_{yr} is obtained by combining Eqs. (6-2) and (6-3), while the expression for F_{yf} is obtained by inserting thus derived rear lateral force F_{yr} back into Eq. (6-2) and neglecting the longitudinal tire force component $F_{xf}\sin\delta$. Note that the tire force reconstruction approach by using (6-16) requires the yaw rate derivative signal, which would make it ineffective in on-line applications due to the noise sensitivity. Also, in the presence of significant braking or accelerating actions in curves, the assumption of small $F_{xf}\sin\delta$ component would not hold and therefore Eq. (6-16a) would no longer be valid (i.e. potentially large errors cannot be neglected).

Moreover, an algebraic analysis of the accuracy of sideslip angle calculation according to Eq. (6-15) related to the accuracy of the longitudinal and lateral vehicle velocities (i.e. the two essential state variables of the underlying vehicle dynamics model) measurements or estimates has been carried out by considering the following sideslip error models:

$$\tilde{\beta}_u = \operatorname{atan}\frac{v}{u+\tilde{u}} - \beta \tag{6-17a}$$

$$\tilde{\beta}_v = \operatorname{atan}\frac{v+\tilde{v}}{u} - \beta\,. \tag{6-17b}$$

For the case of constant longitudinal velocity error $\tilde{u} = \text{const}$. For this analysis let the $\tilde{u} = 0.7\,\text{m/s}$ (or 2.5 kph), then according to Eq. (6-17) the theoretical sideslip angle calculation

relative and absolute error margin $\tilde{\beta}_i = f(v, u_i)$ can be determined for different operating points ($u_i = [15 \quad 10 \quad 5 \quad 4 \quad 3]$ m/s) as illustrated in Fig. 6.4.

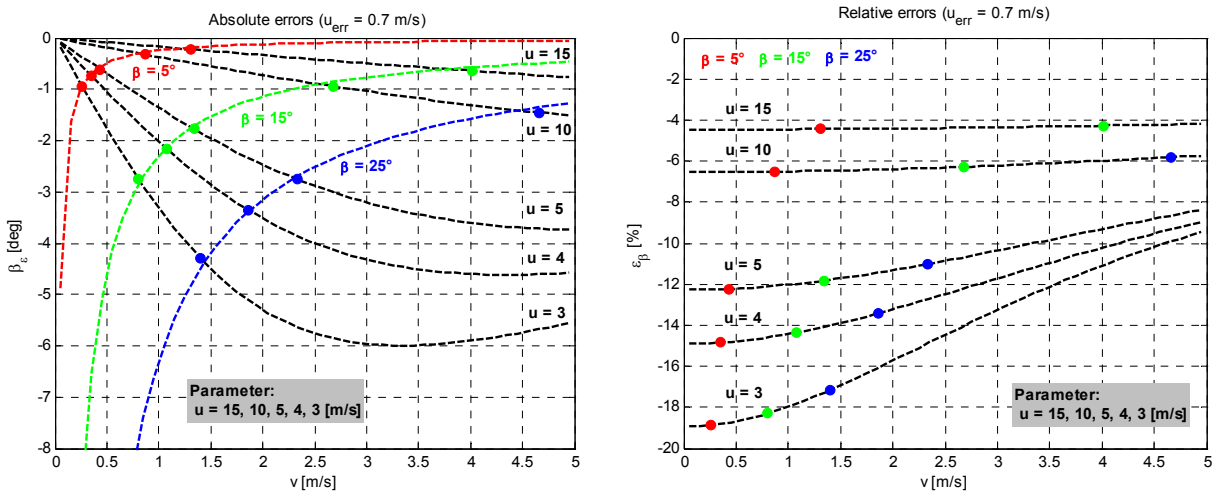

Fig. 6.4 *The absolute (a) and relative (b) sideslip angle errors due to the constant error of the vehicle longitudinal velocity vs. lateral velocity (sideslip angle) magnitude.*

In general, the absolute and relative errors in sideslip angle reconstruction, related to the constant error of vehicle longitudinal velocity signal, increase as the vehicle speed decreases. The relative error increase is more emphasized if the sideslip angles are small. Consequently, the calculation of the sideslip angle by using the Eq. (6-15) becomes rather sensitive to a vehicle velocity measurement or estimation errors when the vehicle velocity is small (the impact of the vehicle longitudinal velocity measurement resolution becomes significant). In such case the performance of the estimator is limited by numerical constraints and cannot be improved by the estimator tuning and therefore the estimation should be discarded as unreliable. However, since the sideslip angle remains small (near zero) in such conditions, and the vehicle handling stability is not likely to be compromised at such small velocities, the sideslip angle estimation is not relevant (the ESP is held inactive).

Initial analysis of the estimator performance (i.e. proof of concept determination) has been carried out by running the estimator offline on a set of prerecorded experimental data from an instrumented test vehicle utilizing the high precision inertial unit measurements for characteristic driving maneuvers on a low-mu road. For the double lane change maneuver in Fig. 6.5 the peak sideslip angle estimation error is approximately 0.5 deg (i.e. 5-10% of the instantaneous sideslip angle values). Apart from the sideslip angle estimation, this estimator also provides the tire forces estimates (i.e. lateral and longitudinal tire forces of the single

track model). The estimates of the front and rear lateral tire forces (F_{yf} and F_{yr}) concur well with the reference values, calculated from the available measurements according to Eq. (6-16). At the same time, these estimates are characterized by much lower noise content (i.e. the estimator effectively filters the measurement noise inherent to force reconstruction approach).

Fig. 6.6 illustrates the estimator performance for driving on a circular track at the velocity of 65kph. This maneuver is characterized with roughly constant lateral acceleration and yaw rate ($a_y \approx 3.5$ m/s^2 and r ≈ 10 °/s) and the peak sideslip angle in the range from 4 to 6 deg. The overall estimation errors are small, except at the beginning and end of the experiment when they increase. Namely, at the start of the maneuver the estimation error of approximately 1 deg (Fig. 6.6) is caused by inaccurate initial conditions of the state vector estimate (cf. Fig 6.3), and this initial error has been eliminated after few seconds in accordance to the EKF convergence dynamics. On the other hand, the increased estimation errors at the end of the maneuver (100-110s interval in Fig. 6.6) are related to the very small vehicle speed and near zero lateral velocity at which the vehicle dynamics model becomes unobservable and β-estimation ineffective. Under these conditions (i.e. vehicle speed under 5 m/s and near zero yaw rate and lateral acceleration), the estimator should be switched off in order to prevent the estimation error build-up (see the above discussion related to numerical constraints of Eq. 6-15 and results given in Fig. 6.4).

Further analysis of the estimator performance has been carried out for slalom (Fig. 6.7) and J-turn maneuvers (Fig. 6.8). These results confirm a generally high accuracy of sideslip angle estimation (the errors are typically less than 0.5°) for a wide range of driving conditions and different types of driving maneuvers. Also, a favorable accuracy of the front and rear lateral tire forces has been achieved, which justifies the assumption that this type of estimator may be used for on-line estimation of cornering stiffness (see Chapter 7).

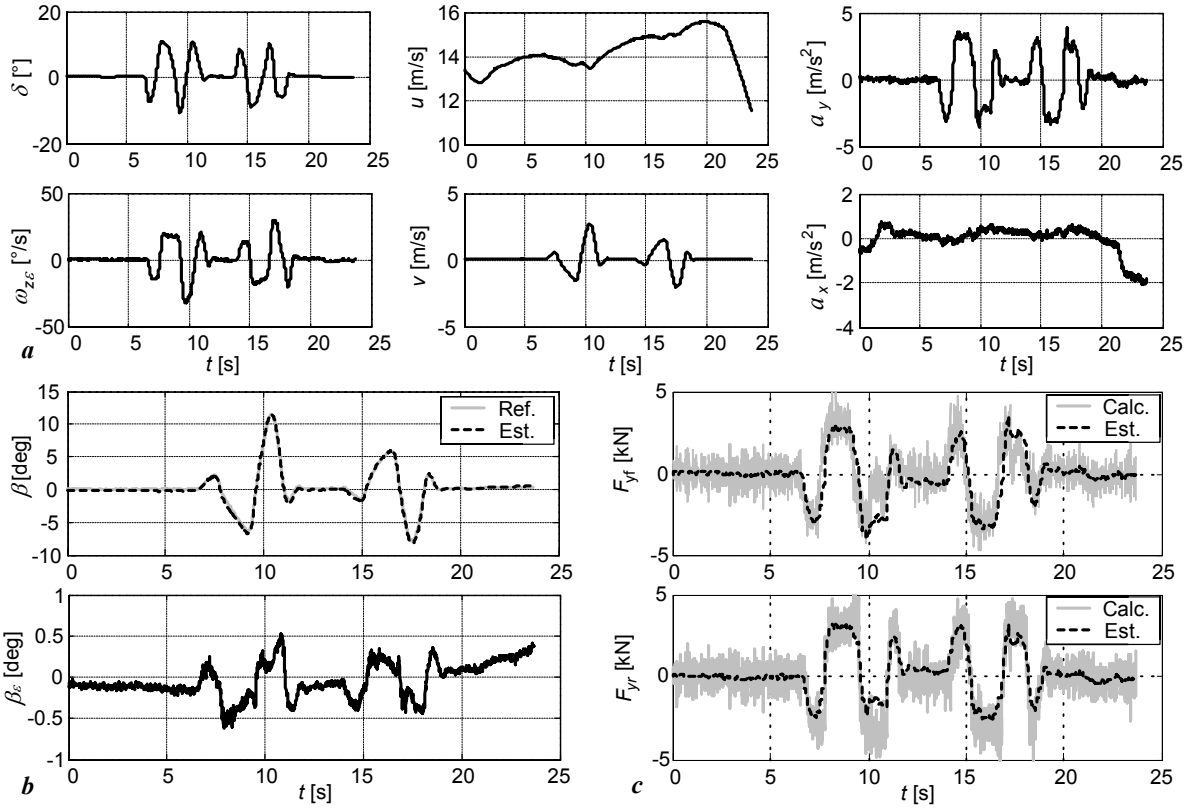

Fig. 6.5 *Measurements of the vehicle dynamics variables (a), sideslip angle estimate and estimation error (b), and calculated and estimated lateral forces (c) for double lane change maneuver carried out on flat road covered with packed snow.*

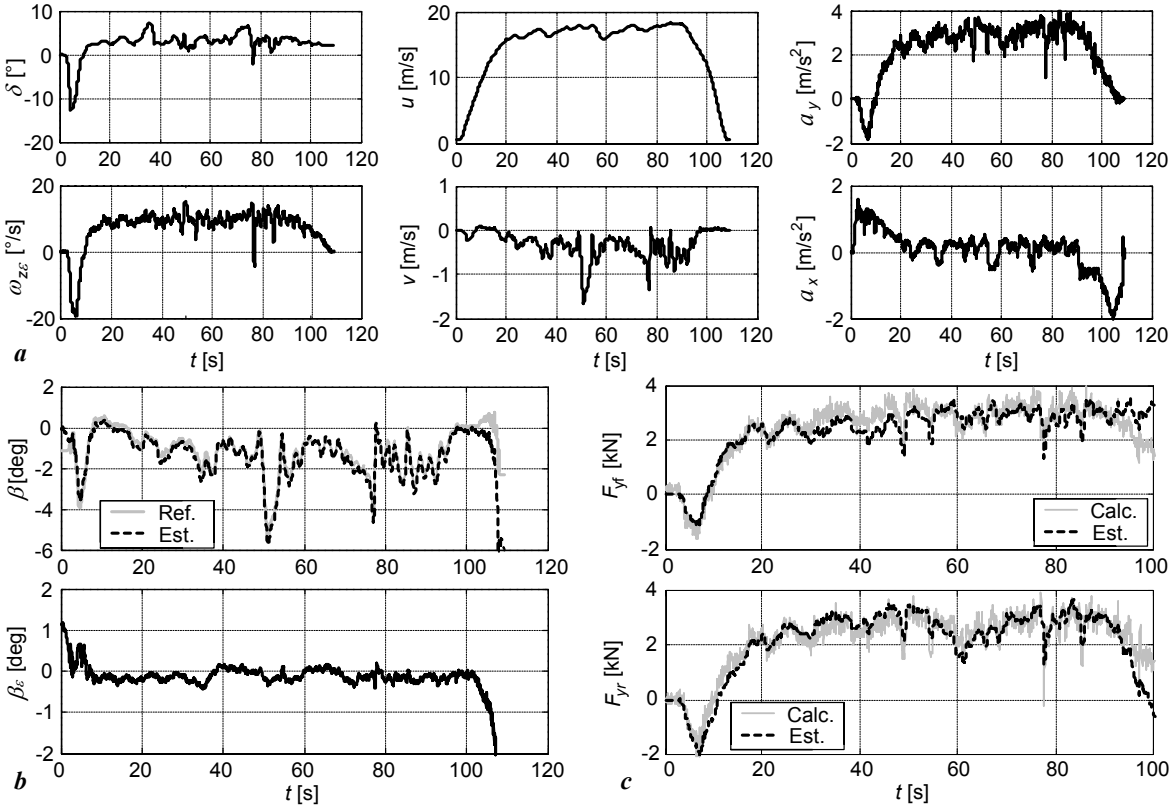

Fig. 6.6 *Measurements of the vehicle dynamics variables (a), sideslip angle estimate and estimation error (b), and calculated and estimated lateral forces (c) for driving on a 100m radius circular track at velocities of 65kph.*

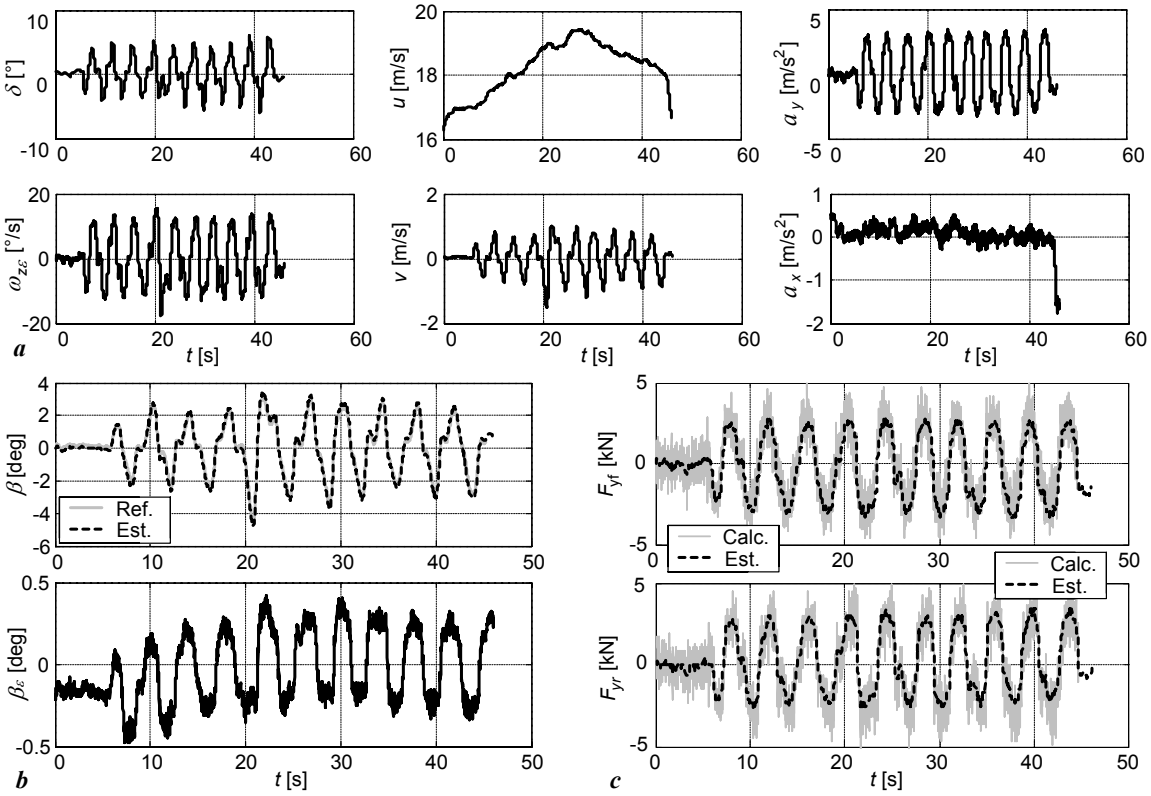

Fig. 6.7 *Measurements of the vehicle dynamics variables (a), sideslip angle estimate and estimation error (b), and calculated and estimated lateral forces (c) for slalom maneuver carried out on flat road covered with packed snow.*

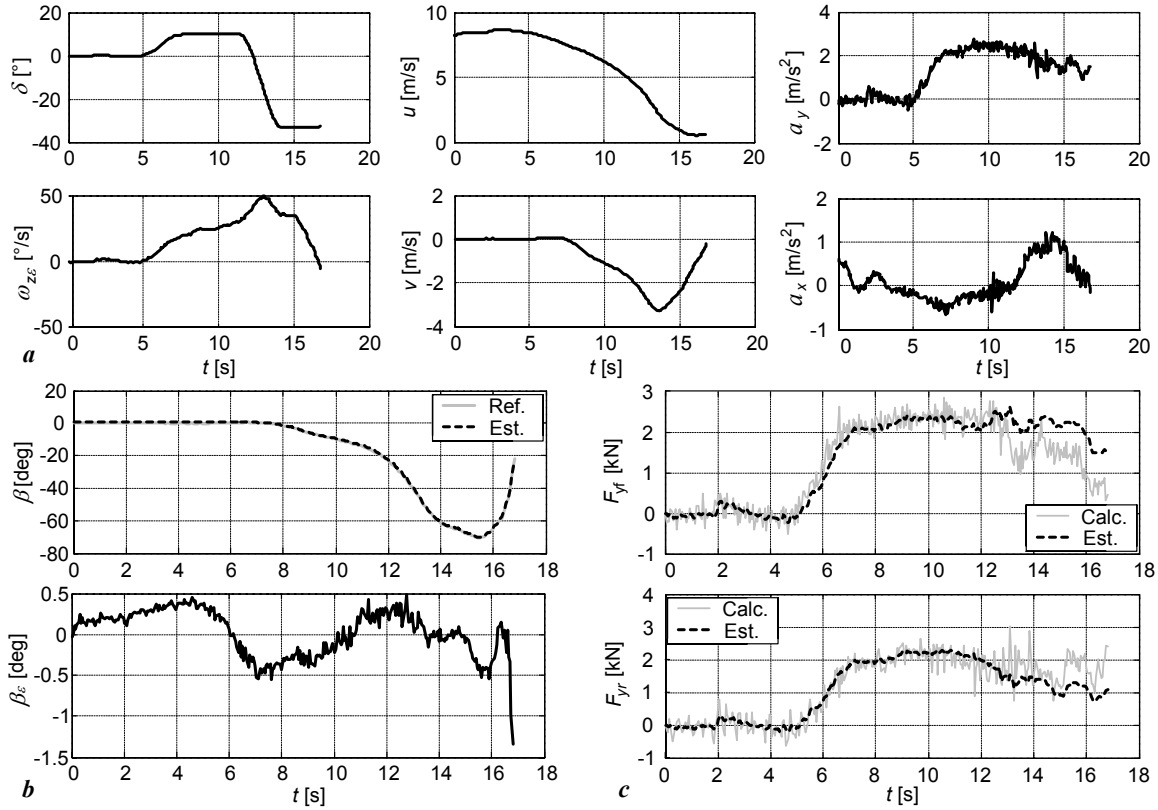

Fig. 6.8 *Measurements of the vehicle dynamics variables (a), sideslip angle estimate and estimation error (b), and calculated and estimated lateral forces (c) for J-turn maneuver carried out on flat road covered with packed snow.*

6.5 Experimental results for standard set of VSD sensors

In order to gain the insight into limitations related to applying the above estimator in the mass production vehicles, the estimator performance degradation has been analyzed for the case of utilizing standard set of the vehicle dynamics sensors (i.e. vehicle on-board sensors utilized by an ESP system) instead of the high precision inertial measurement unit equipped with the GPS receiver. Commonly used vehicle dynamics sensors within the production vehicles include the lateral accelerometer, yaw rate gyro, steering wheel angle, and wheel speed sensors; and nowadays often the longitudinal accelerometer, as well.

The measurement of the vehicle longitudinal velocity enables tighter margins of the sideslip angle estimation errors in comparison to the estimator utilizing the measurement model from [18]. This additional measurement was readily available from the inertial measurement unit utilized for the experimental validation in the previous Subsection. However, in case of using standard VSD sensors the vehicle longitudinal velocity is derived from the nondriven front wheels rotational speed measurements characterized with high noise content. Nevertheless, this additional information remains beneficial, but the reliability of such measurement is decreased during the braking or accelerating actions. More precisely, its accuracy is decreased in case of braking due to the large longitudinal slips (the rear wheel drive vehicle has been considered so the impact of the acceleration action to measurement accuracy should be much less emphasized). In order to mitigate the braking related decrease in the estimator performance the related element of the measurement covariance matrix r_u should be increased (less confidence to the particular measurement). Consequently, the related Kalman gains calculated from the Ricatti equation (6-12) would decrease and the a-posteriori estimates of the state variables would be less affected by the unreliable longitudinal velocity measurement, while the effect of the other measurements on the correction phase would not be influenced.

6.5.1 VSD sensors measurement errors analysis

Commonly used vehicle dynamics sensors have generally significantly larger measurement errors then the aforementioned IMU. The increased level of the measurement errors (such as offset, sensitivity errors, nonlinearity, noise etc.) affects the accuracy of the proposed estimator. In order to gain the insight into the limits imposed by the usage of standard set of sensors, the measurement errors and related sideslip angle estimation errors have been analyzed for different driving maneuvers and environmental conditions. Moreover, dominant sources of estimation errors for different driving maneuvers have been determined and

appropriate compensation procedures have been considered in order to minimize the impact of these measurement errors to the overall estimator performance.

The experimental vehicle's Electronic Stability Program (ESP) system was not equipped with the longitudinal accelerometer, so the required signal is calculated within the ESP algorithm (by calculating the first derivative of the vehicle reference velocity signal available on the vehicle's CAN bus). Consequently, the characterization of the longitudinal accelerometer errors upon the estimator performance was not possible. Nevertheless, the errors of thus reconstructed longitudinal acceleration signal has been analyzed and compared to more realistic longitudinal acceleration measurement model obtained by adding the gravity acceleration component induced by a pitch motion of the vehicle chassis to the reference vehicle longitudinal acceleration measurement obtained from the IMU. This "simplified" measurement model has been applied hereafter for reconstruction of the realistic ESP longitudinal acceleration measurement signal used for the analysis of the accuracy of the proposed estimator in the presence of measurement errors.

Measurement errors of the ESP inertial sensors have been obtained from filtered sensor signals in order to suppress the impact of the measurement noise which is anyway filtered within the KF. For that purpose the 2nd order Butterworth low pass filter with the pass-band frequency of $\omega_p = 0.1\,\omega_n$ has been utilized, where ω_n is a half of the sampling frequency (e.g. $f_s = 20\text{Hz}$, $T_s = 0.05\text{s}$).

Fig. 6.9 illustrates the reference state variables (measured by IMU) and vehicle dynamics sensors measurement errors for double lane change maneuver carried out on a flat road covered with packed snow. Fig. 6.10 shows the associated sideslip angle estimation errors induced by individual vehicle dynamics sensors errors and overall aggregate estimation error for the considered driving maneuver.

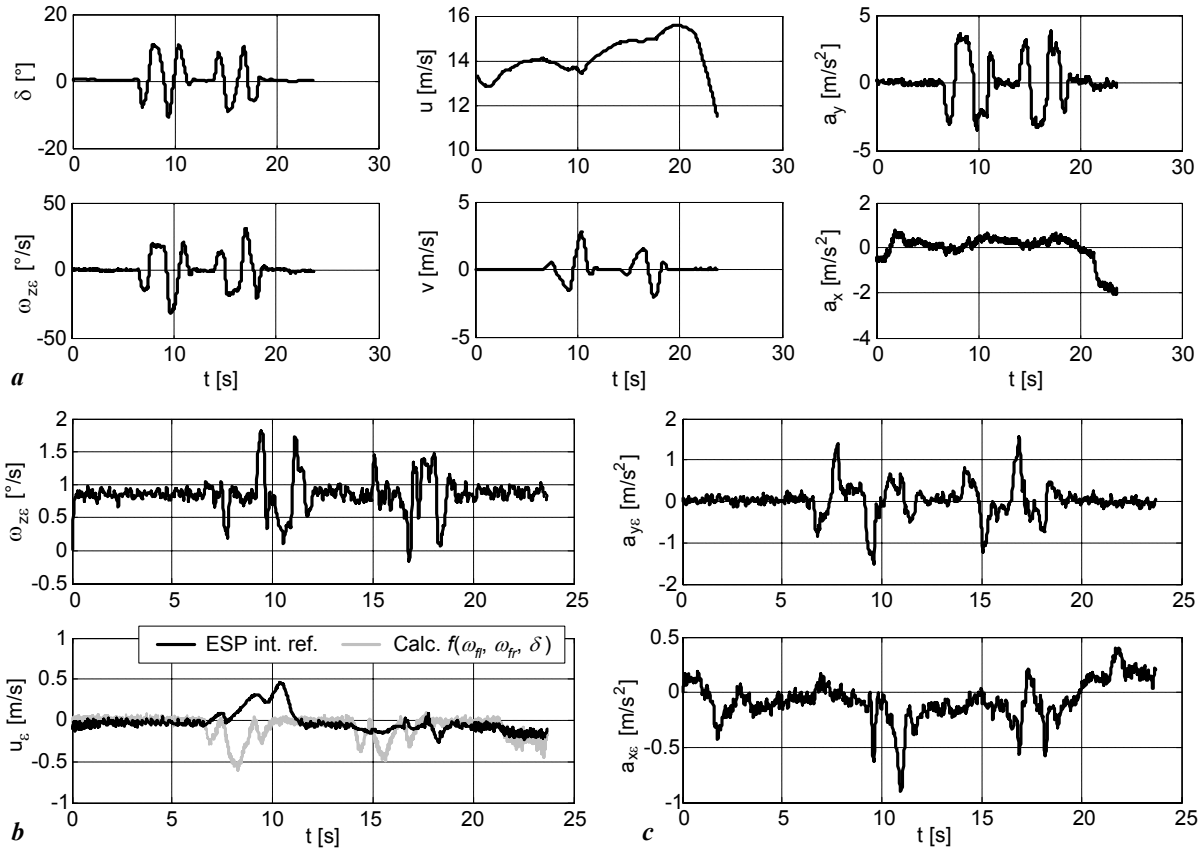

Fig. 6.9 *Measurement errors of the standard VSD sensors for the double lane change maneuver: vehicle dynamics state variables reference signals measured by IMU (a), wheel seed sensors based vehicle velocity and yaw rate gyro measurement errors (b), and lateral and longitudinal acceleration measurement errors (c).*

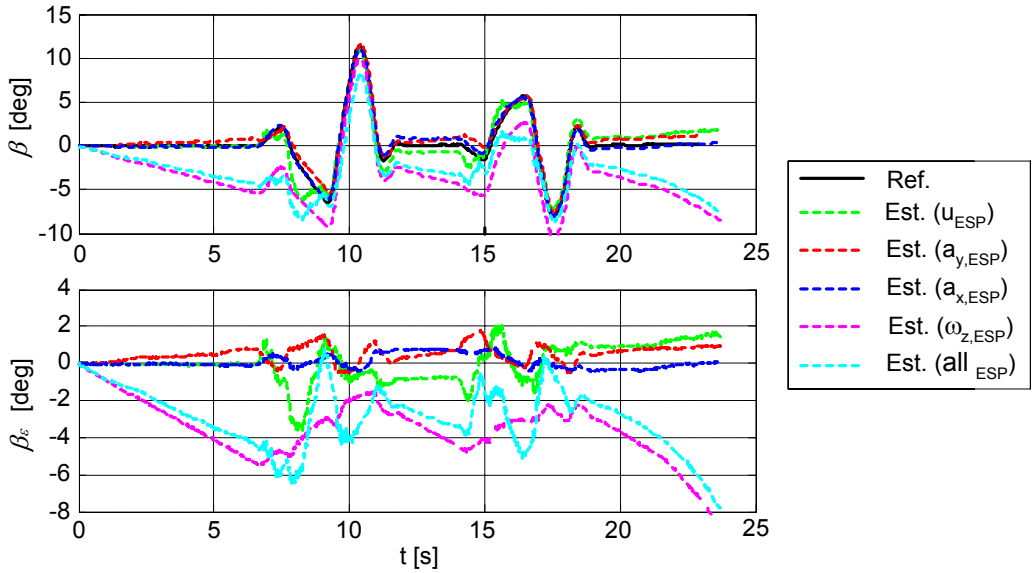

Fig. 6.10 *Sideslip angle estimation errors induced by the measurement errors of the standard VSD sensors for double lane change maneuver at velocities of 50kph.*

The results shown in Fig.6.10 indicate that the largest impact to the estimation error has the yaw rate gyro offset error, which in the initial interval of the experiment (during the straight driving) results in a large drift-like estimation error. Evidently, the offset is present in the yaw rate gyro measurement (see Fig. 6.9b). However, this kind of error can be effectively suppressed by a simple offset compensation action during the straight driving conditions. Moreover, if the estimator measurement update (i.e. correction phase) is disabled during the initial interval of straight driving, the measurement offset related estimation error buildup will be prevented, and the overall estimation errors significantly reduces (see the results presented in Fig. 6.11). Note that all measurement errors in VSD sensor signal are present in those verification tests (i.e. none of the error has been compensated).

More precisely, by switching off the EKF measurement update and related correction of the a-priori state estimates according to Eq. (6-14), during the intervals of the straight driving when the underlying vehicle dynamics model becomes unobservable, helps in reduction of the measurement offsets-related drift-like estimation errors. For this purpose the control variable C_{off} has been defined as (see Fig. 6.11c):

$$C_{off}(k)=\begin{cases}0 & \omega_z(k)<\omega_{z,th}\wedge a_y(k)<a_{y,th}\vee\ u(k)<u_{th}\\ 1 & else\end{cases} \tag{6-18}$$

that is utilized for activating and deactivating the KF measurement update phase, and where $a_{y,th}$, $\omega_{z,th}$, and u_{th} are the preset thresholds representing a tuning parameters. In order to reduce the chattering effects in calculation of the C_{off} (i.e. the measurement noise-related frequent and multiple setting and resetting) the filtered measurement signals have been used. The lateral acceleration and yaw rate measurements are used in Eq. (6-18) for monitoring the vehicle lateral dynamics excitation levels and detecting the conditions of decreased observability of the estimator underlying vehicle dynamics model. Moreover, due to the increased sensitivities of sideslip angle estimation to the longitudinal velocity estimation residuals at low vehicle speeds (see Fig. 6.4) the measurement update and sideslip angle estimation should be held inactive (typically for u < 5 m/s). This restriction, however, does not have effect on the overall performance because in such conditions the sideslip angle is typically very small and vehicle is operating well within the stable region. The results illustrated in Fig. 6.11 have been obtained for the activation thresholds ($a_{y,th}$ = 0.25 m/s^2, $\omega_{z,th}$ = 0.0087 rad/s, and u_{th} = 5 m/s).

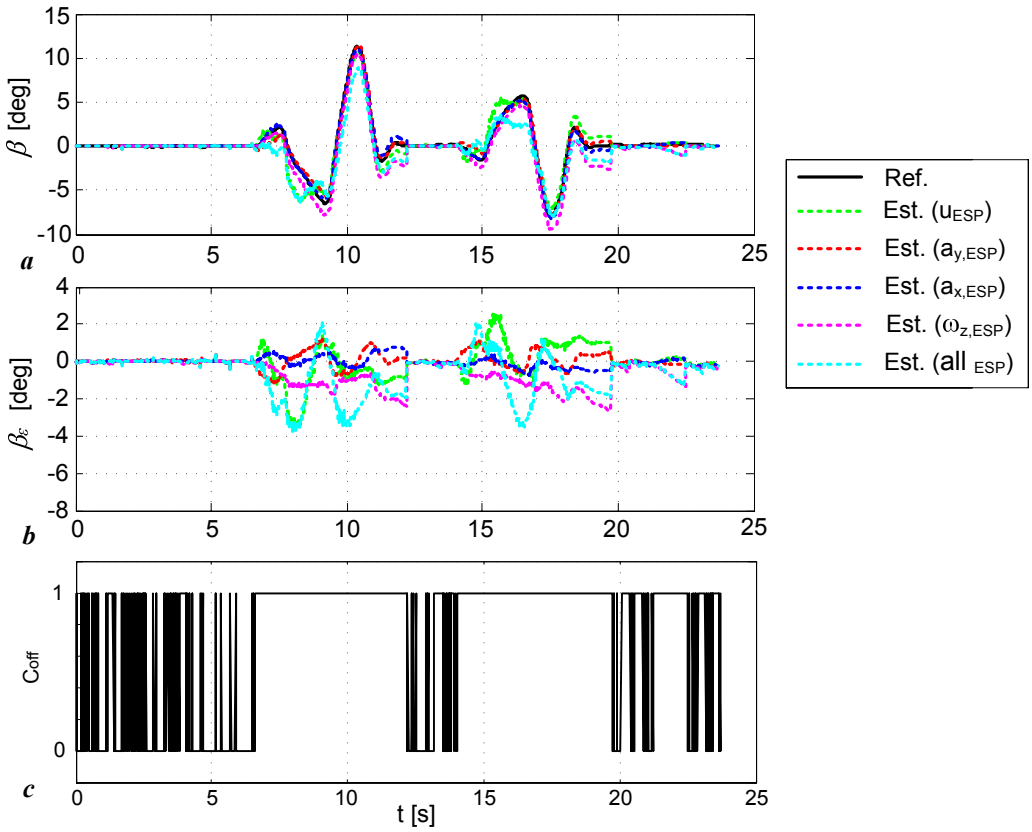

Fig. 6.11 *Sideslip angle estimation errors induced by the measurement errors of the standard VSD sensors for double lane change maneuver at velocities of 50kph in case of activated switching off of the KF a-priori estimation correction during the straight driving: estimates (a), estimation errors (b), and update deactivation signal (c).*

Although, the KF measurement update switching ON/OFF action enables significant reduction in the drift-like estimation error during straight driving conditions, in order to further decrease the estimation errors the sensors offset compensation is required.

Another relevant source of the estimation errors, related to the lateral accelerometer measurement bias, is a result of the gravity acceleration component (i.e. $g\sin\phi\cos\theta \approx g\sin\phi$) see Eq. (5-7). In order to be able to compensate for such errors, the information regarding the vehicle roll is required. On the other hand, the estimation errors induced by the wheel speed and longitudinal acceleration measurement errors are not likely to be resolved by the compensation (i.e. the compensation would require additional sensors and would be highly sensitive to road disturbances, braking, accelerating actions etc.). These errors could be, on the other hand, reduced by performing adequate measuremement preprocesing and/or by tuning of the KF state and measurement covariances.

6.5.2 Roll angle estimation for lateral accelerometer bias compensation

The roll gyro is not the standard vehicle dynamics sensor and therefore the roll angle, aimed for the compensation of the gravity acceleration component in the lateral accelerometer measurement, needs to be estimated somehow. For this purpose, a simple second order model of the vehicle roll dynamics, defined by Eqs. (6-19)-(6-22) has been utilized [49] (see Appendix C for meaning and values of roll model parameters):

$$I_{rc}\ddot{\phi} + \delta F_z\, t - m_r a_y h_1 = 0 \tag{6-19}$$

The moment of inertia for the instantaneous roll axis and change in the tire normal loads can be defined as:

$$I_{rc} = \frac{I_{xx}}{2} + m_r h_1^2 \tag{6-20}$$

$$\delta F_z = b_r \frac{t}{2}\dot{\phi} + k_r \frac{t}{2}\phi \tag{6-21}$$

By inserting the Eqs. (6-20) and (6-21) into Eq. (6-19) the following roll model is obtained:

$$I_{rc}\ddot{\phi} + \frac{b_r t^2}{2}\dot{\phi} + \frac{k_r t^2}{2}\phi = m_r h_1 a_y \tag{6-22}$$

Based on the above equations the transfer function model of the vehicle roll dynamics can be defined as:

$$G(s) = \frac{\phi(s)}{a_y(s)} = \frac{m_r h_1}{I_{rc}} \frac{1}{s^2 + b_1 s + k_1} \tag{6-23}$$

where the coefficient in the denominator of transfer function are defined by the following expressions:

$$b_1 = \frac{b_r t^2}{2I_{rc}}, \qquad k_1 = \frac{k_r t^2}{2I_{rc}} \tag{6-24}$$

The state space representation of the above roll dynamics model can be formulated as:

$$\dot{\mathbf{x}} = \begin{bmatrix} 0 & 1 \\ -k_1 & -b_1 \end{bmatrix}\mathbf{x} + \begin{bmatrix} 0 \\ m_r h_1 / I_{rc} \end{bmatrix}\mathbf{u}$$
$$\mathbf{y} = \begin{bmatrix} 0 & 1 \end{bmatrix}\mathbf{x} \tag{6-25}$$

where $\mathbf{x} = \begin{bmatrix} \phi & \dot{\phi} \end{bmatrix}^T$ and $\mathbf{u} = a_y$.

The dynamic vehicle roll model defined by Eq. (6-22) can be applied in a case of driving on a flat road without skidding, and it presumes the linear damper characteristics. Consequently, it looses its accuracy on a banked road and in the case of understeering or oversteering conditions.

On the other hand, the kinematic roll model based on Eq. (6-26) [67] can be used for rough roll angle estimation in the case of driving on the banked road. The below equations can be derived from the accelerometer measurement model (see Chapter 5 and [30]) from Eqs. (5-7) and (5-8) by neglecting the measurement bias and noise terms:

$$\theta = \arcsin\left(\frac{\dot{u} - a_x - \omega_z v}{g}\right), \quad \phi = \arcsin\left(\frac{a_y - \omega_z u - \dot{v}}{g\cos\theta}\right) \tag{6-26}$$

However, the lateral velocity and its derivative are typically not available, and therefore the approximations of the above expressions are used in [67] for estimation of the pitch and roll angles:

$$\hat{\theta} = \arcsin\left(\frac{\dot{u} - a_x}{g}\right), \quad \hat{\phi} = \arcsin\left(\frac{a_y - \omega_z u}{g\cos\hat{\theta}}\right) \tag{6-27}$$

Note that these rough estimates will be valid in the maneuvers in which the lateral velocity and its derivation are small or moderate. These conditions can be monitored by checking the steering angle derivative and lateral acceleration signals. The benefit of the approach given by Eq. (6-27) when compared to the 2nd order roll dynamics model (6-25) is that it can provide reasonably accurate roll estimates on the banked road. Therefore, the large discrepancies between these two models can be used as an indicator of the bank (under presumption that the severe lateral dynamics excitation conditions characterized with large v and $\dot{v}$ can be detected).

Another issue related to reconstruction and measurement of the roll angle is related to the effect of the so-colled kinematic bias. Namely, a kinematic bias is an additive component in the roll rate gyro signal, which is induced by the combined cornering and pitch motion of the vehicle [67], and it can be derived from the following basic kinematic equations:

$$\dot{\phi} = \omega_x + \omega_y \sin\phi\tan\theta + \omega_z \cos\phi\tan\theta \tag{6-28a}$$

$$\dot{\phi} \approx \omega_x + \omega_z \tan\theta \tag{6-28b}$$

Namely the kinematic bias in the roll rate gyro measurement is induced by the second right-hand side term in Eq. (6-28b), which can result in potentially large roll angle error.

Apparently this kinematic bias, illustrated in Fig. 6.12b for the driving on a circular track maneuver, has not been compensated for within the IMU. Therefore, it should be considered when dealing with the reference roll angle measurement signal that is used for validation of the roll angle estimate obtained from the simple second order roll dynamic model and used for the later compensation of the lateral accelerometer bias in sideslip angle estimator.

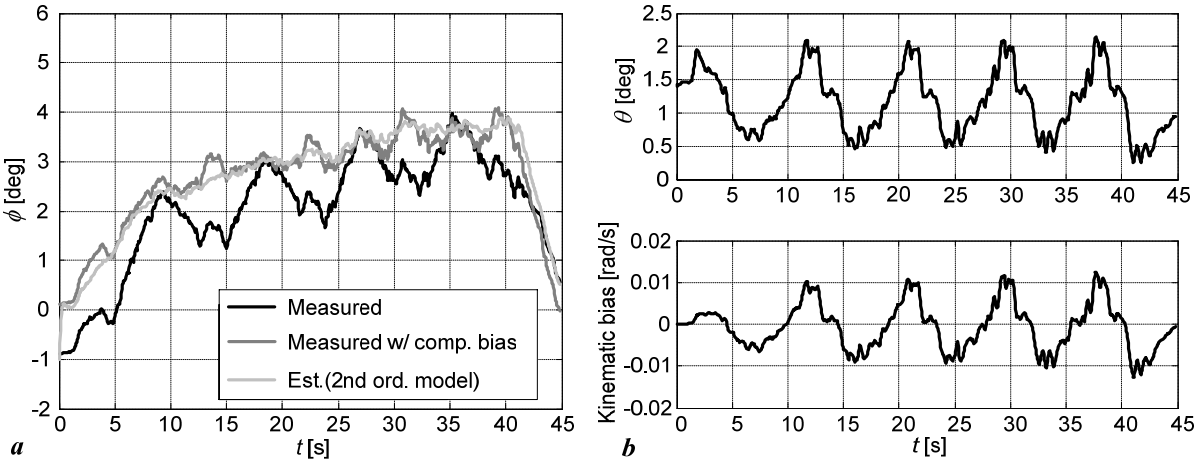

Fig. 6.12 *Evaluation of roll angle estimate for the driving on a circular track with variable road superelevation (pitch angle).*

Kinematic bias present in the reference roll rate sensor measurement (see Fig. 6.12b), induced by a non-negligible $\theta\omega_z$ term in the roll kinematic model (6-28b), directly results with the roll angle reconstruction error represented in this case as a saw tooth signal superimposed upon the true roll angle [67]. Note that the estimated roll angle, based on the second order roll dynamics model (6-23), is not influenced by this kinematic bias since it does not use the roll rate sensor measurement. The results shown in Fig. 6.12a indicate that if the kinematic bias is compensated the estimated and measured roll angle signals are characterized with rather small discrepancies.

Fig. 6.13 illustrates the relevant vehicle dynamics measurement errors, the effectiveness of the compensation of the yaw rate gyro offset and lateral accelerometer gravity-related offset term related errors, and respective improvements in the sideslip angle estimation accuracy for a double lane change maneuver.

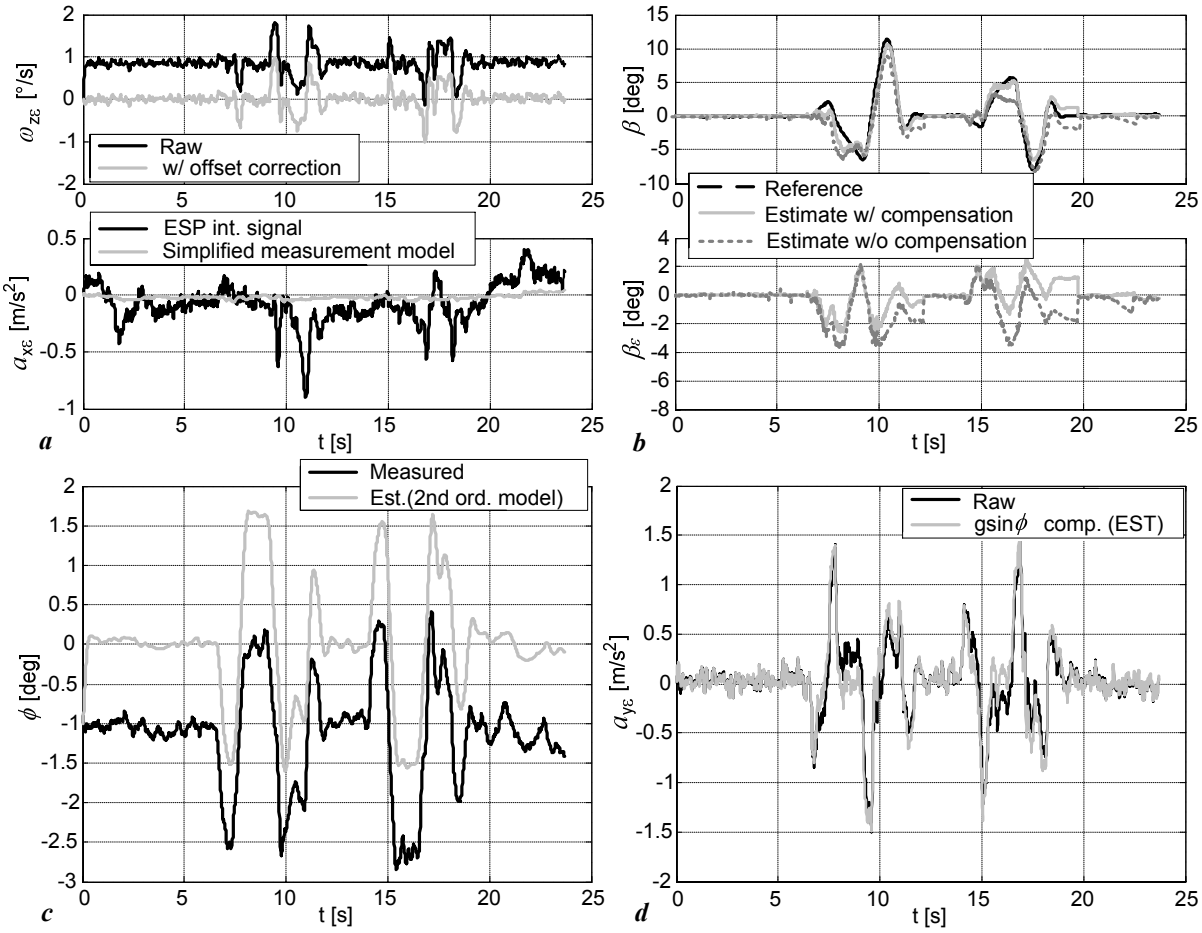

Fig. 6.13 *Estimation errors in case of sensor measurement errors compensation w/o a_y filtering: yaw rate gyro and longitudinal accelerometer errors (a), sideslip angle estimate and estimation error (b), roll angle estimate (c), and lateral accelerometer errors (d).*

The presented results (samling rate T_s = 10ms) have been obtained for the following settings of the state covariance matrix **Q** =diag([1.6, 0.1, 0.02, 0.2, 0.2, 20, 20, 20, 20]·10^7) and measurement covariance **R** = diag([0.01, 0.1, 0.1, 0.1, 0.1, 1]).

According to the results illustrated in Fig. 6.13 there is an offset in the reference roll angle signal obtained from the RT3003 measurement unit (ϕ_{off} = -1deg). Besides this offset in the reference signal, the roll angle estimate, obtained by using the roll dynamics model, is quite accurate. Consequently, the lateral accelerometer gravity component (rather small in this maneuver) can be effectively compensated for (Fig. 6.13d), and related estimation error reduced (Fig. 6.13b).

The lateral accelerometer signal is characterized by relatively large noise that results in the increased sideslip estimation errors, especially under conditions of small lateral dynamics excitation (indicated by small lateral acceleration and yaw rate that result in small lateral velocity and sideslip angle as well). However, these errors can be effectively reduced by

utilizing a low-pass filter and filtering the lateral accelerometer measurement before it is forwarded to the Kalman filter. The efficiency of such pre-filtering is illustrated in Fig. 6.14 for a double lane change maneuver. The 2nd order Butterworth low-pass filter with f_g = 5Hz has been utilized. Moreover, the linear acceleration signals are usually also filtered within the inertial measurement unit in order to generate the reference signals. In this case, in order to compensate for the effect of time delay in accelerometer signal the reference sideslip angle is also filtered and the results of this intervention on the estimation are illustrated in Fig. 6.14. (all other parameters remained the same). According to the results presented in Fig. 6.14b it is evident that the transient estimation errors can be effectively reduced by removing the abovemantioned time delay between the inertial sensors measurements and sideslip angle reference.

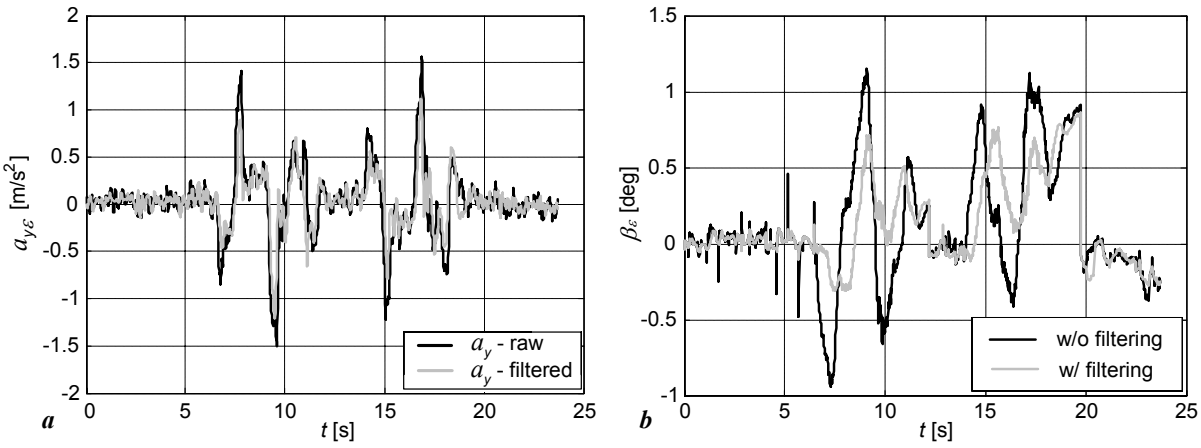

Fig. 6.14 *Sideslip angle estimation error after compensating for the time delay in lateral accelerometer signal: lateral accelerometer measurement error (a) and sideslip angle estimation error (b).*

The effect of the state covariance tuning of the longitudinal velocity state variable upon the accuracy of sideslip angle estimation is illustrated in Fig. 6.15. Namely, by setting the higher value of the longitudinal velocity state variable covariance q_u results in lower sideslip angle peak estimation errors during transients. The simultaneous change of the covariance, of both the longitudinal and the lateral velocities (q_u and q_v), however does not have any affect upon the estimation error (i.e. it is predominantly determined by their ratio).

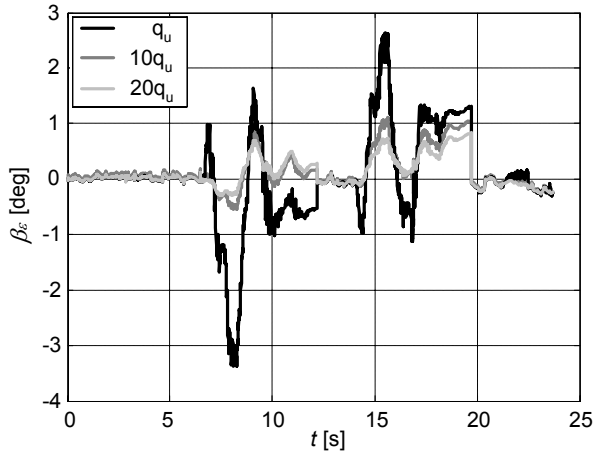

Fig. 6.15 *Sideslip angle estimation error vs. longitudinal velocity state covariance q_u for double lane change maneuver and compensated dominant sensor errors.*

A similar analysis has been carried out for the slalom maneuver on a flat low-μ surface. The vehicle dynamics state variables and sensor measurement errors are shown in Fig. 6.16.

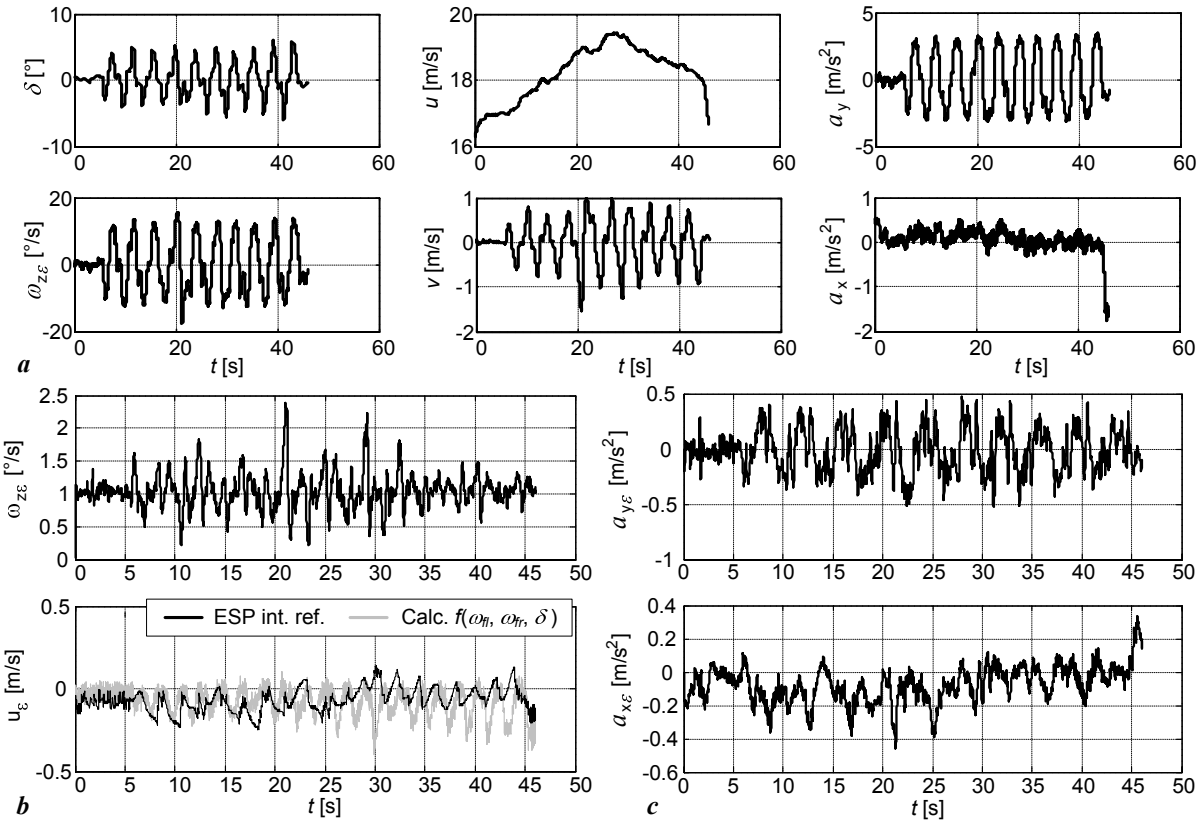

Fig. 6.16 *Measurement errors of the standard VSD sensors for the slalom maneuver: vehicle dynamics state variables reference signals measured by IMU (a), wheel seed sensors based vehicle velocity and yaw rate gyro measurement errors (b), and lateral and longitudinal acceleration measurement errors (c).*

The related sideslip angle estimation results shown in Fig. 6.17, obtained for the case of compensated yaw rate bias and lateral accelerometer gravity component error, indicate that the dominant sources of the remaining estimation errors are uncompensated lateral acceleration measurement error (e.g. in this maneuver the total acceleration measurement error amounts approximately 10% of the peak acceleration value, see Fig. 6.16c) and longitudinal velocity errors. The remaining yaw rate errors (after bias compensation) and longitudinal acceleration-related errors are present, but they are relatively small (less then ±0.3 deg).

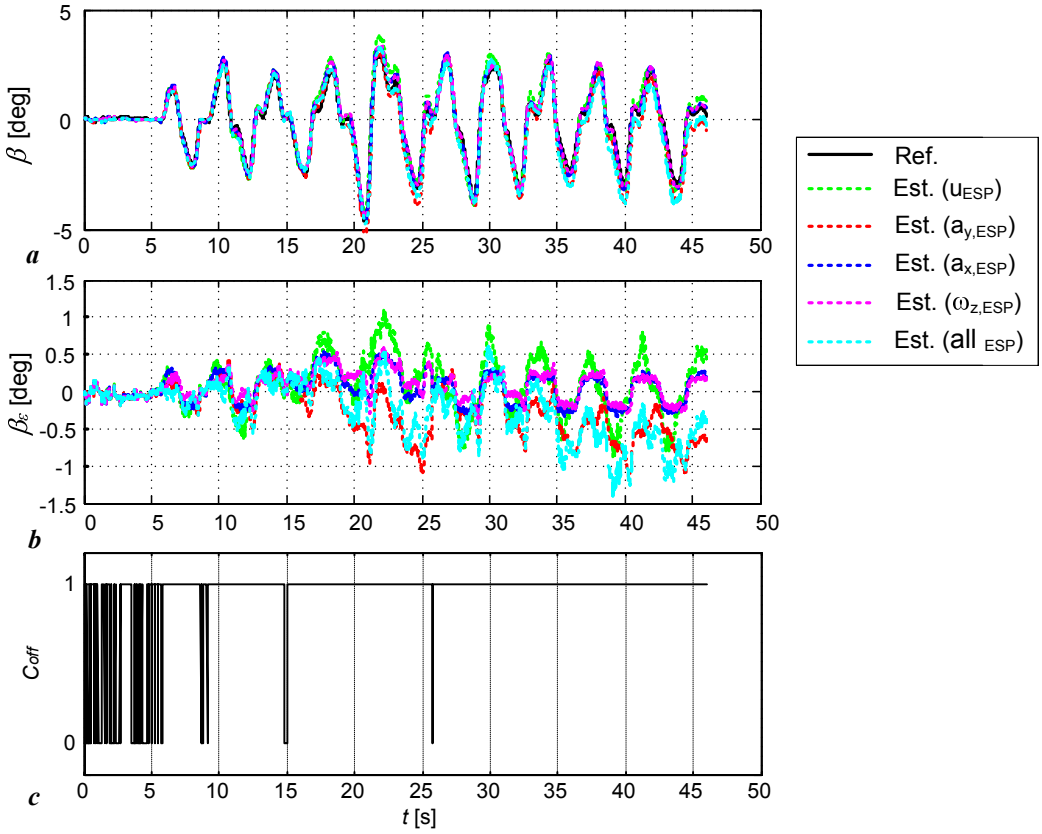

Fig. 6.17 *Sideslip angle estimation errors induced by the measurement errors of the standard VSD sensors for slalom maneuver at velocities of 60kph: estimates (a), estimation errors (b), and update deactivation signal (c).*

Note that the overall estimation errors induced by the standard vehicle dynamics sensors measurement inaccuracies after the compensation are relatively small for the considered slalom maneuver (see Fig. 6.17b, $\tilde{\beta} < 1$ deg). Moreover, the estimator switching-off action, controlled by C_{off} signal (shown in Fig. 6.16c) mitigates the generation of the larger drift-like estimation errors. The effectiveness of the error compensation is highlighted in Fig 6.18b

where the sideslip angle estimates without sensor error compensation is compared to the one obtained after compensation already shown in Fig 6.17b (see light blue colored trace).

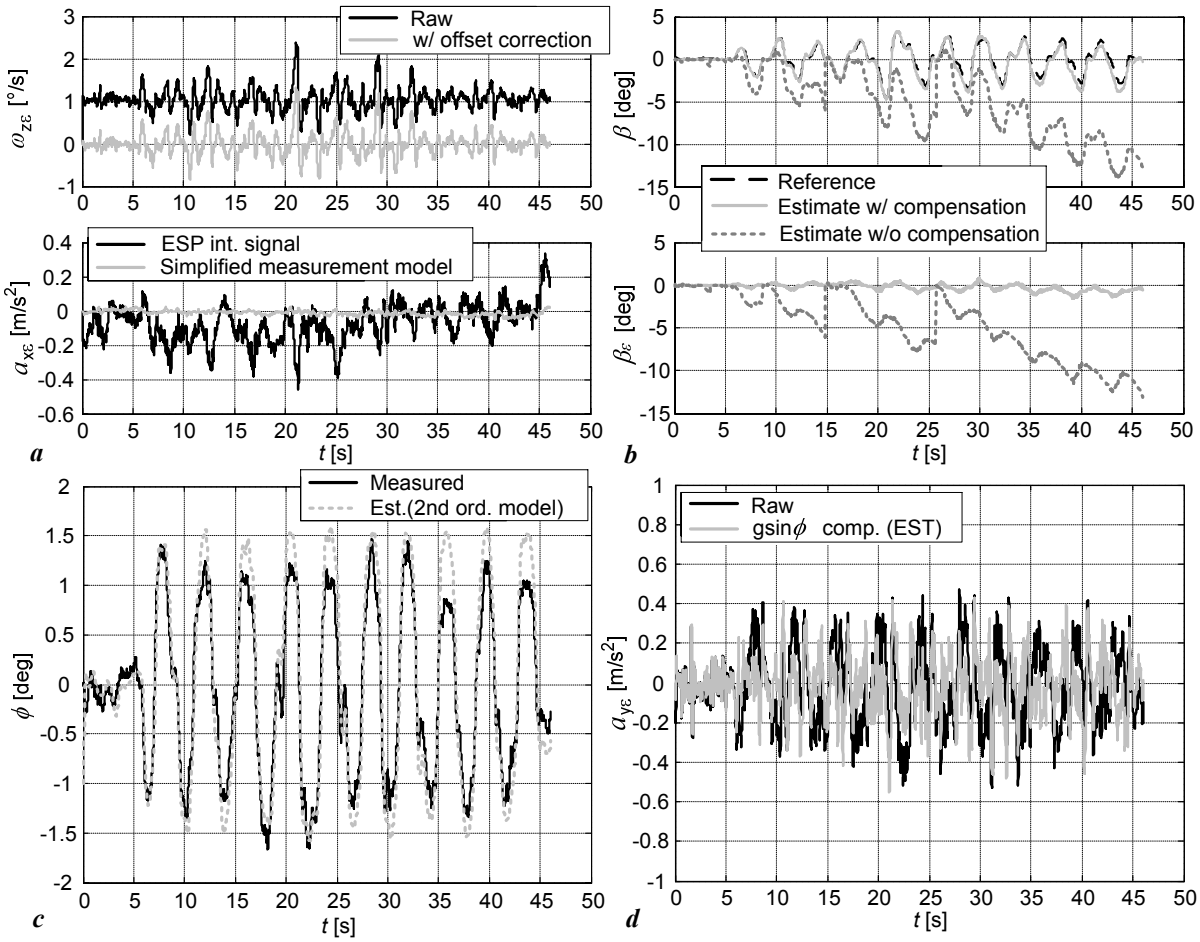

Fig. 6.18 *Estimation errors in case of sensor measurement errors compensation: yaw rate gyro and longitudinal accelerometer errors (a), sideslip angle estimate and estimation error (b), roll angle estimate (c), and lateral accelerometer errors (d).*

The accuracy of the roll angle estimation based on the simple 2nd order dynamic model and related lateral acceleration error compensation are illustrated in Fig. 6.18c and Fig. 6.18d, respectively. The roll angle estimation errors at a peak roll angle values can be related to the presence of the road disturbances, nonlinear damper characteristics etc. Nevertheless, the sideslip estimation error in case of the compensated sensor measurement errors is reduced well within the one degree span (Fig. 6.18b and Fig. 6.17b).

Fig. 6.19 illustrates the estimation results for the steady cornering maneuver on the circular track at low-μ surface, which is characterized with relatively poor excitation of the vehicle lateral dynamics (i.e. small lateral velocities) and consequently represents the challenging maneuver for accurate estimation of the sideslip angle. In Fig. 6.20 the respective sensor measurement errors and roll angle estimate have been presented.

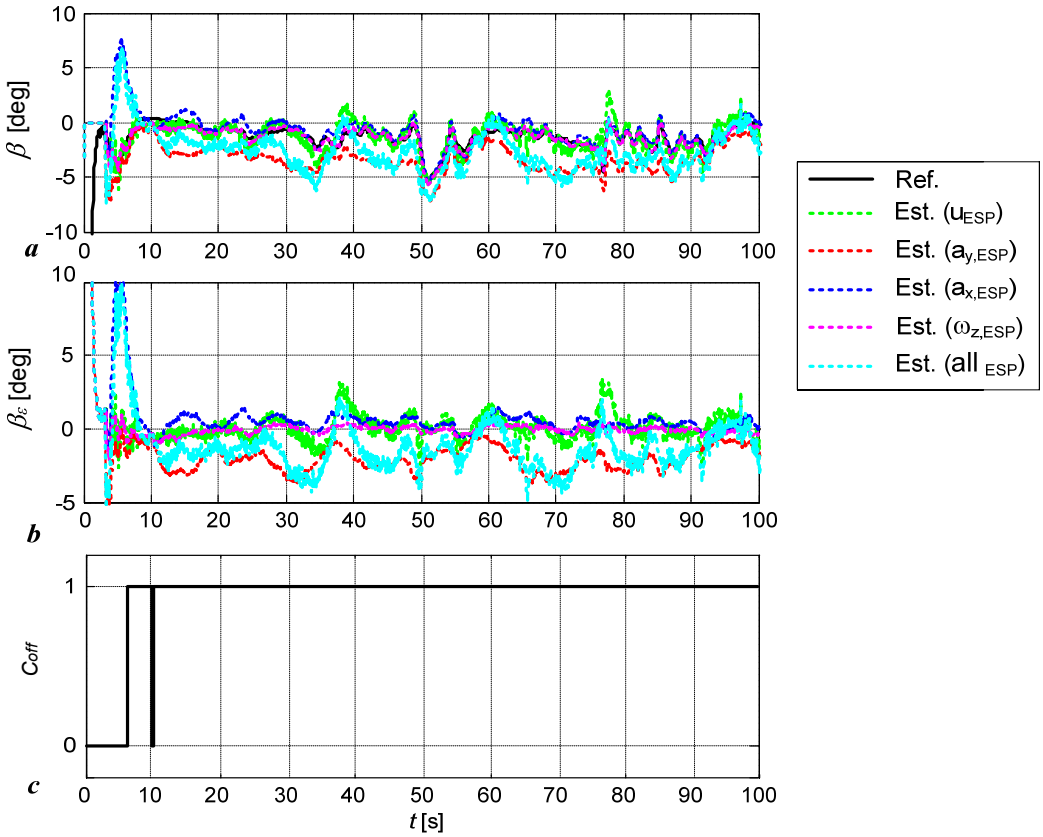

Fig. 6.19 *Sideslip angle estimation errors induced by the measurement errors of the standard VSD sensors for cornering maneuver: estimates (a), estimation errors (b), and update deactivation signal (c).*

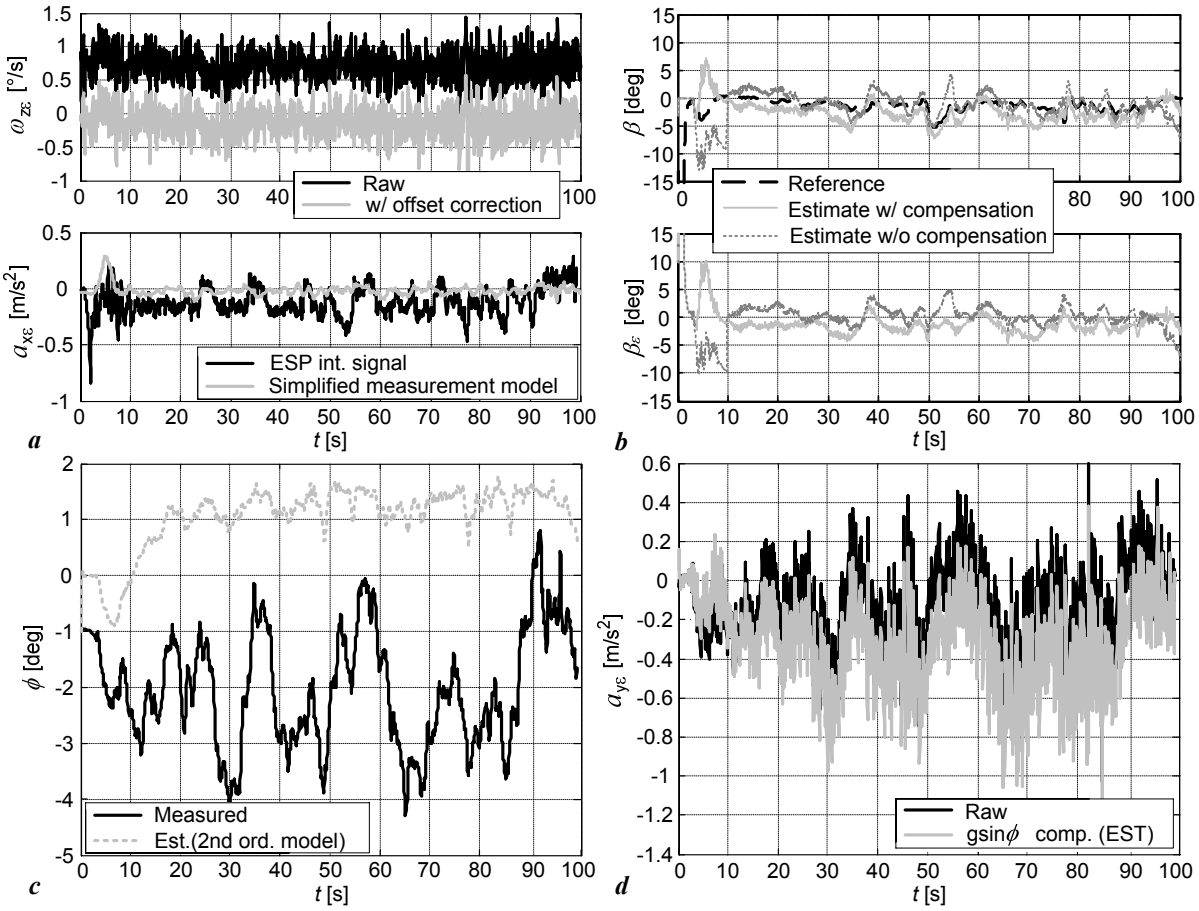

Fig. 6.20 *Estimation errors in case of sensor measurement errors compensation for cornering maneuver: yaw rate gyro and longitudinal accelerometer errors (a), sideslip angle estimate and estimation error (b), roll angle estimate (c), and lateral accelerometer errors (d).*

Evidently in this maneuver the relation between lateral acceleration and roll angle is unreliable while the large component in the measured roll angle signal is caused by the road surface (packed snow) unevenness disturbances and some road bank. In such conditions the lateral accelerometer gravity bias compensation based on the rough roll angle estimate obtained from the simple second order dynamic roll model is ineffective. Moreover if the state covariance matrix is increased (more precisely if the q_u component is increased) the estimation errors becomes much larger and still the compensation remains ineffective. Since this maneuver is characterized by the steady cornering conditions without excessive lateral velocity and its derivative the kinematic roll model defined by Eq. (6-27) can be applied for roll angle estimation. Difference between the two of the roll angle estimates, illustrated in Fig. 6.21, clearly indicates the presence of the road bank or some kind of road unevenness disturbance.

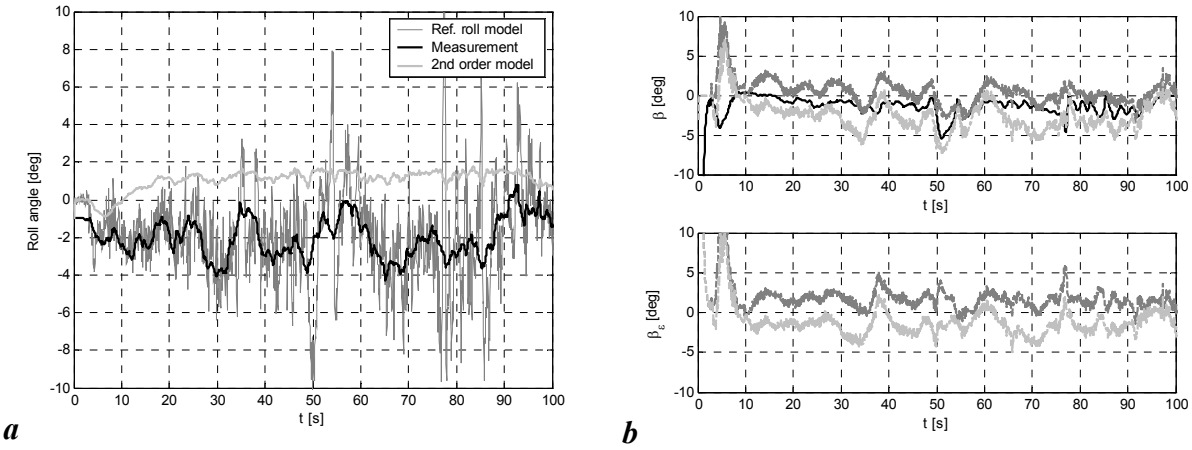

a ***b***

Fig. 6.21 *Comparison of the roll angle estimates (a) and the effectiveness of the lateral acceleration gravity bias compensation and related decrease of the sideslip angle estimation error (b), based on the reference kinematic model and 2nd order dynamic model.*

The results of the roll angle estimate presented in Fig. 6.21a indicate a favorable accuracy of the reference (kinematic) roll model, when compared to the second order dynamic model-based estimate, for the constant cornering maneuver characterized with low excitation level of the vehicle lateral dynamics. Nevertheless, the better estimate of the roll angle and improved compensation of the gravity-related accelerometer bias the sideslip estimation accuracy has not been improved much, as a result of the combined effects of other, uncompensated sources of errors (e.g. longitudinal velocity and acceleration measurement errors), low excitation of the lateral dynamics and related small magnitudes of the sideslip angle (i.e. numerical sensitivity constraints, cf. Fig. 6.4).

In Fig. 6.22 and 6.23 the vehicle dynamics sensor measurement errors and related sideslip angle estimation errors have been analyzed for the J-turn maneuver carried out on a low-μ surface (i.e. packed snow). The KF longitudinal velocity threshold parameter has been decreased (u_{th}=0.25m/s) in order to ensure the valid estimate for the most part of the interval with emphasized sliding of the vehicle (i.e. time interval from 12 to 15th second that is characterized with longitudinal velocity less then 5m/s).

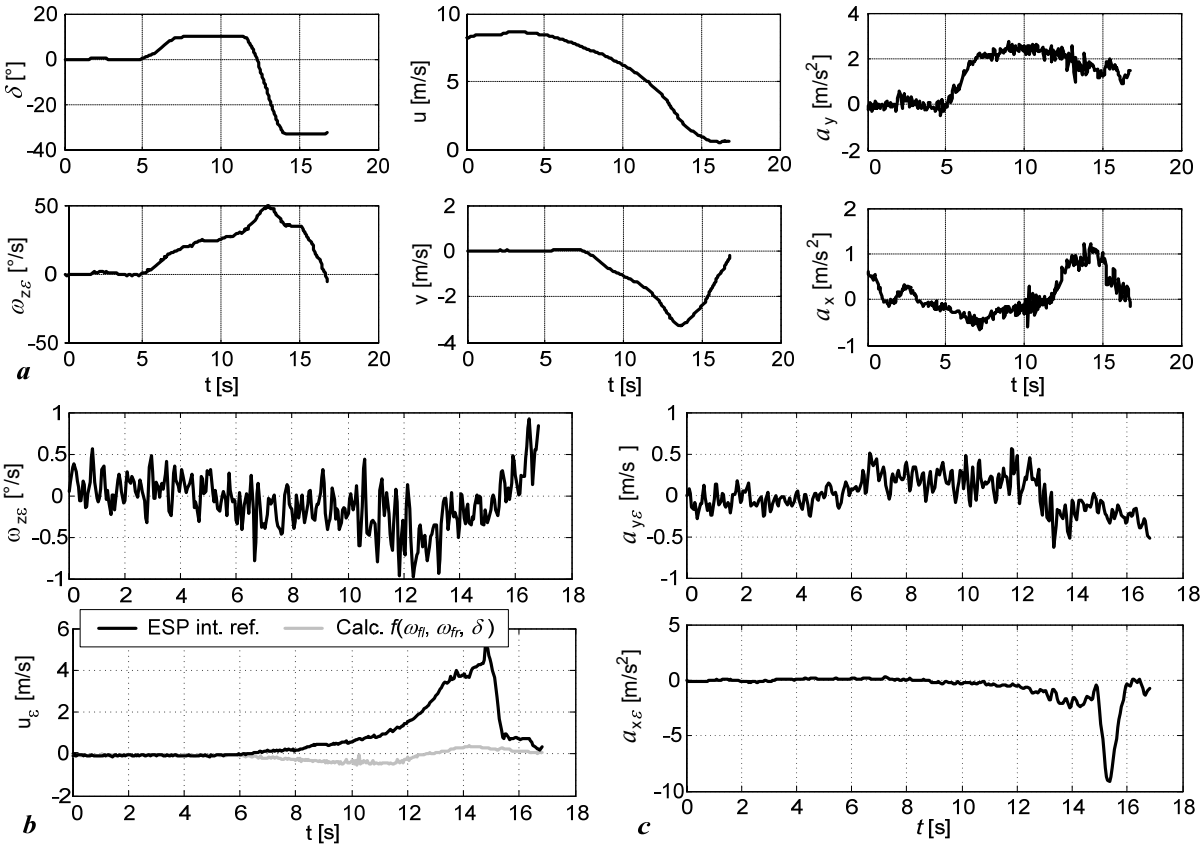

Fig. 6.22 *Measurement errors of the standard VSD sensors for J-turn maneuver: vehicle dynamics state variables reference signals measured by IMU (a), wheel seed sensors based vehicle velocity and yaw rate gyro measurement errors (b), and lateral and longitudinal acceleration measurement errors (c).*

Based on the results given in Fig. 6.22, dominant measurement erros are observed in the longitudinal velocity and longitudinal acceleration measurement signals. Consequently, the sideslip angle estimation error is predominantly determined by the vehicle velocity error as illustrated in Fig. 6.23 (compare the green and cyan trace on time interval 8-16th second).

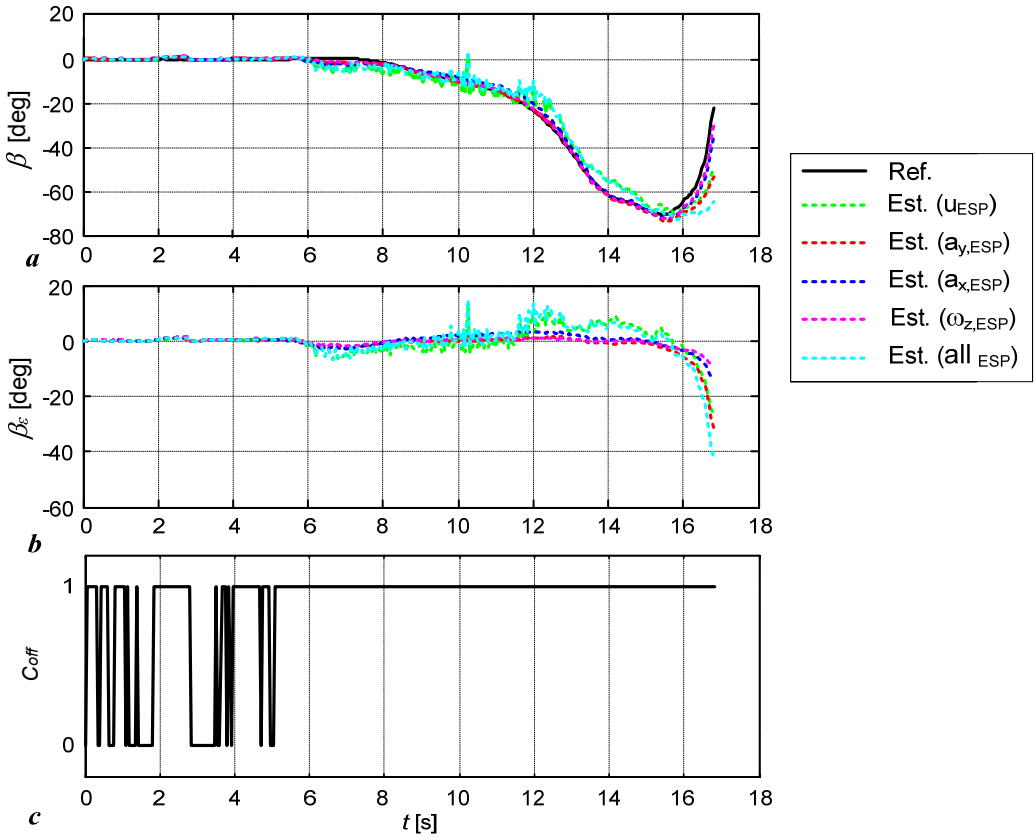

Fig. 6.23 *Sideslip angle estimation errors induced by the measurement errors of the standard VSD sensors for J-turn maneuver: estimates (a), estimation errors (b), and update deactivation signal (c).*

The above results have been obtained for the case of compensated lateral acceleration and yaw rate measurement biases. Problem of large sideslip angle estimation errors at the end of the maneuver characterized with relatively high sideslip values is related to (i) small vehicle longitudinal velocity and related numerical errors in calculating sideslip angle, and (ii) significant longitudinal velocity measurements errors induced by large longitudinal slips due to braking action. Fig. 6.24b illustrates that the β-estimation is effective regardless of the presence of large longitudinal velocity errors observed in Fig. 6.22b. In this case the difference between the proposed approach of calculating the vehicle velocity solely from the front non-driven wheel and the internal reference velocity signal derived directly from vehicle's ESP system is emphasized, and the proposed approach has proved to be much more accurate, because it does not relay on the rear tire speed signals characterized with large longitudinal slips due to severe braking action undertaken at the end of this maneuver. Although the absolute values of the sideslip angle estimation errors are rather high the relative errors are reasonable for this kind of driving maneuver and when considering the accuracy limitations of the standard vehicle dynamics sensors.

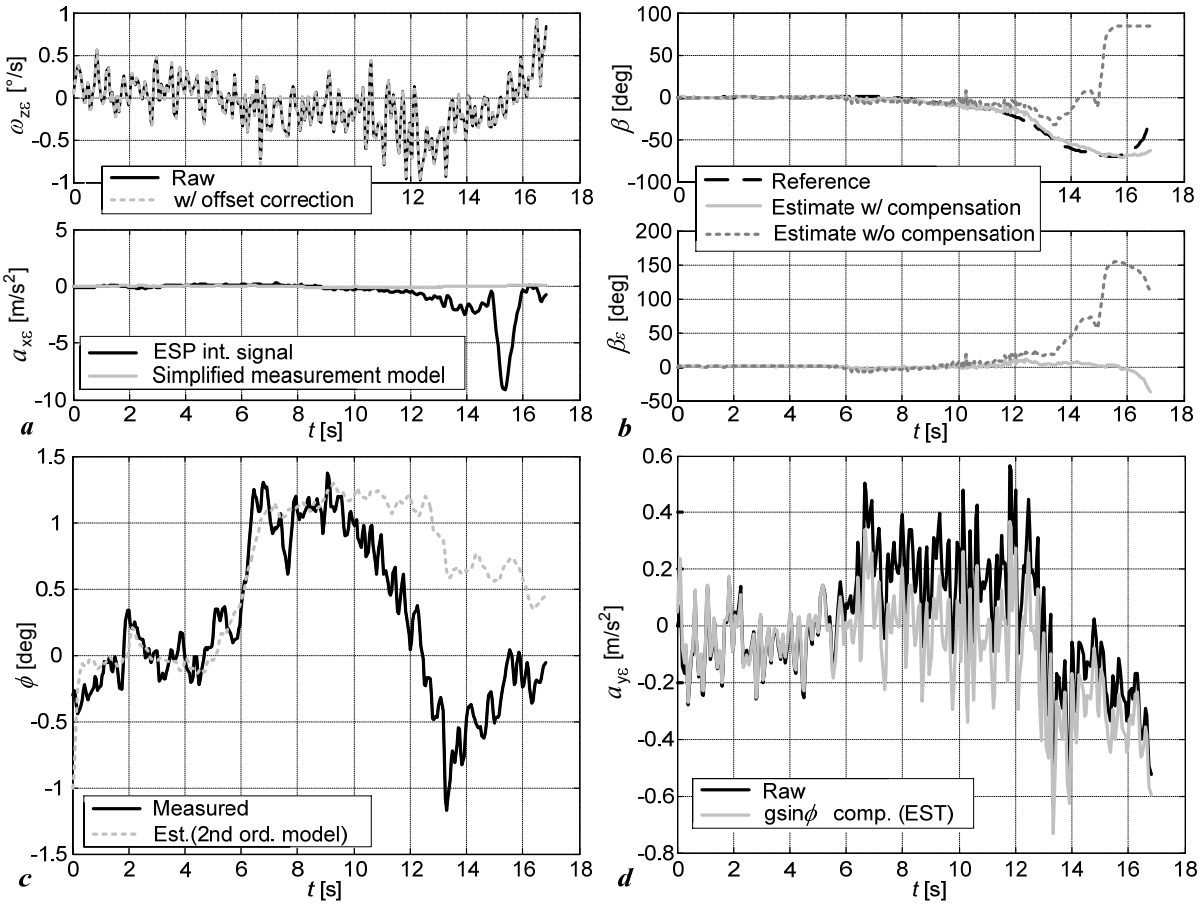

Fig. 6.24 *Estimation errors in case of sensor measurement errors compensation for J-turn maneuver: yaw rate gyro and longitudinal accelerometer errors (a), sideslip angle estimate and estimation error (b), roll angle estimate (c), and lateral accelerometer errors (d).*

In Fig. 6.25 the measurement errors of the standard set of vehicle dynamics sensors are illustrated for the case of gentle slalom maneuver on circular banked high-μ track. This maneuver is exceptionally challenging since the vehicle is driven on a banked road and the lateral dynamics is poorly excited (i.e. the lateral velocity and sideslip angle are small). Also, the measurement errors in lateral acceleration signal are significant (external disturbance) and the roll estimation based on the second order dynamic model becomes highly inaccurate and consequently the error compensation ineffective (see Fig. 6.26). However, in such conditions the kinematic roll model can provide favorably accurate roll angle estimate the can be used for effective lateral acceleration measurement error compensation and significant improvement of the sideslip angle estimation accuracy (see bright gray trace in Fig. 6.26b). It should be noted that this error is consistent with the results obtained for other maneuvers where the error margin of the estimator, when using a standard set of vehicle dynamics

sensors instead of precision IMU and GPS, typically doubles (the error margin for this maneuver in the nominal case amounts approximately 1°).

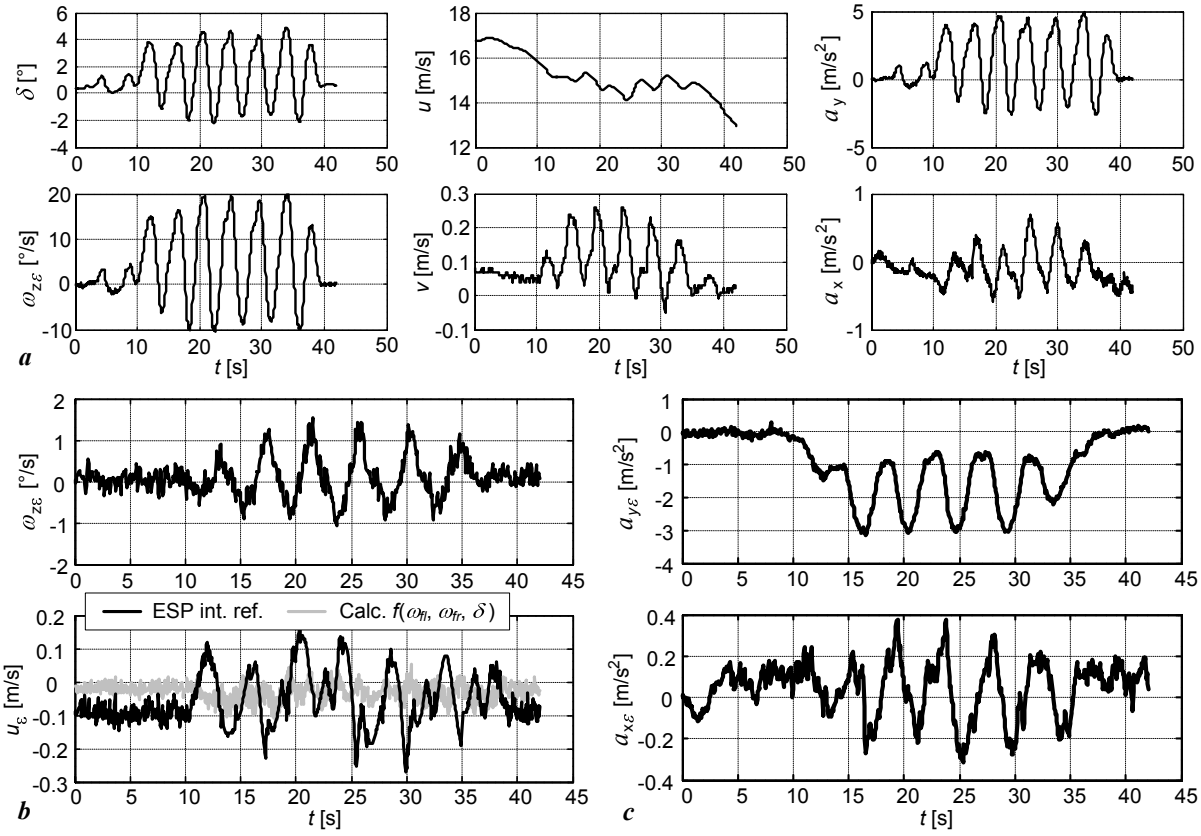

Fig. 6.25 *Measurement errors of the standard VSD sensors for the steady cornering maneuver on banked circular track: vehicle dynamics state variables reference signals (a), wheel speed sensors based vehicle velocity and yaw rate gyro measurement errors (b), and lateral and longitudinal acceleration measurement errors (c).*

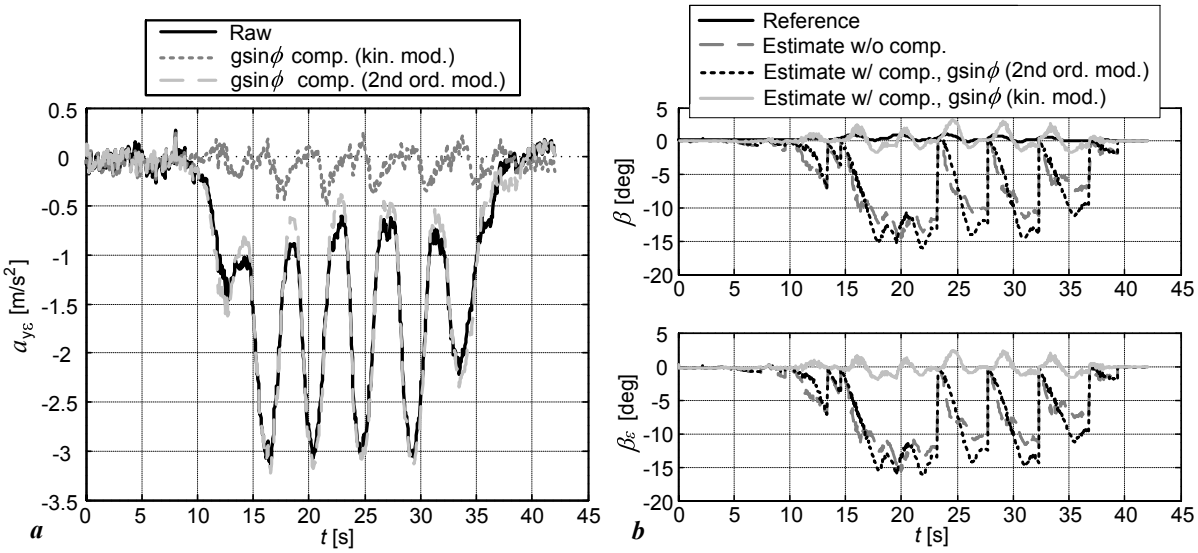

Fig. 6.26 *Lateral acceleration measurement errors compensations based on the roll angle estimation (a) and related sideslip angle estimation errors (b).*

6.6 Adaptive fading EKF - based estimator

In order to improve the overall estimation accuracy of the basic, non-adaptive estimator for a wide range of operating conditions and driving maneuvers the adaptive fading algorithm has been utilized which changes the Kalman filter state and measurement covariance matrices by multiplying them with a certain time-variant scaling factors. More precisely, the single fading and multiple fading factors have been considered for formulation of the adaptive Kalman filter (i.e. SFF or MFF Adaptive Fading Kalman filter respectively, see Chapter 3) aimed for estimator design. Scaling factors are determined based on the difference between the anticipated theoretical measurement residuals or innovation (defined by Eq. (3-29)) and the true residuals obtained from Eq. (3-30). These adaptation algorithms change the state and measurement covariance matrices (and consequently the Kalman gain and a-priori state estimation error covariance matrices) in the presence of the increase of the measurement residuals indicating the decrease in the reliability levels of the process model (i.e. unmodeled disturbance, change in the model) or increased errors in the measurement model (i.e. increased sensor errors). Note that the model observability issues and related estimation errors cannot be avoided by adaptation but only by switching of the estimator (as illustrated in Fig. 6.10).

In Fig. 6.27 the performance of the single scaling factor adaptive fading-based estimator has been compared to the nominal non-adaptive filter for the constant steering driving maneuver on the sloped circular asphalt track (high-μ) and utilization of the high precision sensors measurements. Road bank angle constitute the unmodeled disturbance that affects the reliability of vehicle dynamics and measurement models, and consequently decreases the estimation accuracy. Primary application of such adaptation methods are thus related to dealing with changes in the reliability of the model itself due to the presence of the unmodeled dynamics or external disturbances that induce discrepancies between the predicted and measured residuals.

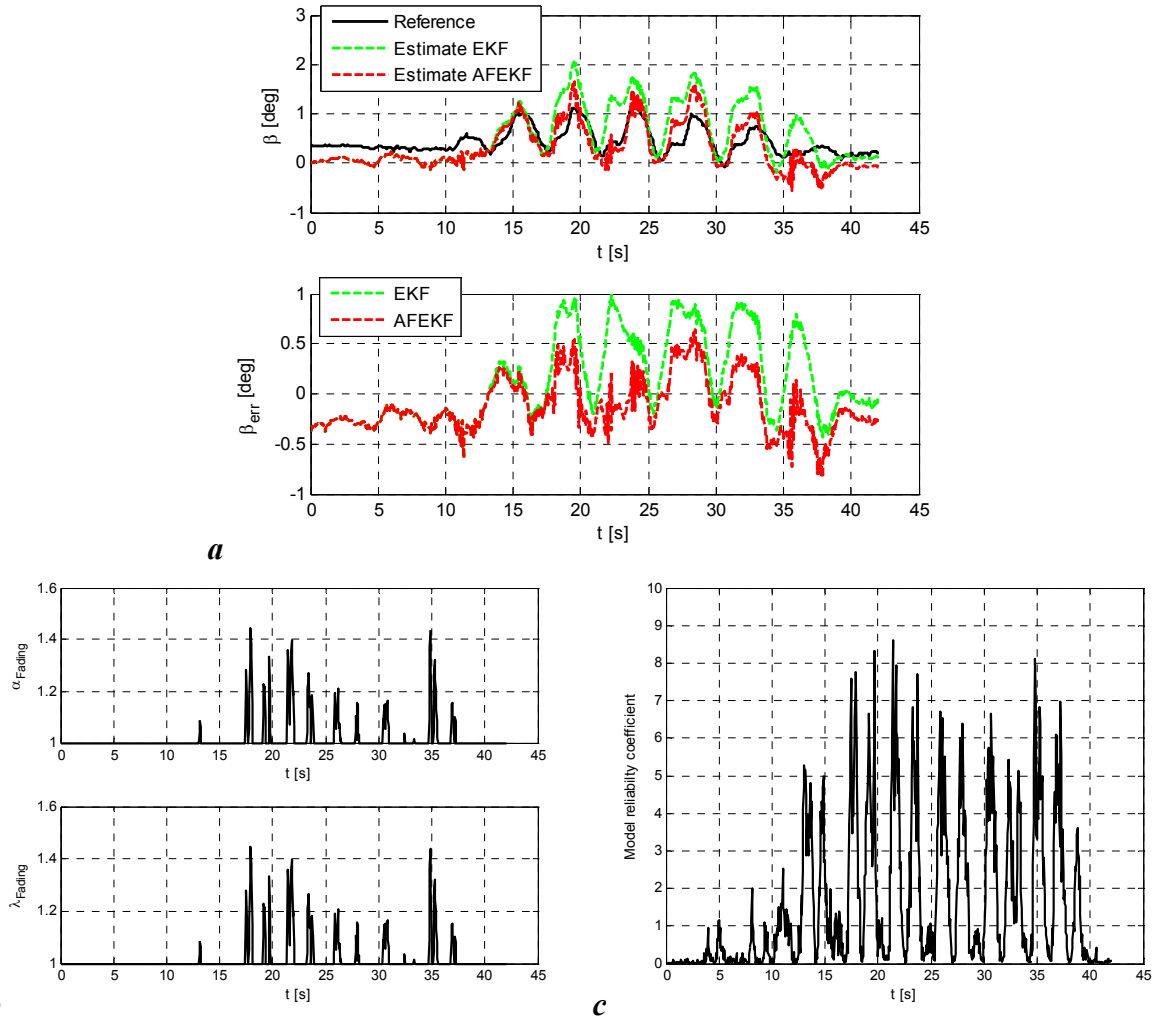

Fig. 6.27 *Single fading factor AFEKF performance for driving on the banked oval concrete track: sidesip angle estimate and estimation error (a), state covariance and measurement covariance fading factor (b), and dynamics model reliability signal (c).*

The initial sideslip angle estimation error of approximately 0.35deg (see Fig. 6.23a) remains constant during the time interval from 0 to12 seconds due to the low excitation of the lateral dynamics and related reduced observability of the dynamics model. These results have been obtained for the case of utilizing the quality IMU and GPS sensors measurements, where the inertial measurements are characterized with compensated gravity acceleration components.

The dynamic model reliability is analyzed by utilizing the expression:

$$\gamma(k) = \tilde{\mathbf{y}}^T(k \mid k-1)(\mathbf{H}(k)\mathbf{P}(k \mid k-1)\mathbf{H}^T(k))^{-1}\tilde{\mathbf{y}}(k \mid k-1) \qquad (6\text{-}29)$$

In general the increase of γ indicates the decrease of the model reliability, predominantly due to the emphasized effects of the unmodeled dynamics or external disturbances (e.g. road bank, road grade etc.)

Fig. 6.28 illustrates the effect of the application of memory fading adaptation algorithms upon the sideslip angle estimation accuracy for J-turn maneuver carried out on a low-μ surface.

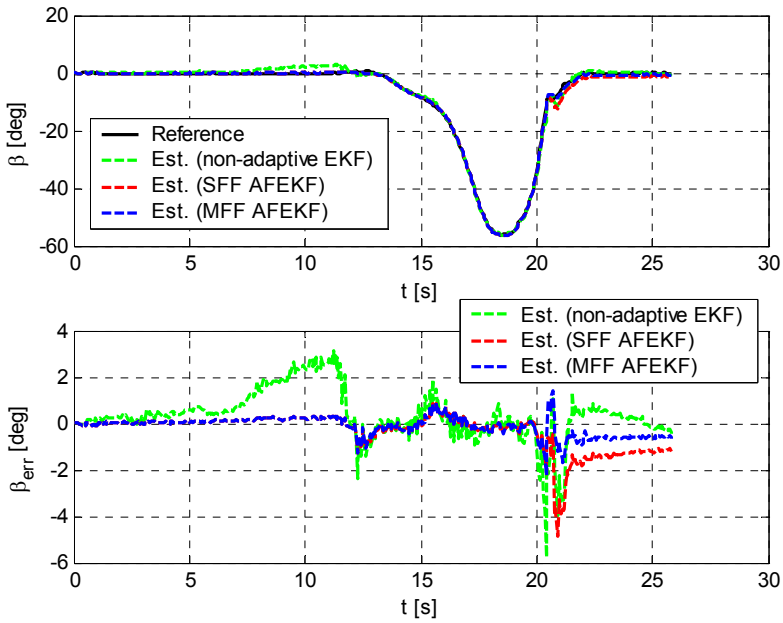

Fig. 6.28 *Comparison of the accuracy of the non-adaptive and adaptive estimators in case of using precission IMU sensors measurements for J-turn maneuver on low-mu surface.*

Based on the results given in Fig. 6.28 it can be concluded that the adaptive estimator surpass the non-adaptive estimator in their performances, where the multiple scaling factor AEKF provides somewhat better estimate than the single scaling factor-based estimator.

It should be noted, that in the double lane change or slalom maneuvers (cf. Figs. 6.9 and 6.15) carried out on the flat road and characterized by the small impact of the unmodeled disturbances (i.e. roll and pitch dynamics) and consequently the small measurement residuals the adaptive estimator becomes less efficient. Namely, having in mind the fact that the measurement model is given much more weight than the state model in tuning of the KF (because the state model comprises the first order random walk type stochastic models of tire forces) the adaptive estimators, in such conditions, provide similar estimates as the basic non-adaptive one.

6.7 Summary

The EKF-based sideslip angle estimator has been proposed, which is based on the 5DoF single-track vehicle dynamics model with a stochastic tire force submodel. The conducted

simulation analysis and experimental verification have shown a favorable accuracy of the proposed sideslip angle estimator for the nominal case of utilizing the high precision INS/GPS measurement unit signals (i.e. estimation errors typically less then 0.5deg) in different driving maneuvers (e.g. double lane change, slalom, steady cornering etc.) thus indicating a good application potential of the proposed approach based on the reduced-order vehicle dynamics model. In addition to the sideslip angle estimate, the estimator also provides accurate estimates of tire forces, thus providing a good foundation for lateral tire curve stiffness and tire-road coefficient of friction estimation (see Chapter 7 for details).

Moreover, in the case of utilizing the standard set of vehicle dynamics sensors, the initially poor estimation accuracy of the proposed sideslip angle estimator can be significantly improved by conducting relatively simple error compensations on yaw rate gyro and lateral accelerometer. For the most considered driving maneuvers the remaining estimation errors can be suppressed below the one-degree margin. The exception is the J-turn maneuver on low-μ surface in which the sideslip angle has reached high values and vehicle has evidently lost the grip and experienced some significant skidding.

The proposed memory fading adaptation of EKF of the sideslip angle estimate provides higher accuracy of the sideslip angle estimates in the case of the emphasized unmodeled dynamics effects (predominantly the roll and pitch dynamics) and in the presence of external disturbances such as the road bank. In the presence of emphasized sensor errors, as it is the case when using the standard vehicle dynamics sensors, the adaptation algorithm becomes less effective. In this case the simple modifications of the ratio of the longitudinal and lateral velocity state variables covariance can provide better estimator performance.

7 Reconstruction of tire cornering stiffness and road coefficient of friction

Although, the estimator presented in Chapter 6 has been primarily developed for estimation of the sideslip angle, it can be also utilized for estimation of other vehicle dynamics variables and parameters. More specifically, based on the results obtained trough estimator experimental verification, it has been found out that the proposed estimator concept has a good potential for application in estimation of tire cornering stiffness and tire-road coefficient of friction.

7.1 Tire sideslip angle and tire lateral force estimation

In order to illustrate these possibilities the estimation results for some relevant driving maneuvers are presented below, for the nominal case of utilizing the high-quality inertial sensors and GPS receiver measurements.

The reference signals for the tire sideslip angle have been derived analytically based on the known vehicle parameters and available high precision inertial measurements by utilizing two-track and single-track vehicle models. Presuming small vehicle sideslip angles β and related trigonometric functions approximations for small angles (i.e. $\sin\beta \approx \beta$ and $\cos\beta \approx 1$), the tire slip angles for individual wheels can be obtained from the following equations of the two-track vehicle model [5]:

$$\alpha_{fl} = \delta - \operatorname{atan}\frac{V_{CoG}\beta + b\omega_z}{V_{CoG} - \frac{t}{2}\omega_z}, \quad \alpha_{fr} = \delta - \operatorname{atan}\frac{V_{CoG}\beta + b\omega_z}{V_{CoG} + \frac{t}{2}\omega_z} \tag{7-1}$$

$$\alpha_{rl} = -\operatorname{atan}\frac{V_{CoG}\beta - c\omega_z}{V_{CoG} - \frac{t}{2}\omega_z}, \quad \alpha_{rr} = -\operatorname{atan}\frac{V_{CoG}\beta - c\omega_z}{V_{CoG} + \frac{t}{2}\omega_z} \tag{7-2}$$

where t is the vehicle track, b and c are longitudinal distances from front and rear axle to vehicle CoG, respectively, V_{CoG} is the vehicle CoG absolute velocity, and δ is the front wheel steering angle.

After substitution of the vehicle longitudinal and lateral velocities $u = V_{CoG}\cos\beta$ and $v = V_{CoG}\sin\beta$, and applying the trigonometric functions approximation for small angles ($u \approx V_{CoG}$ and $v \approx V_{CoG}\beta$), the above equations read:

$$\alpha_{fl} = \delta - \text{atan}\frac{v + b\omega_z}{u - \frac{t}{2}\omega_z}, \quad \alpha_{fr} = \delta - \text{atan}\frac{v + b\omega_z}{u + \frac{t}{2}\omega_z} \tag{7-3}$$

$$\alpha_{rl} = -\text{atan}\frac{v - c\omega_z}{u - \frac{t}{2}\omega_z}, \quad \alpha_{rr} = -\text{atan}\frac{v - c\omega_z}{u + \frac{t}{2}\omega_z} \tag{7-4}$$

The equivalent, lumped front and rear axes tire slip angles are obtained by averaging the individual tire slip angles:

$$\alpha_{f,2} = \frac{\alpha_{fl} + \alpha_{fr}}{2}, \quad \alpha_{r,2} = \frac{\alpha_{rl} + \alpha_{rr}}{2} \tag{7-5}$$

where subscript 2 signifies the two-track model. Alternatively, front and rear tire slip angles reference can be derived from the single-track vehicle model as [5]:

$$\alpha_f = \delta - \frac{v + b\omega_z}{u}, \quad \alpha_r = \frac{-v + c\omega_z}{u}. \tag{7-6}$$

The tire slip angle estimates are derived from the same equation, but instead of the measurements, the estimated velocities and yaw rate signals have been utilized.

$$\hat{\alpha}_f = \delta - \frac{\hat{v} + b\hat{\omega}_z}{\hat{u}}, \quad \hat{\alpha}_r = -\frac{\hat{v} - c\hat{\omega}_z}{\hat{u}} \tag{7-7}$$

Since the tire sideslip angle and tire lateral forces are not measured, the reference signals have been obtained from the following algebraic expressions [25]:

$$F_{yf} = \frac{cma_y + I_z\dot{\omega}_z}{(b+c)\cos\delta}, \quad F_{yr} = \frac{bma_y - I_z\dot{\omega}_z}{b+c} \tag{7-8}$$

while their estimates are readily available in the proposed sideslip angle estimator (i.e. last two elements of the process model state vector, see Eq. (6-6)). The tire slip angle and lateral tire force estimates for the slalom maneuver are given in Fig 7.1, together with the corresponding reconstructed, reference signals. The obtained estimates are characterized with a favorable accuracy.

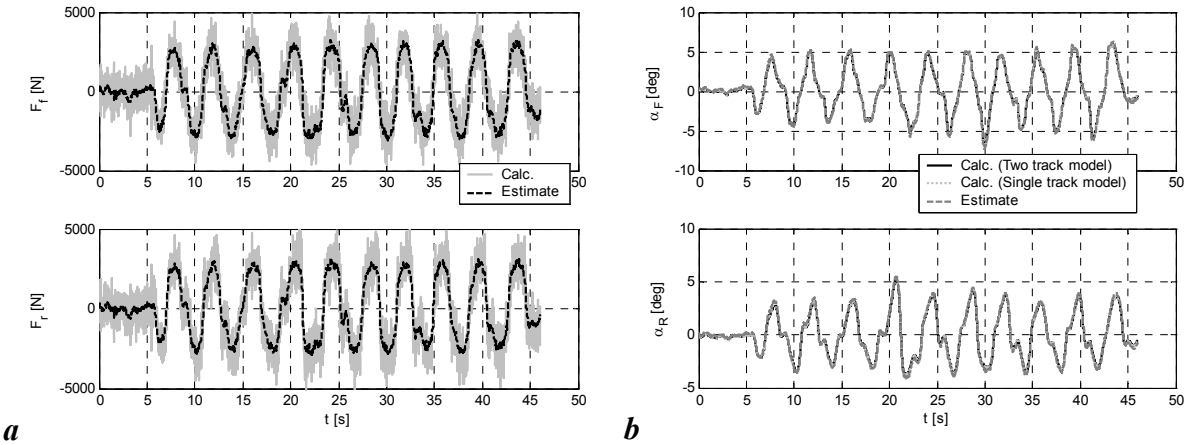

Fig. 7.1 *Estimates of the tire lateral forces (a) and tire sideslip angles (b) for slalom maneuver at 60 kph on packed snow.*

7.2 Cornering stiffness estimation

Fig. 7.2 illustrates the reconstructed (i.e. calculated by using Eqs. (7-6), and (7-8)) and estimated tire static characteristics (i.e. estimated by using the tire force estimates of the sideslip angle estimator developed in Chapter 6, and tire slip angles obtained from Eq. (7-7)) for a slalom maneuver at road covered with packed snow . The corresponding front and rear cornering stiffness has been identified by applying the linear interpolation of the recorded lateral tire static characteristic data derived from the estimated lateral forces and estimated tire slip angles. The linear fitting of lateral tire static characteristic data is carried out for the interval of tire slip angles of ±3 degrees, corresponding to the adhesion part of tire static curve (Fig. 2.5).

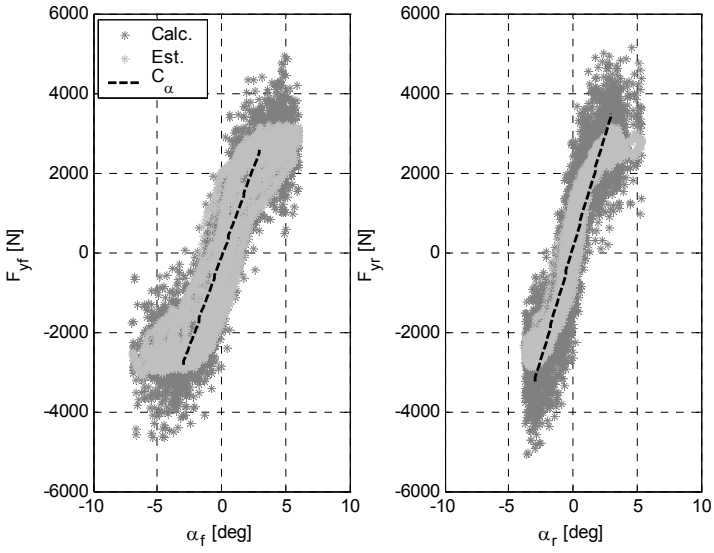

Fig. 7.2 *Reconstruction of the front and rear axis cornering stiffness for slalom maneuver at 60 kph on packed snow.*

The obtained tire cornering stiffness estimates, for number of driving maneuvers on low-μ and high-μ road are summarized presented and compared in Fig. 7.3.

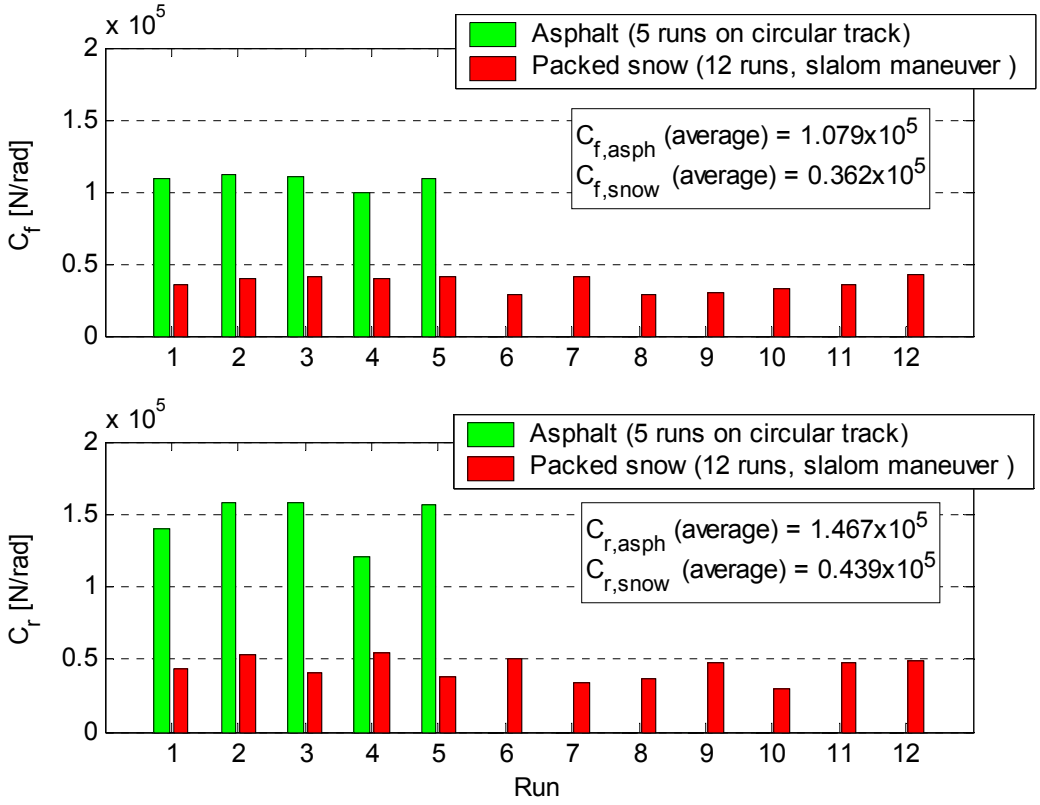

Fig. 7.3 *Cornering stiffness estimates in slalom maneuvers on low-mu and high-mu road surfaces: front axis a) and rear axis b).*

Based on such offline identified tire cornering stiffness parameters (shown in Fig. 7.3), derived by utilizing the same estimator concept used for the sideslip angle estimation in former Chapter and using the procedure described above and illustrated in Fig. 7.2, the information regarding the type of the surface can be extracted. Namely, from the obtained cornering stiffness estimates and according to the relation between the tire cornering stiffness and tire-road coefficient of friction (cf. [38,55,65]), at least the basic classification of the type of the surface seems to be feasible (i.e. low-μ / high-μ surfaces). More precisely the results presented in Fig. 7.3 obtained from a set of driving maneuvers performed on low-μ and high-μ surfaces clearly show that the estimated cornering stiffness significantly differ depending on the type of the surface can be utilized for surface coefficient of friction classification. This effect, of increase of the tire static curve gradient with the increase of the road coefficient of friction has been observed and recognized for tire longitudinal static curves [23,55], but it has not been documented in detail for lateral tire static curves.

The results of on-line cornering stiffness estimation for the case of utilizing the high-precision IMU measurement signals and applying the direct estimation method described in [26] and defined by Eqs. (7-9) and (7-10) are shown in Fig. 7.4.

$$C_{\alpha f} = \frac{c\dot{v}m + c\omega_z mu + I_{zz}\dot{\omega}_z}{-v - b\omega_z + \delta_f u}\frac{u}{t} \tag{7-9}$$

$$C_{\alpha r} = \frac{b\dot{v}m + b\omega_z mu - I_{zz}\dot{\omega}_z}{c\omega_z - v}\frac{u}{t} \tag{7-10}$$

The cornering stiffness reference has been calculated from Eqs. (7-9) and (7-10) by utilizing the available precision IMU measurements (e.g. u, v, and ω_z) and their time derivatives (e.g. $\dot{v}$ and $\dot{\omega}_z$), while the estimates have been obtained from the same equations by using the estimates of these quantities.

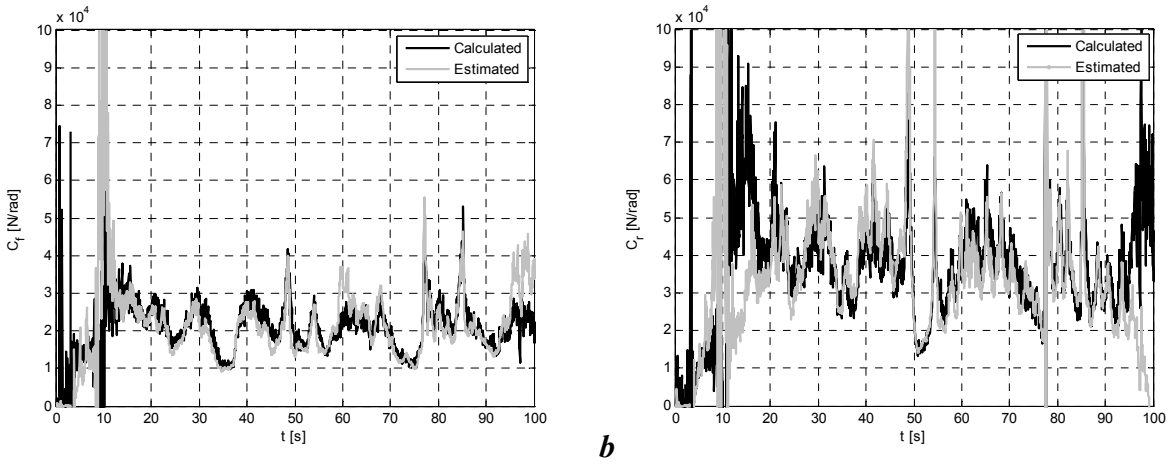

Fig. 7.4 *Cornering stiffness estimates in the steady cornering maneuver on circular track: front axis (a) and rear axis (b).*

The results for the front and rear cornering stiffness given in the Fig. 7.4, obtained for the driving on a circular path on low-μ surface. The front wheel cornering stiffness is somewhat smaller than for the rear wheel. The high noise content in the estimated signals is induced by the yaw rate and lateral velocity time derivative term in the underlying Eqs. (7-9) and (7-10). In order to reduce the noise level in the estimated signals and reduce the sensitivity of the estimation to the sensor outliers some of the closed loop methods (observers), documented in the literature [20,26,38,65,72-74] should be implemented.

Finally, the feasibility of the on-line estimation of the maximum road coefficient of friction from the estimated maximum tire lateral force has been considered below. Namely, Fig. 7.5 shows the measured vehicle dynamics state variables and estimated front and rear tire lateral forces derived from the sideslip angle estimator for a J-turn maneuver on the low-μ packed-snow surface.

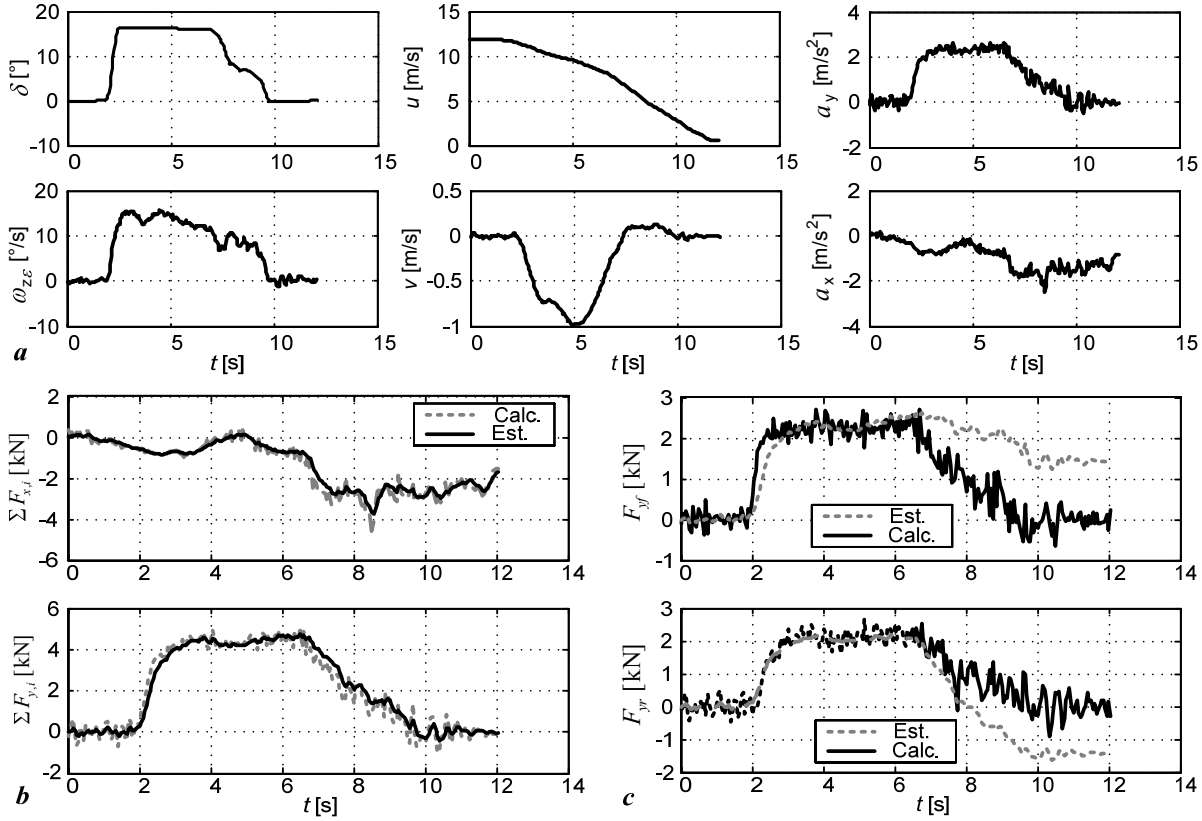

Fig. 7.5 *Estimation of the tire forces for the J-turn maneuver: vehicle dynamics state variables reference signals measured by IMU (a), estimated total lateral and longitudinal tire forces (b), and front and rear tire lateral force estimates (c).*

During the time interval corresponding to the maximum lateral tire forces the longitudinal tire forces are relatively small and consequently the maximum coefficient of friction can be determined from the nominal rear tire normal force F_{zr0} and the estimated lateral force limit according to the following equation [25]:

$$\hat{\mu}_{\max} = \frac{\hat{F}_{yr,\max}}{F_{zr0}} \tag{7-11}$$

where the nominal rear tire normal force can be calculated from the vehicle parameters by using the following equation:

$$F_{zr0} = \frac{mgb}{c+b} \tag{7-12}$$

Fig. 7.6 shows that during the interval characterized with the maximum tire lateral force the vehicle sideslip angle is accurately estimated and it reaches values characteristic for limit of adhesion on snow surface.

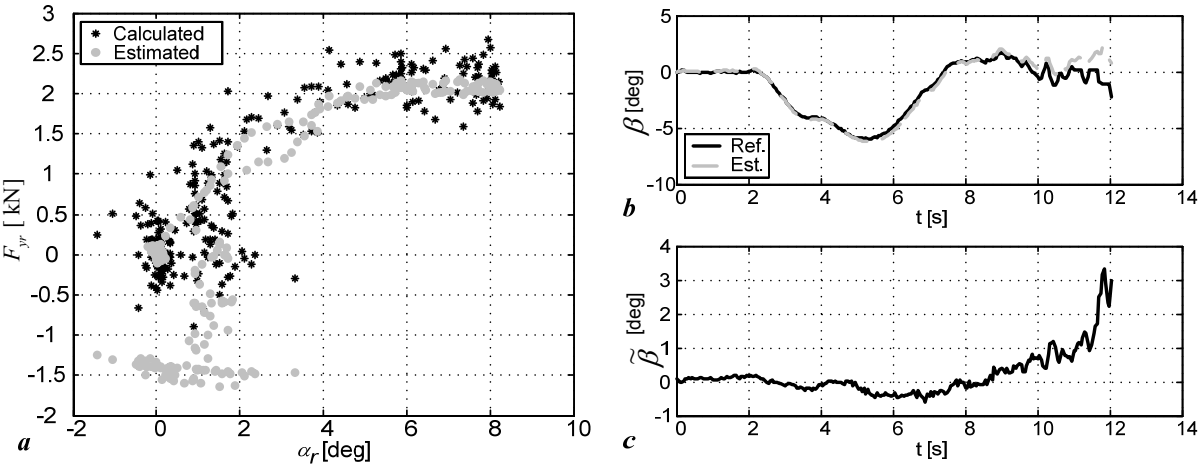

Fig. 7.6 *Estimation of the maximum tire lateral force and related tire-road coefficient of friction: estimated tire static characteristic (a), estimated sideslip angle (b), and sideslip angle estimation error (c).*

Consequently, for this particular case, the estimate of road coefficient of friction, related to the maximum estimated lateral tire force, equals 0.4, what correlates well with the typical values of the coefficient of friction for snow (i.e. 0.35-0.4, according to [25]). This result illustrates a good potential of such estimation concept for online implementation.

8 Conclusion

In this thesis the vehicle yaw rate and sideslip angle estimators, based on the sensor fusion approach and Kalman filter methodology, have been designed. These estimators have been tested by means of computer simulations based on the 10DoF vehicle dynamics model. Moreover, the sideslip angle estimator based on the vehicle dynamic model with stochastic modeling of the tire forces has been verified on the realistic experimental data obtained from the test vehicle.

The proposed adaptive Extended Kalman Filter (EKF)-based kinematic **yaw rate estimator** combines the approach based on two diagonally-placed accelerometers with the approach relying on the non-driven wheels speed sensors. Such a combined estimator, implementing the sensor fusion approach, takes advantage form the complementary benefits of the two individual estimation concepts. The major source of estimation errors for the first approach is the accelerometer offset that causes the drift-like estimation error, while the second approach cannot be used during braking and it is sensitive to the tire effective radii variations and road bump disturbances. The proposed estimator significantly reduces the overall estimation errors by utilizing the fusion concept. Accelerometers are predominantly used during yaw rate transients and when the accuracy of the wheel speed sensors is compromised, while the wheel speed sensors are utilized during the quasi-steady-state yaw rate intervals when the accelerometer-based estimation is sensitive to drift.

Further improvement of the wheel speed sensors reliability has been achieved by performing an open-loop compensation of the dominant wheel speed sensor-based estimation errors. More specifically, the static and dynamic compensation procedures have been derived and embedded into the estimator algorithm in order to reduce the tire deflation/wear and lateral load transfer-related estimation errors. Furthermore, the rule-based adaptation algorithm is extended with the road bump disturbance detection feature, in order to remove potentially large, environment-related wheel speed sensors-based estimation errors.

The performance of the adaptive EKF-based yaw rate estimator has been verified by means of computer simulation against the reference 10DoF vehicle dynamics model, and the obtained results have pointed out that in various driving maneuvers the proposed estimator provides

superior overall estimation accuracy when compared to performances of the individual kinematic estimators. The yaw rate estimation errors are mostly well below 10% for a wide range of driving conditions.

The GPS and INS fusion-based **kinematic sideslip angle estimator** has been designed by utilizing the adaptive EKF methodology. This estimator combines the low sampling rate GPS-based vehicle velocity measurements with the high sampling rate inertial sensors measurements (lateral acceleration and yaw rate), in order to compensate for the potentially large drift-like sideslip angle estimation errors caused by the inertial sensor offsets.

The estimator performance has been tested by running the computer simulations using the accurate 10DoF vehicle dynamics model, and the conducted analysis has indicated that the estimator can be rather sensitive to small errors of pre-estimated longitudinal vehicle velocity, due to the static and dynamic tire radii variations. Dominant estimation errors related to the static tire radii variation can be effectively compensated for during the periods of straight driving by comparing the GPS velocity and wheel speeds measurements. Further refinements of the longitudinal velocity pre-estimation may include the compensation of relatively small dynamic errors. In order to mitigate potentially large degradation of the sideslip angle estimation accuracy during breaking, due to significant vehicle velocity pre-estimation errors related to large tire longitudinal slip, the sideslip angle is, in such conditions, estimated in the open-loop mode.

The road bank effect represents a potentially large unmodeled disturbance that may reduce the sideslip angle estimation accuracy by inducing significant drift-like estimation errors. These errors are related to the additional accelerometer offset caused by gravity acceleration component. In order to reduce these errors, two compensation methods have been considered: first method modifies the EKF tuning in order to speed up the accelerometer offset estimation and effectively cancel the additional offset, while the second method uses road bank-related gravity acceleration estimate. The first method proved to be ineffective in the case of EKF estimates averaging, needed for compensation of the GPS measurement latency-related errors, that results in icreased filter response time, while the second method provides good results. Namely, the GPS measurement latency has proved to be a major source of the sideslip estimation transient errors. However, by presuming that this latency is known and that it remains constant over time, it can be compensated by introducing the same latency in the EKF prediction error calculation.

The proposed estimator adaptation algorithm changes the Kalman filter state covariance matrix in order to account for the changes in the vehicle dynamics conditions. More specifically, the two sets of state variables covariance parameters have been used: one for quasi-steady-state conditions and other for the intense dynamic behavior. The main idea of the adaptation is to make the sensor offset estimation faster during the steady-state conditions and slower during transients, where the transient intensity detection relies on the lateral acceleration measurement and the estimate of the lateral velocity time derivative. The adaptation algorithm enables adjusting optimal estimator performance with respect to estimator response time, and damping of the oscillations in the estimated sensor offsets and consequently the magnitude of errors in sideslip angle estimate. The performance of such fully tuned, adaptive EKF-based estimator has been tested by simulations for double lane change and double step-steer maneuvers. The obtained results have shown that the sideslip estimation error of less than approximately 2 deg is achievable for a wide range of non-braking operating conditions.

A vehicle dynamics model-based sideslip angle estimator has been designed by using an adaptive EKF. The nonlinear single-track vehicle dynamics model with five degrees of freedom has been utilized for the purpose of estimator design. Tire forces have been modeled as first-order random walk state variables.

The estimator performance has been verified by computer simulations based on a detailed, two-track 10 DoF vehicle dynamics model, as well as by off-line estimator execution based on the experimental data recorded on the test vehicle equipped with both a high precision IMU/GPS unit and a standard set of the vehicle dynamics sensors. The memory fading algorithms have been used for making the estimator adaptive. However, when using the precision inertial measurement unit signals, even for the constant tuning of the KF, the favorable estimation accuracy have been obtained. More specifically, in the case of using the nonadaptive estimator design the maximum sideslip angle estimation error less than 0.5° has been obtained for the most considered driving maneuvers on a flat road. On the other hand, the adaptive estimator surpasses the accuracy of the basic, nonadaptive estimator for steady cornering and slalom maneuvers carried out on banked roads. Namely, in these, particularly challenging maneuvers, the adaptive estimator has provided the estimation errors less than 0.5° compared to estimation errors somewhat over 1° for the nonadaptive estimator.

In the case of utilizing the standard onboard vehicle dynamics sensors, a significant degradation of the estimation accuracy has been observed. However, by utilizing relatively

simple measurement error compensation interventions for the two most critical sensors (i.e. the yaw rate gyro and the lateral accelerometer) and by proper modifications of the KF tuning parameters, the significant improvement of the estimator performance can be achieved. More specifically, for the most driving maneuvers the estimation errors can be reduced to the 1° margin (in comparison to the 0.5° error margin for utilizing the high precision IMU measurement).

The proposed memory fading adaptation of EKF of the sideslip angle estimate provides higher accuracy of the sideslip angle estimates in the case of the emphasized unmodeled dynamics effects (predominantly the roll and pitch dynamics) and in the presence of external disturbances such as the road bank. In the presence of emphasized sensor errors, as it is the case when using the standard vehicle dynamics sensors, the adaptation algorithm becomes less effective. In this case the simple modifications of the ratio of the longitudinal and lateral velocity state variables covariance can provide better estimator performance.

It has been demonstrated that the proposed dynamic sideslip angle estimator can also be used as a basis for estimation of the tire slip angles, tire cornering stiffness and tire-road coefficient of friction. The feasibility and performance of such simultaneous estimation of additional vehicle dynamics variables and parameters, has been analyzed by presuming the use of high precision IMU/GPS sensor measurements.

9 References

[1] Van Zanten, A. T. "Bosch ESP Systems: 5 Years of Experience", SAE technical paper, No. 2000-01-1633, 2000.

[2] Grewal, M. S. and Andrews, A. P., "Kalman Filtering – Theory and Practice", John Wiley and Sons, New York, USA, 2001.

[3] Welch, G. and Bishop, G., "An introduction to Kalman filter", tutorial, 81 pages, Department of Computer Science, University of North Carolina, Chapel Hill, 2001.

[4] Gustafsson, F. et al., "Sensor fusion for accurate computation of yaw rate and absolute velocity", SAE technical paper, No. 2001-01-1064, 2001.

[5] Kiencke, U. and Nielsen, L., "Automotive Control Systems: For Engine, Driveline, and Vehicle", Springer, 2005.

[6] Hac, A. and Simpson, M. D., "Estimation of Vehicle Side Slip Angle and Yaw Rate", SAE technical paper, No. 2000-01-0696, 2000.

[7] Carlson, C. R., Gerdes, J. C., and Powell, J. D. "Practical position and yaw rate estimation with GPS and differential wheelspeeds", Proceedings of AVEC 6th International Symposium, 2002.

[8] Sivashankar, N. and Ulsoy, A. G., "Yaw Rate Estimation for Vehicle Control Applications", Journal of Dynamic Systems, Measurement, and Control, Vol. 120, pp 267-274, 1999.

[9] Chee, W., "Yaw rate estimation using two 1-axis accelerometers", American Control Conference, June 2005.

[10] Nishio, A. et al. "Development of Vehicle Stability Control System Based on Vehicle Sideslip Angle Estimation", SAE technical paper, No. 2001-01-0137, 2001.

[11] Piyabongkarn, D., Rajamani, R., Grogg, J. A., and Lew, J. Y., "Development and Experimental Evaluation of a Slip Angle Estimator for Vehicle Stability Control", IEEE Transactions on Control Systems Technology, Vol. 17, No. 1, January 2009, pp. 78-88.

[12] Farelly, J. and Wellstead, P., "Estimation of Vehicle Lateral Velocity", Proceedings of IEEE Conference on Control Applications, pp. 552-557, September 1996.

[13] Panzani, G. et al., "Control-oriented vehicle attitude estimation with online sensors bias compensation", Proceedings of the ASME Dynamic Systems and Control Conference DSCC2009, October, 2009.

[14] Klier, W., Reim, A., and Stapel, D., "Robust Estimation of Vehicle Sideslip Angle – An Approach w/o Vehicle and Tire Models", SAE technical paper, No. 2008-01-0582, 2008.

[15] Ryu, J. and Gerdes, J. C., "Integrating Inertial Sensors with GPS for Vehicle Dynamic Control", Journal of Dynamic Systems, Measurement, and Control, June 2004.

[16] Bevly, D. M., "Global Position System (GPS): A Low-Cost Velocity Sensor for Correcting Inertial Sensor Errors on Ground Vehicles", Journal of Dynamic Systems, Measurement, and Control, Vol. 126, pp 255-264, June 2004

[17] Bevly, D. M., Ryu, J., and Gerdes, J. C., "Integrating INS Sensors with GPS Measurements for Continuous Estimation of Vehicle Sideslip, Roll, and Tire Cornering Stiffness", IEEE Transactions on Intelligent Transportation Systems, Vol. 7, No. 4, December 2006.

[18] Ray, L. R., "Nonlinear State and Tire Force Estimation for Advanced Vehicle Control", IEEE Transactions on Control System Technology, Vol. 3, No. 1. pp. 117-124, 1995.

[19] You, S. H., Hahn, J. O., and Lee, H., "New Adaptive Approach to Real-time Estimation of Vehicle Sideslip Angle", Control Engineering Practice, (17), pp. 1367-1379, 2009.

[20] Baffet, G., Charara, A., and Lechner, D., "Estimation of vehicle sideslip, tire force, and cornering stiffness", Control Engineering Practice, 17, pp. 1255-1264, 2009.

[21] Anderson, R. and Bevly, D. M., "Estimation of Slip Angles using a Model Based Estimator and GPS", Proceedings of American Control Conference, Vol. 3, pp. 2122-2127, 2004.

[22] Leung, K. T., Whidborne, J. F., Purdy, D., and Barber, P., "Road vehicle state estimation using low-cost GPS/INS", International Journal of Mechanical Systems and Signal Processing, Vol. 25, (6), pp. 1988-2004, 2011.

[23] Hancock, M., "Vehicle Handling Control using Active Differentials", Doctoral Thesis, Loughborough University, 2006.

[24] Kalman, R. E., "A New Approach to Linear Filtering and Prediction Problems", ASME Journal of Basic Engineering, 82(1), pp. 35-45, 1960.

[25] Ahn, C., Peng, H., and Tseng, E. T., “Robust Estimation of Road Friction Coefficient using Lateral and Longitudinal Vehicle Dynamics”, Vehicle System Dynamics, Vol. 50, No. 6, pp, 961-985, June 2012.

[26] Sierra, C., Tseng, E., Jain, A., and Peng, H., “Cornering Stiffness Estimation Based on Vehicle Lateral Dynamics”, Vehicle System Dynamics, Vol. 44, No. 1, pp.24-38 2006.

[27] Hartung, C. Nuthong, and F. Svaricek, “Stochastic Models for Tyre Force Estimation: An Overview about Recent Developments and Trends”, Proceedings of the 6th IFAC symposium Advances in Automotive Control, Munich, Germany, 2010.

[28] Ray, L. R., “Nonlinear Tire Force Estimation and Road Friction Identification: Simulation and Experiments”, Automatica, Vol. 33, No. 10, pp. 1819-1833, 1997.

[29] Hrgetić, M., Deur, J., Ivanović, V., Tseng, E., “Vehicle Sideslip Angle EKF Estimator based on Nonlinear Vehicle Dynamics Model and Stochastic Tire Forces Modeling”, SAE International Journal of Passenger Cars - Mechanical Systems, 2014.

[30] Hrgetić, M., Deur, J., Kranjčević, N., Tseng, H. E., and Lakehal-Ayat, M., "Analysis of Accelerometer-based Kinematic Yaw Rate Estimators", Proceedings of AVEC 9th International Symposium on Advanced Vehicle Control, Kobe, Japan, 2008.

[31] H. Baruh, “Analytical Dynamics”, McGraw-Hill Companies Inc, 1999.

[32] Tseng, H. E. et al., “The Development of Vehicle Stability Control at Ford,” IEEE/ASME Transactions on Mechatronics, Vol. 4, No. 3, pp. 223-234, 1999.

[33] Pacejka, H. B., “Tyre and Vehicle Dynamics, Second Edition”, Butterworth-Heinemann / Elsevier Publishing, UK, 2006.

[34] Deur, J., Assadian, F., and Hancock, M., "A Linearized Vehicle Dynamics Model for Global Chassis Control", Proceedings of ASME international Mechanical Engineering & Exposition IMECE2007, November, Seattle, WA, USA, 2007.

[35] Genta, G., "Motor Vehicle Dynamics - Modeling and Simaulation", World Scientific, Singapore, 1997.

[36] Gustafsson, F., "Slip-based Tire-Road Friction Estimation", Automatica, Vol. 33, No. 6, pp. 1087-1099, 1997.

[37] B. P. Gibbs, “Advanced Kalman Filtering, Least-Squares and Modeling: A Practical Handbook”, A John Wiley & Sons Inc., New Jersey, 2011.

[38] D. Pavković, “Automotive powertrain state estimation with control applications,” (in Croatian) Ph.D. dissertation, Department of Robotics and Automation of Manufacturing Systems, University of Zagreb, Zagreb, Croatia, 2007.

[39] Gustafsson, F., "Adaptive Filtering and Change Detection", John Wiley & Sons, Chichester, UK, 2000.

[40] Almagbile, A., Wang, J., and Ding, W., “Evaluating the Performance of Adaptive Kalman Filter Methods in GPS/INS Integration”, Journal of Global Positioning Systems, Vol. 9, No. 1, pp. 33-40, 2010.

[41] Einicke, G. A., White, L. B., and Bitmead, R. R., "The Use of Fake Algebraic Riccati Equations for Co-Channel Demodulation", IEEE transactions on signal processing, Vol. 51, No. 9, September 2003.

[42] Hajiyev, C. and Soken, H. E, "Robust Adaptive Kalman Filter for estimation of UAV dynamics in the presence of sensor/actuator faults", Aerospace Science and Technology, 2013.

[43] Hu, C., Chen, W., Chen, Y., and Liu, D., “Adaptive Kalman Filtering for Vehicle Navigation”, Journal of Global Positioning Systems, Vol.2, No. 1, pp. 42-47, 2003.

[44] Fokin, L. A., Shchipitsyn, A. G., "Innovation-based Adaptive Kalman Filter Derivation", Proceedings of Siberian Conference on Control and Communications, SIBCON, 2009.

[45] Fathabadi, V., Shahbazian, M., Salahshour, K., Jargani, L., "Comparison of Adaptive Kalman Filter Methods in State Estimation of a Nonlinear System Using Asynchronous Measurements", Proceedings of the World Congress on Engineering and Computer Science, San Francisco, USA, 2009.

[46] Halbe, I., Isermann, R., “A Model-based Fault-tolerant Sensor-platform for Vehicle Dynamics Control”, IFAC, 2007.

[47] Hrgetić, M., Deur, J., Pavković, D., Lakehal-Ayat, M., Tseng, E., “Adaptive Kalman Filter-based Yaw Rate Estimation Using Accelerometers and Wheel Speed Sensors”, Proceedings of the ASME Dynamic Systems and Control Conference (DSCC 2009), Hollywood, California, USA, 2009.

[48] Zegelaar, P. W. A., “The dynamic response of Tyres to Brake Torque Variations and Road Unevennesses”, PhD Thesis, Delft University of Technology, Nederland, 1998.

[49] Hrgetić, M., Deur, J., Cifrek, M., Lakehal-Ayat, M., Tseng, E., “Analysis and Compensation of Wheel Speed Sensor-based Kinematic Yaw Rate Estimation Errors”, Proceedings of the 21st International Symposium on Dynamics of Vehicles on Roads and Tracks (IAVSD 2009) Stockholm, Sweden, 2009.

[50] Deur, J. et al., “Modeling and Analysis of Active Differential Dynamics”, ASME Journal of Dynamics Systems, Measurement, and Control, Vol. 132, No. 6, October, 2010.

[51] Gopal, M., “Modern Control System Theory”, Wiley Eastern, New Delhi, India, 1984.

[52] Franklin, G. F., Powell, J. D., Workman, M. L., “Digital Control of Dynamic Systems”, Third Edition, Addison-Wesley-Longman Inc., 1998.

[53] Kariss, S. T., “Signals and Systems with MATLAB Applications”, Second Edition, Orchard Publications, 2003.

[54] Hrgetić, M., Deur, J., Pavković, D., Barber P., “Adaptive EKF-Based Estimator of Sideslip Angle Using Fusion of Inertial Sensors and GPS”, SAE Intenational Journal of Passenger Cars - Mechanical Systems, Vol. 4, No. 1; pp. 700-712, 2011.

[55] Deur, J., Ivanović, V., Pavković, D., Asgari, J., Hrovat, D., Troulis, M., Miano, C., “On low-slip tire friction behavior and modeling for different road conditions”, CD Proceedings of 19th IAVSD Symposium, Milano, Italy, 2005.

[56] Leung, K. T., Whidborne, J., Purdy, D., Dunoyer, A., Williams, R., “A Study on the Effect of GPS Accuracy on a GPS/INS Kalman Filter”, Proceedings of UKACC Control Conference, Manchester, UK, 2008.

[57] Leung,, K. T., Whidborne, J., Purdy, D., Dunoyer, A., “Ideal Vehicle Sideslip Estimation Using Consumer Grade GPS and INS”, SAE 09AE-0111, 2008.

[58] Ryu, J., Rossetter, E., and Gerdes, J., “Vehicle Sideslip and Roll Parameter Estimation Using GPS”, Proceedings of AVEC 6th International Symposium, 2002.

[59] Alban, S., “An Inexpensive and Robust GPS/INS Attitude System for Automobiles”, Proceedings of the 15th International Technical Meeting of the Satelite Division of the Institute of Navigation ION GPS2002, pp. 1075-87, September, 2002.

[60] Kreyszig, E., “Advanced Engineering Mathematics”, Chapter 6, John Wiley and Sons, New York, USA, 1999.

[61] Armesto, L., Tornero, J., Vincze, M., “On multi-rate fusion for non-linear sampled-data systems: Application to a 6D tracking system”, Robotics and autonomous systems, Vol. 56, pp. 706-715, 2008.

[62] Cristi, R., Tummala, M., “Multirate, multiresolution, recursive Kalman filter”, IEEE Transections on Signal Processing Vol. 80, pp. 1945-1958, 2000.

[63] Isermann, R., “Digital Control Systems”, Springer-Verlag New York, 1981.

[64] Xu, L. and Tseng, H. E., "Robust Model-Based Fault Detection for a Roll Stability Control System", IEEE Transactions on Control Systems Technology, Vol. 15, No. 3, May 2007.

[65] Doumiati, M., Victorino, A., Lechner, D., Baffet, G., and Charara, A., "Observers for vehicle tyre/road forces estimation: experimental validation", Vehicle System Dynamics: International Journal of Vehicle Mechanics and Mobility, Vol. 48, No. 11, pp. 1345-1378, 2010.

[66] Anderson, R. and Bevly, D. M., "Using GPS with a model-based estimator to estimate critical vehicle states", Vehicle System Dynamics: International Journal of Vehicle Mechanics and Mobility, Vol. 48, No. 12, pp. 1413-1438, 2010.

[67] Tseng, H. E., Xu, L, and Hrovat, D., "Estimation of land vehicle roll and pitch angles", Vehicle System Dynamics, Vol. 45, No. 5, pp. 433-443, 2007.

[68] El-Rabbany, A., "Introduction to GPS: the Global Positioning System", Artech House, Boston, 2002.

[69] Grewal, M. S., Weill, L. R., Anrews, A. P., "Global Positioning Systems, Inertial Navigation, and Integration", A John Wiley & Sons Inc., New York, 2001.

[70] Ungoren, A. Y., Peng, H., and Tseng, H. E., "Experimental Verification of Lateral Speed Estimation Methods", Proceedings of AVEC 6th International Symposium on Advanced Vehicle Control, 2002.

[71] Ungoren, A. Y., Peng, H., and Tseng, H. E., "A Study on Lateral Speed Estimation Methods", International Journal of Vehicle Autonomous Systems, Vol. 2, pp 126-144, 2004.

[72] Lundquist, C. and Schön, T. B., "Recursive Identification of Cornering Stiffness Parameters for an Enhanced Single Track Model", Proceedings of the 15th IFAC Symposium on System Identification, Vol. 15, Part 1, 2009.

[73] Pavković, D., Deur, J., Asgari, J., and Hrovat, D., "Experimental Analysis of Potentials for Tire Friction Estimation in Low-Slip Operating Mode", SAE Technical paper No. 2006-01-0556, 2006.

[74] Nguyen, B. M., Nam, K., Fujimoto, H., and Hori, Y, "Proposal of Cornering Stiffnes Estimation without Vehicle Side Slip Angle Using Lateral Force Sensor", Proccedings of IEEJ Technical Meeting, Vol. 11, pp. 140, 2011.

[75] Chen, B. C. and Hsieh, F. C., "Sideslip Angle Estimation Using Extended Kalman Filter", Proceedings of 20th IAVSD International Symposium, August 2007.

[76] Cherouat, H., Braci, M., and Diop, S., "Vehicle Velocity, Side Slip Angles and Yaw Rate Estimation", Proceedings of the IEEE International Symposium on Industrial Electronics ISIE 2005, Vol. 1, pp. 349-354, 2005.

[77] Daily, R., and Bevly, D. M., "The Use of GPS for Vehicle Stability Control Systems", IEEE Transactions on Industrial Electronics, Vol. 51, No. 2, 2004.

[78] Doumiati, M., Victorino, A., Charara, A., and Lechner, D., "A Method to Estimate the Lateral Tire Force and the Sideslip Angle of a Vehicle: Experimental Validation", Proceedings of American Control Conference, 2010.

[79] Fukada, Y., "Slip-Angle Estimation for Vehicle Stability Control", Vehicle System Dynamics, Vol. 32, No. 4, pp. 375-388, 1999.

[80] Hahn, J., Rajamani, R., You, S., and Lee, K., "Road Bank Angle Estimation Using Disturbance Observer", Proceedings of AVEC 6th International Symposium on Advanced Vehicle Control, 2002.

[81] Liu, C. and Peng, H., "A State and Parameter Identification Scheme for Linearly Parametrized Systems", ASME Journal of Dynamic Systems, Measurement and Control, Vol. 120, No. 4, pp. 524-528, 1998.

[82] Miller, S. L., Youngberg, B., Millie, A., Schweizer, P., and Gerdes, J. C., "Calculating Longitudinal Wheel Slip and Tire Parameters Using GPS Velocity", Proceedings of the American Control Conference, Arlington, VA, 2001.

[83] Tseng, H. E., "Dynamic estimation of road bank angle", Vehicle System Dynamics, Vol. 36, No. 4-5, pp. 307-328, 2001.

[84] Van Zanten, A. T., Erhardt, R., and Pfaff, G., "VDC, the vehicle dynamics control system of Bosch", SAE technical paper, No. 950759, 1995.

[85] Van Zanten, A. T., et al., "Simulation for the developement of the Bosch-VDC", SAE technical paper, No. 960486, 1996.

[86] Van Zanten, A. T., Erhart, R., Landesfeind, K., and Pfaff, G., "VDC systems development and perspective", SAE technical paper, No. 980235, 1998.

[87] Kim, J., "Identification of lateral tyre force dynamics using an extended Kalman filter from experimental road test data", Control Engineering Practice, (17), pp. 357-367, 2009.

[88] Leung, K. T., Whidborne, J. F., Purdy, D., and Dunoyer, A., "A review of ground vehicle dynamic state estimations utilising GPS/INS, Vehicle System Dynamics" International Journal of Vehicle Mechanics and Mobility, Vol. 49, No. 1-2, pp. 29-58, 2011.

[89] Best, M. C., "Identifying tyre models directly from vehicle test data using an extended Kalman filter", Vehicle System Dynamics, Vol. 48, No. 2, pp. 171–187, 2010.

Appendix – A

Derivation of the Euler angles from local frame angular velocities

For any two given coordinate frames A and B which origins coincide, the coordinate transformations between these two coordinate frames can be obtained through the successive rotations of the one of the coordinate frames (Fig. A-1) by application of the Euler angles (ϕ - roll, θ - pitch, and ψ - yaw). In this particular case coordinate frame A corresponds to the reference inertial frame, while the frame B is the body-fixed rotating coordinate frame with angular velocities about its axes (ω_x, ω_y, and ω_z).

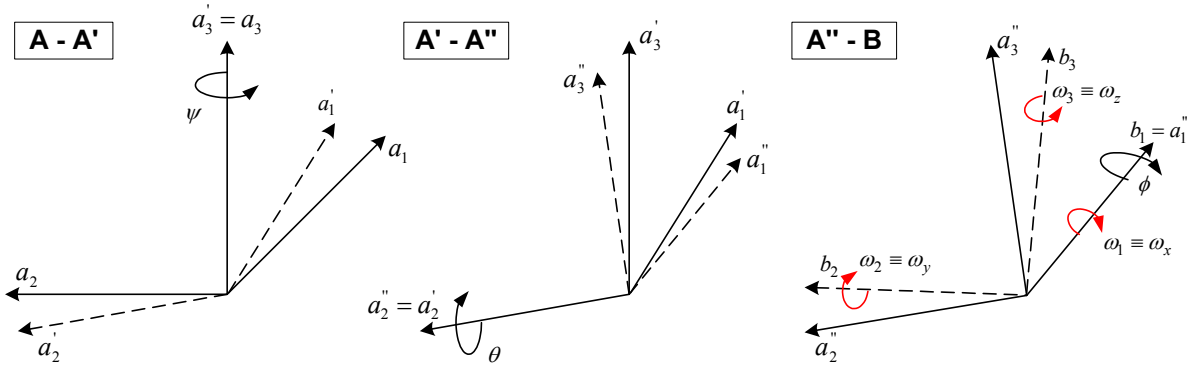

Fig. A-1. *Euler angles derivation from the body-fixed frame angular velocities.*

Angular velocity vector of the rotating frame B, resolved to the inertial coordinate frame A, is denoted as ${}^{A}\omega^{B}$ (as used in [Baruh]). The velocity vector has three components, one for each of the successive rotations (A – A', A'–A'', and A''–B) of the inertial coordinate frame A, and related to the corresponding Euler angle (Fig. A-1).

Angular velocity vector of the rotating frame B, resolved to the inertial coordinate frame A, is denoted as ${}^{A}\omega^{B}$ (as used in [31]). The velocity vector has three components, one for each of the successive rotations (A – A', A'–A'', and A''–B) of the inertial coordinate frame A, and related to the corresponding Euler angle (Fig. A-1).

$$ {}^{A}\boldsymbol{\omega}^{B} = {}^{A}\boldsymbol{\omega}^{A'} + {}^{A'}\boldsymbol{\omega}^{A''} + {}^{A''}\boldsymbol{\omega}^{B} = \dot{\psi}\cdot\mathbf{a}_3 + \dot{\theta}\cdot\mathbf{a}_2' + \dot{\phi}\cdot\mathbf{a}_1'' \qquad \text{(A-1)} $$

The angular velocity vector can be resolved on the components of the rotating coordinate frame B, if the appropriate coordinate transform is performed by utilizing the inverse of the cosine transformation matrix $\mathbf{R}_{321}^{T}$.

$$ \mathbf{A} = \mathbf{R}_{321}^{T}\,\mathbf{B} \qquad \text{(A-2)} $$

$$\mathbf{R}_{321}=\begin{bmatrix} c\psi\cdot c\theta & s\psi\cdot c\theta & -s\theta \\ -s\psi\cdot c\theta+c\psi\cdot s\theta\cdot s\phi & c\psi\cdot c\theta+s\psi\cdot s\theta\cdot s\phi & c\theta\cdot s\phi \\ s\psi\cdot s\phi+c\psi\cdot s\theta\cdot c\phi & -c\psi\cdot s\phi+s\psi\cdot s\theta\cdot c\phi & c\theta\cdot c\phi \end{bmatrix} \tag{A-3}$$

The vectors of the successive rotational axes $\mathbf{a}_3, \mathbf{a}_2^{'}, \text{and}\, \mathbf{a}_1^{''}$ from the inertial coordinate frame A can be resolved to the rotating, body-fixed frame B components according to the following expressions:

$$\mathbf{a}_3=-\mathbf{b}_1\sin\theta+\mathbf{b}_2\sin\phi\cos\theta+\mathbf{b}_3\cos\phi\cos\theta \tag{A-4}$$

$$\mathbf{a}_2^{'}=\mathbf{b}_2\cos\phi-\mathbf{b}_3\sin\phi \tag{A-5}$$

$$\mathbf{a}_1^{''}=\mathbf{b}_1 \tag{A-6}$$

When the terms from Eqs. (A-4)-(A-6) are substituted in Eq. (A-1) the angular velocity vector can be expressed as:

$$\begin{aligned} {}^{A}\boldsymbol{\omega}^{B}&=\dot{\psi}(-\mathbf{b}_1\sin\theta+\mathbf{b}_2\sin\phi\cos\theta+\mathbf{b}_3\cos\phi\cos\theta) \\ &+\dot{\theta}(\mathbf{b}_2\cos\phi-\mathbf{b}_3\sin\phi)+\dot{\phi}\cdot\mathbf{b}_1 \end{aligned} \tag{A-7}$$

After rearranging Eq. (A-7) the following result is obtained:

$$\begin{aligned} {}^{A}\boldsymbol{\omega}^{B}&=(\dot{\phi}-\dot{\psi}\sin\theta)\mathbf{b}_1+(\dot{\psi}\sin\phi\cos\theta+\dot{\theta}\cos\phi)\mathbf{b}_2 \\ &+(\dot{\psi}\cos\phi\cos\theta-\dot{\theta}\sin\phi)\mathbf{b}_3 \end{aligned} \tag{A-8}$$

According to the Eq. (A-8), the components of the angular velocity vector as functions of the Euler angles and in terms of the body fixed coordinate frame are obtained as:

$${}^{A}\omega_1^{B}=\dot{\phi}-\dot{\psi}\sin\theta \tag{A-9}$$

$${}^{A}\omega_2^{B}=\dot{\psi}\sin\phi\cos\theta+\dot{\theta}\cos\phi \tag{A-10}$$

$${}^{A}\omega_3^{B}=\dot{\psi}\cos\phi\cos\theta-\dot{\theta}\sin\phi \tag{A-11}$$

These equations, relating the angular velocities of the rotating body-fixed frame to the first derivatives of the Euler angles can also be written in the matrix form as:

$${}^{A}\boldsymbol{\omega}^{B}=\mathbf{B}\cdot\dot{\mathbf{E}} \tag{A-12}$$

where $\mathbf{E}=\begin{bmatrix}\phi & \theta & \psi\end{bmatrix}^T$ is the vector of the Euler angles and the **B** matrix reads:

$$\mathbf{B}=\begin{bmatrix} 1 & 0 & -\sin\theta \\ 0 & \cos\phi & \sin\phi\cos\theta \\ 0 & -\sin\phi & \cos\phi\cos\theta \end{bmatrix} \tag{A-13}$$

The Euler angles as functions of the body-fixed frame angular velocities in a form of the nonlinear state-space dynamic system could be obtained as follows.

$$\dot{\mathbf{E}} = \mathbf{B}^{-1}\begin{bmatrix}\omega_1\\ \omega_2\\ \omega_3\end{bmatrix} \tag{A-14}$$

where the inverse of the matrix B reads:

$$\mathbf{B}^{-1} = \begin{bmatrix}1 & \sin\phi\tan\theta & \cos\phi\tan\theta\\ 0 & \cos\phi & -\sin\phi\\ 0 & \dfrac{\sin\phi}{\cos\theta} & \dfrac{\cos\phi}{\cos\theta}\end{bmatrix} \tag{A-15}$$

When this matrix equation is resolved on the algebraic equations and after the substitutions $\omega_1 \equiv \omega_x, \omega_2 \equiv \omega_y,$ and $\omega_3 \equiv \omega_z$ (Fig. A-1) following expressions are obtained [30,31]:

$$\dot{\phi} = \omega_x + (\omega_y \sin(\phi) + \omega_z \cos(\phi))\tan(\theta) \tag{A-16}$$

$$\dot{\theta} = \omega_y \cos(\phi) - \omega_z \sin(\phi) \tag{A-17}$$

$$\dot{\psi} = (\omega_y \sin(\phi) + \omega_z \cos(\phi))\frac{1}{\cos\theta} \tag{A-18}$$

Appendix – B

Specifications of the RT3003 inertial measurement unit

Model: RT3003 - two antenna unit

Table B.1 *Performance specifications for RT3003 measurement unit*

Parameter	Value	Parameter	Value
Position accuracy		Acceleration accuracy	
CEP SPS	1.5m	Bias	10mm/s^2 (1σ)
CEP SBAS	0.6m	Linearity	0.01% (1σ)
CEP DGPS	0.4m	Scale Factor	0.1% (1σ)
		Range	100m/s^2
Angular rate			
Bias	0.01°/s (1σ)	Heading	0.1° (1σ)
Scale factor	0.1% (1σ)	Pitch/Roll	0.03° (1σ)
Range	100°/s	Velocity accuracy	0.05kph (RMS)
		Lateral velocity	0.2% (1σ)
		Slip angle (at 50kph)	0.15° (1σ)
		Track (at 50kph)	0.07° (1σ)

Update rate of the unit signals is in the range of 100/250Hz.

Appendix – C

Vehicle dynamics model parameters

Table C.1 *Vehicle dynamics model parameters*

Parameter	Description	Value [unit]
m	Vehicle mass	1858 kg
I_{zz}	Yaw moment of inertia	3515 kgm^2
b	Front axis distance from CoG	1.432 m
c	Rear axis distance from CoG	1.472 m
t	Vehicle track	1.625 m
I_{xx}	Roll moment of inertia	655.2 kgm^2
I_{rc}	Roll center moment of inertia	521.7 kgm^2
m_r	Rear suspension mass	1011 kg
b_r	Roll damping rate	5022 Ns/m
k_r	Roll spring rate	41328 N/m
h_1	Roll center height at vehicle CoG	0.4382 m
l	Wheel base	2.904 m
r_n	Wheel nominal radius	0.337 m
I_w	Wheel moment of inertia	1 kgm^2

Notation

Symbol	Description	Symbol	Description
C_i	cornering stiffness	$\mathbf{H}(k)$	output matrix
β	sideslip angle	$\mathbf{G}(k)$	input matrix
l_f, l_r	longitudinal distance from front and rear axle to vehicle CoG	$\mathbf{P}(k\|k\text{-}1)$	a-priori error propagation covariance matrix
ω_x	roll rate	$\mathbf{P}(k\|k)$	a-posteriori error propagation covariance matrix
ω_y	pitch rate	$\mathbf{K}(k)$	Kalman filter gain matrix
ω_z	yaw rate	$\mathbf{x}(k)$	state vector
a_x	longitudinal acceleration	$\mathbf{y}(k)$	measurement (output) vector
a_y	lateral acceleration	δ	steering angle
a_z	vertical acceleration	T_s	sampling time
θ	pitch angle	F_y	vehicle lateral force
ϕ	roll angle	q_i	state variance ($q_i \equiv q_{ii}$)
ψ	yaw angle (heading)	r_i	measurement variance ($r_i \equiv r_{ii}$)
u	longitudinal velocity (body frame)	$\hat{\mathbf{x}}(k \mid k)$	a-posteriori state vector estimate
v	lateral velocity (body frame)	$\hat{\mathbf{x}}(k \mid k-1)$	a-priori state vector estimate
w	vertical velocity (body frame)	h_g	vehicle CoG height
t	vehicle track	g	gravity acceleration constant
r_n	nominal tire radius	I_{xx}	roll moment of inertia
r_e	effective tire radius	b	longitudinal distance from front axle to CoG
r	measurement covariance	c	longitudinal distance from rear axle to CoG
q	state covariance	$\boldsymbol{\lambda}$	adaptive fading scalling matrix
$\mathbf{Q}$	state covariance matrix	$\boldsymbol{\Gamma}$	adaptive fading measurement covariance scalling matrix
$\mathbf{R}$	measurement covariance matrix	$\boldsymbol{\Lambda}$	adaptive fading state covariance scalling matrix
τ_b	braking torque	κ	state covariance scaling factor
α_f, α_r	tire slip angle (front and rear)	φ	measurement covariance scaling factor
m	vehicle mass	α_{ad}, λ_{ad}	scaling coefficients of SSF adaptive Kalman filter
I_z	yaw moment of inertia	$\mathbf{C_r}$	innovation covariance matrix
η_i	tire longitudinal slip	$\tilde{x}$, x_ε	residual (absolute error) of x
$\mathbf{F}(k)$	state transition matrix	ε_x	relative error of x

Table of Figures

List of Tables

Curriculum Vitae

Mario Hrgetić (b. 1979) received his B.Sc. degree in Electrical Engineering in 2004 from the Faculty of Electrical Engineering and Computing of the University of Zagreb. Since December 2005 he has joined the Automotive Control Group at the Faculty of Mechanical Engineering and Naval Architecture, University of Zagreb as a research assistant. From March 2009 he has been employed as a research/teaching assistant at the Department of Robotics and Production System Automation, where he participates in teaching activities in the field of electrical engineering, electronics, and sensors.

Over the past five years he has participated on one research and one technology project supported by the Ministry of Science, Education and Sport of the Republic of Croatia, one research project supported by University of Zagreb, three bilateral research projects financed by international automotive industry, and two collaboration research projects, one supported by European Commission (FP7 framework programme), and the other supported by Croatian Science Foundation.

His research interests include: development of the estimators based on the sensor fusion methodology with applications to the vehicle dynamics and automotive mechatronics systems; modelling of DC/DC converters with applications to battery and ultracapacitor energy storage systems.

He is the author or co-author of one journal paper indexed in CC/SCI/SCI-Ex databases, three papers in other journals, 10 papers presented at international conferences.

Publications:

1. M. Kostelac, Z. Herold, and M. Hrgetić, “Valovitosti momenta vrtnje direktnog pogona”, Strojarstvo 50 (1) 2008.
2. Hrgetić, M.; Deur, J., Ivanović, V., Tseng, E., “Vehicle Sideslip Angle EKF Estimator based on Nonlinear Vehicle Dynamics Model and Stochastic Tire Forces Modeling”. SAE International Journal of Passenger Cars- Mechanical Systems. 7 (1); pp. 86-95, 2014.

3. Hrgetić, M., Deur, J., Pavković, D., and Barber, P., "Adaptive EKF-based Estimator of Sideslip Angle Using Fusion of Inertial Sensors and GPS", SAE Intenational Journal of Passenger Cars - Mechanical Systems 4 (1), pp. 700-712, 2011.

4. Deur, J., Kostelac, M., Herold, Z., Ivanovic, V., Pavkovic, D., Hrgetic, M., Asgari, J., Miano, C., Hrovat, D., "An In-Wheel Motor-based Tyre Test Vehicle", International Journal of Vehicle System Modeling and Testing, Vol. 2, No. 3, pp. 252-275, 2007.

5. Pavković, D., Lobrović, M., Hrgetić, M., Komljenović, A., Smetko, V., "Battery Current and Voltage Control System Design with Charging Application", Proceedings of the 2014 IEEE Control Systems Society Multiconference on Systems and Control, Nice, France, October, 2014.

6. Pavković, D., Smetko, V., Hrgetić, M., Komljenović, A., "Dual Kalman Filter-Based SoC/SoH Estimator for an Ultracapacitor Module" Proceedings of the 2014 IEEE Control Systems Society Multiconference on Systems and Control, Nice, France, October, 2014.

7. Pavković, D., Komljenović, A., Hrgetić, M., "Control-Oriented Modeling and Experimental Identification of a VRLA Battery", Proceedings of 2013 Electrical Drives & Power Electronics Conference (EDPE 2013), Dubrovnik, Croatia, October, 2013.

8. Pavković, D., Hrgetić, M., Komljenović, A., "Control-Oriented Modeling and Experimental Identification of an Ultracapacitor Module", Proceedings of 2013 Electrical Drives & Power Electronics Conference (EDPE 2013), Dubrovnik, Croatia, October, 2013.

9. Pavković, D., Hrgetić, M., Komljenović, A., Lisac, A., Deur, J., "Battery/Ultracapacitor Test Setup Control System Design and Verification", Proceedings of IEEE Eurocon 2013, pp. 1050-1057, Zagreb, Croatia, 2013.

10. Hrgetić, M., Deur, J., Pavković, D., and Barber, P., "Adaptive EKF-based Estimator of Sideslip Angle Using Fusion of Inertial Sensors and GPS", Proceedings of the SAE 2011 World Congress, Detroit, Michigan, USA, 2011.

11. Hrgetić, M., Deur, J., Cifrek, M., Lakehal-Ayat, M, and Tseng, E., "Analysis and Compensation of Wheel Speed Sensor-based Kinematic Yaw Rate Estimation Errors",

Proceedings of the 21st Internationa Symposium on Dynamics of Vehicles on Roads and Tracks (IAVSD 2009), Stockholm, Sweden, 2009.

12. Hrgetić, M., Deur, J., Pavković, D., Lakehal-Ayat, M., and Tseng, E., "Adaptive Kalman Filter-based Yaw Rate Estimation Using Accelerometers and Wheel Speed Sensors", Proceesings of the 2009 ASME Dynamic Systems and Control Conference (DSCC 2009), Hollywood, California, USA, 2009.
13. Hrgetić, M., Deur, J., Kranjčević, N., Tseng, E., Lakehal-Ayat, M., "Analysis of Accelerometer-based Kinematic Yaw Rate Estimators", AVEC'08, 9th International Symposium on Advanced Vehicle Control, Kobe, Japan, October 2008.

Životopis

Mario Hrgetić (rođ. 1979) stekao je titulu diplomiranog inženjera (polje elektrotehnika) 2004. godine na Fakultetu elektrotehnike i računarstva Sveučilištu u Zagrebu. U listopadu 2005. godine zapošljava se na Zavodu za robotiku i automatizaciju proizvodnih sustava Fakulteta strojarstva i brodogradnje Sveučilišta u Zagrebu kao stručni suradnik, a od ožujka 2009. na istom Zavodu radi u svojstvu znanstvenog novaka/asistenta, gdje sudjeluje u nastavi na preddiplomskom studiju iz područja elektrotehnike i električnih strojeva, elektronike i senzora.

U posljednjih 5 godina bio je angažiran na jednom znanstvenom te jednom tehnologijskom projektu podržanom od strane Ministarstva znanosti, obrazovanja i športa Republike Hrvatske, jednom istraživačkom projektu podržanom od strane Sveučilišta u Zagrebu, dvama projektima financiranim od strane automobilske industrije, jednom kolaboracijskom projektu podržanom od strane Europske komisije (u sklopu FP7 okvirnog programa), te jednom projektu Hrvatske zaklade za znanost (HRZZ).

Njegovi istraživački interesi uključuju primjenu postupaka sažimanja (fuzije) senzora te razvoj estimatora s primjenom na dinamiku vozila i mehatroničke automobilske sustave, modeliranje DC/DC energetskih pretvarača u sklopu baterijskih, ultrakondenzatorskih sustava za pohranu električne energije.

Mario Hrgetić je suautor jednog rada u CC/SCI časopisima, tri rada u ostalim časopisima, te 10 radova u zbornicima skupova s međunarodnom recenzijom, te niza studija i tehničkih izvještaja.